SCUOLA DI DOTTORATO
UNIVERSITÀ DEGLI STUDI DI MILANO-BICOCCA

Dipartimento di / Department of

SCIENZE DELL'AMBIENTE E DELLA TERRA / EARTH AND ENVIRONMENTAL SCIENCES

Dottorato di Ricerca in alto apprendistato in / high apprenticeship PhD program in SCIENZE CHIMICHE, GEOLOGICHE E AMBIENTALI / CHEMICAL, GEOLOGICAL AND ENVIRONMENTAL SCIENCES
Ciclo / Cycle 36°

Curriculum in SCIENZE GEOLOGICHE / GEOLOGICAL SCIENCES

Innovation applied to artificial freezing of soils: an experimental study to enhance theoretical and numerical analysis

Cognome / Surname BAVARESCO Nome / Name NICOLA

Matricola / Registration number 766910

Tutore universitario / University tutor: Prof. Paolo Frattini

Tutore aziendale / Company tutor: Dott. Bruno Perra

Supervisor: Prof. Eng. Riccardo Pietro Castellanza

Co-supervisor: Eng. Paolo Caffaro

Coordinatore / Coordinator: Prof. Marco Giovanni Malusà

ANNO ACCADEMICO / ACADEMIC YEAR 2022/2023

Fu forse questa mia confidenza con la neve e con il freddo che mi permise di superare inverni ben più duri? E questa mia familiarità con il bosco e con gli animali che mi aiutò a sopravvivere in certi momenti? Sì, questo. Ma anche tanta fortuna.

Mario Rigoni Stern – Inverni Lontani

Acknowledgements

At the end of this three-year journey, the moments to remember and the people to thank are many.

First of all, I want to thank my supervisor, Prof. Riccardo Castellanza, who, starting from my master's thesis, instilled in me passion and enthusiasm for this field of study and always followed me with commitment and friendship. His creative and sometimes bold stimuli have spurred me to always give my best and grow from a personal and professional point of view.

Groutfreezlab srl, the spin-of of Bicocca for whom I work, that believed in me from the beginning and allowed me to have many experiences and meet professionals in the field who have made me grow professionally, as well as having given me the opportunity to work with unique colleagues such as Dr. Andrea Galli.

A big thank you to Eng. Andrea Pettinaroli and Eng. Paolo Caffaro, who first introduced me to the world of Artificial Ground Freezing, and who through long talks and discussions transmitted me their experience and provided me with insights for the development of this PhD project.

These 3 years spent in DISAT have given me the opportunity to know and work with many people whom I feel I should thank, such as Dr. Nicoletta Fusi for the discussions on the execution of experimental laboratory tests and the lighthearted talks about hobbies and Valsassina events, Prof. Giovanni Crosta for always keeping me on track and helping me in the moments when doubt took over, Prof. Valter Maggi and Dr. Claudio Artoni for sharing the EuroCold Lab with me, Dr. Prof. Elena De Ponti for working overtime to perform CTs on my samples at San Gerardo Hospital.

For the priceless opportunity to visit some construction sites where Artificial ground Freezing has been used in these years in Italy I have to thank Webuild S.p.A., represented by Geom. Antonio Celot, Eng. Angelo Restaini and Geol. Massimiliano Oppizzio. These experiences have been unforgettable.

The realization of the nitrogen-fed freezing pipe would never have been possible without the technical support of Roberto Fantoni and the availability of GTS Riva srl, in particular Michelangelo Riva.

Moreover, a good part of the activities carried out and the results obtained was made possible thanks to the cooperation with master students Dr. Alessia Arcudi, Dr. Alessia Vai, Dr. Fabio Conti, Dr. Fabio Stroppa and Marco Maffeis.

This wonderful adventure would never have begun, nor so much as hand ended, if first my parents and my brother had not pushed me to try. To them I dedicate this milestone.

To my whole family and to Fietta, that represent the roots of my being.

Warm thanks go to lifelong friends and those I have met along this journey, who have been an invaluable resource and have gifted me with lighthearted and joyfull moments.

And finally to you, my Serena!

Milano, autumn of 2023

Nicola Bavaresco

Contents

Introduction iv
List of symbol vi
Chapter 1 1
1 Artificial Ground Freezing: review and aims 1
  1.1 Introduction 1
  1.2 AGF technology 3
    1.2.1 Freezing methods 4
    1.2.2 Design methodology 8
    1.2.3 Building site operations 14
  1.3 Frozen Soils: an overview 15
    1.3.1 Thermal aspects 20
    1.3.2 Mechanical aspects 22
  1.4 Goals of the study 25
  1.5 Case studies 27
Chapter 2 31
2 Preliminary investigation of geomaterials 31
  2.1 Materials 34
    2.1.1 Sample characterization 35
  2.2 Methods 41
    2.2.1 Specimen preparation 41
    2.2.2 Mechanical tests 42
      2.2.2.1 Unconfined compression test 43
      2.2.2.2 Triaxial compression test 45
      2.2.2.3 Brazilian test 47
      2.2.2.4 Point load test 47
    2.2.3 Thermal tests 48

2.2.3.1 Thermal conductivity measurement 48

2.2.3.2 Thermal conductivity estimation..............................49

2.2.3.3 Volumetric heat capacity...53

2.2.3.4 Freezing point of soils 55

2.3 Results 57

2.3.1 Mechanical parameters 57

2.3.2 Thermal parameters...81

2.4 Discussion 86

2.4.1 Mechanical properties 86

2.4.2 Thermal properties 95

Chapter 3 99

3 FEM & IRT: laboratory validation and calibration 99

3.1 Materials and Methods 101

3.1.1 Heat flow modeling...101

3.1.2 Unidirectional freezing tests 104

3.1.3 Infrared Thermography technology - IRT 107

3.1.4 Numerical model - FEM 110

3.2 Results 113

3.2.1 Unidirectional freezing test...113

3.2.2 IRT test...114

3.2.3 Numerical data 118

3.3 Discussion 123

3.3.1 Experimental vs. numerical...123

3.3.2 IRT vs. Thermocouples...130

Chapter 4 132

4 On-site innovative aspects 132

4.1 Materials and Methods 134

4.1.1 On-site activities 134

4.1.1.1 Infrared thermography...134

4.1.1.2 Point load tests 136
4.1.1.3 From site to laboratory 137
4.1.2 Laboratory tests 141
4.2 Results 143
4.2.1 On-site 143
4.2.2 Laboratory tests 146
4.3 Discussion 150
Chapter 5 157
5 Liquid Nitrogen Freezing Pipe 157
5.1 Material and Methods 159
5.2 Results 165
5.3 Discussion 172
Chapter 6 178
6 Conclusions 178
Regulations and References 182
Appendix A 203
Appendix B 207
Appendix C 218

Introduction

Artificial ground freezing (AGF) is a ground improvement technique that originated in the nineteenth century and is now widely known and used worldwide in various fields of geotechnics, mainly as a support for underground or open-air excavations, with structural or waterproofing functions. Over the years, this technique has developed greatly due to the continuous modernization of the technologies used. In addition, scientific research, which began by studying the behavior of naturally frozen soil, has wisely guided its growth and development.

The work carried out in this project came from the collaboration between Groutfreezlab srl and a number of specialists involved in some AGF interventions carried out starting in 2019 in Italy, which are the “Isarco River underpass” and cross-passages of “Line 4 of the Milan subway”. The opportunity to interact with these professional figures, who designed and followed the AGF interventions, and to frequently visit the building sites allowed to create an innovative comprehensive study that provided support from the preliminary design phase to the control and monitoring phase during tunnel excavation operations. In fact, many geomaterials coming from the above sites (soil, concrete lining of tunnel and cement-mixture treated soil), and others such as saline soils, coming from other sites not subject to AGF, were taken into consideration.

These geomaterials were subjected to mechanical and thermal tests to identify the mechnical and thermal parameters under different thermal conditions, and the data provided an important database upon which to base the final design. The data obtained show great consistency with previous work.

A constructive comparison also identified some shady areas that represented points of early development, such as performing point load tests in situ on frozen soil samples to estimate the true strength of the frozen soil shell or monitoring the temperature at the excavation face with an infrared imaging camera to assess intervention quality and frozen wall thickness. The collection furthermore of frozen material from a site gave the opportunity to study undisturbed samples, through a workflow consisting of storage stages, investigation by Computed Tomography (CT), and dry coring, and to compare the results with test values inherent in the design phase to assess their reliability at the preliminary stage.

These type of interventions, like any other massive intervention in the ground, is supported by numerical modeling that allows the effects of a process within a domain to be calulated in a distributed manner. Similarly, the AGF makes use of FEM-based thermal analyses that allow to predict cold front propagation within the ground and to perform possible "adjustments" to the arrangement of the freezing pipes to reach the established temperature targets, furthermore such a tool allows to estimate execution times, and in an indirect way also costs. Based on these considerations, a simple and fast laboratory test of unidirectional freezing of a soil sample was developed to be able to provide useful data for validation of commercial numerical codes.

The use of LN_2 at visited construction sites as a coolant has prompted a search for methods to numerically simulate the freezing effect induced by an LN_2-fed freezing pipe, since the thermodynamic processes that takes place within it are very complex. In the state of the art, there are oversimplified methods that are based on the often sparse data referring to what happens in the probe in vertical position. This has led to the design and construction of an innovative freezing pipe with a large number of temperature sensors positioned to capture the level of liquid nitrogen inside the pipe, external and internal temperatures, and to compare the distribution of temperatures in vertical and horizontal positions, with dry or wet sand, and to monitor liquid nitrogen consumption. The data collected are of great value for detailed numerical simulation.

After a general introduction in which AGF and frozen soils are described, and pointing out some weaknesses or shortcomings of the method, the objectives of the study are stated and the building sites considered are described. Then the activities carried out are described in Chapters 2, 3, 4 and 5, divided into a brief introduction, materials and methods, results and discussion. Chapter 6 contains general conclusions about the individual chapters and the project overall.

List of symbol

Greek symbols

α	thermal diffusivity
γ_n	natural specific weight
ε	emissivity of a body
η	material properties (eq. 2.9)
θ_w	volumetric water content
θ_w	volumetric water content
θ_{uwc}	volumetric unfrozen water content
θ'_{uwc}	normalized unfrozen volumetric water content
κ	empirical parameter (eq. 2.5)
ρ_d	dry density
ρ_m	bulk density of mineral
ρ_s	bulk density of soil matrix
ρ_w	density of water
σ_1	major stress
σ_3	minor stress/radial stress
σ_c	compression strength
σ_n	normal stress
σ_t	tensile strenght
-	Stefan-Boltzmann constant
τ_n	shear stress
ϕ, φ	friction angle

ϕ	diameter
χ	material properties (eq. 2.9)
ω	percentage in weight of minerals (eq. 2.8)

Roman symbols

a_r	factor that define radius of influence of freezing pipe
c	specific heat
-	cohesion
c_{air}	specific heat of air
c_i	specific heat of ice
c_m	specific heat of each mineral
c_s	specific heat of soil grains
c_w	specific heat of water
C	volumetrci heat capacity
-	correlation factor between Is(50) and σc (eq. 2.25)
C_a	apparent volumetric heat capacity
C_f	volumetric heat capacity at frozen state
C_{unf}	volumetric heat capacity at unfrozen state
D	diameter
D'	distance between points at the end of PLT
D_{max}	maximum diameter
e	void index
$E_{sec(0.4)}$	Young’s modulus secant at 40% of UCS
E_{t50}	Young’s modulus tangent of 50% of UCS
h	convection heat transfer coefficient
H	heat capacity
-	height

I_s	strenght index of PLT
$I_{s(50)}$	normalized strenght index of PLT
J	thermal radiant exitance
k	thermal conductivity
k_0	thermal conductivity of other minerals (eq. 2.17)
k_{dry}	thermal conductivity of dry soil
k_f	thermal conductivity at frozen state
k_i	thermal conductivity of ice
k_m	thermal conductivity of each mineral
k_{qtz}	thermal conductivity of quartz
k_r	normalized thermal conductivity
k_s	thermal conductivity of soil grains
k_{sat}	thermal conductivty of saturated soil
$k_{sat(f)}$	thermal conductivity of saturated soil at frozen state
$k_{sat(u)}$	thermal conductiviy of saturated soil at unfrozen state
k_{unf}	Thermal conductivity at unfrozen state
k_w	thermal conductivity of water
k_x, k_y, k_z	thermal conductivity along x, y and z axis
K_e	Kersten’s number
L	latent heat
-	length
L_f	latent heat of fusion of water
m	mass of soil
m_{air}	mass of air
m_i	mass of ice
m_s	mass of solid
m_w	mass of water

n	porosity
n_f	soil porosity at frozen state
n_u	soil porosity at unfrozen state
P	load of failure under PLT
q	quartz fraction
-	specific heat flux
Q	heat flux
r	thermal resistivity
r_s	thermal resistivity of soil grains
r_w	thermal resistivity of water
S	soil salinity
-	thickness
S_r	saturation degree
S_{rf}	saturation degree at frozen state
S_{ru}	saturation degree at unfrozen state
S_w	water salinity
t	time
T	temperature
T_{air}	temperature of air
T_{bottom}	temperature at the bottom of specimen
T_{fp}	temperature of freezing point
T_{sc}	temperature of super-cooled state
T_{sur}	temperature of exchanging surface
T_{top}	temperatore at the top of specimen
T_∞	temperature of fluid at infinite distance
x	volumetric proportion of minerals
x, y, z	axis of the 3D space

w	water content
w_i	frozen water content
$w_t\%$	percentage in weight
w_u	unfrozen water content

Chapter 1

1 Artificial Ground Freezing: review and aims

1.1 Introduction

Artificial ground freezing (AGF) is a method of ground improvement used as a support for open-air and underground excavations in fully or partially saturated soils.

This method, first used in civil engineering in 1862 in South Wales and patented in Germany by Poetsch in the same year, first appeared in Italy in 1937, when it was applied to recover the *Ara Pacis Augustae* in Rome (Rocca, 2011).

The ground freezing process is achieved by extracting heat through specific heat exchangers called *freezing pipes* fed with coolant fluids and installed in the ground with a specific geometric configuration established during the design phase (Figure 1.1.a). These pipes consist of two coaxial metal tubes, usually of stainless steel or copper where the outer tube is plugged at the end. The coolant fluid flows into the gap between the inner and the outer tube, so that it exchanges heat with the ground through the outer wall of the pipe. The flow is defined as *direct* when the coolant inflow is in the inner tube and the outflow is in the gap between the two, or *reverse* if it flows in the opposite direction. By cooling the soil, its properties change in such a way that for a given time the soil acts as an independent, supporting and/or impermeable element (Jessberger, 1980) because water naturally present in it turns into ice, and the ice acts as a bonding agent between the soil particles, increasing the mechanical strength and decreasing the hydraulic permeability of the soil.

The freezing of the ground starts around each single freezing pipe, forming a column of frozen ground (Figure 1.1b). This column grows over time until it merges with the column formed around the neighbouring pipes, so several separate columns form a wall. In this way it is possible to obtain a portion of frozen ground of the desired shape and size.

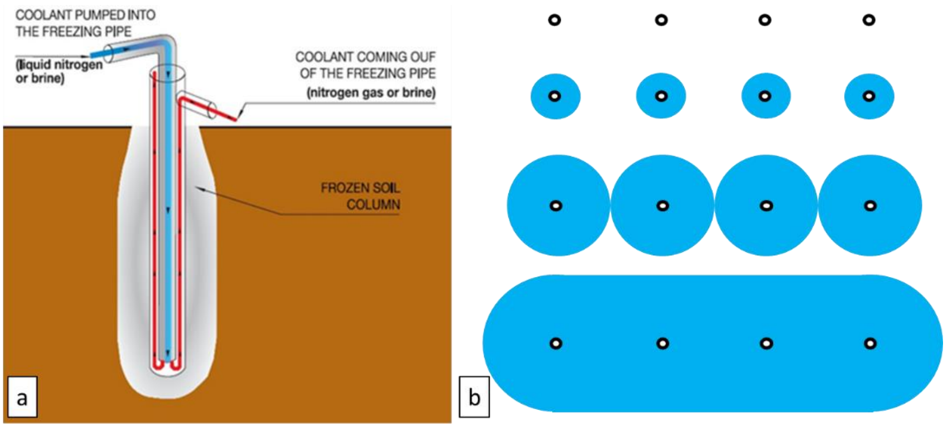

Figure 1.1: Artificial ground freezing principles: a) coolant flowing layout into a freezing pipe; b) section of the soil freezing process starting from the freezing pipes (FP) to the merging of frozen soil columns to the formation of frozen soil wall.

From a wider point of view, an AGF operation can be divided into three phases: the freezing phase, in which the desired volume and shape of frozen soil wall is achieved; the maintenance phase, where this portion is maintained frozen during excavation and concrete lining of the excavation (Gallavresi, 1981); and the thawing phase, in which the freezing system is switched off and soil settlements are monitored.

Over the years, several methods of soil consolidation and soil sealing, like concrete or chemical mixture injection, have emerged and developed, but AGF is the most versatile. As shown by Harris (1995) in Figure 1.2, compared to the other methods AGF is applicable to soils of any grain size distribution. The only requirement for using AGF is to operate below the water table. Moreover, it offers several advantages:

- AGF is a temporary type of treatment: at the end of it, the entire cooling plant is dismantled, and site conditions are restored.
- It is adaptable to practically any size, shape, or depth of excavation or structure and can be done with the same physical plant from site to site, despite wide variation in these factors (Braun et al., 1979).
- it is characterised by a higher level of homogeneity of treatment (Rocca, 2010).

- it’s environmentally friendly on site; no product remains in the soil and no polluting vapours, vibrations or noise pollution are produced.
- allows to obtain the so-called *water-tight box*. In the case of open-air excavations, this is usually achieved by embedding the frozen wall in a low permeability layer at the base of the excavation (Braun et al., 1979).

All these aspects have allowed for the increasing popularity of this technique as a replacement for traditional soil improvement techniques in hundreds of projects, including Vienna Subway Section U 6/3 (1989), Düsseldorf Subway Section 3.4H (1993), Milano Subway MM3 section 2B (1994), Boston Central Artery/Tunnel (2002), Munich Subway Station Marienplatz (2006), Warsaw Underground Line II Station C13 (2012), BBT Isarco underpass (2020) and Milano Subway MM4 (2021). In addition to tunnelling, AGF was also widely used for the development of mineral deposits, in the mining and coal industry (Sadovsky and Dorman, 1981).

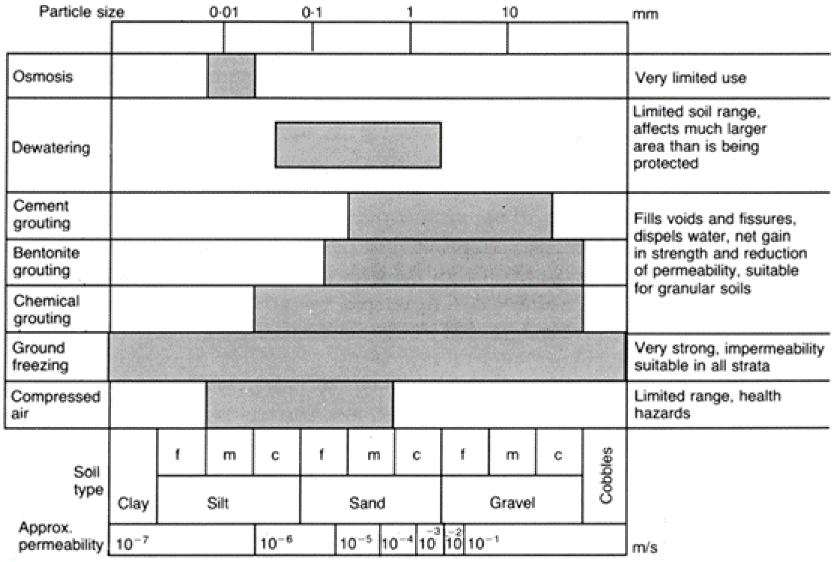

Figure 1.2 Applicability of geotechnical processes according to soil type, after Harris (1995)

1.2 AGF technology

The use of freezing is still a challenging task since the factors that need to be considered are of a different nature. These include the choice of the freezing method, the intervention design and the forecast calculation of time and costs, and finally the execution phase, crowned by monitoring and control. These factors depend on the interaction between site-specific conditions and the structural requirements of the design excavation.

1.2.1 Freezing methods

Three freezing methods based on the type of coolant fluid fedding the freezing pipes exist: direct (liquid nitrogen, LN_2), indirect (brine) and combined method (LN_2 + brine).

The direct method consists of an open circuit fed with LN_2 (Figure 1.3). This liquid gas is stored under pressure (2÷3 bars) inside tanks where the insulated distribution line carrying nitrogen to each freezing pipe starts. The liquid nitrogen flows through the inner tube of the freezing pipe and returns in gaseous form through the space between the inner and outer tubes. The phase transition, which occurs due to the heat exchange between LN_2 (-196 °C) and the surrounding ground (typically 10/20 °C), initially occurs at the end of the inner pipe, but depending on cooling trend and the arrangement of the device, it can move along the pipe. During evaporation phase, 1 lt of liquid absorbs 80.57 kJ of heat and expands up to 650 times (see Colombo, 2010).

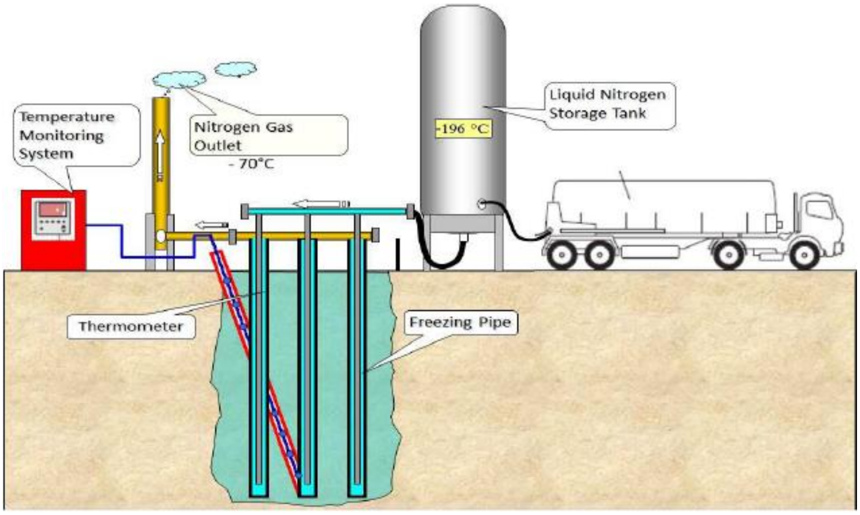

Figure 1.3: Principal scheme of the liquid nitrogen freezing system, after Mira-Cattò et al. (2016)

This volumetric expansion requires great care in the sizing of the two coaxial tubes that compose the freezing pipe. In fact, the diameter of the outer pipe can be up from 3 to 4 times greater than that of the inner pipe. The inflow of LN_2 is regulated by a system of opening/closing cryogenic electromagnetic valves that supply coolant to guarantee an outlet gas temperature usually between -60 and -90 °C, measured by thermoresistors or thermocouples. If the system permits, these valves can control groups of 2 or more freezing pipes, connected by clarinets. The gas, because of its cold temperature, exchanges 0.0013 kJ/lt °C with the soil (e.g., 1 lt of LN_2 evaporating at -196 °C and venting in a gaseous state at -80 °C will be able to absorb 80.57 kJ + 97.48 kJ from the soil, see Colombo, 2010). Once the nitrogen is gassed, it is channelled and vented away from the construction area through a ventilation system and chimneys. Even though it is an inert gas and the main component of atmospheric air (N_2= 78%, O_2= 20.95%, others= 1.05%), it poses a danger since an increase in N_2 would lead to an under-oxygenation of the air, which at values below 19.5%, causes human diseases and, at a lower values in the worst cases, death.

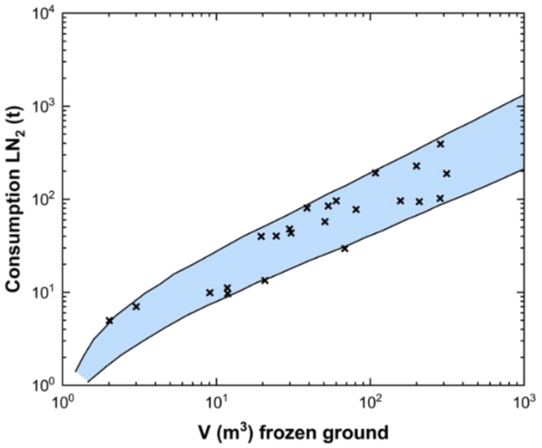

Figure 1.4 LN_2 consumption as function of frozen volume, after Veranneman and Rebhan (1979)

This method is usually chosen when there is only limited time available to perform AGF or the groundwater flow is very high. The huge cooling power resulting from the use of LN_2 in fact allows to freeze the soil very quickly, reducing the formation of ice lenses in soils sensitive to freezing (Stoss and Valk, 1979). Despite on-site equipment and installations are simple, it is difficult to design and control the system in such a way that a regular shape of the frozen wall is achieved, because its refrigerant power is not equally distributed along the pipe. Furthermore, the coolant, since it is non-reusable, is very expensive. To evaluate the costs of liquid nitrogen needed, Veranneman and Rebhan (1979) investigated the correlation between LN_2 consumption and frozen soil volume (Figure 1.4).

The indirect method consists of a closed circuit with a constant volume of liquid, usually brine, flowing through it at a temperature between -28 and -.35°C (see Figure 1.5). This coolant is chilled through a second circuit powered by a refrigeration system fed with Freon or ammonia. Once cooled, the brine is supplied into the insulated distribution system at 5÷10 bar (Rocca, 2011) leading to each freezing pipe. The brine flows through the inner tube and returns through the gap between the inner and outer tubes extracting heat from the soil. The type and velocity of flow and the thermal gradient between coolant and soil determine the cooling power of this method. The tubes that constitute the pipe must be sized to avoid significant variations in the brine inlet and outlet flow section. After exchanging heat with the soil, the brine is collected and returned to the refrigeration system where it is cooled again to the desired temperature and pumped back into the distribution system. This method is a simple technology that guarantees more homogeneous results, because the homogenous cooling power along the pipe, and, after an expensive initial cost for the plant, does not imply additional costs as the coolant is re-utilised. The low overall cost and low cooling power make this method preferable when soil volumes are greater than 500 m^3 (Rocca, 2011) and groundwater flow is low.

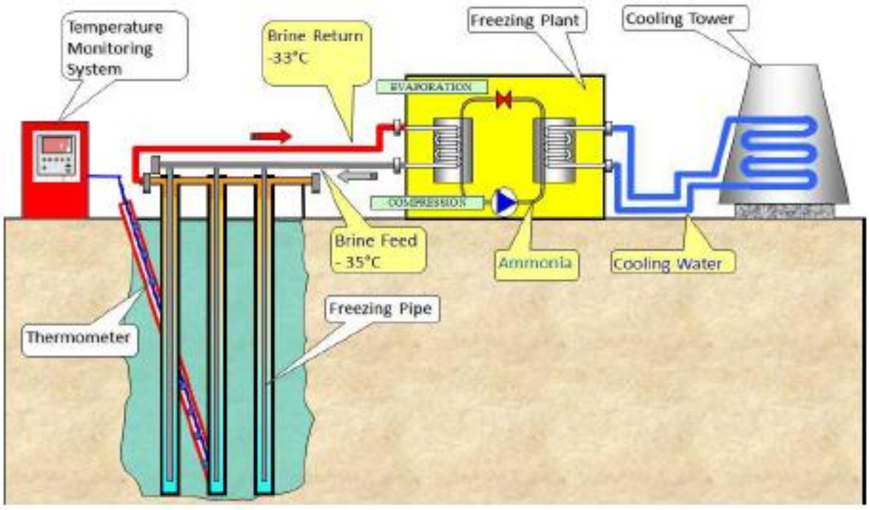

Figure 1.5: Principal scheme of the brine freezing system, after Mira-Cattò et al. (2016)

The two methods, as compared by Stoss and Valk (1979) (Table 1.1), have very different characteristics that must be considered in relation to site conditions and available time and costs.

As shown in Figures 1.3 and 1.5, both freezing methods are supported by temperature monitoring systems consisting of thermometric probes that measure temperature trends in the soil. These probes are equipped with various temperature sensors such as thermoresistors, thermocouples or optic fibers and are placed in the soil in strategic positions in relation to the arrangement of the freezing pipes. These thermometers are used to manage the freezing and maintenance phases.

The third method consists of a combination of the direct and indirect methods for the freezing and maintenance phases, respectively. This combination, accurately described by Gallavresi (1981), incorporates the positive key aspects of the two methods but requires a careful cost analysis as the switch from one system to another takes time, two types of refrigerant plant will be required, and the freezing pipes need to be changed or well designed to be efficient with the two different coolant fluids. In the combined method, therefore, once the freezing phase is complete, the indirect method replaces the direct one. In some projects, however, the two methods were used simultaneously in different areas of the intervention, such as in Warsaw Underground Line II Station C13 (see, Balossi Restelli et al., 2016).

Table 1.1: Characteristics of LN_2 and brine freezing, after Stoss and Valk (1979).

	Quality	**LN_2**	**Brine**
Site installations	Electric power	Not required	Required
	Water for cooling	Not required	Required
	Refrigeration plant	Not required	Required
	Storage tank	Required	Required
	Circulation pumps	Not required	Required
	Pipe system for distribution of coolant	Supply only	Supply and return
	Low temperature material for surface pipes, valves, etc.	Required	Not required
	Low temperature material for freezing pipes	Not required	Not required
Execution of freezing	Physical condition of coolant	Liquid / vapour	Liquid
	Minimum temperature achievable (theoretic)	-196 °C	-34 °C, $MgCl_2$ -55 °C, $CaCl_2$
	Re-use of coolant	Impracticable	Standard
	Shape of freeze wall	Difficult	Easy
	Temperature profile in freeze wall	Often irregular	Regular
	Frost penetration	Great differences	Small differences
	Impact on freeze wall in case of damage to freeze pipe	None	Thawing effect
	Noise	None	Little

1.2.2 Design methodology

The design of any freezing system requires a thorough knowledge of the mechanics of the freezing process and the effects of the freezing process on the soil. Some of the major considerations in design of a freezing program include site and laboratory data gathering, thermal design, associated ground movements and structural design (Jones, 1981), strength of the frozen and unfrozen soil and cost of the freezing system (Jones and Brown, 1979).

The design phase mainly consists of the following activities (Rocca, 2011):

- preliminary soil investigation
- definition of the geometry of the intervention and subsequent positioning of the freezing pipes;
- calculation of the cooling power and the time required to reach the desired target;
- structural dimensioning of the frozen wall, in case it has to perform the function of supporting the excavation;
- choice of the most suitable materials for pipes and distribution line constructions;
- design of the monitoring system.

The geometry of the frozen soil volume is strictly related to the type and shape of the excavation to be carried out and can be modified according to site-specific conditions. The length of the spacing between the freezing pipes, typically between 60 and 100 cm, is calculated on the basis of thermal, execution and economic considerations. The correct positioning of the pipes ensures that there is adequate interpenetration and welding between the single columns of frozen soil. It is also advisable to provide for crowding of the pipes in crucial areas, such as in the crown in the case of freezing in support of tunnel excavation. The deviation of boreholes, drilled to accommodate the freezing pipes, should be measured using inclinometer, optical or electrical devices as described by Heinrich et al., (1978) to evaluate the supplementary holes drilling. The arrangement of the pipes must also not be uneconomical; this may occur in the case of freezing a large portion of soil that is to be excavated.

The function of the frozen soil wall determines the size of its thickness: for strictly waterproofing reasons it is usually 1m; for structural functions 2÷2.5m. The mechanical properties of frozen soils in connection with the thermal conditions are the governing parameters for the design of structures of frozen soils (Jessberger, 1981) because they allow a more precise calculation of the target thickness of the frozen soil wall in order to avoid underestimates, and thus stability problems, or overestimates, which lead to over costs. In the case of interference with existing structures, such as tunnels, shafts, or others, it is imperative to know the mechanical and thermal parameters of their constituent materials such as concrete, as Winkler et al., (2004), Li et al., (2016) and Abbas and Nehdi

(2021) did, in order to integrate them into a geotechnical model (see Zhao et al., 2023). A preliminary knowledge of the mechanical properties of all involved geomaterials is therefore certainly advantageous to make a good structural design. it is important to emphasize that these properties refer to the frozen condition that represents the intermediate stage of the AGF process, not the initial one, so it is important to perform tests on geomaterials in which the working conditions are recreated in the laboratory.

The thermal design of freezing process is aimed at defining the cooling power and time required to obtain the desired frozen ground geometry and is defined by solving a complex problem such as the heat transfer process with phase transitions, in a three-phase medium such as saturated ground.

Traditionally, thermal design has been performed by analytical methods of Stephan and Neumann type, amongst many described by Carlaw and Jaeger (1959), and Harlan and Nixon (1978). A more elaborate model of semi-empirical nature was presented by Khakimov (1957) and refined by Sanger and Sayles (1979).

By Sanger and Sayles (1979) method, design computation for the amount of energy to be extracted for freezing, the time required for freezing and the refrigeration plant capacity can be determined. In this method, thermal calculations are made for three stages: stage I, the frozen soil column grows around the single freezing pipe; stage II, the separate frozen soil columns merge to form a continuous wall; stage III, two walls formed by two different rows of freezing pipes merge to form a single wall. This approach is widely used in the design phase to assess the time required to complete the frozen wall (stage I), which is the most crucial phase of the entire intervention.

In this stage, for steady state heat flow the temperature distribution around a single pipe (see Figure 1.6) is described by the following expressions:

$$T_f = \frac{T_s}{\ln\frac{R}{r_0}} \ln\frac{R}{r_f}; \text{ for } r_o < r_f < R \tag{1.1}$$

$$T_u = \frac{T_o}{\ln a_r} \ln\frac{r_u}{R}; \text{ for } r_u > R \tag{1.2}$$

where T_f is the temperature at radius r_f in the frozen cylinder, T_u the temperature at radius r_u in the unfrozen region, R the radius to the interface between unfrozen and frozen soil,r_o the radius of the freezing pipe, T_s the difference between the temperature at the surface of the freezing pipe and the freezing point of water, T_0 the difference between the original temperature of the ground and the freezing point of water and a_r the factor which when multiplied by R defines the radius of temperature influence of the freezing pipe. Because there is a change in phase of water to ice, the change in thermal parameters of soil, like conductivity and capacity, causes a discontinuity in the temperature versus distance curve at the boundary between unfrozen and frozen soil.

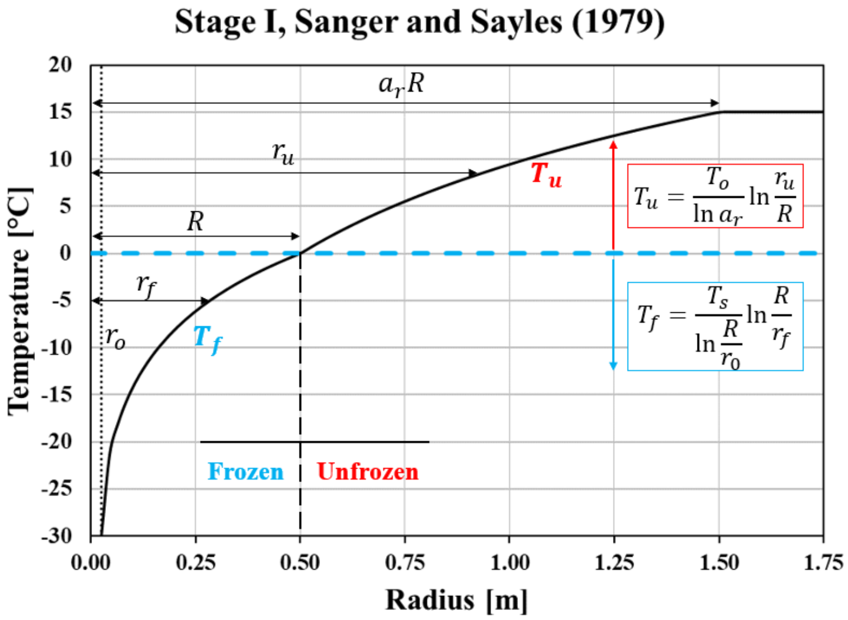

Figure 1.6: Temperature distribution over distance around a single freezing pipe: Stage I. In this example T_0= 15°C, T_s= 30°C, r_0=0.025m, R=0.5 and a_r=3.

In stage I, total energy extracted from ground to freeze a cylinder of radius R is the sum of several factors as follows:

$$Q_I = \pi R^2 \left[L + \left(\frac{a_r^2 - 1}{2 \ln a_r} \right) C_u T_0 + \frac{C_f T_f}{2 \ln(R/r_0)} \right] \qquad (1.3)$$

where L is the volumetric latent heat of fusion of the soil water and C_u and C_f the volumetric heat capacity for unfrozen and frozen soi, respectively.

The time t_I required to freeze the soil column to a radius R can be obtained by the equation:

$$t_I = \frac{R^2 L_I}{4 k_f T_s} \left[2 \ln\left(\frac{R}{r_0}\right) - 1 + \frac{C_f T_s}{L_I} \right] \tag{1.4}$$

where

$$L_I = L + \left(\frac{a_r^2 - 1}{2 \ln a_r} \right) \tag{1.5}$$

and k_f is the thermal conductivity of the frozen soil. For problems of triple-row or multi-row -piped frozen temperature field Hu et al., (2017) proposed their analytical solution.

The Sanger and Sayles (1979) method , recently adjusted by Calderón et al., (2023), allows preliminary evaluations of the energy consumption and time required to reach specific thermal targets but is not a tool for solving intricate 3D problems because freezing soil field is a complicated transient heat conduction problem involving soil-water phase change, moving freezing front, internal heat source and complex moving boundary conditions (Song et al., 2016). For this reason, numerical codes based on finite element (FEM) methods, that solve the basic differential equations for heat transfer with realistic geometries, material properties and boundary conditions (Frivik and Thorbergsen, 1981), has become the most used tool as support of thermal AGF design.

Over years, several authors have proposed and used different models, thermal or thermo-hydro-mechanical (THM) as done by Nishimura et al. (2009) and Zhou and Meshke (2013) who combined the variation of mechanical, thermal and hydraulic properties of the soil at changing temperature. Generally, it can be said that many authors have dealt with numerical modeling of AGF from the development of new analytical solutions, previous authors work, or from experimental studies that provided the basis for model validation. Anyway, one of the most interesting points of the thermal modeling is the boundary conditions of the problem used to simulate the cooling effect of the freezing pipes. If the coolant considered is brine, the literature returns many interesting works in which the freezing pipes have been simulated as lines with a constant temperature equal to -20 °C (see Zhou and Meshke, 2013) and -30 °C (see

Song et al., 2016 and Hu et al., 2018), or decreasing linearly until reaching -30 °C (see Liu et al., 2022). To do this, boundary conditions of the type $T = f(t)$ were imposed on the lines corresponding to the pipes. In other cases, heat extraction can be simulated by an heat outflow, which results from a forced convective movement of the cold brine inside the freezing pipe (Geoslope, 2020). A detailed understanding of this phenomenon allows to simulate cooling following Newton's law of convection heat exchange with the surrounding soil. More refined studies have also considered the heat exchange occurring inside the freezing pipe as done by Vitel et al., 2015 who considered heat transfer in the freezing pipe and the surrounding ground in a coupled way. The solution of the problem is obtained through an iterative process that couples the problem in the well and in the ground. Once the model is developed, it can be applied to cases in which a high speed seepage is considered (see Vitel et al., 2016).

Performing a numerical simulation of a freezing intervention carried out with liquid nitrogen is much more complex because of the processes that, as explained in Section 1.2.1, occur and move within the pipe very fast. The only information usually available is the nitrogen state transition temperature and the exhausted gas outlet temperature measured at the site. To carry out simplified 3D thermal modeling, many authors have considered freezing pipes as lines where T= -183°C (see Gioda et al., 1994), T= -80°C (Colombo, 2010 and Cai et al., 2018), T linearly varying from -196°C to -110°C (Mauro et al., 2020), T exponentially varying from -150°C to -60°C along the pipe (see Kang et al., 2021). All of these simplified models are widespread and widely used, but the increasing development of cases where LN_2 is used as a coolant requires more sophisticated and comprehensive models that take into account many aspects of LN_2 such as its phase transition, which covers half of the cooling power of nitrogen, and the position of the pipe, since they are mainly installed in a subhorizontal position and this could affect the distribution of the coolant within it.

A fundamental element of all proposed numerical models and analytical solutions is prior knowledge of the frozen and unfrozen soil thermal parameters that govern the flow of heat by conduction within a soil. The following sections will discuss methods for calculating or measuring thermal conductivity, volumetric heat capacity, and freezing point temperature.

Typically, specialists who need to perform thermal analyses rely on commercial software such as Abaqus, COMSOL Multiphysics, TEMP/W and FeFlow, or others for which no further implementation is necessary. Only knowledge of the code and its proper use confer reliable predictive power to the modeling, which is the most important issue of a code since an incorrect forecast could lead to errors in the evaluation of frost propagation and consequently an increased consumption of time, resources, and costs.

Verification of an effective fit between model and reality is, however, possible by performing laboratory tests at a preliminary stage of the project, so that a code whose robustness is known can be used.

1.2.3 Building site operations

From a practical point of view, an AGF intervention consists of the following main site phases (see Braun et al., 1979):

- Site investigation
- Mobilisation of equipment and materials
- Site preparation
- Drilling and installation of freezing pipes
- Installation of a distribution system and refrigeration system
- Installation of freezing process monitoring instruments
- Freezing the ground
- Insulation of the frozen wall during and/or after excavation
- Maintenance of the frozen wall
- Removal of the installation

The success of a freezing operation is monitored and evaluated through a dense network of monitoring systems consisting of temperature sensors and piezometers. The first ones are placed along thermometric probes, usually outside the alignment of the freezing pipes, and signal when the thermal targets and thicknesses of the frozen wall have been reached; the second ones help to understand, depending on the water pressure inside the watertight box, whether an impermeable shell has formed. Freezer probes are rarely placed inside the probe alignment as these would interfere with excavation operations. This means that temperatures inside are not monitored, although it should be noted that if a thickness is reached externally, where conditions are unfavorable, it will surely be reached internally, where conditions are more favorable. The monitoring system is active during both freezing and maintenance phases. Imperfections in the shell can be caused by groundwater flows that are not compatible with AGF technology (i.e. greater than 50 m/s, see Shuster, 1972), noncompliance with the established pipe spacing, and proximity to structures that contribute external heat fluxes.

These critical issues can be resolved in the execution phase by reducing the spacing, installing additional pipes, decreasing the temperature of the coolant or clogging the subsoil using traditional methods (e.g. permeation grouting) to reduce hydraulic permeability (Rocca, 2011).

Like any building site activity, artificial ground freezing presents risks, which can be identified through careful analysis. These risks must be eliminated or mitigated through a series of safety measures implemented by all those involved in the activity. In addition to the traditional precautions three additional risks must be considered in freezing operations:

- Cold injuries from contact with refrigerant distribution lines;
- Projection of pressurised refrigerant fluid onto body parts;
- Anoxia due to under-oxygenation of the atmosphere.

The first two types of risks are easily solved by simple operations, such as thermal insulation of line pipes, protection of pipes from accidental shocks and the use of suitable clothing. The third risk deserves greater attention in terms of the security measures to be taken since it does not manifest itself and can therefore be difficult to manage. There are essentially four main safety measures: continuous monitoring of the percentage of oxygen in the atmosphere; automatic system for cutting off the liquid nitrogen supply from the tanks; permanent presence of staff, both in the shaft/tunnel and near the nitrogen storage tanks and continuous, forced air ventilation through fresh air supply.

Another point, which does not represent a real risk, as much as a shadow area is the real mechanical strength of the soil forming the frozen shell around the excavation, in case this should also act as a structural function. In the state of the art, in fact, preliminary tests can be carried out, or samples of frozen soil can be taken to certified laboratories during construction and there subjected to mechanical tests, but this takes a long time.

1.3 Frozen Soils: an overview

Frozen ground is soil or rock with a temperature below 0 °C. The definition is based entirely on temperature and is independent of the water and ice content of the soil or rock (Andersland and Ladanyi, 2004)

Frozen ground, spread principally in the form of permafrost, covers about 1/5 of the world (Brown, 1981), and for this reason, in regions where it is present and interacts with geotechnical structures, it has been studied for decades, so much so that a glossary was created by Harris et al., 1988 to resolve semantic issues about the meaning of some terms to describe it. In recent decades, studies of natural frozen ground have focused on the effects of permafrost warming (see Osterkamp and Romanovsky, 1999), with much attention to the effects in the alpine environment (see Harris et al., 2003) and related to alpine rock wall destabilization (see Gruber et al., 2004). From physical appearance Linell and Kaplar (1966) decoded a description for both naturally and artificially frozen soils, still currently in use.

The freezing process of porewater is at the heart of the transition from the unfrozen to the frozen state. The formation of ice in soil pores involves the cooling of a soil-water system, as is illustrated in Figure 1.7.

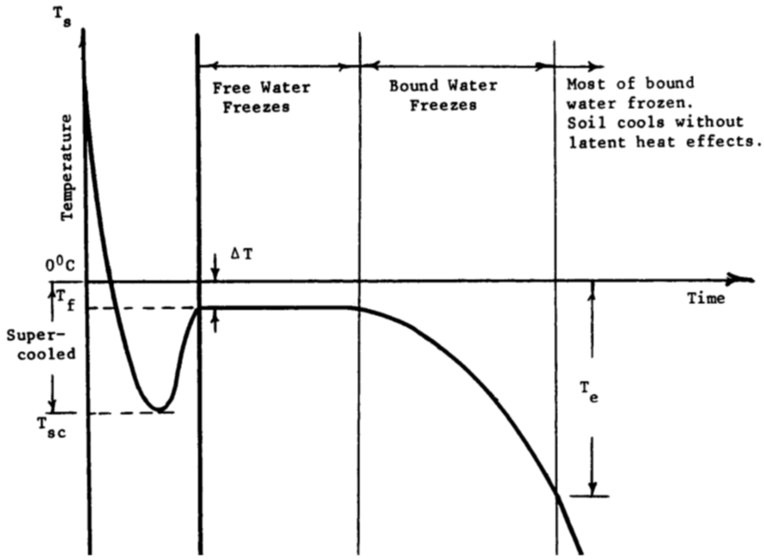

Figure 1.7: Cooling curve for soil water and ice, after Lunardini (1981)

The pore water does not start to freeze until the temperature drops to T_{sc}. The supercooled water is in a metastable equilibrium state until an abrupt transformation of free water to ice is triggered by nucleation centers. These nuclei can be aggregations of water molecules or soil particles. The formation of ice releases latent heat, causing a rise in temperature to T_{fp}, the initial freezing temperature. For cohesionless soils with small specific surface areas, T_{fp} will be close to 0 °C. For fine-grained soils (silts and clays), the temperature depression (DT) can be as much as 5 °C. Free water in the soil pores will now freeze at the temperature T_{fp} . As free water changes to ice, the release of latent heat will slow the rate of cooling until a temperature T_e is reached (see Andersland and Ladanyi, 2004).

Data reported by Anderson and Tice (1972) show that part of pore-water remains unfrozen in the form of thin, liquid like layers on the particle surfaces, during freezing processes. Current practice neglects the vapor phase and divides the total water content w (dry weight basis) into two categories: unfrozen water, w_u, and ice, w_i. Thus the water content w is expressed as:

$$w = w_u + w_i \tag{1.6}$$

The relationship between the two water contents changes over temperature and is a function of the mineralogical composition, particle size distribution of the soil and the specific surface area of mineral particles. Models including that of Anderson and Tice (1972), Michalowski (1993), McKenzie et al. (2007), Kozlowski (2007) and Zhang et al. (2017) have been developed to define the water content that remains unfrozen during cooling of a soil. By freezing, water gradually transforms into ice, whereby the H_2O molecules arrange themselves following a well-defined crystal lattice that gives this medium completely different characteristics and properties than in the liquid state. This also causes a change in the properties and characteristics of the rock mass or soil that previously contained water, and now ice. The thermal, optical, electrical, and chemical properties of ice have been extensively studied in the past by several authors including Pounder (1965) and Petrenko and Withsworth (1999) and Mellor (1980), according to whom non-saline polycrystalline ice displays a wide range of mechanical properties, including elasticity, non-linear viscosity, creep rupture and brittle fracture. Ice has a lower density than water, which means that for the same mass, ice has a larger volume (+9%) (Figures 1.8).

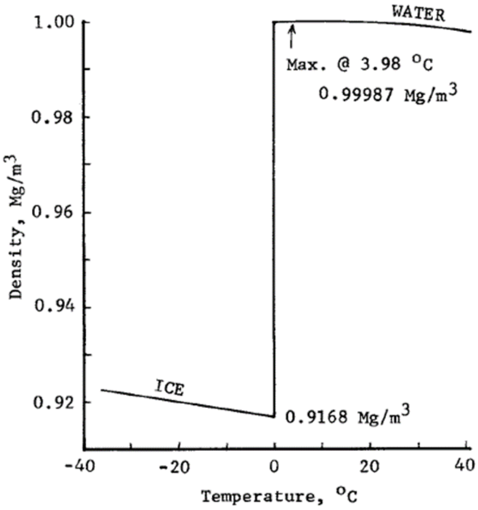

Figure 1.8: Density variation for water and ice, after Pounder (1965)

Ice expansion can have direct effects on the soil in which it is contained, manifested by heaving and thawing processes in the freezing and melting phases, respectively. Heaving is of great interest for studying the interaction with roads or railways in places where superficial layers of frozen ground seasonally form. Heaving is the result of ice segregation during the freezing process. The advance of the freezing front causes alternating bands of soil and ice to form. When the ice melts, the aggregates of soil particles usually cannot reabsorb all the water immediately after thawing. Consequently, soils are frequently weaker after thawing than before freezing (Chamberlain, 1981). This gave rise to the definition of frost-suceptible soil that is defined in terms of its frost-heaving and thaw-weakening behavior. Both can cause considerable damage to engineering structures, the former during freezing and the latter during thawing (Andersland and Ladanyi, 2004), so much so that ASTM D5918-13 was created to study them. Frost heave, which depends on the index properties of a soil (Konrad, 1999), is most significant on fine soils (Hendry et al., 2016). Models have also been created to simulate this process (see Ma et al., 2015). This swelling generates forces (Kinosita, 1966) that act horizontally, vertically, and inclined in bodies embedded in the soil (Domaschuk, 1982). These forces interpreted as pressures (Frost Heave Pressure - FHP) are to be considered in the case of investigating the heave of a portion of frozen soil under burying conditions (see Takashi et al., 1978, Hopke, 1980, Wang and Zhou, 2018). The study of thawing is also very important because susceptible soils have been seen to generate considerable subsidence at this stage (Figures 1.9), which for compressible soils Morgensten and Nixon (1971) likened to monodirectional consolidation based of heat conduction and of a linear consolidation. Thawing also, by causing a reduction in void ratio, can have an effect on the hydraulic permeability of a soil after several freeze/thaw cycles (Viklander, 1998), which generally increases, especially in the vertical direction (Chamberlain and Gow, 1979) but, in the presence of loads, decreases (Othman and Benson, 1993).

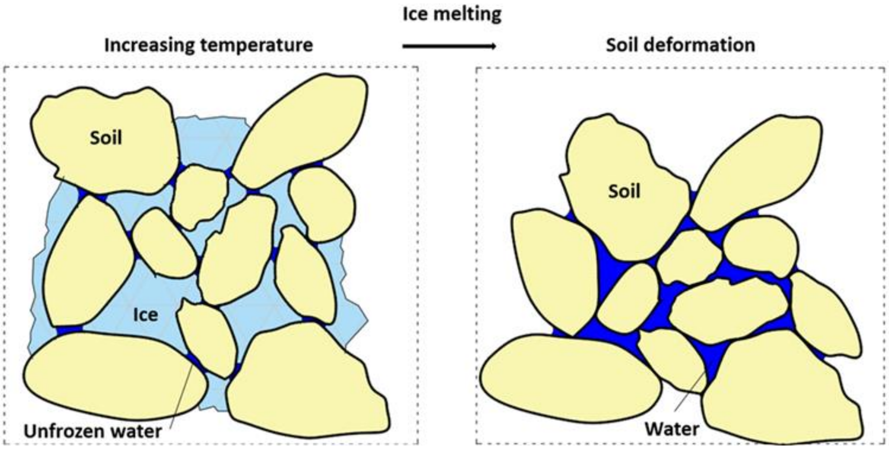

Figure 1.9: Schematic representation of a) frozen soil, and b) thawed soil (with associated volume changes), after Shastri et al., 2021.

As described above, a soil is frozen to form a portion of the wall with such low permeability that a safe excavation can be made. Previous studies have shown that the hydraulic conductivity of frozen soil is difficult to measure both in the laboratory and in the field , and it is usually assumed to be zero in the majority of cases, however, tests, have shown that water flows still occurs in frozen soil, especially when the frozen soil temperature is between 0 and -1°C (Ming et al., 2020). In fact the hydraulic conductivity coefficient depends on soil type and temperature and is related to the unfrozen water content (Burt and Williams, 1976), as verified also by Watanabe and Osada (2016). Andersland et al. (1996) performed hydraulic conductivity measurements on frozen granular soils and observed that an increase in ice saturation with decrease in the oipen pore speace reduced the frozen soil conductivity. At full ice saturation, measured conductivity values were less than 10^{-4}mm/sec.

1.3.1 Thermal aspects

The water-to-ice transformation also results in a change in the thermal properties of a soil. These properties are of vital importance to know the response of soil materials to thermal changes. They are thermal conductivity, heat capacity, thermal diffusivity, latent heat and thermal expansion.

Thermal conductivity k [W/m°C] is the rate at which heat energy flows across a unit area of the soil due to a unit temperature gradient (Farouki, 1981). This property, which has been studied for decades, including in porous rocks permeated by different fluids (see Adivarahan et al., 1962), has led to the development of many models from empirical data to calculate the conductivity of a soil in the frozen and unfrozen state. These models, more or less complex, take into account the thermal conductivities of the components of a soil (usually composed of 4 phases (minerals, water, ice, gas) with respect to porosity n, degree of saturation S_r, and dissolved salt content. The most widespread and well-known models are those of Kersten (1949), Johansen (1975), Donazzi (1977), Côté and Konrad (2005), Chen (2008). Harlan and Nixon (1978) summarized much of Kersten's work in graphs (Figure 1.10 and 1.11) that can be simply used to evaluate the soil thermal conductivity based on soil type, dry density, water content, and degree of water saturation.

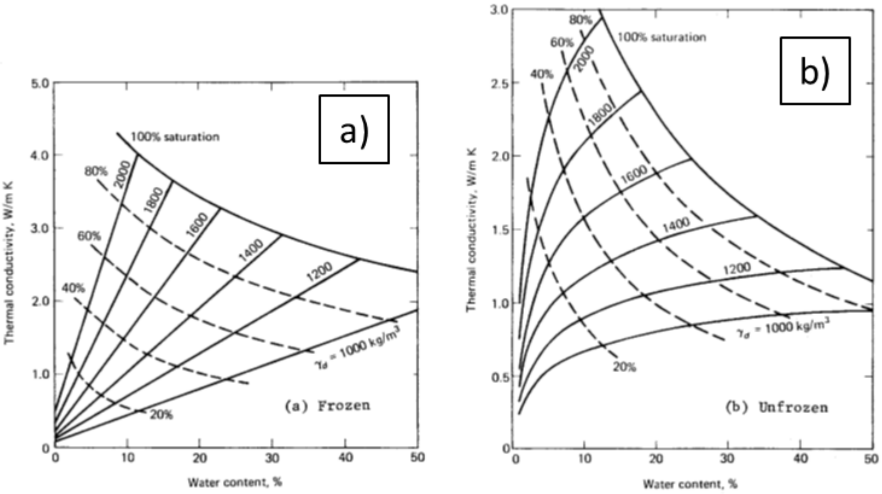

Figure 1.10: Average thermal conductivity for sands and gravel: a) frozen; b) unfrozen, after Harlan and Nixon (1978)

From the mentioned models' authors such as Abu-Hamdeh and Reeder (2000), Tarnawski et al. (2011) and Haigh (2012) have made comparisons with models and experimental data to assess their accuracy. The conductivities of water and ice are very different, and are a function of temperature and salt content, which must therefore be considered when estimating soil conductivity (see Pounder, 1965, Sakazume and Seki, 1980, Fukusako, 1990, Ramires et al., 1995, Sharqawy, 2013, Rashid et al., 2016,).

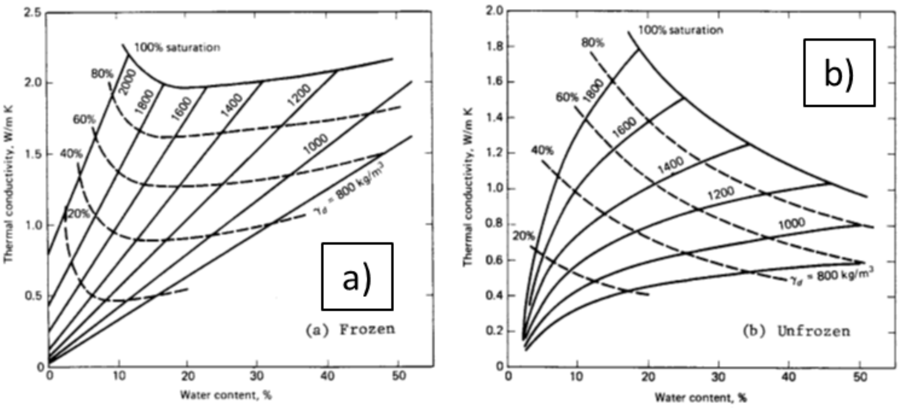

Figure 1.11: Average thermal conductivity for silt ansd clay soils: a)frozen and b) unfrozen, after Harlan and Nixon (1978)

The heat capacity of a soil sample is the amount of heat required to raise its temperature 1 degree (Andersland and Ladanyi, 2004). Commonly, soil heat capacity is referred to a unit mass (i.e. specific heat – c [J/kg°C]) or to a volume unit (i.e. volumetric heat capacity – C [J/m^3°C]). Both are estimated as weighted mean of heat capacity of different materials that compose the soil (soil water, ice and gas) as described by De Vries (1963), Anderson and Tice (1973) and Farouki (1981). Ice has different heat capacity values than water that are a function of temperature and dissolved salt content (see Ono, 1967 and Millero et al., 1973). These values can be calculated, using equations, or alternatively they can be measured experimentally (see Li et al., 2018).

The thermal diffusivity α [m^2/sec] is the ratio of k and C:

$$\alpha = \frac{k}{C} \tag{1.7}$$

Thermal diffusivity of ice is much higher than that of water. This means that the average temperature of a mass of saturated frozen soil will increase more quickly than that of a mass of unfrozen soil with equal dimensions at an equal difference between the initial temperature of the soil mass and that of the surrounding soil.

The amount of heat energy absorbed when a unit mass of ice is converted into a liquid at the melting point is defined as its latent heat of fusion (Andersland and Ladanyi, 2004) that is the same amount of heat (333.7 kJ/kg) liberated when the water is converted into ice with no change in temperature. For soils, the total energy involved in the phase change is function of the total water and the fraction of water that changes phase contained in a given soil volume.

Once formed, ice undergoes thermal expansion and contraction processes depending on whether it is heating or cooling, respectively. Thermal expansion ranges from $50*10^{-6}$/°C at 0°C to 10^{-5}/°C at -180°C. This phenomenon affects the soil in which it is contained (Bourbonnais, 1984).

1.3.2 Mechanical aspects

Despite the presence of unfrozen water, when ice fills most of the pore space, the mechanical behavior of a frozen soil closely reflects that of the ice. Under ordinary conditions, its response to deviatoric stresses is governed by a power law creep equation of the Norton-Bailey type (Andersland and Ladanyi, 2004). The behavior of a frozen soil under an increase of hydrostatic pressure is considered to be the result of combined mechanical and thermodynamic effects, the former governing the stress sharing, and the latter the pressure melting phenomena. On the basis of findings made by many investigators who studied systematically the shear behavior of frozen sands, and on the basis of their own investigations, Ting (1981) and Ting et al., (1983) concluded that the shear behavior of frozen sand is controlled essentially by the following four physical mechanisms: pore ice strength; soil strength, consisting of interparticle friction, particle interference, and dilatancy effects; increase in the effective stress due to the adhesive ice bonds resisting dilation during shear of a dense soil; and synergistic strengthening effects between the soil and ice matrix preventing the collapse of the soil skeleton. It is clear that, in addition to soil density, the importance of any mechanisms in the observed strength of a frozen soil will also depend on such factors as temperature, confining pressure, and deformation history (Andersland and Ladanyi, 2004). Although the sources of strength are qualitatively well known, a proper evaluation of their respective contributions is still considered to be a difficult task, because the impossibility to directly measuring the value and variation of intergranular stresses in a frozen soil that are produced by external loading.

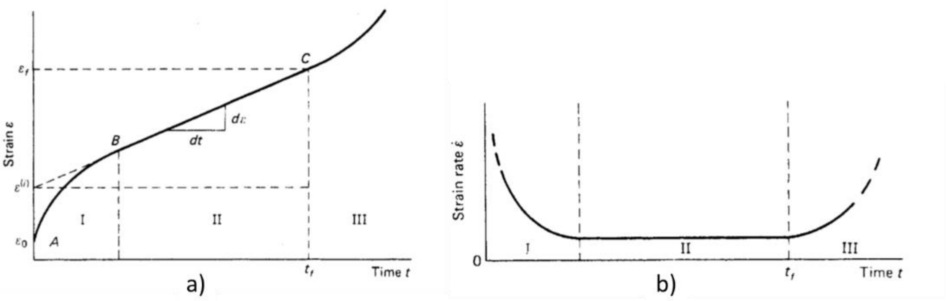

Figure 1.12: Constant-stress creep test: a) basic creep-curve; b) true strain rate versus time, after Andersland et al. (1978)

When a frozen soil specimen is subjected to a load, it will respond with an instantaneous deformation and a time-dependent deformation. The basic creep curve consists of three periods of time during which the creep rate is decreasing, remaining essentially constant, and increasing and these are called stages of primary (I), secondary (II) and tertiary (III) creep (see Figure 1.12). The shape of creep curve for frozen soils is influenced by temperature, magnitude of applied stress, soil type and density (see Sayles, 1968, Yuanlin and Carbee, 1987). If a series of uniaxial compression creep tests are carried out on identical samples, at the same temperature, but at various applied loads, a set of creep curves is obtained. The mechanical behavior of frozen soils depends, to a great degree, on that part of the pore ice which normally binds the grains together and fills most of the pore space. The strength of ice depends on many factors; the most important are temperature, pressure, and strain rate, as well as the size, structure, and orientation of grains. The strength of ice increases with decreasing temperature, and its mode of failure is strain-rate dependent.

Because of its direct influence on the strength of intergranular ice and on the amount of unfrozen water in a frozen soil, temperature has a marked effect on all aspects of the mechanical behavior of frozen soils. In general, a decrease in temperature results in an increase in strength of a frozen soil, but at the same time it increases its brittleness, which is manifested by a larger drop of strength after the peak and an increase in the ratio of compressive strength to tensile strength (see Bragg and Andersland, 1981, Haynes and Karalius, 1977). Similarly, the imposed strain rate can influence the strength of a soil; in particular, a frozen soil sample subjected to a high strain rate will return greater mechanical strength, and vice versa (Baker, 1979).

In addition, the behavior of soils subjected to confinement has been studied extensively (Parameswaran and Jones, 1981; Zhang et al., 2007; Tang et al., 2010; Yamamoto and Springman, 2014) in order to construct a stress field in which soils have different types of behavior. Studies done on the mechanical properties of frozen soils number in the hundreds and cover a very wide range of investigations, so much so that Arenson et al. (2006) summerized some research and puts into the context to help with understanding and assessing the influence of different variables on geomechanical behavior of various frozen soils.

These variables include dissolved salt. The latter must be considered because it can cause many effects on the thermal and mechanical properties of a soil. Water within soil pores may contain dissolved salts which increase the freezing-point depression and will increase the unfrozen water content. The presence of dissolved salts results in a reduced soil frost susceptibility under seasonal temperature conditions due to a decrease in the freezing index and an increase in the thawing index. A review by Ladanyi (1989) showed that increased salinity reduced the ice content, thereby reducing the frozen soil strength and increasing its creep rate at a given temperature.

1.4 Goals of the study

The goals of this PhD project were identified starting from real needs that AGF companies face in the design and execution phase and from shaded area that have yet to be explored. These goals were achieved by applying innovative and unconventional methods to the study of AGF. They can be summarized as follows:

- Studying behavior of geomaterials subjected to ground freezing interventions. These geomaterials, which include non-saline and saline soils, concrete lining, and cement-mixture treated soil, were subjected to mechanical and/or thermal testing in order to provide a database of values useful and necessary for conducting stability and thermal analyses and to verify the effect that freezing may have on pre-existing structures (Chapter 2).
- Validating TEMP/W, FEM code for performing transient thermal analysis from an in-depth study of the differential equations implemented in the code and the thermal parameters of non-saline and saline soils, and by conducting innovative unidirectional freezing laboratory tests on saturated soil specimens. From these experimental tests, various numerical models were produced, assuming various scenarios. Thie validation of considered code, if achieved, provides increased reliability to the code (Chapter 3).
- Evaluating the potential of Infrared Thermography technology in the temperature monitoring phase during a real tunnel excavation process. This could help to measuring the effective closure and thickness of the frozen wall at a specific reference temperature (Chapter 4).
- Creating a workflow to test undisturbed specimens and compare the results with those obtained in the preliminary phase starting from undisturbed frozen sample collected from excavation face (Chapter 4).
- Verifying use of point load test to estimate in situ mechanical strength of frozen soil through on-site and laboratory tests, in order to implement this test to safety and control procedures of on-site activities because it is a quick and easy-to-use test that provide mechanical index of investigated mass (Chapter 4).
- Building and testing under different operating conditions a liquid nitrogen-fed freezing pipe equipped with many thermal sensors so as to collect a large amount of data that can be made available to develop better performing numerical or analytical models. This device was

designed so that many of its components were interchangeable so that sensitivity analysis can also be performed based, for example, on the diameters and materials used (Chapter 5).

Some contents of Chapters 2, 3 and 4 have been placed as supplementary material in Appendices A, B and C, respectively. Each reference to figures and tables is thus indicated by the letter A, B and C followed by a sequential number.

The activities reported in this thesis project were carried out in full collaboration with Groutfreezlab srl, a spin-off of the University of Milano-Bicocca.

GroutFreez LAB

EuroCold Lab
European Cold Laboratory Facilities

The achievement of some of the goals was made possible in part through collaboration with EuroCold Lab (Figure 1.13), which is a cold laboratory for the study of ice cores from glaciers around the world (including Antarctica) sited within the Department of Earth and Environmental Sciences of University of Milano-Bicocca, which has a total facility of 600m^2 including a 50m^2 cold chamber that can reach temperatures of -50°C and a smaller one of 30m^2 that can reach temperatures of -25°C.

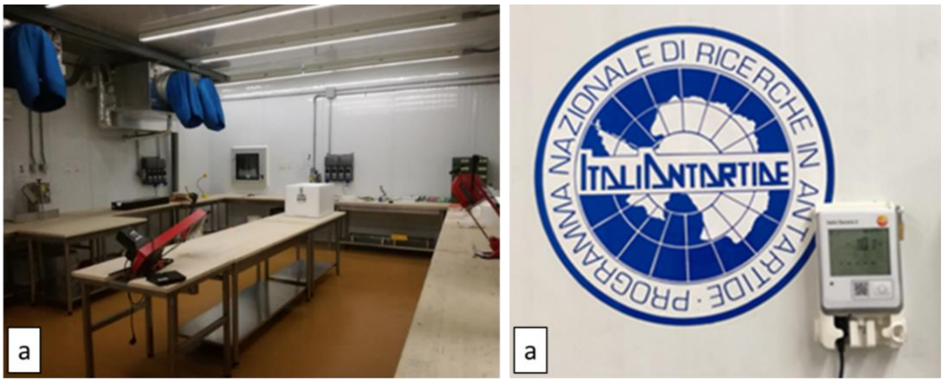

Figure 1.13: EuroCold Lab: a) cold chamber of 50m^2; b) Termostat of cold chamber set to -10 °C.

1.5 Case studies

During the realization of this PhD project some important Artificial Ground Freezing interventions have been made in Italy. The collaboration with some general contractors responsible for the design and execution of this intervention allowed to carry out a study focused on the real needs, with respect to the two sites of Isarco and Milan.

The “Underpass of the Isarco River” lot is the southernmost part of the Brenner Base Tunnel (BBT), that is the central and most important element of the Trans European Network-Transport (TEN-T). The crucial point of the whole intervention was the Isarco River underpass, with four tunnels to be dug at full section operating from four shafts about 30m deep: two on each riverside (Figure 1.14 and 1.15).

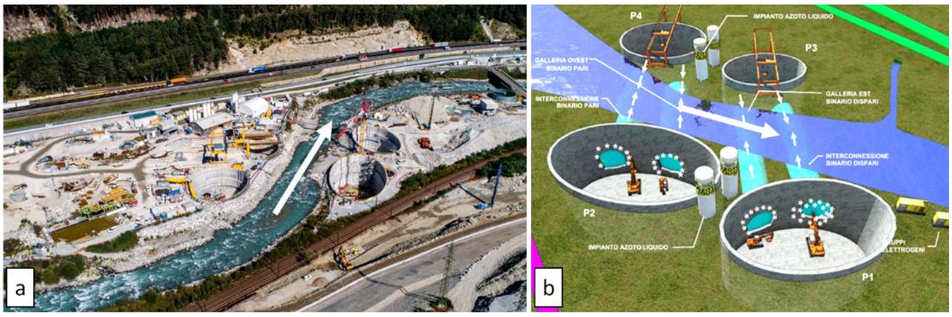

Figure 1.14: Isarco River underpass construction site: a) aerial photo of the excavation stages of four shafts; b) layout of AGF intervention in support of four tunnels under the river, starting from shafts.

The natural underground of the Isarco River valley, in correspondence of the site area, was characterized by the presence of alluvial alpine deposits, heterogenous debris flow deposits and landslide deposit. The four tunnels had lengths that varied from 50 to 60 m. The groundwater velocity was 16 m/day, which was too high to make a support shield to the excavation by traditional methods. Therefore, it was decided to use AGF to support and waterproof the excavation of the 4 tunnels. To reduce the ground water velocity, jet grouted sheets between the tunnels and cement permeation grouting treatment were performed until it was reached 10 m/day. This velocity prompted the choice of the combined method in which freezing was done with nitrogen and maintenance with brine.

The tunnels excavation section was around 80 m^2 and the freezing has been carried out by operating simultaneously from two shafts placed on opposite sides of Isarco River. From each shafts around 80 drillings were carried out and equipped with stainless steel freezing pipes with a mean distance between them fixed in 0.7m (Figure 1.16).

Figure 1.15: Excavation activities: tunnel excavation also continues at night from the north shaft P4 and b) is also carried out simultaneously from the opposite direction (south shaft P2).

Additional 20 holes has been performed for the installation of thermometric chains. According to the calculation of the tunnels excavation, the thickness of the frozen soil to be obtained with freezing treatment, was 1 m for the invert and the sides and 1.60 m for the crown. The values were referred to a maximum temperature of -10 °C at the frozen soil wall boundaries with an expected mechanical strength of 5 MPa (see Celot et al., 2023).

Figure 1.16: a) External portion of freezing pipe working during maintenance phase; b) temporary lining made by iron ribs covered by shortcrete on sides and crown, at the end frozen soil shell is notable.

For the construction of the Metro-Line 4 in Milan, a systematic use of artificial ground freezing has been made for digging 42 cross-passage (length from 3 to 10 m) in the city centre (20÷30 m under the ground level) connecting stations and facilities shafts to the two main tunnels excavated with TBMs. The necessity to reduce the impact of the works on the city life, and to respect the general works schedule led to use AGF to the protection of the cross-passage excavation in the urban area, preceded by a permeation grouting treatment that contributed to reduce the water content of the soil and to improve its mechanical properties (Pettinaroli et al., 2023). Milan soil is characterized by alluvial deposit of gravel and sand in which the finer grains percentage gradually grows in the depth, from 10 % to 30% at -30 m. For each site it has been implemented a 3D georeferenced geometrical model, that included the topography surveyed position of the shaft diaphragm walls (DW) and of the tunnels excavated with the TBMs, as well as the cross-passage to connect the shaft to the tunnels.

41 Cross-passages were carried out using the open method for both freezing and maintenance phases, supplying LN_2 overnight, without workers; 1 cross-passage, on the other hand, was carried out using only the closed method. Freezing pipes were installed by drilling from stations with an interaxis fixed in 0.8m (Figures 1.17a).

Figure 1.17: a) Installed freezing pipe from DW; b) demolition of diaphragm and excavation of frozen soil by hydraulic hammer.

Figure 1.18: Lining of cross-passage: a) temporary lining of shotcrete merged to the external surface of tunnel concrete lining bored by TBM; b) definitive concrete lining of cross-passage, view from shaft.

For the statical stability of the section during the phases of excavation (Figure 1.17b), lining cast (Figure 1.18), concrete curing, the structural designer calculated and provided the necessary thickness of the frozen soil shell, referred to a temperature of -10°C.

Chapter 2

2 Preliminary investigation of geomaterials

Understanding the soil's physical, mechanical, hydraulic, and thermal parameters is a crucial factor in designing an Artificial Ground Freezing operation. Every phase depends on these parameters, starting with the rig's construction, drilling, calculating the stability of the excavation, and predicting time and cost by running numerical models.

This section presents some mechanical and thermal tests carried out on frozen soil specimens, concrete and cement mix-treated soil, at a design stage, when these informations are indispensable and allow the feasibility of the intervention and possible changes that could cost a lot of time and money during construction to be evaluated at a preliminary stage.

The mechanical tests performed on geomaterials are four: unconfined compression test (UCS), triaxial compression test (TRX), brazilian test (BRZ) and Point Load test (PLT).

Unconfined compression tests are typically the first mechanical tests performed on frozen soil samples and provide strength values that depend on the strain rate (see Baker, 1979) and the environmental temperature (see Bragg and Andersland, 1981). This test, given its simplicity, is also the first step of investigation for concrete under very high-temperature conditions up to 600°C (see Malhotra, 1956) or extremely low to -20°C (see Wang et al., 2020) or even, subjected to resting at $T<0°C$ (see Rubene and Vilnitis, 2017).

Triaxial tests on frozen soils are now well-established tests mainly employed to investigate the mechanical parameters of alpine permafrost as carried out by Yamamoto and Springaman (2014) and Yamamoto and Springman (2019) where specimens were subjected to confinements of maximum 400 kPa and $-3°C<T< -0.3$ °C or generic frozen soils, as carried out by many authors, including Jones (1978) and Parameswaran and Jones

(1981) and Zhang et al., (2007). Triaxial tests provide useful data for understanding soil behaviour under lateral confinement conditions and for defining failure criteria. These data, in addition to direct applications, can provide databases for creating analytical models capable of predicting the mechanical behaviour of a material, as Samani and Attard (2012) have done for concrete.

Brazilian tests are laboratory tests performed to indirectly identify the tensile strength of a specimen when the preparation of a specimen with a specific shape or the available equipment does not allow direct testing. At the state of the art, bending tests have been performed by Tao et al. (2020) on frozen soil specimens and tensile tests on frozen soil samples with T between -2 and 0°C by Akagawa and Nishisato (2009) with properly designed devices. Brazilian tests were performed on frozen fractured rock mass-based specimens (see Wang et al. 2022) and on unfrozen/frozen saturated sandstone (Wang et al. 2019).

The point load test is a very straightforward mechanical test used to quickly estimate the mechanical strength of a rock in the laboratory or in situ. Such a test, used for hard rocks and soft rocks (see Elhakim, 2015), is used in this study to assess the existence of a relationship between σ_c and $I_{S(50)}$ even in frozen soils. The existence of such a factor could make the PLT even more feasible for estimating the mechanical parameters of frozen soil directly on the construction site and thus provide a quick and simple tool for verifying the estimated mechanical parameters.

Thermal tests are a key aspect of a thermal analysis because they provide values of the thermal parameters of a material and their evolution as a function of temperature. The parameters investigated in this study are thermal conductivity, volumetric heat capacity (only estimated by equations) and freezing point temperature.

Thermal conductivity was directly measured by needle probe instrument, a method extensively described by Glatzmaier and Ramirez (1985), Bristow (1998), Putkonen, (2003) and Waite et al., (2006) and employed to define the thermal diffusivity of soil.

At the same time, thermal conductivity values have been evaluated through empirical models (see Kersten, 1949), Farouki, 1981, Johansen, 1975 and Côtè and Konrad, 2005) based on chemical and physical properties of soils. The freezing point of soil, particularly in the presence of salt content, is also a crucial parameter and is strictly related to the water content of the soil and the concentration of porewater salt content (see Bing and Ma, 2011 and Xiao et al., 2017).

The soils considered in this study and analysed with the above-mentioned tests were derived from two sites where AGF was used as a consolidation and waterproofing method to support tunnel excavation: Isarco River underpass - BBT railway and in the cross-passages of Milan Underground Line 4 – MetroBlu.

Subsequently, some thermal tests were carried out on saline soils taken from the coastal area of Genoa. This was done considering the strong effect of salt content on the mechanical and thermal properties of soil, as evidenced by many scientific works (Roman, 1994; Hivon and Sego, 1995; Aksenov et al., 2003; Chen et al., 2013; Xiao et al., 2017; Kotov and Stanilovskaya, 2022;) and by the increasing application of AGF in different types of soils, including saline soils.

2.1 Materials

Materials considered in this study were taken from sites where artificial freezing interventions were carried out.

- Isarco soil was sampled in 2019 from a drilling survey performed on the riverside of the Isarco in alpine fluvial deposits in the locality of Fortezza (BZ). The core confirmed the presence of a very heterogeneous soil, ranging from decimetric blocks to fine particles consisting of granitoid material identified in the Bressanone Granite. From this borehole, portions of the material that were visually examined to be gravelly to fine were taken at the depth at which freezing would be performed (Figure A1). The borehole did not exhibit any levels of fine material and was considered overall representative of the soil involved in freezing. From these soil samples, all particles with D > 9.5 mm were excluded because, at the laboratory test scale, soil particles should not measure more than 1/10 of the diameter of the tested samples. During coring, storage and transport of the drilling survey material, the natural moisture of the soil was lost.

- The soil from the Milan subsoil, taken at a depth of -20 to -30 m, consists of Quaternary alluvial mixed deposits of Po Valley. The soil samples were taken by an excavator bucket that mixed the material during the excavation stages by gathering natural levels of gravel, sand, and silt. In this way, a mixed heterogeneous soil was sampled. This led to the reconstitution in the laboratory of the original particles size distribution of the levels that were involved in the AGF.

- Soil sampled on the Ligurian coast near Genoa was taken at a depth of 30 m below the seabed using a Shelby sampler, which allowed undisturbed sampling in which the inner structure and water and salt content remained unmodified. A water sample was also collected from the hole drilled for sampling immediately after the material was recovered.

In addition to soil specimens, the mechanical and/or thermal behaviour of further geomaterials that may be frozen during an AGF intervention and that actively contribute to the waterproofing and stability of the excavation, and of existing structures: concrete (CO) and treated soil (TS) were also investigated. The investigation of the former was done from a core taken from an existing structural line of M4 with a diamond-tipped core barrel; the latter on soil specimens injected in the laboratory with cement mixture. The mixture injection technique, as discussed in Chapter 1, is often used to plug the soil before performing an AGF to improve initial soil conditions. This significantly increases the effectiveness of the AGF.

2.1.1 Sample characterization

Soil samples

All soil samples were disaggregated and oven-dried at 65°C for 48 hours. Dry samples of Isarco and Genoa were subjected to dry particle size analysis (*ASTM D422-63*). Samples from Milan were sieved to divide the soil into different particle size classes with D max= 9.5 mm. From these classes, soil samples with desired particle size distributions were reconstituted. The label used to identify each soil sample was compounded by the prefix I-, M- and G- to indicate the origin (Isarco, Milan and Genoa). This prefix is followed by a number (i.e. 1, 2 and 3) that identifies the particle size distribution and physical and chemical properties of different soil samples.

Because the shallow depth and the large porosity of the samples, Genoa soils were assumed as saline soils and the samples were divided into two categories: non-saline (Isarco and Milan) and saline soils (Genoa), so the last letters of the labels indicates if the soil is non-saline (N) or saline (S).

To briefly summarize, the soils considered are:

I (1,2)-N: disturbed sample of non-saline soil collected from Isarco (see Figure 2.1a and 2.1b);

M (1,2,3)-N: disturbed sample of non-saline soils collected from Milan (see Figure 2.1c);

G (1,2)-S: undisturbed sample of saline soil collected from Genoa, (see Figure 2.1d).

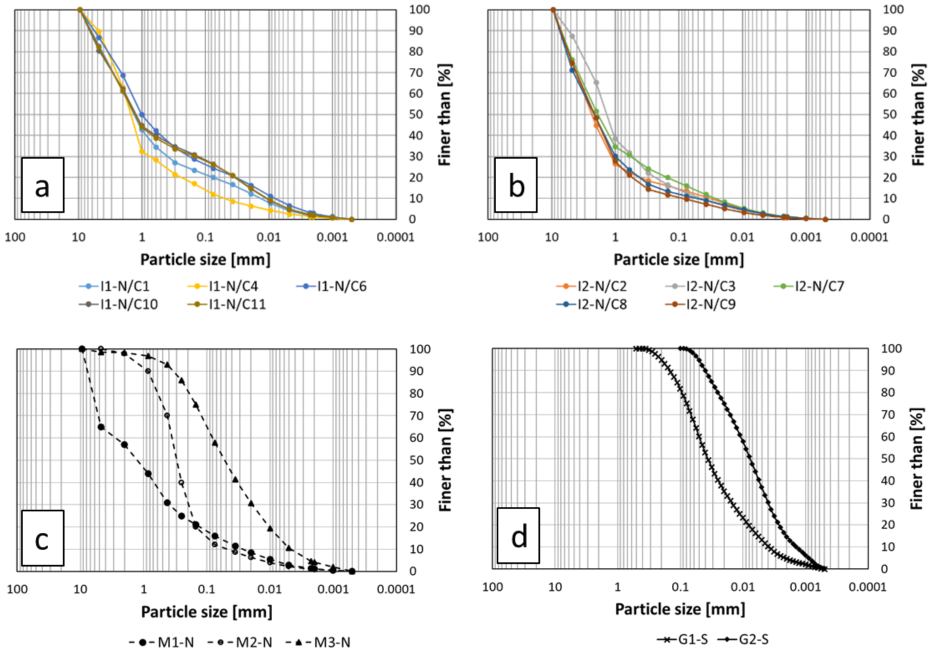

Figure 2.1: Particles size distributions of considered soils: a) I1-N (Isarco); b) I2-N (Isarco); c) M1,2,3-N (Milan); d) G1,2-S (Genoa).

Void index, porosity, and saturation degree of disturbed non-saline soils (I and M samples) were determined from available indirect in situ investigations (Standard Penetrometric Tests); once dried, void index, porosity and saturation degree were calculated for undisturbed samples of saline soils (G samples) (Table 2.1).

Table 2.1: Physical properties of considered soils.

			non-saline					**saline**	
			Isarco		**Milan**			**Genoa**	
Soil sample property	**Symbol**	**U.M.**	**I1-N**	**I2-N**	**M1-N**	**M2-N**	**M3-N**	**G1-S**	**G2-S**
porosity	n	[-]	0.25	0.30	0.33	0.35	0.45	0.44	0.40
void index	e	[-]	0.33	0.43	0.49	0.54	0.82	0.79	0.67
saturation degree	S_r	[-]	0.99	0.99	1	1	1	0.99	0.99

A small portion of each soil was powdered to perform X-ray Diffraction (XRD) analyses. XRD on powders allows the identification of mineralogical phases, with a detection limit of about 0.5 to 1 wt%, depending on the phases present. Qualitative phase analysis was performed with the PANalytical High-Score Plus software, which allows comparison between measured I/2θ profile and standard I/2θ profile of pure substance contained in the ICSD PDF2 database. The instrument used for these analyses was a X'Pert PRO PANalytical Powder Diffractometer in Bragg-Brentano θ/θ parafocal geometry with Spinner PW3064 sample holder. The results of XRD analysis are shown in Table 2.2.

Table2.2: Mineralogical composition of considered soils obtained by X-ray Diffraction (XRD) analysis.

Mineralogical Phase	**NON-saline soils** [Wt. %]				**Saline soils** [Wt. %]	
	I-N	**M1-N**	**M2-N**	**M3-N**	**G1-S**	**G2-S**
Quartz	58.5	53.7	42.7	38.7	45-50	25-30
Plagioclase	15.6	18.1	16.2	22.9	10-15	-
K-feldspar	-	3.7	12.3	1.7	-	-
Muscovite	20.4	12.0	21.2	24.1	15-20	20-25
Chlorite	5.4	3.6	4.0	4.4	-	-
Serpentine	-	2.4	0.5	1.8	-	-
Anphibole	-	5.6	1.4	2.8	-	-
Calcite	-	1.0	1.7	3.6	15-20	40-45
Clay	-	-	-	-	<5	5.0
Dolomite	-	-	-	-	-	<5
Aragonite	-	-	-	-	-	<5
Pyrite	-	-	-	-	<2	-

Porewater chemical analysis

The groundwater from the borehole, from which the saline soil specimens were collected, was sampled, and transported to the laboratory following standard ISO 5667-1:2020. Here a pH measurement was taken, and the main ions identified through chromatography analysis (Figure 2.2). The electrical conductivity was 23501 µS/cm allowing an estimation of the total water salinity S_w of 12.39‰ which defined this as a brackish water.

Water parameters	U.M.	
Alcalinity	[meq/lt]	3.16
pH	[-]	8.31
Electral conductiviy	[µS/cm]	23,501
Salinity	[‰]	12.39

Genoa sea salinity, after Ruggieri et al., (2011)	[‰]	35

		Concentration [ppm]
Cations	Na^+	4319.578
	K^+	179.744
	Mg^{2+}	495.782
	Ca^{2+}	379.719
Anions	F^-	0
	Cl^-	9073.813
	SO_4^{2-}	1019.5
	NO_2^-	33.694

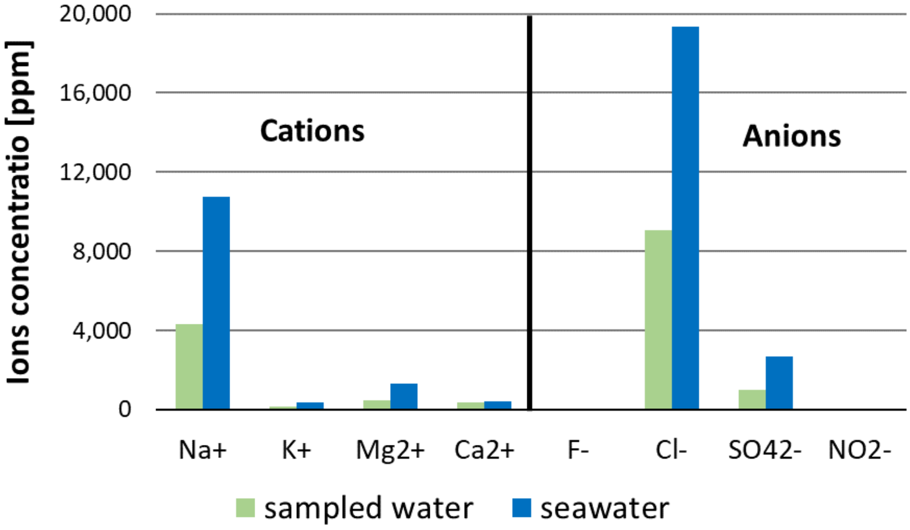

Figure 2.2: Chemical analysis and salinity definition on sampled water from borehole. A comparison with cations and anions concentration of seawater (after, Turekian 1968) is provided.

These analyses demonstrate that the borehole water has a salinity that is about 1/3 that of seawater. Assuming that the soil porewater has the same salinity of the water sampled through the borehole of the drilling survey might be incorrect because: (I) during drilling, water, usually fresh, is injected to help material flushing and the cutting tools cooling, and therefore the water sampled could be the result of a dilution of the original porewater; (II) the shallow depth and porosity of the soil, already deposed in a marine environment, should have enabled homogenization with the salinity of seawater. For these reasons, the two assumptions of porewater salinity: 12.39‰ and 35‰ were always considered for thermal calculations.

Other geomaterial samples

The concrete cores were cut to obtain cylindrical specimens of the desired height, and the upper and lower faces were polished to have two parallel faces and thus be subjected to laboratory testing.

Treated soil specimens were created in the laboratory by 1D column injections of cement mixtures, as done by Zebovitz et al., 1989 and Anagnostopoulos et al. 2020. From a specific particle size distribution, shown in Figure 2.3b, a column with D = 38 mm and H = 600 mm were prepared and injected following the standard ASTM D4320-02 (Figure 2.3a and c) with a laboratory-prepared cement mixture according to API RP 13B-1/ISO 10414-1, (2003) with the following ratios:

- *g* water/*g* cement = 2.5
- *g* water/*g* bentonite = 29.4
- *g* water/*g* fluidifying additive = 285.7

After being injected from the bottom to the top at controlled pressure, the column was opened and let resting in a humid environment for 28 days.

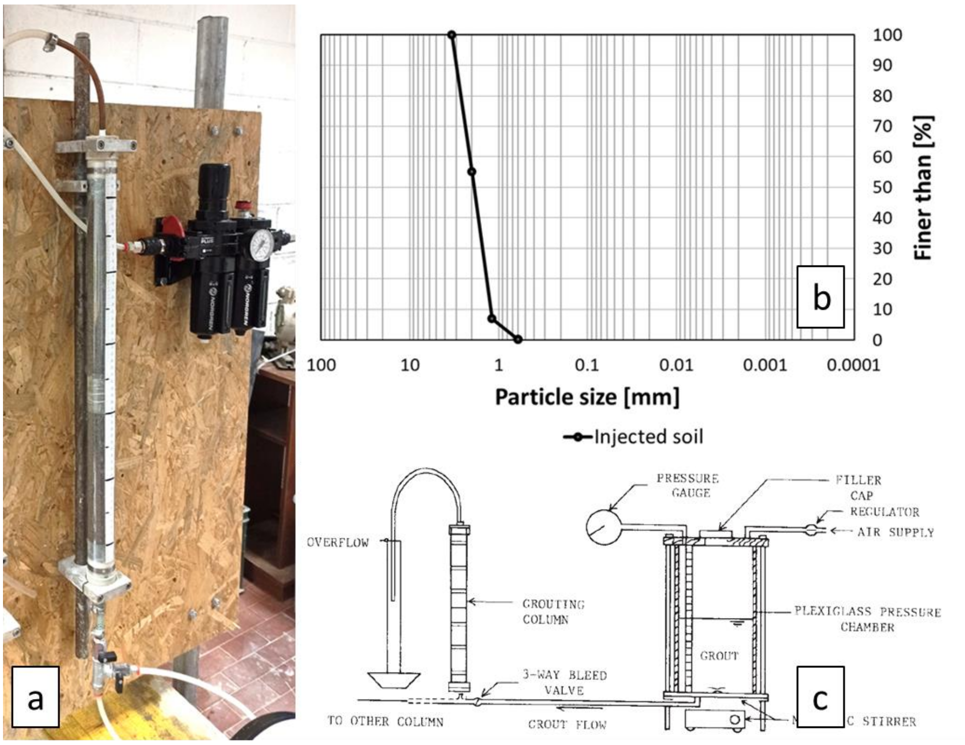

Figure 2.3: 1D injection of concrete mixture into soil column in order to obtain treated soil sample: a) layout of soil column during injection from bottom to top; b) particles size distribution of considered soil; c) sketch of the injection laboratory test, after ASTM D4320-02.

2.2 Methods

2.2.1 Specimen preparation

Being still in the preliminary stage, the AGF intervention was not yet performed, and it was not possible to take already frozen soil samples. For this reason, it was necessary to prepare frozen soil samples in the laboratory from the available soil samples.

Non-saline disaggregated material samples (I- and M- samples) were reconstituted in the laboratory using the tamping technique. An opening mould with an internal latex membrane was attached to a cylindrical base, with D equal to the internal diameter of the mould (50 or 70 mm). The base was greased and covered with filter paper. Quantities of distilled water and soil were poured into the mould to fill 20 mm at a time, obtaining the values of the physical parameters listed in Table 2.1. Once the desired height was reached, a metallic cylinder of the same size as the lower one was placed on the upper base of the sample, greased, and provided with filter paper. Concerning the undisturbed saline soil (G- sample), the cores were cut into shorter pieces and trimmed in order to exclude the external part of core that was slightly disturbed and obtain specimen with D = 70 mm and H = 140 mm. Studies carried out by Wang et al. (1995) and Viklander and Eigenbrod (2000) demonstrated how freeze-thaw cycles influence the particle size distribution of a soil, therefore, pure material, i.e. not subject to previous freeze-thaw cycles, was used for each test.

The concrete cores (CO) were cut using a circular saw with diamond paste and polished to obtain perfectly cylindrical samples with an H/D ratio of 2. Each CO sample was soaked in distilled water for 3 days inside a vacuum chamber to ensure complete saturation of the pores.

Similarly, the treated soil column (TS), after 28 days of resting in a moist environment, was cut into shorter pieces with a circular saw. The granulometry of the column made it impossible to obtain flat bases, so it was necessary to make some fast-setting concrete "shoes" to compensate for the roughness of the column specimens, applied for the unconfined and triaxial tests, visible in Figure 2.4; the Brazilian tests did not require this solution.

Figure 2.4: Treated soil specimen equipped with specific cement plinth to ensure a flat base.

All samples after preparation were placed in a freezer at -10°C. After 24 hours, the soil samples were extracted from the moulds and brought into the *EuroCold Lab*, set at -10 °C, where they rest for 2 days wrapped in latex membranes (I and M samples) or transparent film (G, CO and TS samples) to avoid possible ice sublimation.

The obtained samples were subjected to mechanical and thermal tests as shown in Table 2.3.

Table 2.3: Mechanical and thermal tests performed on the considered geomaterial samples.

		mechanical tests				**thermal tests**	
Sample code	**Sample**	***UCS***	***TRX***	***BRZ***	***PLT***	k_u ; k_f	T_{fp}
I1-N	Isarco 1 - non saline	X	X	-	X	-	X
I2-N	Isarco 2 - non saline	X	X	-	X	X	X
M1-N	Milan 1 - non saline	X	X	X	-	X	-
M2-N	Milan 2 - non saline	X	X	X	-	X	-
M3-N	Milan 3 - non saline	X	X	X	-	X	-
G1-S	Genoa 1 - saline	-	-	-	-	X	X
G2-S	Genoa 2 - saline	-	-	-	-	X	X
CO	Concrete core	X	-	-	-	-	-
TS/u	Treated Soil	X	X	X	-	X	-

2.2.2 Mechanical tests

The design of stable structure on frozen soil requires a knowledge of its strength and deformation characteristics (Sayles, 1968).

All the mechanical tests performed and described on the following pages were carried out under controlled thermal conditions. The identification codes of the samples used are composed of a prefix indicating the constituent material, followed by -u, -t, -b, -p in the case of UCS, TRX, BRZ or PLT respectively. At the end there is a progressive number indicating the test number. At the very end there is eventually an additional letter which defines particular test conditions (e.g., I2-N/u1-h is the uniaxial test #1 performed on a specimen made by material I2-N at -6°C, instead of -10°C).

2.2.2.1 *Unconfined compression test*

The unconfined tests on geomaterials were performed under environmental conditions that reproduce the type of thermal perturbation that each of them undergoes during an AGF operation. These conditions are summarised in Table 2.4.

Table 2.4: Thermal conditions applied to considered samples during UCS tests.

UCS Specimen	Sample	Thermal condition
I1-N/u	Isarco 1 - non saline	T= -10°C
I2-N/u	Isarco 2 - non saline	T= -10°C
I2-N/u-h	Isarco 2 - non saline	T= -6°C
M1-N/u	Milano 1 - non saline	T= -10°C
M2-N/u	Milano 2 - non saline	T= -10°C
M3-N/u	Milano 3 - non saline	T= -10°C
CO/u-e	Concrete core	T= 20 °C
CO/u-s	Concrete core	T_{top}= -30°C; T_{bottom}= -80°C
CO/u-f	Concrete core	T= -20°C
CO/u-c	Concrete core	T= 20°C (after freezing cycle at -10 °C)
TS/u	Treated Soil	T= -10 °C

These tests were performed using load presses in axial strain rate control. All the unconfiend tests *u-h, u* and *u-f* at T= -6, -10 or -20 °C respectively, were performed with a 100 kN press from *Controls* equipped with a 100 kN load cell and 30 mm LVDT permanently positioned inside *EuroCold Lab* (see Figure 2.5). In order to prevent the liquid crystals inside the control panel from freezing, it was disassembled and placed outside the cold chamber. Special cables made it possible to control the press located inside the cold chamber from the outside. The execution of the test on frozen ground followed the ASTM D7300 standard, which prescribes an axial deformation of 1%/min and the acquisition of axial deformation and axial strength for the first test, and to continue with tests with lower strain rates; those on concrete and treated soil followed the ASTM C666 standard.

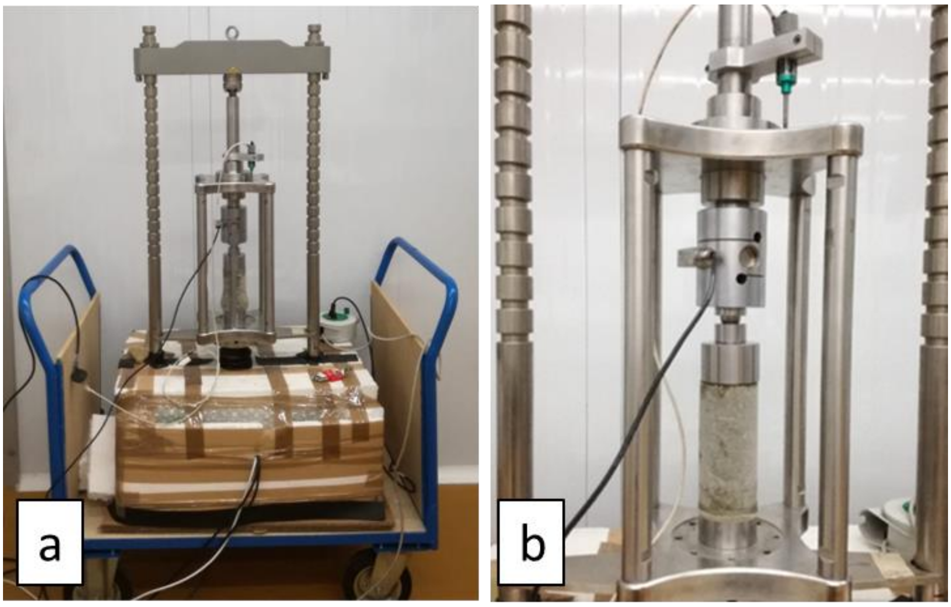

Figure 2.5: Press used to uniaxial compression test in EuroCold Lab: a) the press is placed on a trolley and the LCD screen panel is missing; b) frozen soil specimen under load with load cell and LVDT measuring strength and deformation.

Tests performed on concrete and treated soil samples under the various thermal conditions were carried out in a laboratory at 20 °C using a *GDS* press equipped with a 200 kN load cell, a 6 mm LVDT and strain gauges for reading the local axial strain, and the ASTM C666 standard was followed. The *u-s* tests performed on concrete samples were carried out by equipping the load base with a tray that could store liquid nitrogen (LN_2), which was poured in order to induce a flow of heat inside the sample and obtain the desired conditions (see Figure 2.6). Two thermocouples placed on the lower and upper face of the CO samples made it possible to measure the thermal gradient inside the sample during the uniaxial test. The *u-c* tests were performed at room temperature on specimens that underwent a complete freeze-thaw cycle (T = 20→-10→20°C). The samples tested with uniaxial tests are listed in Table A1.

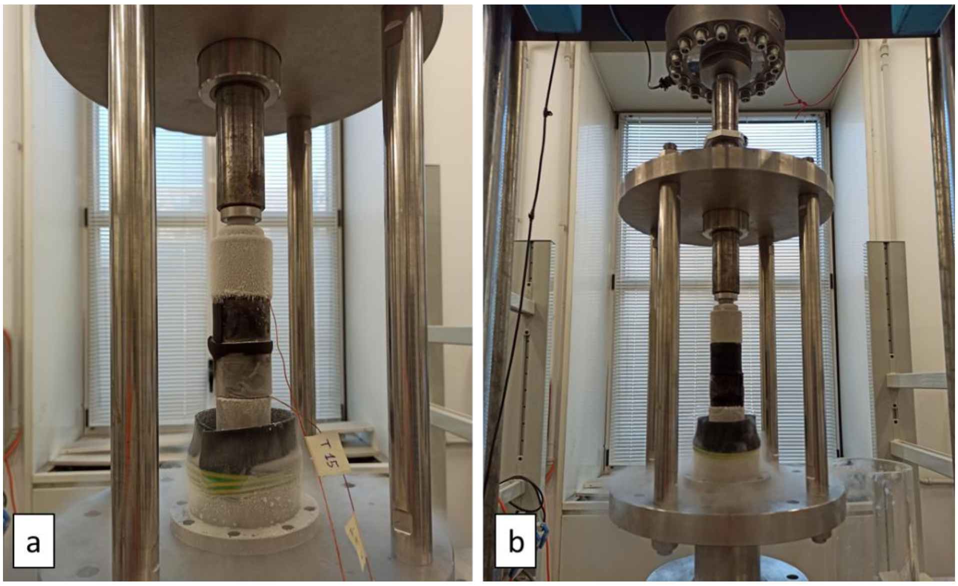

Figure 2.6: Layout of UCS test on concrete specimen under temperature gradient thermal condition (u-s condition): a) LN_2 tray and T-type thermocouples at the extremes of specimen ensure the needed thermal gradient; b) loading system, gaseous nitrogen is evident.

2.2.2.2 Triaxial compression test

Triaxial tests on geomaterials were all performed at T= -10°C within *Eurocold Lab* (Table 2.5).

Table 2.5: Thermal conditions applied to considered samples during TRX tests.

TRX Specimen	Sample	Thermal condition
I1-N/t	Isarco 1 - non saline	T= -10°C
I2-N/t	Isarco 2 - non saline	T= -10°C
M1-N/t	Milano 1 - non saline	T= -10°C
M2-N/t	Milano 2 - non saline	T= -10°C
M3-N/t	Milano 3 - non saline	T= -10°C
TS/t	Treated Soil	T= -10 °C

These tests were carried out using load press under axial strain rate control. All triaxial tests were performed with a 50 kN *Matest* press equipped with a 50 kN load cell and 30 mm LVDT mounted inside *EuroCold Lab*. The execution of the test was carried out in accordance with ASTM STP1568, which provides guidance on the methodologies used to this point. Each test specimen was placed inside a triaxial cell covered by a latex membrane, which was fixed at the bottom and top with the bases using o-rings. In this way, the antifreeze liquid used for confinement never came into contact with the specimen. This liquid was pressurised by means of a pressure multiplier (x2) and an air-water bladder, (Figure 2.7a) connected to an air compressor located outside the cold chamber. The maximum achievable confinement pressures inside the triaxial cell with these devices was 1600 kPa. The temperature of the liquid inside the cell was measured by means of a specially designed T type thermocouple (see Figure 2.7b), and the confining pressure was monitored by using a pressure transducer. Axial strain, axial strength and confining pressure were recorded for each test. The specimens subjected to triaxial tests are listed in Table A2.

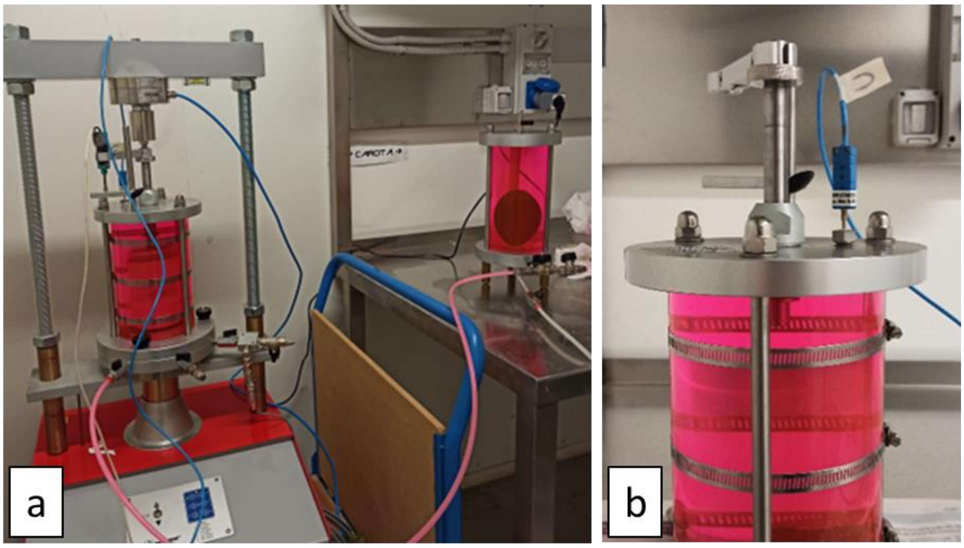

Figure 2.7. Triaxial compression test machine in EuroCold Lab: a) glycol is used as confinement liquid; b) T-type thermocouple (blue) inserted into the triaxial cell.

2.2.2.3 Brazilian test

Brazilian tests on geomaterials were all performed at T= -10°C within *Eurocold Lab* (Table 2.6).

Table 2.6: Thermal conditions applied to considered samples during TRX tests.

BRZ Specimen	Sample	Thermal condition
M1-N/b	Milano 1 - non saline	T= -10°C
M2-N/b	Milano 2 - non saline	T= -10°C
M3-N/b	Milano 3 - non saline	T= -10°C
TS/b	Treated Soil	T= -10 °C

These were made on discoidal specimens in order to indirectly measure tensile strength. The specimen was placed between two metal jaws with a semi-cylindrical shape, inserted in a 50 kN *Matest* load press under strain rate control, which impressed a compression along the diameter of the specimen. This test is guided by ASTM D3967-95a for rock and returns the axial (diametral) strain and indirect tensile strength. Table A3 lists the geomaterial specimens tested by the Brazilian tests.

2.2.2.4 Point load test

The test, standardised by ASTM D5731-02, consists of crushing a regular or irregular centimetric pebbles of rock between two conical steel points until the specimen breaks. During the test, the 3 main axes of the specimen (a, b and c where $a>b>c$) and the maximum strength offered by the specimen before failure are measured. From these values, a strength value $I_{s(50)}$ normalised to a specimen with an equivalent diameter of 50 mm can be calculated. This strength value, multiplied by a factor C (as described by ASTM D5731-02), provides an estimation of the UCS value. The PLTs were performed at T=-10 °C and -6 °C and are indicated as */p* and */p-h* (see Table 2.7), respectively. Table A4 shows the specimens tested.

Table 2.7: Thermal conditions applied to considered samples during PLT tests

PLT Specimen	Sample	Thermal condition
I1-N/p	Isarco 1 - non saline	T= -10°C
I2-N/p	Isarco 2 - non saline	T= -10°C
I2-N/p-h	Isarco 2 - non saline	T= -6°C

2.2.3 Thermal tests

2.2.3.1 Thermal conductivity measurement

The thermal conductivity of the soil can be measured using instruments (see Kurtz at al., 2017) or can be determined using equations from several authors.

In this study Thermtest Portable TLS-100 conductivity meter according to ASTM D5334-08, was used.

This measuring instrument consists of a needle probe (ϕ=2-4mm, L=100-50mm) that is inserted into a soil sample and of an external computing processor. The minimum dimensions of the sample are defined by the ASTM D5334-08 and are ϕ=50mm and L=100mm.

After allowing the needle to reach thermal equilibrium with the soil, a fixed and known amount of heat is irradiated into the soil through the needle. The transient response of the soil to this thermal perturbation is measured by the instrument, which automatically returns the thermal conductivity value.

The needle probe was inserted axially into the specimens and the unfrozen thermal conductivity was measured for non-saline, saline, and treated soil (Figure 2.8).

Non-saline, saline and treated soil specimens were placed inside a cold room set at -10 °C with the needle probe already inserted. In this way the contact between the metal sleeve of probe and the soil was guaranteed. Once the specimens and the needle-probe reached the temperature of -10 °C the frozen thermal conductivity of soils was measured (Figure 2.9).

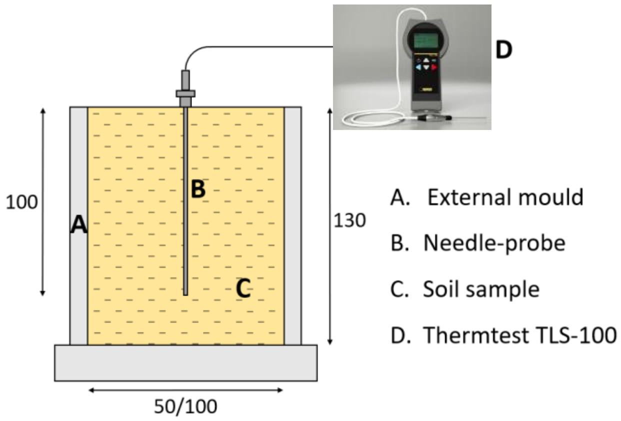

Figure 2.8: Thermal conductivity measurement on soil specimen in laboratory by the needle probe method. Dimensions are expressed in mm.

Figure 2.9: Frozen soil specimen of dimension according with ASTM D5334-08 with needle probe of Thermtest Portable TLS-100 during thermal conductivity measurement.

2.2.3.2 Thermal conductivity estimation

Kersten (1949), Johansen (1975) and Côtè and Konrad (2005*)* and Haigh (2012) studied, among the others, the relationships between thermal conductivity and porosity, soil moisture, salt content and mineralogical composition. Empirical solutions were proposed to estimate the value of thermal conductivity at unfrozen and frozen state starting from physical and chemical properties of soil. Using some of the data provided by Kersten (1949) for medium and fine sands and for fine-grained soils, Johansen (1975) developed the normalized thermal conductivity concept and proposed an equation to calculate thermal conductivity of a porous unfrozen and frozen medium. This estimation is based on porosity, saturation degree, grain-size distribution (fine or coarse), origin of grains, shape, and the percentage of quartz. The main equation for computing soil thermal conductivity is:

$$k = \left(k_{sat} - k_{dry}\right)k_r + k_{dry} \tag{2.1}$$

where the normalized thermal conductivity concept is used:

$$k_r = \frac{k - k_{dry}}{k_{sat} - k_{dry}} \tag{2.2}$$

where k_{sat} and k_{dry} are the saturated and dry thermal conductivity of soil (W/m°C), respectively.
Kersten (1949) defined $k_r$equal to Kersten's number K_e as:

$$K_e = 0.7 \log S_r + 1.0 \tag{2.3}$$

for an unfrozen coarse-grained soil with saturation degree $S_r > 0.05$; and

$$K_e = \log S_r + 1.0 \tag{2.4}$$

for an unfrozen fine-grained soil with $S_r > 0.1$, whereas for all types of frozen soil, $K_e = S_r$.

A generalized thermal conductivity model for unfrozen and frozen soil was proposed by Côté and Konrad (2005):

$$k_r = \frac{\kappa\, S_r}{1 + (\kappa - 1)\, S_r} \tag{2.5}$$

where κ is an empirical parameter used to account for the different soil types and fabrics in the unfrozen and frozen state. This model has lower and upper limits as follows:

- lower limit: $S_r = 0 \rightarrow k_r = 0$
- upper limit: $S_r = 1 \rightarrow k_r = 1$

For dry natural soils Johansen (1975) proposed a semi-empirical equation to estimate k_{dry} as follow:

$$k_{dry} = \frac{0.137\rho_d + 64.7}{2{,}700 - 0.947\rho_d} \pm 20\% \tag{2.6}$$

where ρ_d is dry density (kg/m^3)

$$\rho_d = \rho_s(1-n) \tag{2.7}$$

From the density values of various minerals provided by Horai (1971), the density of the solid matrix of each soil ρ_s can be computed by the following equation:

$$\rho_s = \sum_j (\rho_{m_j} * \omega_j) \quad \text{with} \quad \sum_j \omega_j = 1 \tag{2.8}$$

where ρ_m (kg/m^3) is the bulk density of each mineral j and ω is the percentage in weight of that mineral.
Côté and Konrad (2005) proposed a generalized exponential relationship between dry thermal conductivity of soil and its porosity, *n*:

$$k_{dry} = \chi \cdot 10^{-\eta n} \tag{2.9}$$

where χ and η are material properties accounting for the particles shape effect. For natural mineral soils they are 0.75 W/m°C and 1.2, respectively.

For saturated soils, both unfrozen and frozen, Johansen (1975) Tarnawski et al. (2011) and Tarnawski and Leong (2016) proposed the use of a geometric mean equation based on thermal conductivity of the soil constituents and their volume fractions:

$$k_{sat} = k_s^{1-n} k_i^{n-\theta_{uwc}} k_w^{\theta_{uwc}} \tag{2.10}$$

where k_s, k_i and k_w are thermal conductivities of soil grains, ice, and water, respectively; θ_{uwc} is unfrozen volumetric water content. In saturated unfrozen state $\theta_{uwc} = n$ and Eq. (2.10) reduces to:

$$k_{sat} = k_s^{1-n} k_w^{n} \tag{2.11}$$

and in the complete frozen state $\theta_{uwc} = 0$, Eq. (2.10) reduces to:

$$k_{sat} = k_s^{1-n} k_i^{n} \tag{2.12}$$

Considering the change of water volume at the phase change the Eq. (2.11) and Eq. (2.12) can be rewritten as (Côté and Konrad, 2005):

$$k_{sat(u)} = k_s^{1-n_u} k_w^{n_u} \tag{2.13}$$

$$k_{sat(f)} = k_s^{1-n_f} k_i^{n_f} \tag{2.14}$$

where:

$$n_f = \frac{1.09 n_u}{(1 + 0.09 n_u)} \tag{2.15}$$

and $n_u = n$ is soil porosity at unfrozen state. Being the degree of saturation affected by the expansion during freezing, Côté and Konrad (2005) proposed the following equation:

$$S_{rf} = \frac{1.09 S_{ru}}{(1 + 0.09 S_{ru})} \tag{2.16}$$

where $S_{ru} = S_r$ is soil saturation degree at unfrozen state.

Johansen (1975) proposed the calculation of the thermal conductivity of soil grains as a geometric mean based on the fraction of different minerals:

$$k_s = k_{qtz}^{q} k_0^{1-q}; \quad \begin{cases} k_0 = 2.0 \dfrac{W}{mK} & if\ q > 0.2 \\ k_0 = 3.0 \dfrac{W}{mK} & if\ q \leq 0.2 \end{cases} \tag{2.17}$$

where q is the quartz fraction of the total solid components, k_{qtz} is the thermal conductivity of quartz and k_0 is the thermal conductivity of other minerals. If the mineralogical composition of the rock is known, the thermal conductivity can be calculated by taking a generalised geometric mean of the values for the minerals composing it (Farouki, 1981; Côté and Konrad, 2005; Tarnawski and Leong, 2016):

$$k_s = \prod_j k_{m_j}^{x_j} \quad \text{with} \quad \sum_j x_j = 1 \tag{2.18}$$

where k_m is the thermal conductivity of each rock-forming mineral j (W/m°C), and x is the volumetric proportion of each rock-forming mineral j. Values of density and thermal conductivity of main minerals listed by Horai (1971) are shown in Table 2.8.

Donazzi (1977*)* proposed an exponential function to express the relationship of thermal resistivity r [m°C/W] of soil with its porosity and saturation degree.

$$r = \mathrm{r}_w^{n} r_s^{1-n} \exp\left(3.081(1 - S_r)n\right) \tag{2.19}$$

where r_w and r_s are the thermal resistivity of water and soil grains (m°C/W), respectively. For sandy soils the values of r_w and r_s are equal to 1.70 m°C/W and 0.25 m°C/W, respectively. For other soils, specific values of r_w and r_s are used.

2.2.3.3 Volumetric heat capacity

Heat capacity of a soil is calculated as the sum of the heat capacities of its different constituent (Abu-Hamdeh, 2003) and it depends on mineralogical composition (Wierenga et al., 1969), water content and density (De Vries, 1963):

$$H\ [MJ/°C] = (c_s m_s + c_w m_w + c_i m_i + c_{air} m_{air}) \tag{2.20}$$

that divided by total mass m becomes:

$$c\ [MJ/kg°C] = \frac{1}{m}(c_s m_s + c_w m_w + c_i m_i + c_{air} m_{air}) \tag{2.21}$$

dividing by volume V and ignoring the very small air term Eq. (2.21) becomes:

$$C_u [MJ/m^3 °C] = \rho_{d_u}(c_s + c_w w_u) \tag{2.22}$$

$$C_f [MJ/m^3 °C] = \rho_{d_f}(c_s + c_i w_i) \tag{2.23}$$

for completely unfrozen and frozen state, where ρ_{d_u} and ρ_{d_f} are unfrozen and frozen dry density, respectively, c_s, c_w and c_i are specific heat respectively of mineralogical (solid) phase, water and ice, w_u and w_i are unfrozen and frozen water content.

The value of c_s is a function of the mineralogical composition of the soil and can be calculated using the equation:

$$c_s = \sum_j (c_{m_j} * \omega_j) \quad \text{with} \quad \sum_j \omega_j = 1 \tag{2.24}$$

where c_m (kJ/kg°C) is the specific heat of each mineral and ω_j is the corresponding percentage in weight. Values of c_m were listed by Waples and Waples (2004*)* (see Table 2.8).

Table 2.8: Values of density, thermal conductivity and specific heat of mineraloglogical phase identified in considered soils through X-ray Diffraction (see Table 2.2).

Mineralogical Phase	**Density,** ρ_m [g/cm^3] Horai (1971)	**Thermal conductivity,** k_s [W/m°C] Horai (1971)	**Specific heat,** c_s [kJ/kg°C] Waples and Waples (2004)
Quartz	2.65	7.69	0.74
Plagioclase	2.70	1.70	0.73
K-feldspar	2.58	2.32	0.63
Muscovite	2.85	3.48	0.76
Chlorite	2.75	5.15	0.60
Serpentine	2.66	2.95	0.65
Anphibole	3.18	2.81	0.75
Calcite	2.71	3.59	0.82
Clay	-	-	-
Dolomite	2.90	5.51	0.87
Aragonite	-	-	-
Pyrite	-	-	-

2.2.3.4 *Freezing point of soils*

As is well known, the mass of water contained in a soil freezes over a more or less wide temperature range starting from the freezing point of a soil. From this value freezing processes take place within the soil that led to a change in the thermal parameters of the soil until total freezing is reached. Freezing points of non-saline (I) and saline (G) soils were investigated performing laboratory tests based on study of Bing and Ma (2011). Two specimens, one of I1-N and the other of I2-N, were reconstituted following the same phases of preparation of disturbed soil specimen for UCS tests; two saline soil specimens, one of G1-S and the other of G2-S, were resampled so to obtain cylinders with diameter and height of 50 mm and 60 mm, respectively (Figure 2.10). A T-type thermocouple was inserted in the inner middle part of each specimen. The two non-saline and saline specimens were placed in a cold room set to -10°C, and -11.8°C respectively, and the temperature inside the soil was monitored until it reached room temperature. Two additional thermocouples were placed inside a container with distilled and sampled brackish water, respectively.

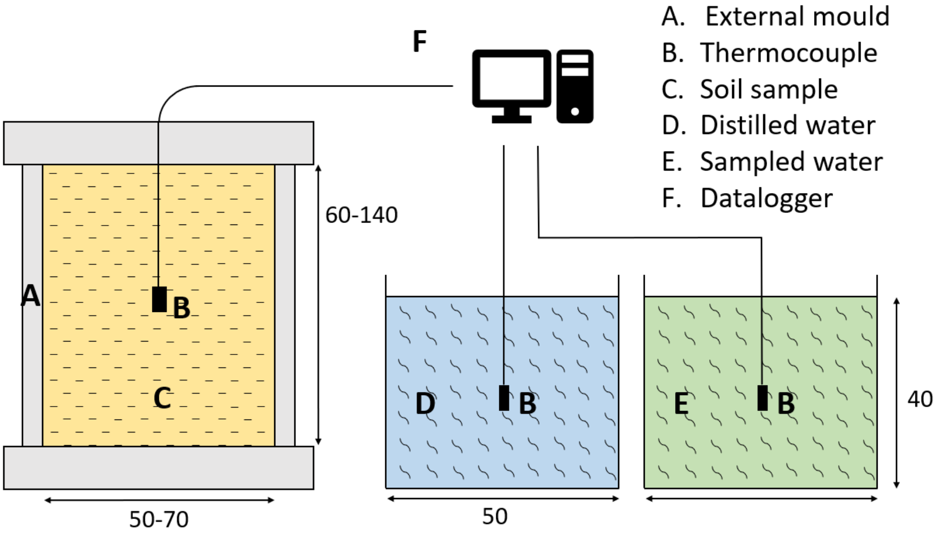

Figure 2.10: Freezing point test layout inspired by Bing and Ma (2011). Dimensions are expressed in mm.

2.3 Results

2.3.1 Mechanical parameters

The results of the mechanical tests (UCS, TRX, BRZ, PLT) are shown for each soil so that it is possible to have an overview of the mechanical parameters of each individual sample. For each group of tests performed on a geomaterial, a summary table of the results and a stress/strain graph are provided. The materials analysed, and their respective tests, are listed as follows:

- I1-N → */u, /t, /p*
- I2-N → */u, /u-h, /t, /p, /p-h*
- M1-N → */u, /t, /b*
- M2-N → */u, /t, /b*
- M3-N → */u, /t, /b*
- CO → */u-e, /u-s, /u-f, /u-c*
- TS → */u, /t, /b*

In those graphs in which a peak was reached, this was taken as the failure value even though it occurred at large deformations (~0.15). In the graphs in which a true peak was not reached (e.g., in the graphs all the mechanical tests on M2-N and M3-N), the resistance values correspond to the ordinate of the intersection point between the straight lines that bisect the two linear stretches of the stress-strain curve.

Regarding Isarco, it can be seen that the specimens with porosity of 0.25 (I1-N/u) generally show higher values than those with porosity of 0.3 (I2-N/u) and that among these the temperature increases from -10 to -6°C results in a reduction of σ_c worth 5.26 MPa. The triaxial tests, on the other hand, returned higher strength values for the specimens with a porosity of 0.3 with the same confinement. The PL tests were performed rapidly and efficiently on cylindrical specimens of frozen soil. The values of $I_{s(50)}$ returned for soil specimens I1-N and I2-N at -10°C are 4 in total, and the values are almost similar in pairs; while the values found at T= -6°C range from 0.43 to 1.12 MPa.

The average UCS values are 6.72, 3.18 and 4.48 for M1-N, M2-N and M3-N respectively. The tensile strength ranges from 1.27 to 0.96 to 0.86 MPa. The triaxial tests showed that under confined conditions, M1-N and M2-N specimens show an increase in σ_c while specimen M3-N is not greatly affected by the effect of confinement, although in the triaxial tests the stiffness of the soil increases significantly, as well as for M2-N. The constant temperature at which the tests were carried out did not appear to influence the compressive strength of the concrete, which had an average value of 43.5 MPa at 20°C and 47.4 MPa at -20°C; however, the imposition of a freeze/thaw cycle resulted in a decrease in strength which reached 38.1 MPa. The thermal gradient imposed within the specimen (-80°C at the bottom and -30°C at the top) provided the highest results, 62.4 MPa. The stiffness of the concrete, however, seems to maintain very similar average values, except for the tests performed at -20 °C for which average $E_{\text{sec}\ (0.4)}$ increases by 50%.

The following pages provide the results of all the mechanical tests performed, described with a table (from Table 2.9 to Table 2.32), a graph and, where possible, pictures of the equipment and specimens before or after failure (from Figure 2.11 to Figure 2.32).

I1-N

Table 2.9: Unconfined compression tests results of I1-N soil sample at -10 °C.

Soil specimen	Axial strain rate [%/min]	σ_3 [MPa]	σ_c [Mpa]	E_{t50} [Gpa]	σ_t [Mpa]
I1-N/u1	1	-	7.62	1.37	-
I1-N/u2	0.5	-	6.48	1.10	-
I1-N/u3	0.1	-	5.18	1.08	-

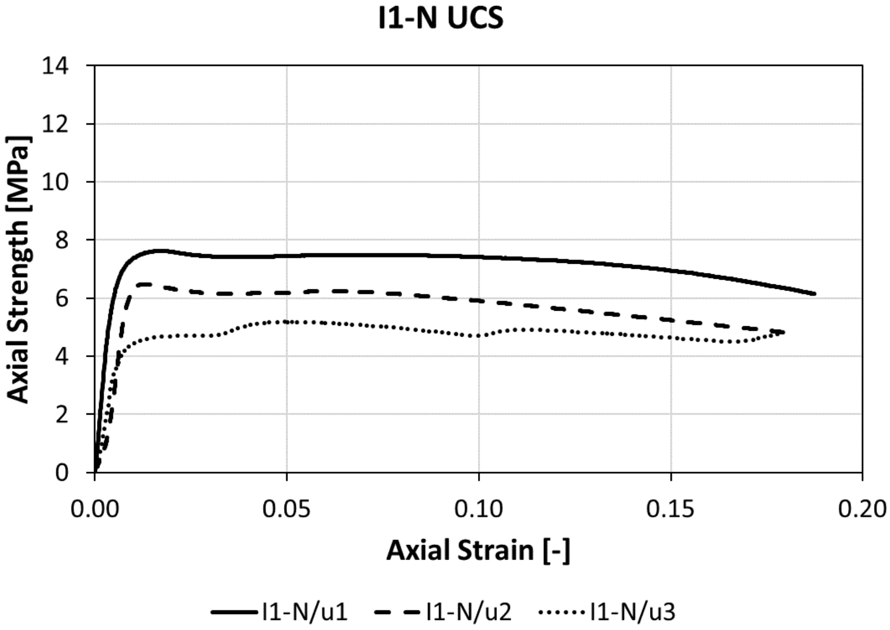

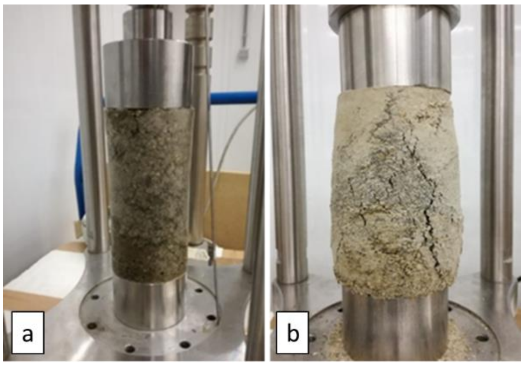

Figure 2.11: Unconfined compression tests results of I1-N soil sample at -10 °C. a) pre and b) post failure.

Table 2.10: Triaxial compression tests results of I1-N soil sample at -10 °C.

Soil specimen	Axial strain rate [%/min]	σ_3 [MPa]	σ_c [Mpa]	E_{t50} [Gpa]	σ_t [Mpa]
I1-N/t1	0.43	0.3	8.84	1.24	-
I1-N/t2	0.43	0.6	8.35	0.96	-
I1-N/t3	0.43	0.9	10.77	1.01	-
I1-N/t4	0.43	1.2	11.26	0.77	-

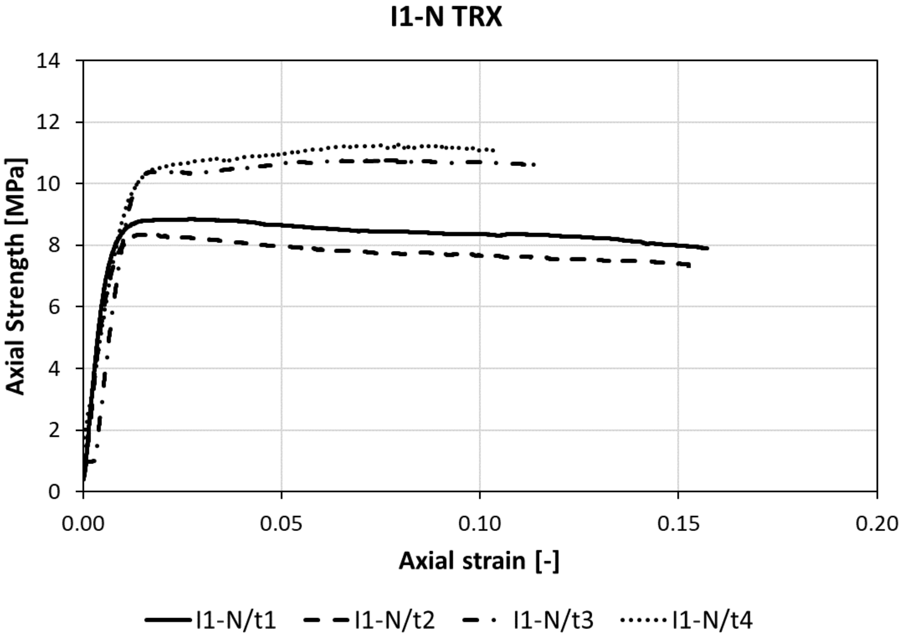

Figure 2.12: Triaxial compression tests results of I1-N soil sample at -10 °C.

Table 2.11: Point load tests results of I1-N soil sample at -10 °C.

Soil specimen	D' [mm]	P max load [kN]	I_s index PLS [Mpa]	$I_{s(50)}$ ASTM D5731 [MPa]
I1-N/p1	36.0	1.50	0.65	0.64
I1-N/p2	36.0	1.77	0.77	0.76

I2-N

Table 2.12: Unconfined compression tests results of I2-N soil sample at -10 °C.

Soil specimen	Axial strain rate [%/min]	σ_3 [MPa]	σ_c [Mpa]	E_{t50} [Gpa]	σ_t [Mpa]
I2-N/u1	1	-	6.26	0.99	-
I2-N/u2	0.5	-	6.38	0.50	-
I2-N/u3	0.1	-	5.02	1.51	-

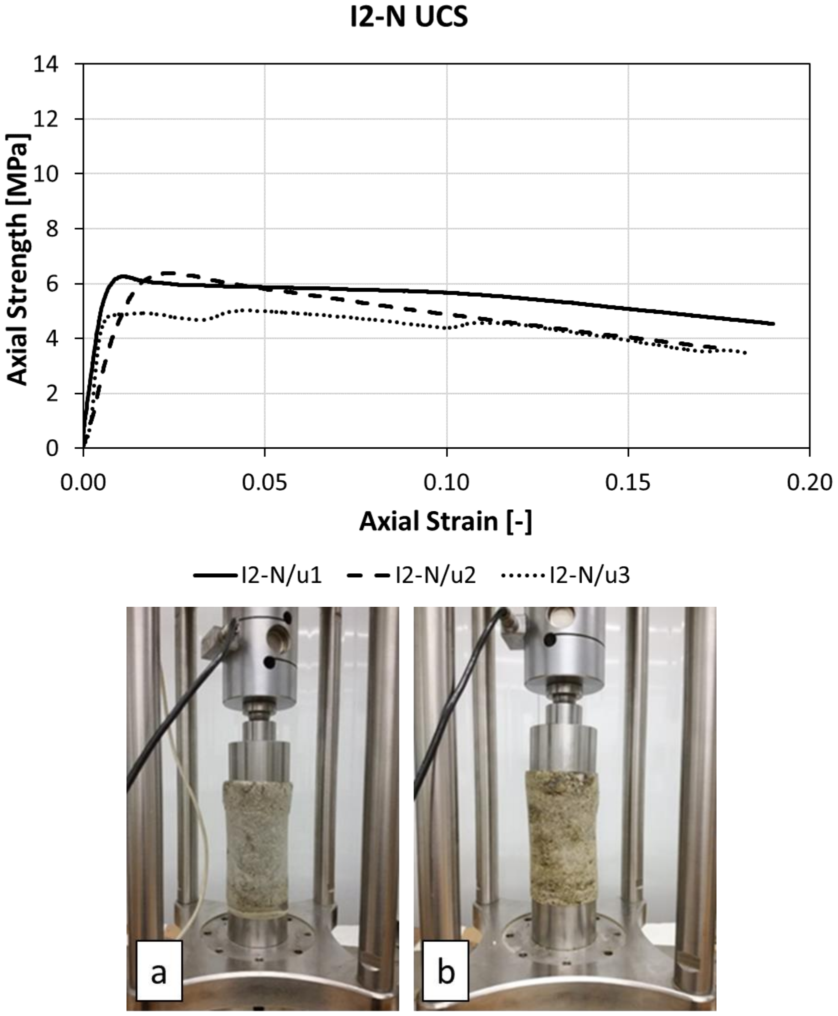

Figure 2.13: Unconfined compression tests results of I2-N soil sample at -10 °C. a-b) post -failure.

Table 2.13: Unconfined compression tests results of I2-N soil sample at -6 °C.

Soil specimen	Axial strain rate [%/min]	σ_3 [MPa]	σ_c [Mpa]	E_{t50} [Gpa]	σ_t [Mpa]
I2-N/u1-h	1	-	5.52	0.67	-
I2-N/u2-h	1	-	5.35	0.45	-
I2-N/u3-h	1	-	5.20	0.63	-
I2-N/u4-h	0.5		4.97	0.71	

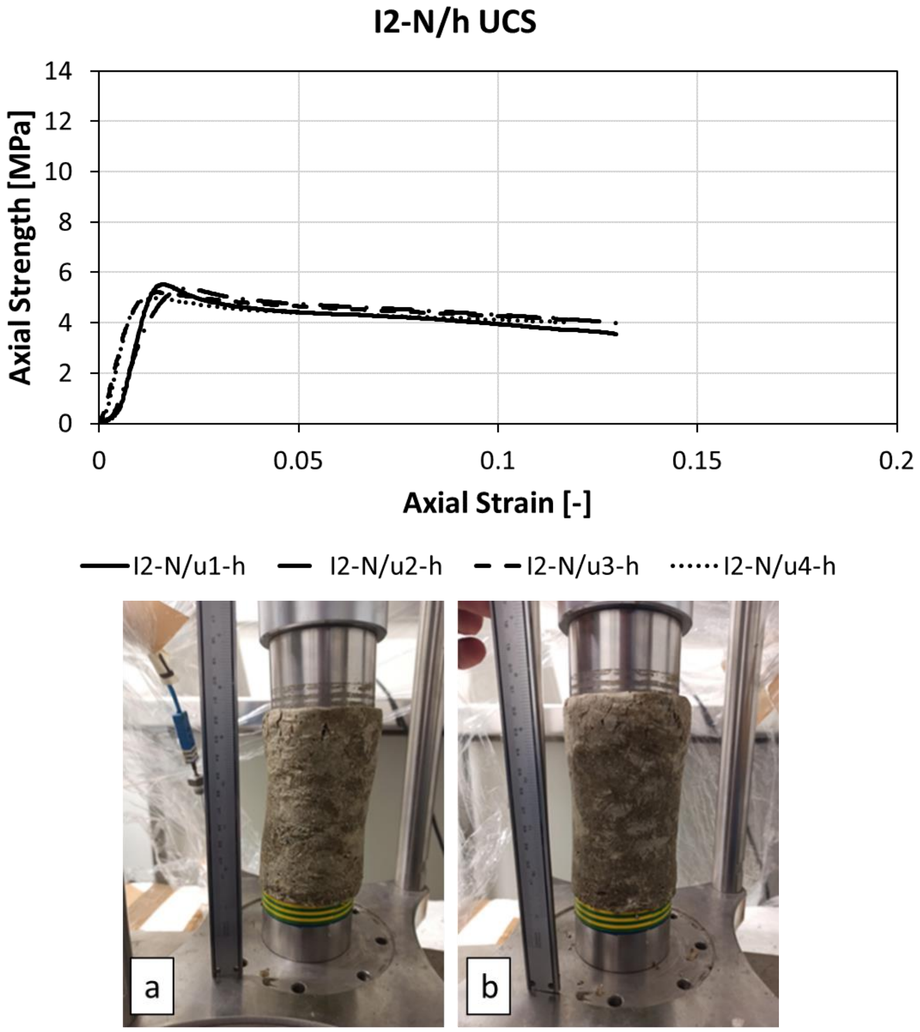

Figure 2.14: Unconfined compression tests results of I2-N soil sample at -6 °C. a-b) post-failure.

Table 2.14: Triaxial compression tests results of I2-N soil sample at -10 °C.

Soil specimen	Axial strain rate [%/min]	σ_3 [MPa]	σ_c [Mpa]	E_{t50} [Gpa]	σ_t [Mpa]
I2-N/t1	0.43	0.3	11.19	0.98	-
I2-N/t2	0.43	0.6	9.67	1.04	-
I2-N/t3	0.43	0.9	12.68	1.33	-
I2-N/t4	0.43	1.2	10.88	0.95	-

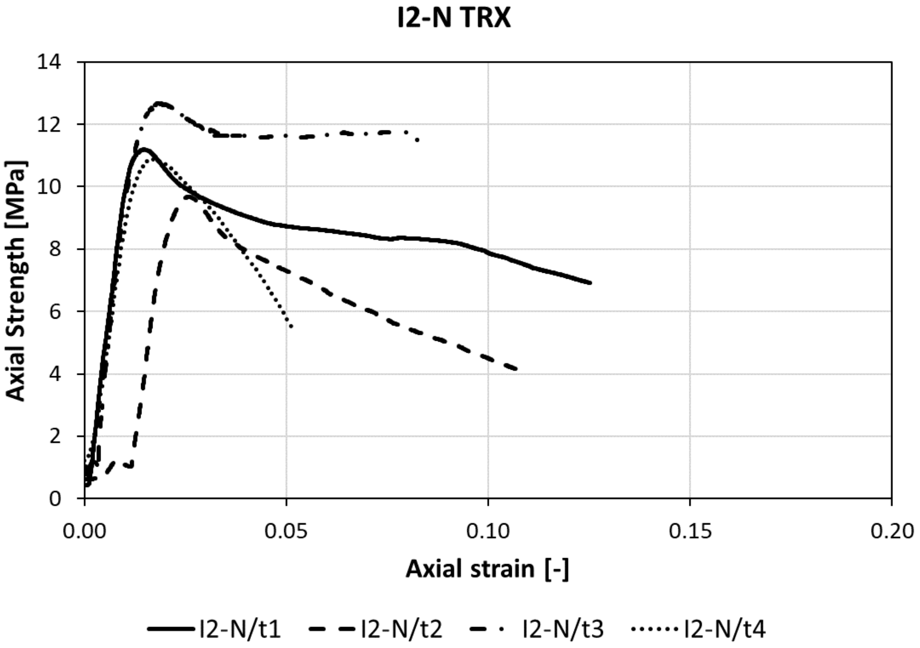

Figure 2.15: Triaxial compression tests results of I2-N soil sample at -10 °C.

Table 2.15: Point load tests results of I2-N soil sample at -10 °C.

Soil specimen	**D'** [mm]	**P** max load [kN]	**I_s** index PLS [Mpa]	**$I_{s(50)}$** ASTM D5731 [MPa]
I2-N/p1	32.0	1.62	0.80	0.76
I2-N/p2	39.0	2.10	0.85	0.84

Table 2.16: Point load tests results of I2-N soil sample at -6 °C.

Soil specimen	**D'** [mm]	**P** max load [kN]	**I_s** index PLS [Mpa]	**$I_{s(50)}$** ASTM D5731 [MPa]
I2-N/p1-h	38.0	0.79	0.46	0.43
I2-N/p2-h	36.5	2.03	1.23	1.12
I2-N/p3-h	17.5	1.10	1.10	0.89
I2-N/p4-h	18.0	0.70	0.68	0.56
I2-N/p5-h	37.0	1.36	0.81	0.74
I2-N/p6-h	21.0	0.85	0.71	0.60
I2-N/p7-h	37.0	1.29	0.77	0.71
I2-N/p8-h	31.0	1.60	1.15	1.01
I2-N/p9-h	20.0	1.09	0.95	0.80
I2-N/p10-h	44.0	2.48	0.98	0.99

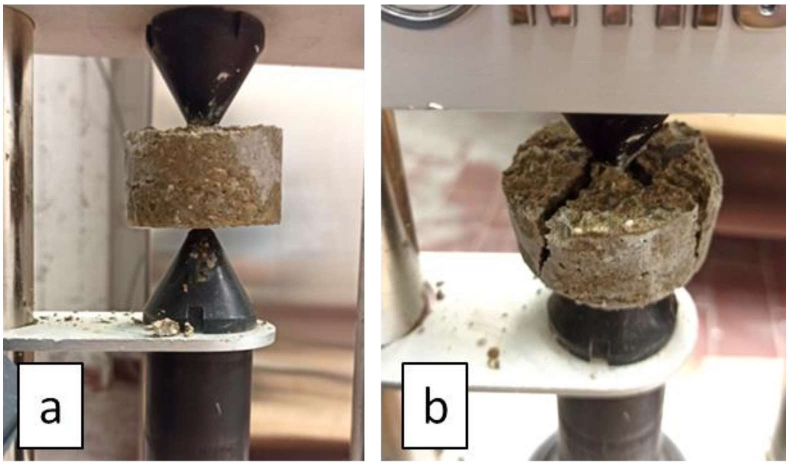

Figure 2.16: Point load tests on I2-N soil sample at -6 °C. a) pre-failure; b) post-failure.

M1-N

Table 2.17: Unconfined compression tests results of M1-N soil sample at -10 °C.

Soil specimen	Axial strain rate [%/min]	σ_3 [MPa]	σ_c [Mpa]	E_{t50} [Gpa]	σ_t [Mpa]
M1-N/u1	1	0	6.69	1.13	-
M1-N/u2	0.5	0	5.86	0.85	-
M1-N/u3	1	0	7.63	0.56	-

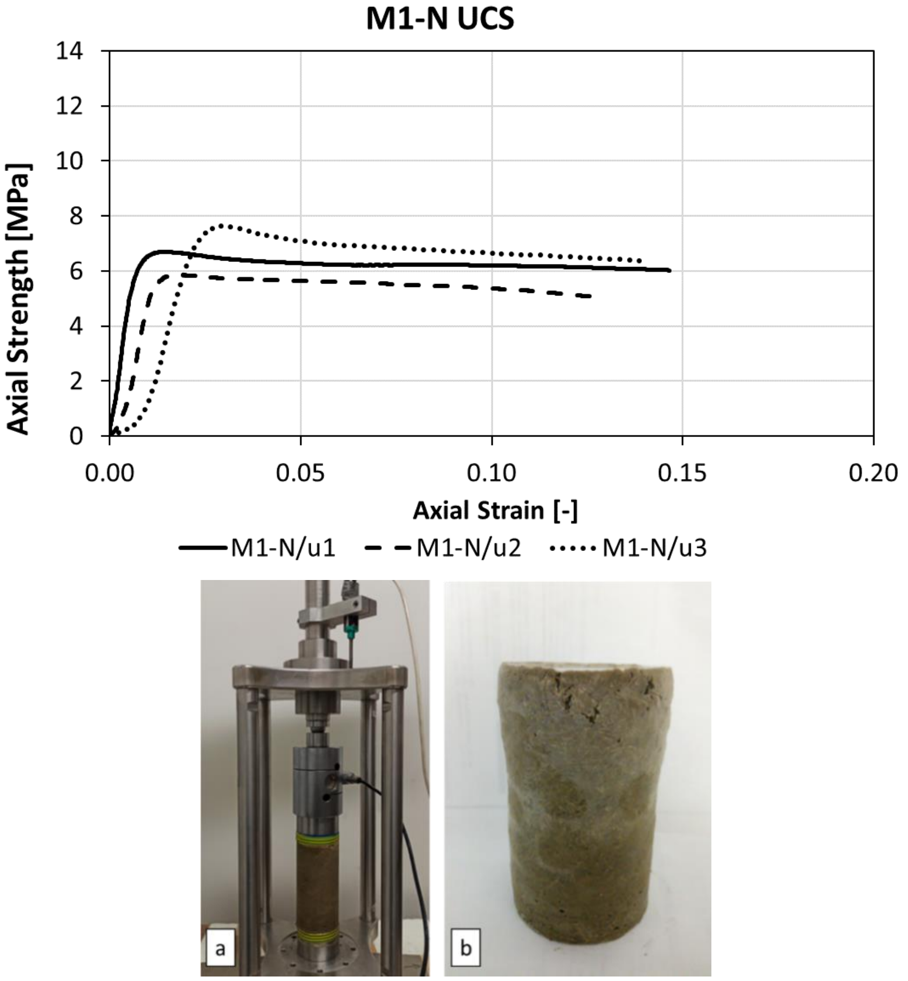

Figure 2.17: Unconfined compression tests results of M1-N soil sample at -10 °C. a) pre- and b) post-failure.

Table 2.18: Triaxial compression tests results of M1-N soil sample at -10 °C.

Soil specimen	Axial strain rate [%/min]	σ_3 [MPa]	σ_c [Mpa]	E_{t50} [Gpa]	σ_t [Mpa]
M1-N/t1	0.43	0.3	8.06	0.63	-
M1-N/t2	0.43	0.6	8.14	0.95	-

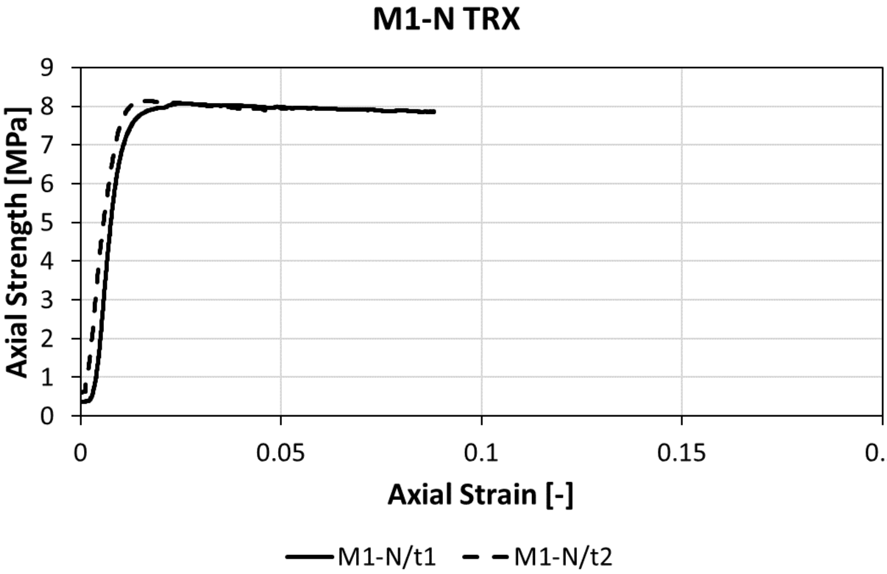

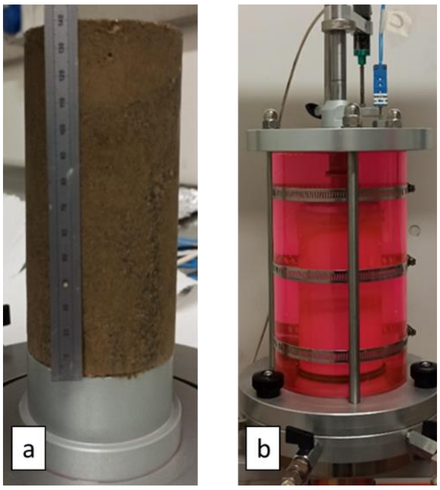

Figure 2.18: Triaxial compression tests results of M1-N soil sample at -10 °C. a) M1-N frozen soil sample; b) sample in the cell.

Table 2.19: Brazilian tests results of M1-N soil sample at -10 °C.

Soil specimen	Axial strain rate [%/min]	σ_3 [MPa]	σ_c [Mpa]	E_{t50} [Gpa]	σ_t [Mpa]
M1-N/b1	0.5	0	-	-	1.2
M1-N/b2	1	0	-	-	1.33
M1-N/b3	0.5	0	-	-	1.29

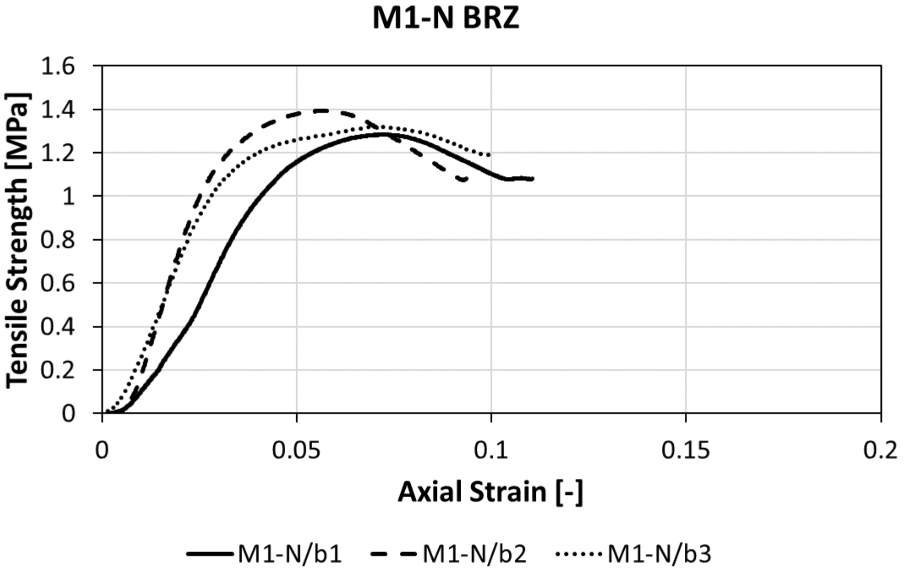

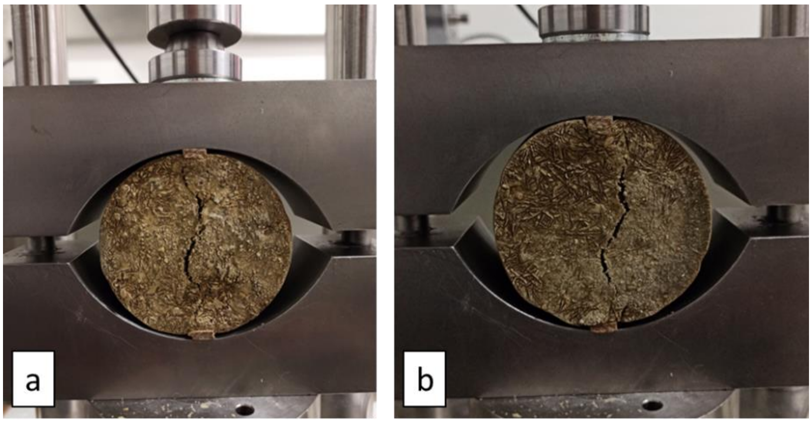

Figure 2.19: Brazilian tests results of M1-N soil sample at -10 °C. a-b) cracks formation at the failure point.

M2-N

Table 2.20: Unconfined compression tests results of M2-N soil sample at -10 °C.

Soil specimen	Axial strain rate [%/min]	σ_3 [MPa]	σ_c [Mpa]	E_{t50} [Gpa]	σ_t [Mpa]
M2-N/u1	1	0	3.62	0.29	-
M2-N/u2	1	0	3.54	0.23	-
M2-N/u3	0.5	0	2.38	0.27	-

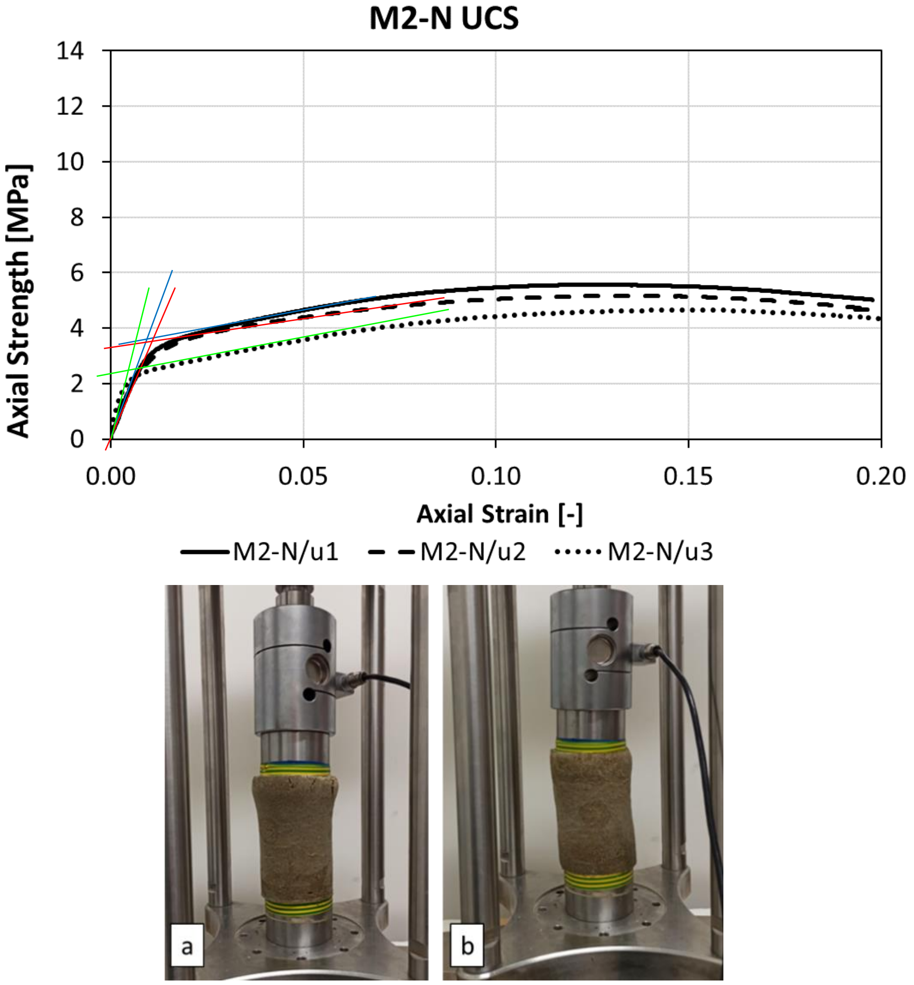

Figure 2.20: Unconfined compression tests results of M2-N soil sample at -10 °C. a-b) post-failure.

Table 2.21: Triaxial compression tests results of M2-N soil sample at -10 °C.

Soil specimen	Axial strain rate [%/min]	σ_3 [MPa]	σ_c [Mpa]	E_{t50} [Gpa]	σ_t [Mpa]
M2-N/t1	0.43	0.3	5.98	0.79	-
M2-N/t2	0.43	0.6	6.31	0.85	-

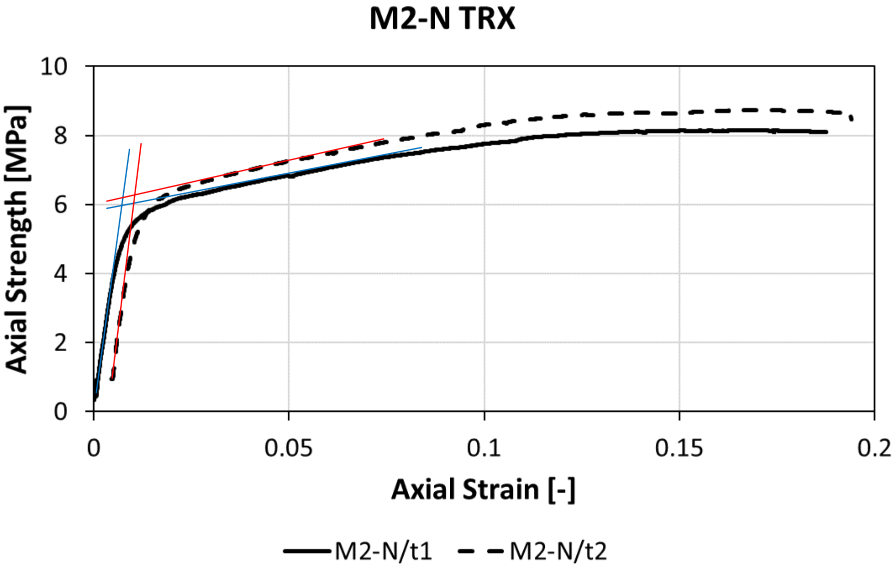

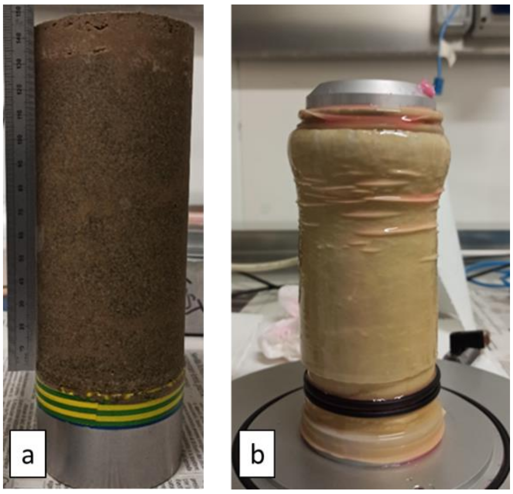

Figure 2.21: Triaxial compression tests results of M2-N soil sample at -10 °C. a) M2-N frozen soil sample; b) sample post-failure.

Table 2.22: Brazilian tests results of M2-N soil sample at -10 °C.

Soil specimen	Axial strain rate [%/min]	σ_3 [MPa]	σ_c [Mpa]	E_{t50} [Gpa]	σ_t [Mpa]
M2-N/b1	0.5	0	-	-	0.91
M2-N/b2	1	0	-	-	0.96
M2-N/b3	1	0	-	-	1.02

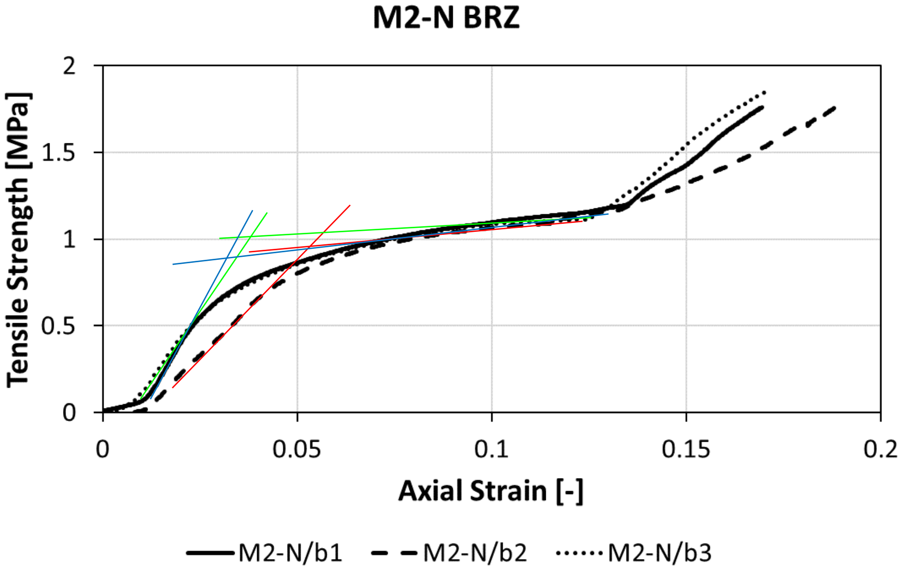

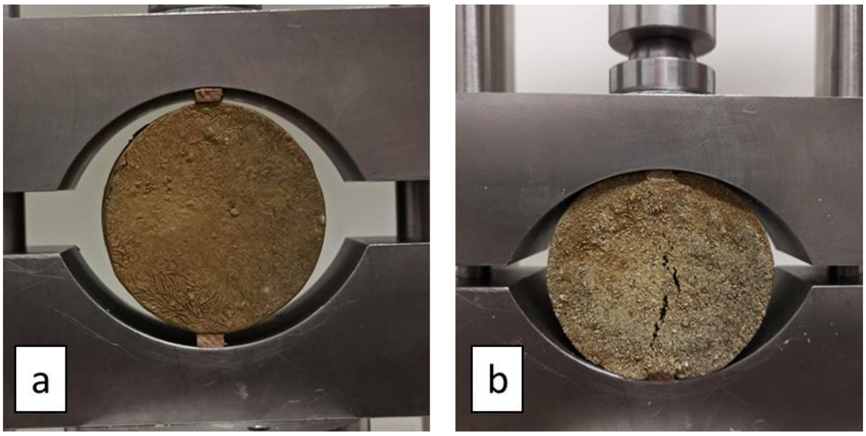

Figure 2.22: Brazilian tests results of M2-N soil sample at -10 °C. a) pre-failure; b) cracks formation at the failure point.

M3-N

Table 2.23: Unconfined compression tests results of M3-N soil sample at -10 °C.

Soil specimen	Axial strain rate [%/min]	σ_3 [MPa]	σ_c [Mpa]	E_{t50} [Gpa]	σ_t [Mpa]
M3-N/u1	1	0	4.1	0.41	-
M3-N/u2	1	0	4.47	0.2	-
M3-N/u3	1	0	4.89	0.23	-

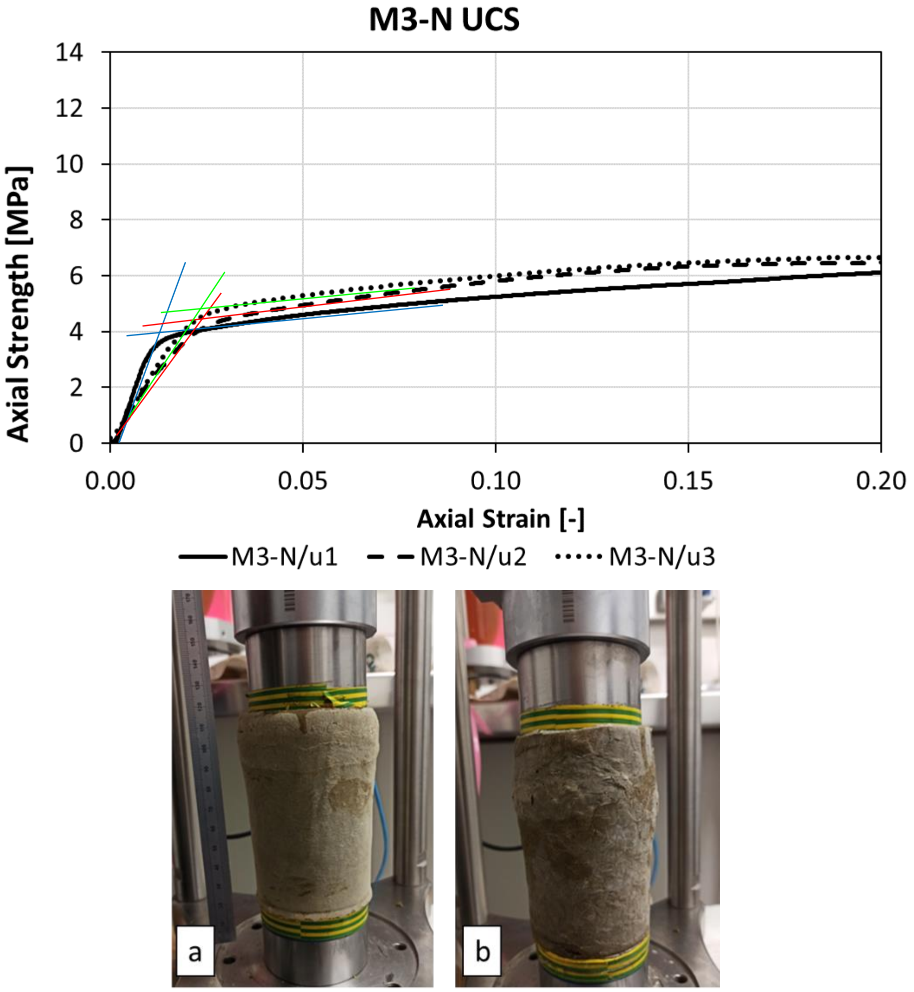

Figure 2.23: Unconfined compression tests results of M3-N soil sample at -10 °C. a-b) post-failure.

Table 2.24: Triaxial compression tests results of M3-N soil sample at -10 °C.

Soil specimen	Axial strain rate [%/min]	σ_3 [MPa]	σ_c [Mpa]	E_{t50} [Gpa]	σ_t [Mpa]
M3-N/t1	0.43	0.3	4.89	0.6	-
M3-N/t2	0.43	0.6	5.58	0.69	-

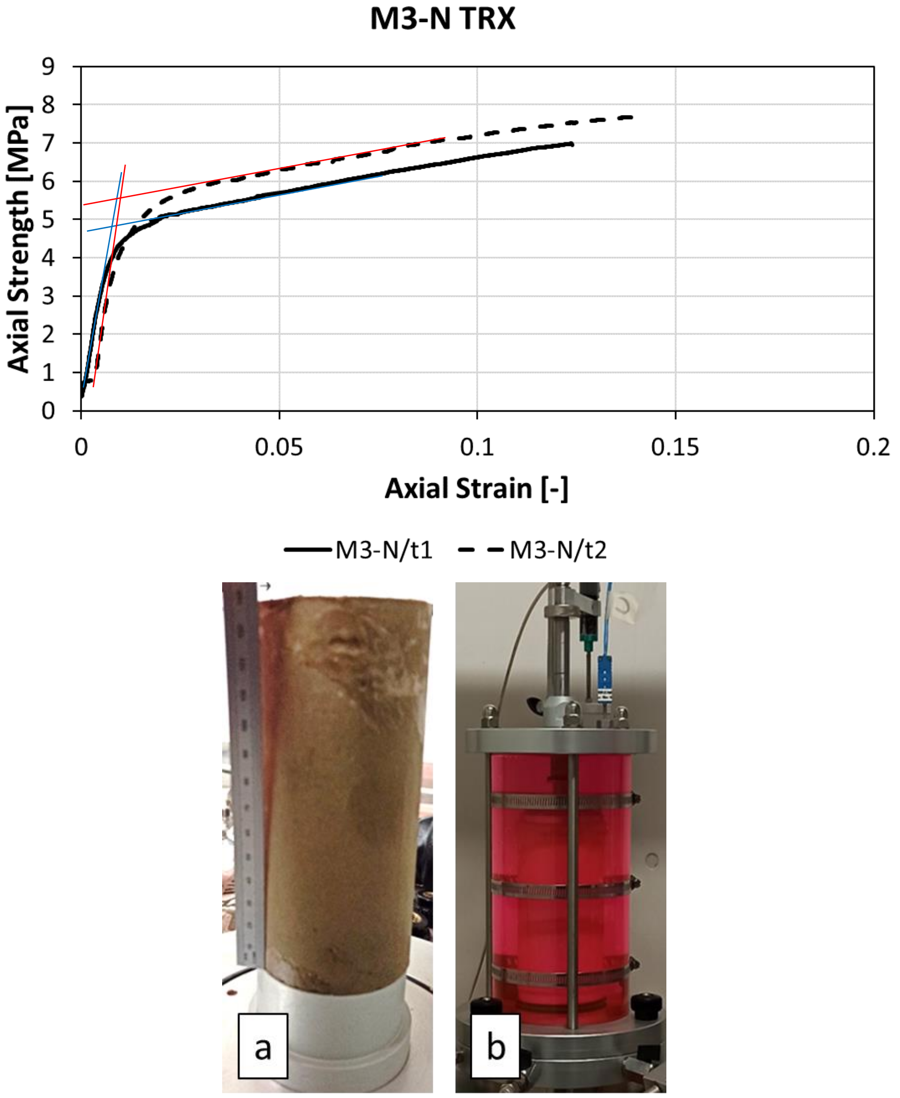

Figure 2.24: Triaxial compression tests results of M3-N soil sample at -10 °C. a) M3-N frozen soil sample; b) sample in the cell.

Table 2.25: Brazilian tests results of M3-N soil sample at -10 °C.

Soil specimen	**Axial strain rate [%/min]**	**σ_3 [MPa]**	**σ_c [Mpa]**	**E_{t50} [Gpa]**	**σ_t [Mpa]**
M3-N/b1	1	0	-	-	0.99
M3-N/b2	0.5	0	-	-	0.82
M3-N/b3	0.5	0	-	-	0.78

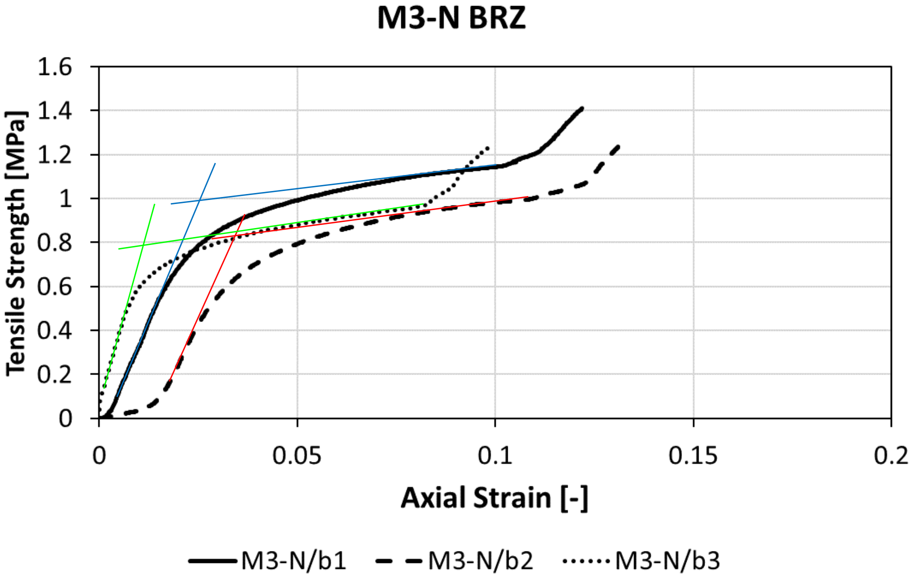

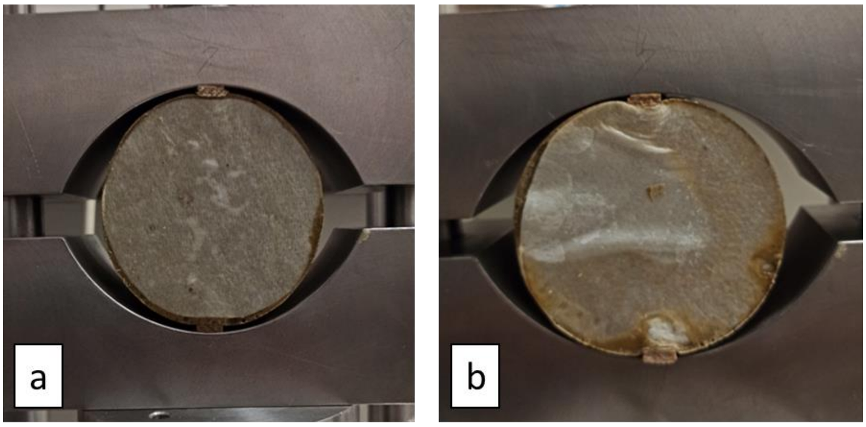

Figure 2.25: Brazilian tests results of M2-N soil sample at -10 °C. a) pre-failure; b) post-failure.

CO

Table 2.26: Unconfined compression tests results of CO sample at 20 °C.

Soil specimen	**Axial strain rate [%/min]**	**σ_c [MPa]**	**$E_{sec0.4}$ [GPa]**
CO/u1-e	0.033	48.34	30.36
CO/u2-e	0.05	42.44	31.24
CO/u3-e	0.05	39.61	23.05

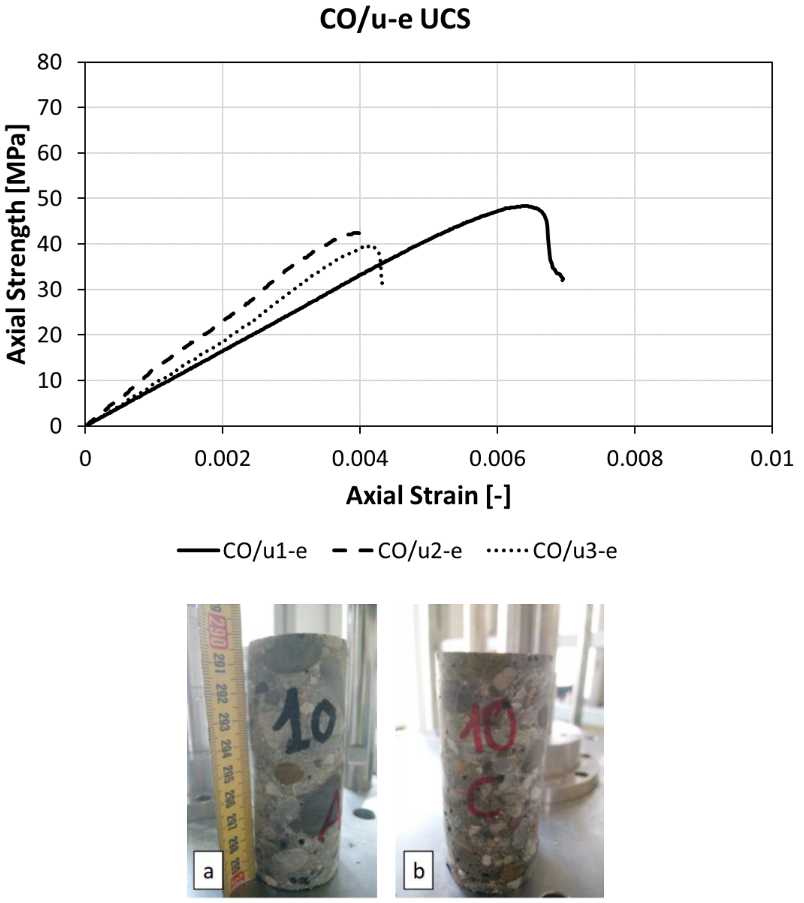

Figure 2.26: Unconfined compression tests results of CO sample at 20 °C. a-b) pre-failure.

Table 2.27: Unconfined compression tests results of CO sample under thermal gradient (-80°C and -30°C to bottom and top, respectively).

Soil specimen	Axial strain rate [%/min]	σ_c [MPa]	$E_{sec0.4}$ [GPa]
CO/u1-s	0.05	68.43	27.93
CO/u2-s	0.05	57.00	29.30
CO/u3-s	0.05	61.89	29.20

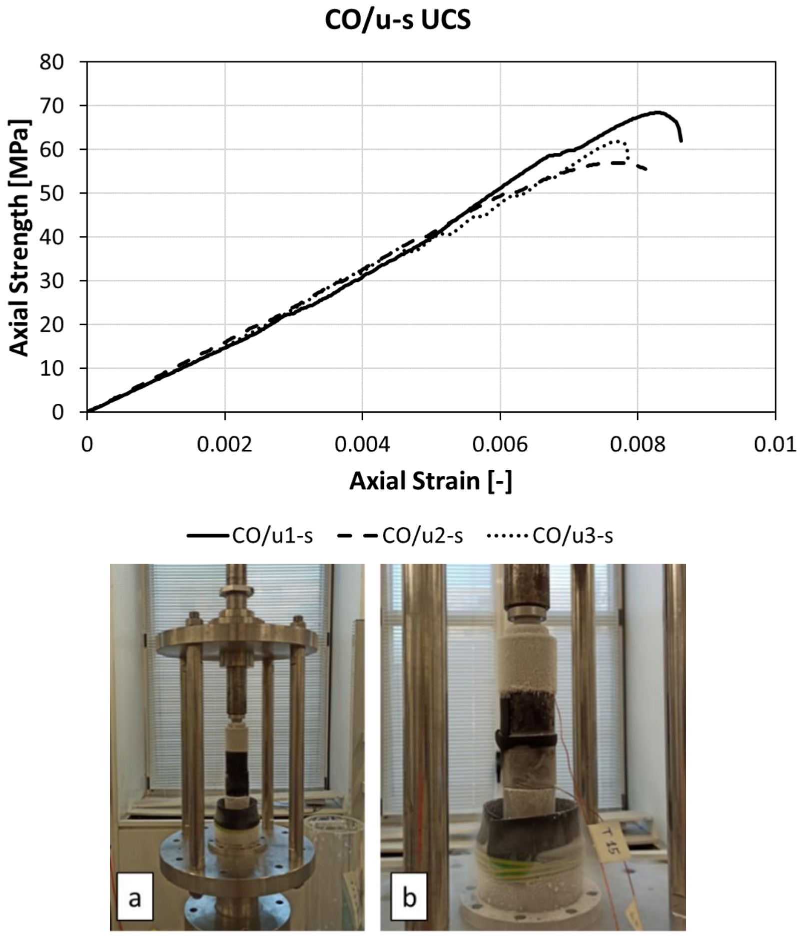

*Figure 2.27**:** Unconfined compression tests results of CO under thermal gradient (-80°C and -30°C to bottom and top, respectively). a) Loading and LN_2 fedding system; b) detail on thermocouples and gaseous nitrogen.*

Table 2.28: Unconfined compression tests results of CO sample at -20 °C.

Soil specimen	Axial strain rate [%/min]	σ_c [MPa]	$E_{sec0.4}$ [GPa]
CO/u1-f	0.05	47.15	34.85
CO/u2-f	0.05	39.98	33.32
CO/u3-f	0.05	54.94	37.40

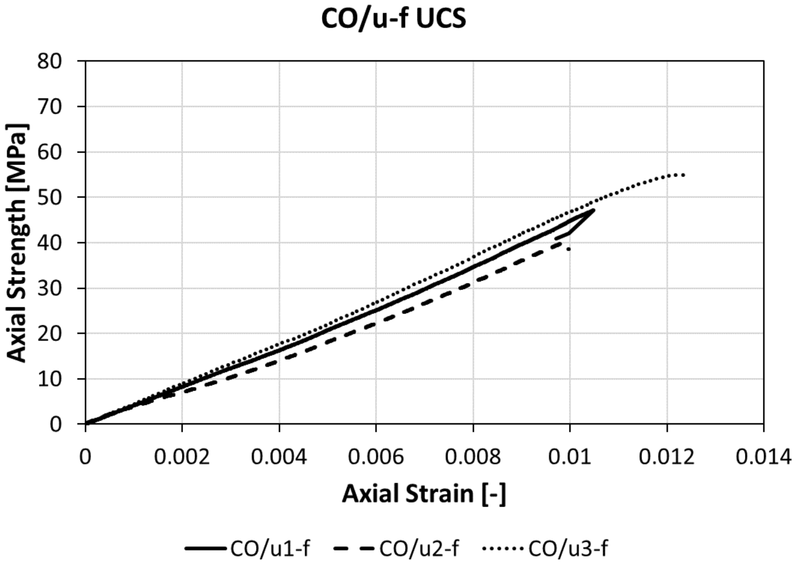

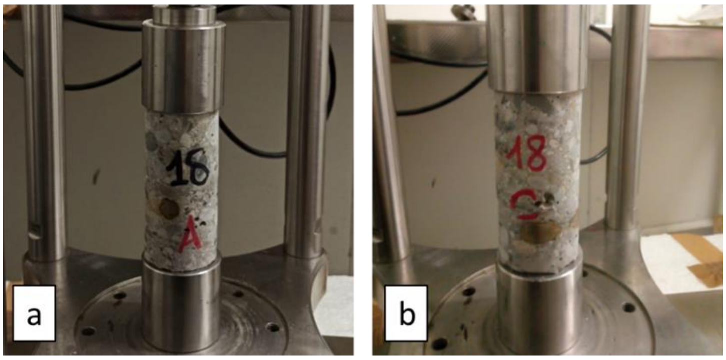

Figure 2.28: Unconfined compression tests results of CO sample at -20 °C. a-b) pre-failure.

Table 2.29: Unconfined compression tests results of CO sample after at 20°C after freezing phase ad -10°C.

Soil specimen	Axial strain rate [%/min]	σ_c [MPa]	$E_{sec0.4}$ [GPa]
CO/u1-c	0.05	44.01	23.2
CO/u2-c	0.05	34.25	25.95
CO/u3-c	0.05	36.05	22.56

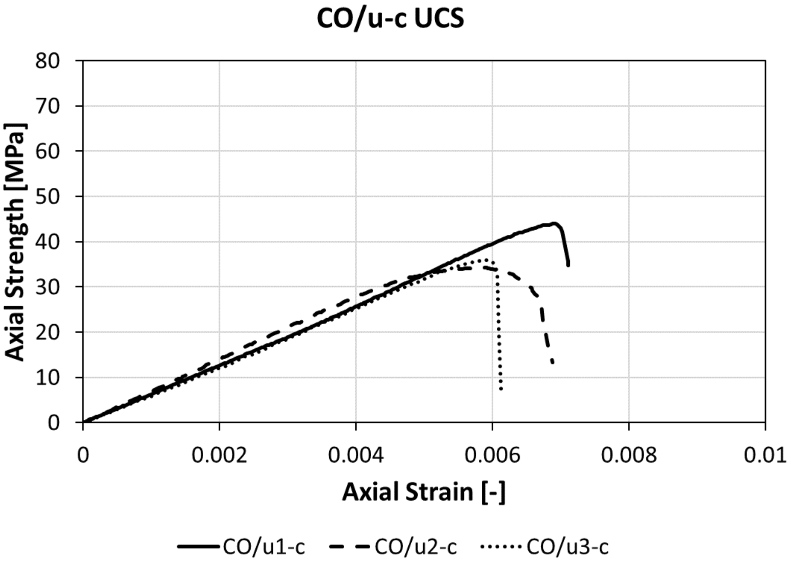

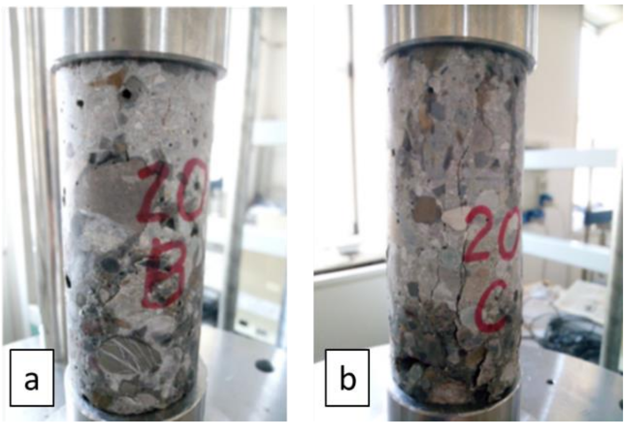

Figure 2.29: Unconfined compression tests results of CO sample at 20 °C after freezing phase ad -10°C. a) pre- and b) post-failure (crack formation).

TS

Table 2.30: Unconfined compression tests results of TS sample at -10 °C.

Soil specimen	Axial strain rate [%/min]	σ_3 [MPa]	σ_c [Mpa]	E_{t50} [Gpa]	σ_t [Mpa]
TS/u1	0.79	-	13.08	0.85	-
TS/u2	0.79	-	13.57	0.92	-
TS/u3	0.79	-	13.07	1.22	-

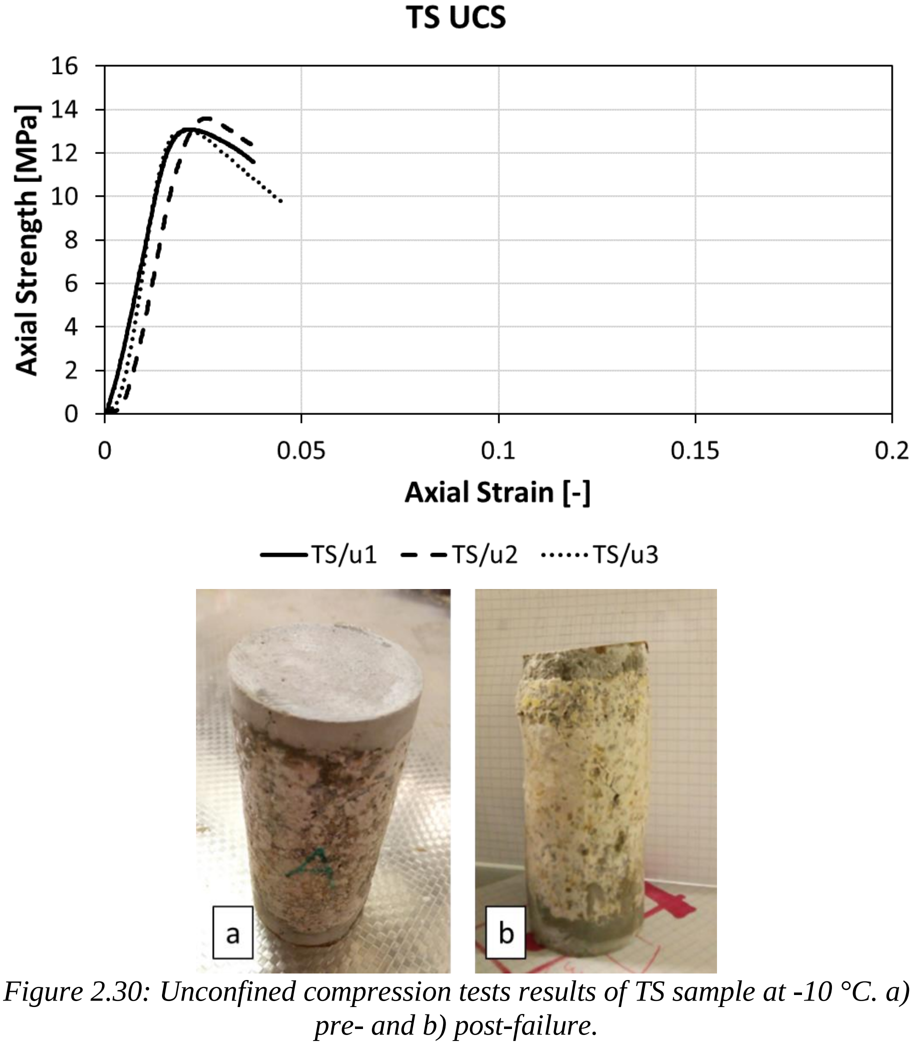

Figure 2.30: Unconfined compression tests results of TS sample at -10 °C. a) pre- and b) post-failure.

Table 2.31: Triaxial compression tests results of TS sample at -10 °C.

Soil specimen	Axial strain rate [%/min]	σ_3 [MPa]	σ_c [Mpa]	E_{t50} [Gpa]	σ_t [Mpa]
TS/t1	0.75	0.6	13.20	1.10	-
TS/t2	0.75	0.8	11.59	0.64	-

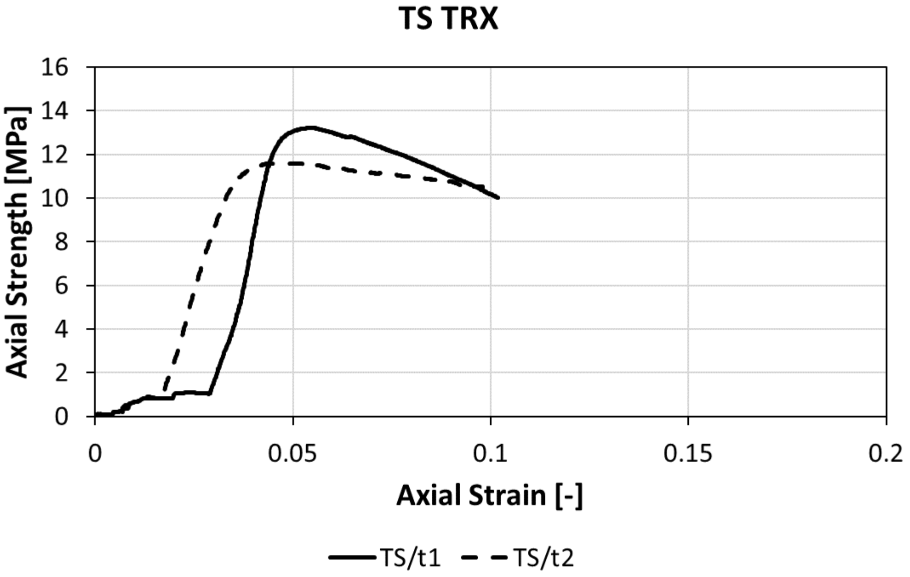

Figure 2.31: Triaxial compression tests results of TS sample at -10 °C.

Table 2.32: Brazilian tests results of TS sample at -10 °C.

Soil specimen	Axial strain rate [%/min]	σ_3 [MPa]	σ_c [Mpa]	E_{t50} [Gpa]	σ_t [Mpa]
TS/b1	1	0	-	-	2.41
TS/b2	1	0	-	-	2.21
TS/b3	0.5	0	-	-	2.24

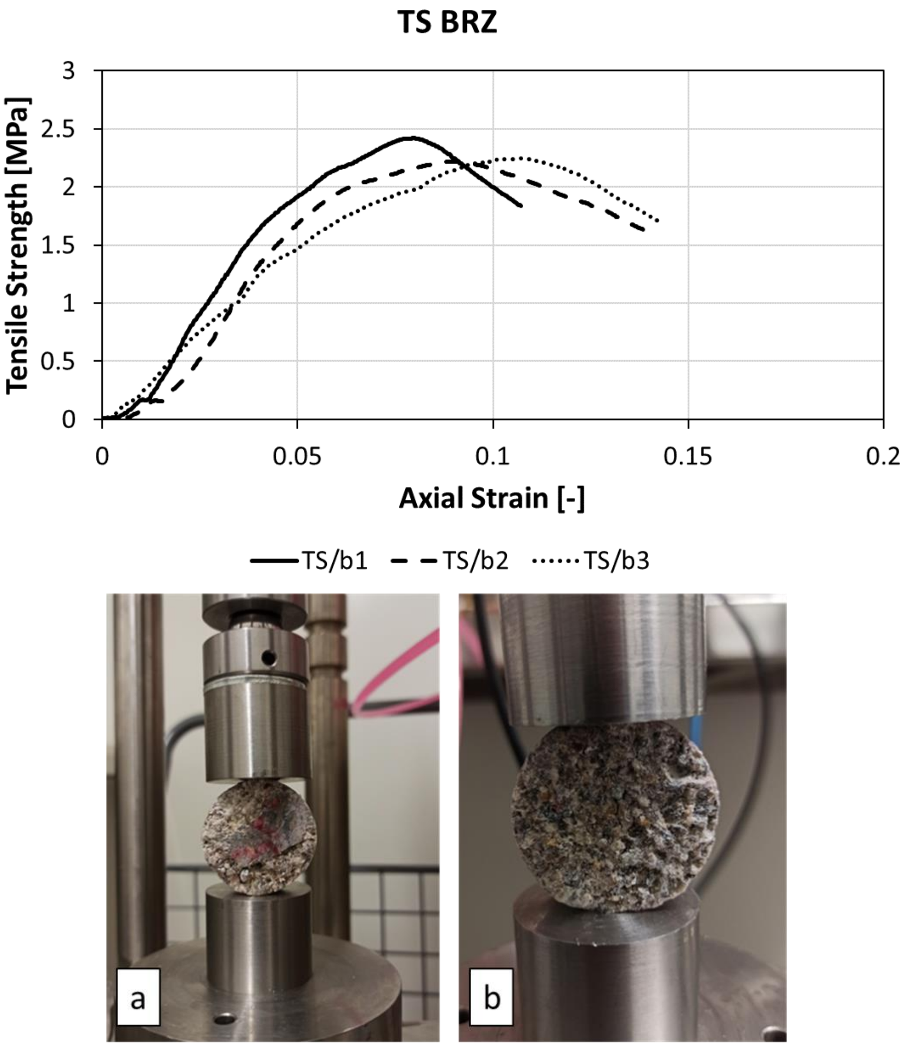

Figure 2.32: Brazilian tests results of TS sample at -10 °C. a) pre- and b) post-failure (crack formation)

2.3.2 Thermal parameters

Measured values of unfrozen (20 °C) and frozen (-10 °C) thermal conductivity of non-saline (Isarco and Milano), saline (Genoa) and treated soils are reported in Table 2.33.

Table 2.33: Measured thermal conductivity at unfrozen (k_{unf}.) and frozen ($k_{f.}$) state of investigated samples.

		NON-saline soils				Saline soils		
Symbol	**U. M.**	**I2-N**	**M1-N**	**M2-N**	**M3-N**	**G1-S**	**G2-S**	**TS**
k_{unf}	[W/m°C]	2.24	2.08	1.93	1.52	1.55	1.68	2.09
k_f	[W/m°C]	3.34	3.28	3.06	2.69	2.43	2.06	3.05

The estimated thermal conductivity values of soil in the unfrozen and frozen state were derived from the equations proposed by Johansen (1975), Côté and Konrad (2005) and Donazzi (1977) and from the values of the thermal parameters of water and ice taking the salt content into account (Table 2.34). The calculated values for non-saline and saline soils are shown in Table 2.35 and Table 2.36, respectively.

Table 2.34: Thermal conductivity values of water and ice considering different salt content, from literature.

Water sample	Salinity	Thermal conductivity [W/m°C]	Reference
fresh water (20 °C)	0 ‰	0.598	b
fresh ice (-10 °C)		2.320	d, c
sampled water (20 °C)	12.39 ‰	0.594	e
sampled ice (-10 °C)		1.650	d, c
sea water (20 °C)	35 ‰	0.593	e
sea ice (-10 °C)		1.500	a

a) Fukusako, 1990; b) Ramires et al., 1995; c) Rashid et al., 2016;
d) Sakazume and Seki, 1978; e) Sharqawy, 2013.

Table 2.35: Thermal conductivity values at unfrozen and frozen state of non-saline soils estimated using equation proposed by different authors.

			non saline			
	Symbol	**U.M.**	**I2-N**	**M1-N**	**M2-N**	**M3-N**
Johansen, 1975	$k_{unf.}$	[W/m°C]	2.403	2.179	1.904	1.546
	k_f	[W/m°C]	3.564	3.410	3.061	2.848
Côté and Konrad, 2005	$k_{unf.}$	[W/m°C]	2.669	2.361	2.102	1.712
	k_f	[W/m°C]	3.929	3.645	3.342	3.116
Donazzi, 1977	$k_{unf.}$	[W/m°C]	2.371	2.179	1.904	1.546
	k_f	[W/m°C]	3.523	3.372	3.036	2.825

Table 2.36: Thermal conductivity values at unfrozen and frozen state of saline soils estimated using equation proposed by different authors, considering different porewater salinity.

Pore-water salinity			**12.39‰**		**35‰**	
	Symbol	**U.M.**	**G1-S**	**G2-S**	**G1-S**	**G2-S**
Johansen, 1975	$k_{unf.}$	[W/m°C]	1.671	1.531	1.670	1.530
	k_f	[W/m°C]	2.605	2.292	2.498	2.206
Côté and Konrad, 2005	$k_{unf.}$	[W/m°C]	1.905	2.006	1.904	2.005
	k_f	[W/m°C]	2.900	2.940	2.776	2.824
Donazzi, 1977	$k_{unf.}$	[W/m°C]	1.655	1.518	1.654	1.517
	k_f	[W/m°C]	2.550	2.259	2.440	2.170

The estimated heat capacity values in the unfrozen and frozen state (Table 2.37 and Table 2.38) were determined using Equations 2.22, 2.23 and 2.24 and the values of the thermal parameters of water and ice taking the salt content into account (see Table 2.39).

Table 2.37: Volumetric heat capacity values at unfrozen and frozen state of non-saline soils estimated using equation proposed by De Vries, 1963.

			non-saline			
	Symbol	**U. M.**	**I2-N**	**M1-N**	**M2-N**	**M3-N**
Volumetric heat capacity (T=20 °C)	C_{unf}	[kJ/m^3°C]	2,609.2	2,713.0	2,848.5	2,989.0
Volumetric heat capacity (T=-10 °C)	C_f	[kJ/m^3°C]	1,953.4	1,963.6	2,051.0	1,967.0

Table 2.38: Volumetric heat capacity values at unfrozen and frozen state of saline soils estimated using equation proposed by De Vries, 1963, considering different porewater salinity.

Pore-water salinity			**12.39‰**		**35‰**	
	Symbol	**U.M.**	**G1-S**	**G2-S**	**G1-S**	**G2-S**
Volumetric heat capacity (T=20 °C)	**C_{unf}**	[kJ/m^3°C]	2,868.5	2,889.2	2,824.5	2,849.2
Volumetric heat capacity (T=-10 °C)	**C_f**	[kJ/m^3°C]	2,790.1	2,817.0	4,515.3	4,390.8

Table 2.39 Specific heat values of water and ice considering different salt content, from literature.

Water sample	**Salinity**	**Specific heat [kJ/kg°C]**	**Reference**
fresh water (20 °C)	0 ‰	4.182	b
fresh ice (-10 °C)		2.094	a
sampled water (20 °C)	12.39 ‰	4.098	b
sampled ice (-10 °C)		4.132	c
sea water (20 °C)	35 ‰	3.997	b
sea ice (-10 °C)		8.210	c

a) Fukusako, 1990; b) Millero et al., 1973; c) Ono, 1967

Results of the freezing tests on soil samples and on distilled and brackish water are shown in Figure 2.33 and 2.34.

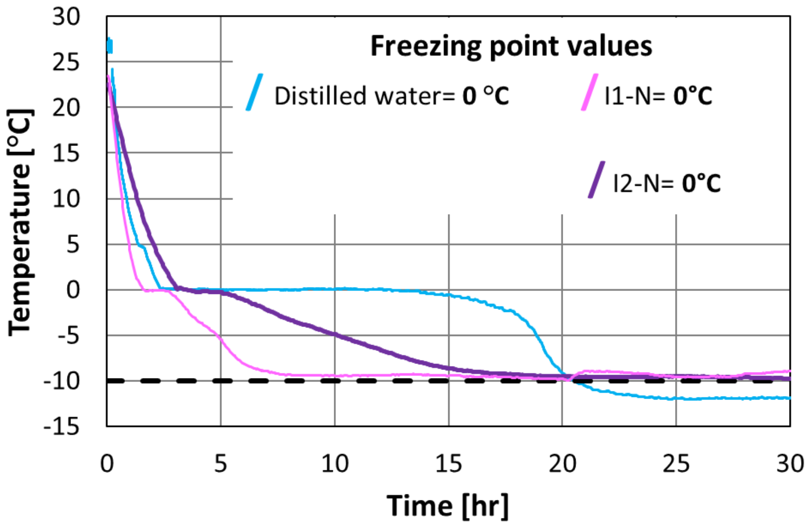

Figure 2.33: Freezing point test results of Isarco non-saline samples. The flat portion of the curve represent the freezing temperature of sample.

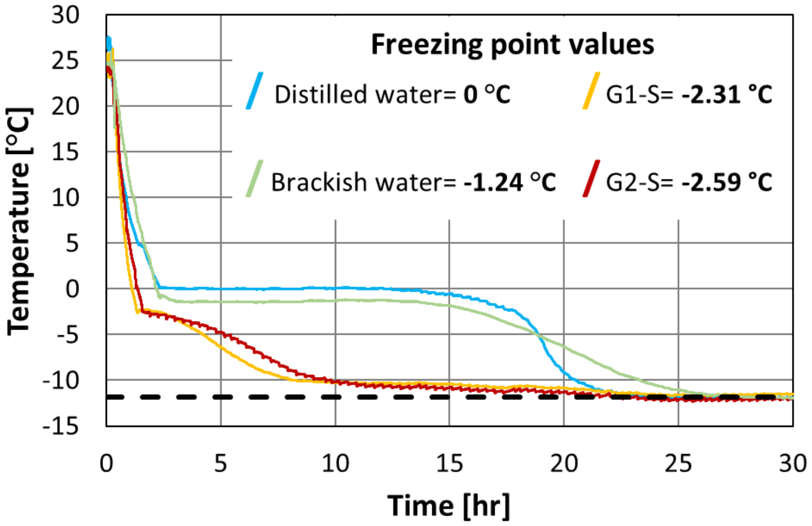

Figure 2.33: Freezing point test results of Genoa saline samples. The flat portion of the curve represent the freezing temperature of sample.

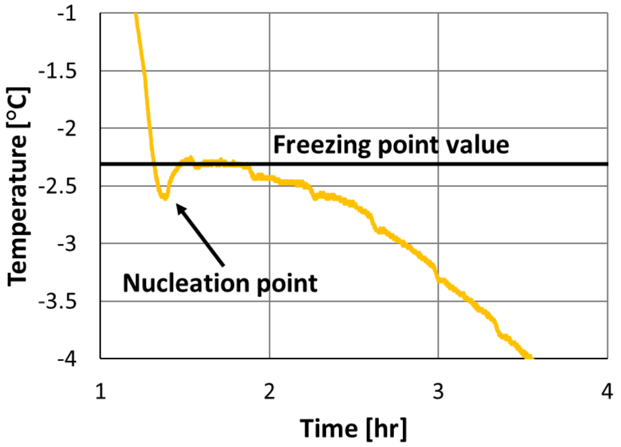

Figure 2.35: Nucleation point of G1-S reached during freezing point test of G1-S.

During cooling, the temperature decreases of linearly until an inflection point was reached. From this point, ice crystals began to form within the sample, resulting in a general slowdown of the cooling process until the cold room temperature was reached. This inflection point is called freezing point and in soil saturated with distilled water (I1-N and I2-N) was located at 0°C, whereas in G1-S and G2-S samples was at -2.31°C and -2.59°C, respectively. In the case of G1-S, the freezing curve shows a small depression before the freezing point indicating the nucleation temperature (Figure 2.35), as identified by Bing and Ma (2011) and Zhang et al. (2015).

2.4 Discussion

The results obtained are considered consistent and satisfying, and the equipment and measuring apparatus used for both mechanical and thermal tests proved to be easy to use and efficient even under unconventional temperature conditions.

2.4.1 Mechanical properties

Unconfined compressive strength tests on frozen soils in every case returned higher values for greater strain rates as demonstrated by Zhu and Carbee (1984) and Lee et al. (2016). Performing UCS tests at -6 °C confirmed the studies of Bragg and Andersland (1981) and Haynes and Karalius (1977) who extensively discussed the decrease in mechanical strength of frozen soil with increasing temperature.

The σ_c values of the triaxial tests, except for the treated soil samples, showed that when confined, frozen soils increase their mechanical strength. Concerning the values of $I_{s(50)}$ determined for soils I1-N and I2-N at -10°C and I2-N at -6°C, they are similar to those of a calcarenite/sandstone (see Elhakim, (2015)) but by computing the correlation factor C, so that:

$$\sigma_c = C * I_{s(50)} \tag{2.25}$$

This was equal to 9.17, 7.35 and 6.74 in the *I1-N/p*, *I2-N/p* and *I2-N/p-h* tests, respectively (see Table 2.40).

Table 2.40: "C" correlation factor between $I_{s(50)}$ index and σ_c of I- samples.

Soil specimen	**Temperature** [°C]	**mean $I_{s(50)}$** [MPa]	**mean σ_c** [MPa]	**C** factor
I1-N/p	-10	0.70	6.42	9.17
I2-N/p	-10	0.80	5.88	7.35
I2-N/p-h	-6	0.78	5.26	6.74

The *C* values are therefore higher than that indicated by Elhakim (2015) (i.e., 2.59) but about 1/3 of that recommended by ASTM D5731-02 for hard rock, which is equal to 23.

In the mechanical tests performed on Milan soils, a clear dependence of strength values with porosity is visible. M3-N indeed shows a porosity of 0.45 and returned the lowest strength values in addition to not exhibiting any well-defined breaking points, like M2-N; it in fact shows in all tests a split behaviour characterised by two well-defined segments with two visibly distinct stiffnesses. In contrast, M1-N, with porosity of 0.33 and a larger particles size distribution always reaches clear failure points in both compression and tensile tests. Using *RocLab1.0*, it was possible to calculate the values of friction angle ϕ [°] and cohesion c [MPa], which for frozen soils range from 32.97 to 42.1 ° and 1.06 to 1.63 MPa, respectively (see Table2.41).

According to Lai et al, (2010) the behaviour of a frozen sand does not follow the Mohr-Coulomb criterion linearly between confining pressures lower and greater than 3 MPa. According to Yang et al. (2010), this value is 18 MPa for a temperature of -4°C. However, this criterion can be applied in this study since the depths at which the AGF operations were performed generated confinements much lower than 3 MPa, so the results of the tests performed can be used to extrapolate the parameters to satisfy the Mohr Coulomb criterion of failure according to which:

$$\tau_n = \sigma_n * \tan\phi + c \tag{2.26}$$

where τ_n is shear stress [MPa], σ_n is normal stress [MPa], ϕ is friction angle [°] and c is the cohesion [MPa]. The mohr circles and the processing with *RocLab1.0* are shown from Figure 2.36 to Figure 2.40.

Table 2.41: Values of friction angles and cohesion of samples evaluated by RocLab1.0.

Sample code	**Friction angle φ** $[°]$	**Cohesion c** [MPa]
I1-N	39.72	1.440
I2-N	42.10	1.439
M1-N	34.73	1.630
M2-N	33.59	1.037
M3-N	32.97	1.064
TS/u	33.90	2.946

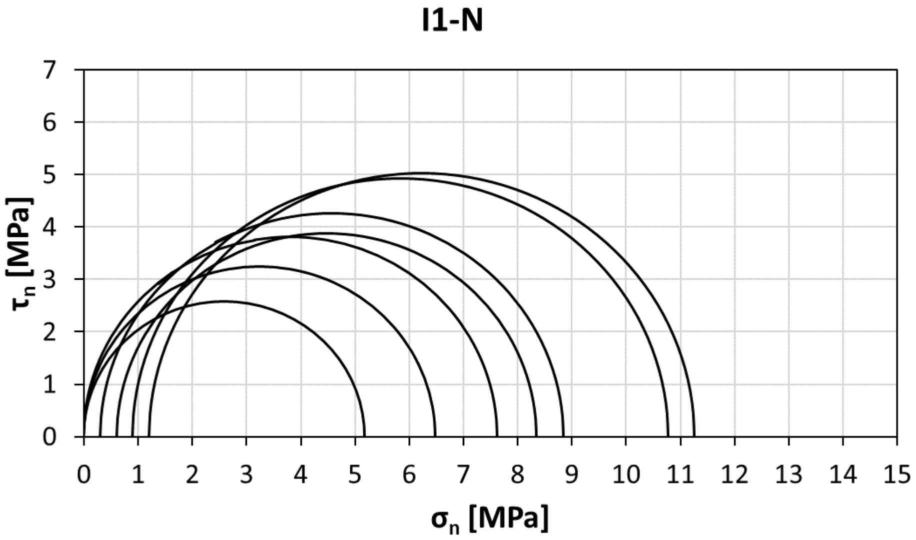

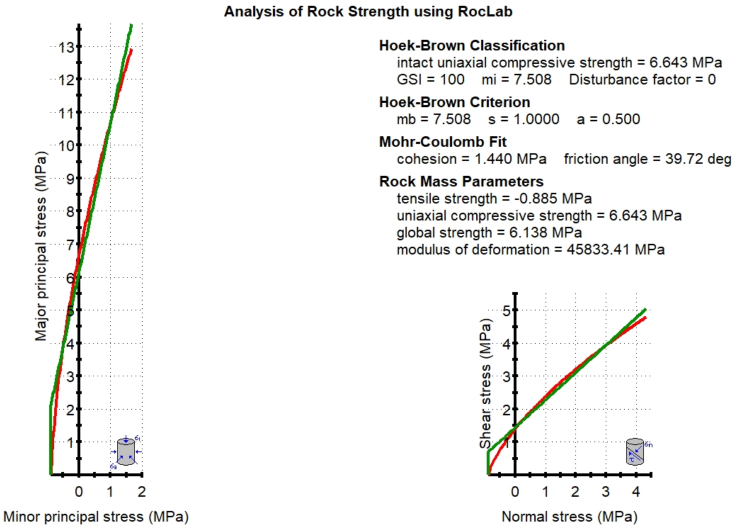
Analysis of Rock Strength using RocLab

Hoek-Brown Classification
intact uniaxial compressive strength = 6.643 MPa
GSI = 100 mi = 7.508 Disturbance factor = 0

Hoek-Brown Criterion
mb = 7.508 s = 1.0000 a = 0.500

Mohr-Coulomb Fit
cohesion = 1.440 MPa friction angle = 39.72 deg

Rock Mass Parameters
tensile strength = -0.885 MPa
uniaxial compressive strength = 6.643 MPa
global strength = 6.138 MPa
modulus of deformation = 45833.41 MPa

Figure 2.36: Mohr circles and Mohr-Coulomb failure criteria developed by RocLab1.0 of I1-N frozen soil sample.

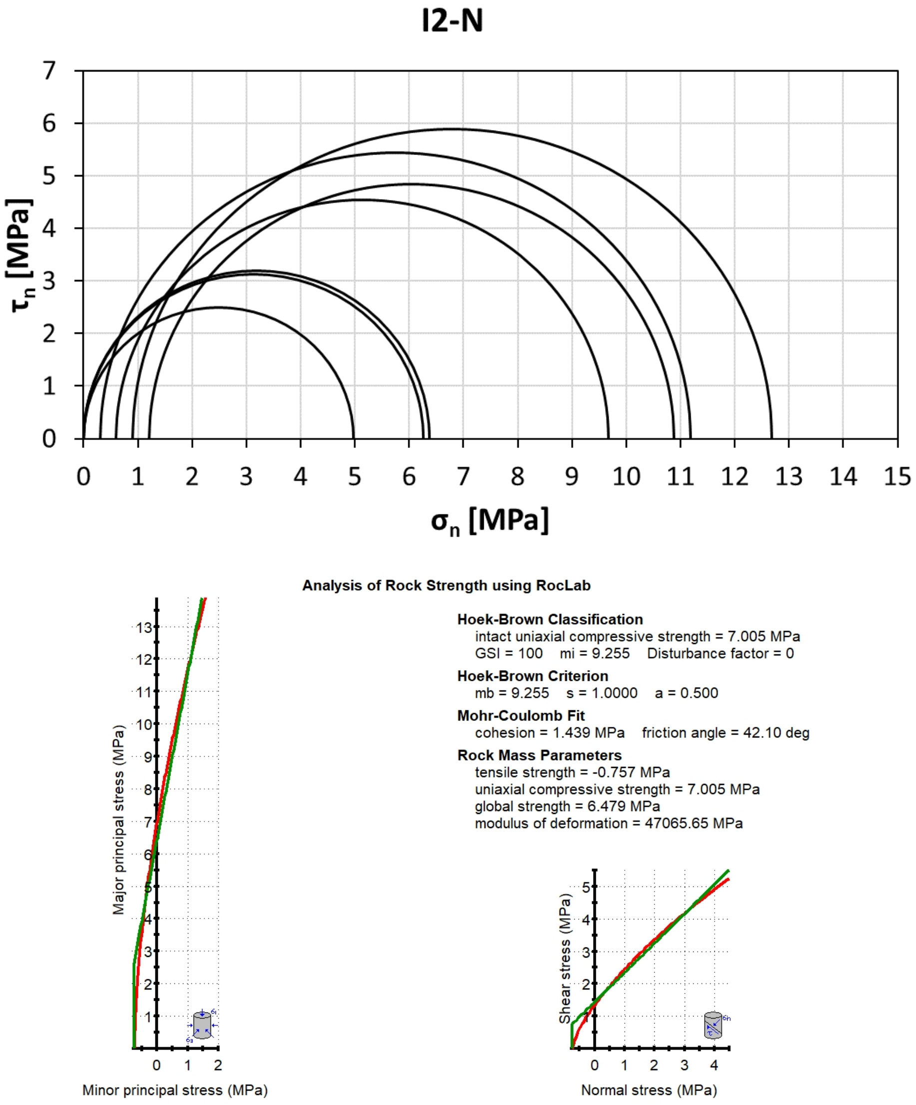

Analysis of Rock Strength using RocLab

Hoek-Brown Classification
intact uniaxial compressive strength = 7.005 MPa
GSI = 100 mi = 9.255 Disturbance factor = 0

Hoek-Brown Criterion
mb = 9.255 s = 1.0000 a = 0.500

Mohr-Coulomb Fit
cohesion = 1.439 MPa friction angle = 42.10 deg

Rock Mass Parameters
tensile strength = -0.757 MPa
uniaxial compressive strength = 7.005 MPa
global strength = 6.479 MPa
modulus of deformation = 47065.65 MPa

Figure 2.37: Mohr circles and Mohr-Coulomb failure criteria developed by RocLab1.0 of I2-N frozen soil sample.

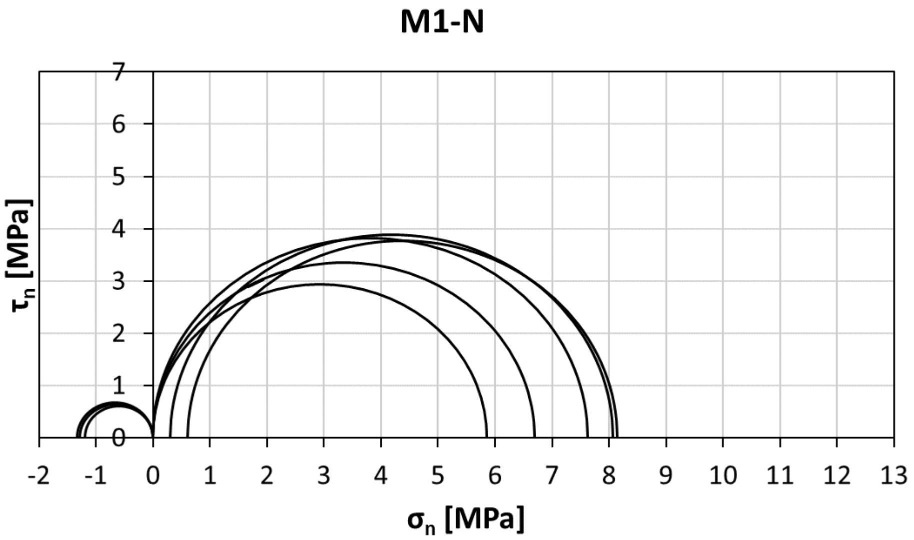

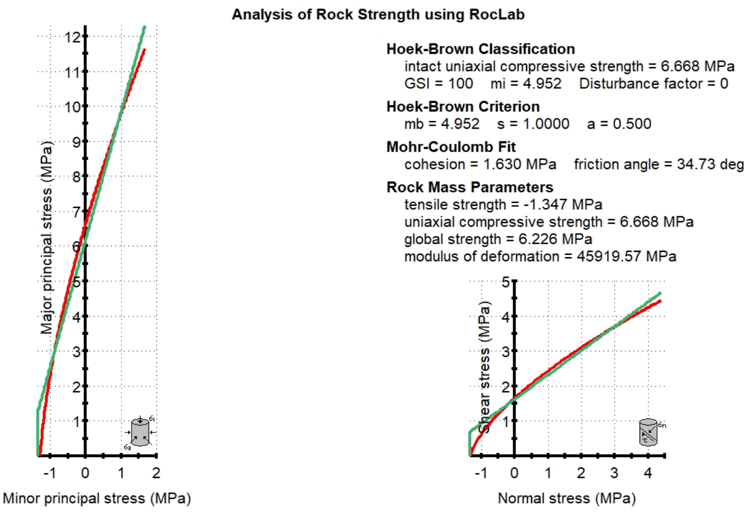

Analysis of Rock Strength using RocLab

Hoek-Brown Classification
intact uniaxial compressive strength = 6.668 MPa
GSI = 100 mi = 4.952 Disturbance factor = 0

Hoek-Brown Criterion
mb = 4.952 s = 1.0000 a = 0.500

Mohr-Coulomb Fit
cohesion = 1.630 MPa friction angle = 34.73 deg

Rock Mass Parameters
tensile strength = -1.347 MPa
uniaxial compressive strength = 6.668 MPa
global strength = 6.226 MPa
modulus of deformation = 45919.57 MPa

Figure 2.38: Mohr circles and Mohr-Coulomb failure criteria developed by RocLab1.0 of M1-N frozen soil sample.

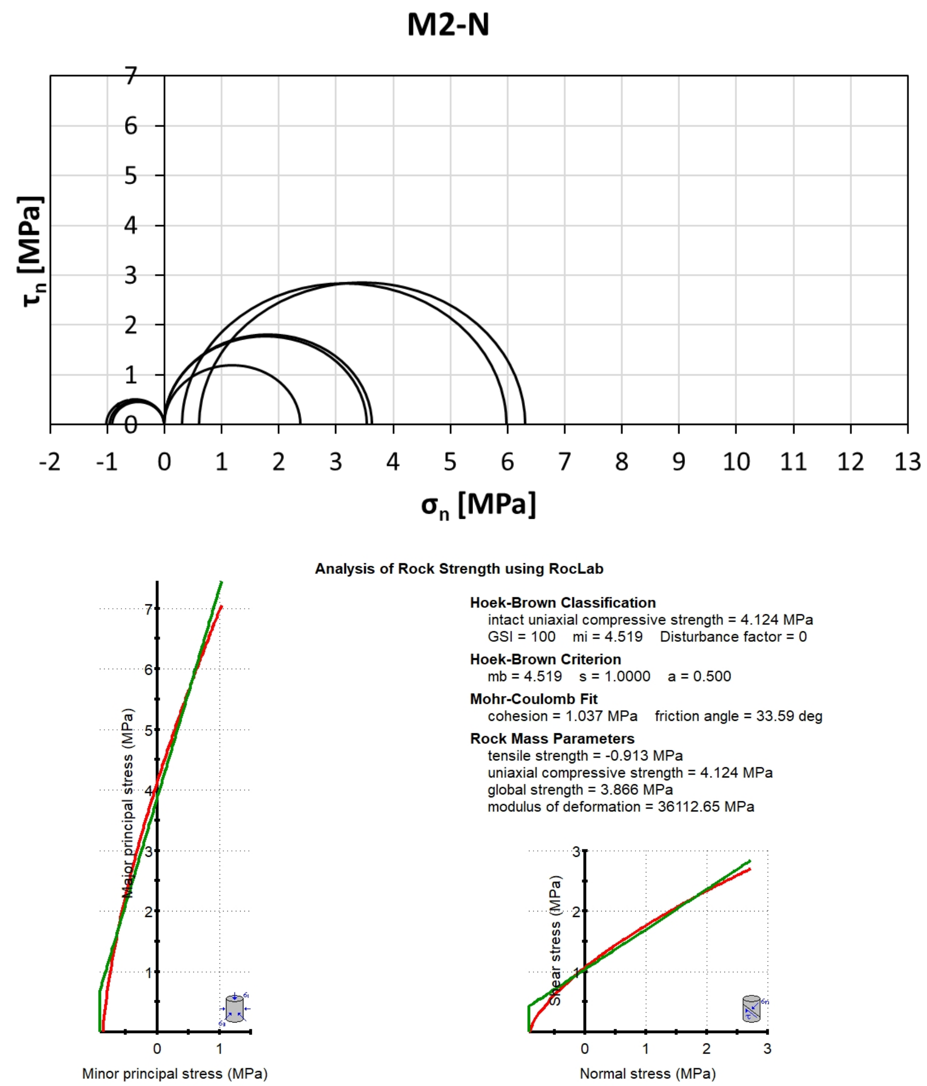

Analysis of Rock Strength using RocLab

Hoek-Brown Classification
intact uniaxial compressive strength = 4.124 MPa
GSI = 100 mi = 4.519 Disturbance factor = 0

Hoek-Brown Criterion
mb = 4.519 s = 1.0000 a = 0.500

Mohr-Coulomb Fit
cohesion = 1.037 MPa friction angle = 33.59 deg

Rock Mass Parameters
tensile strength = -0.913 MPa
uniaxial compressive strength = 4.124 MPa
global strength = 3.866 MPa
modulus of deformation = 36112.65 MPa

Figure 2.39: Mohr circles and Mohr-Coulomb failure criteria developed by RocLab1.0 of M2-N frozen soil sample.

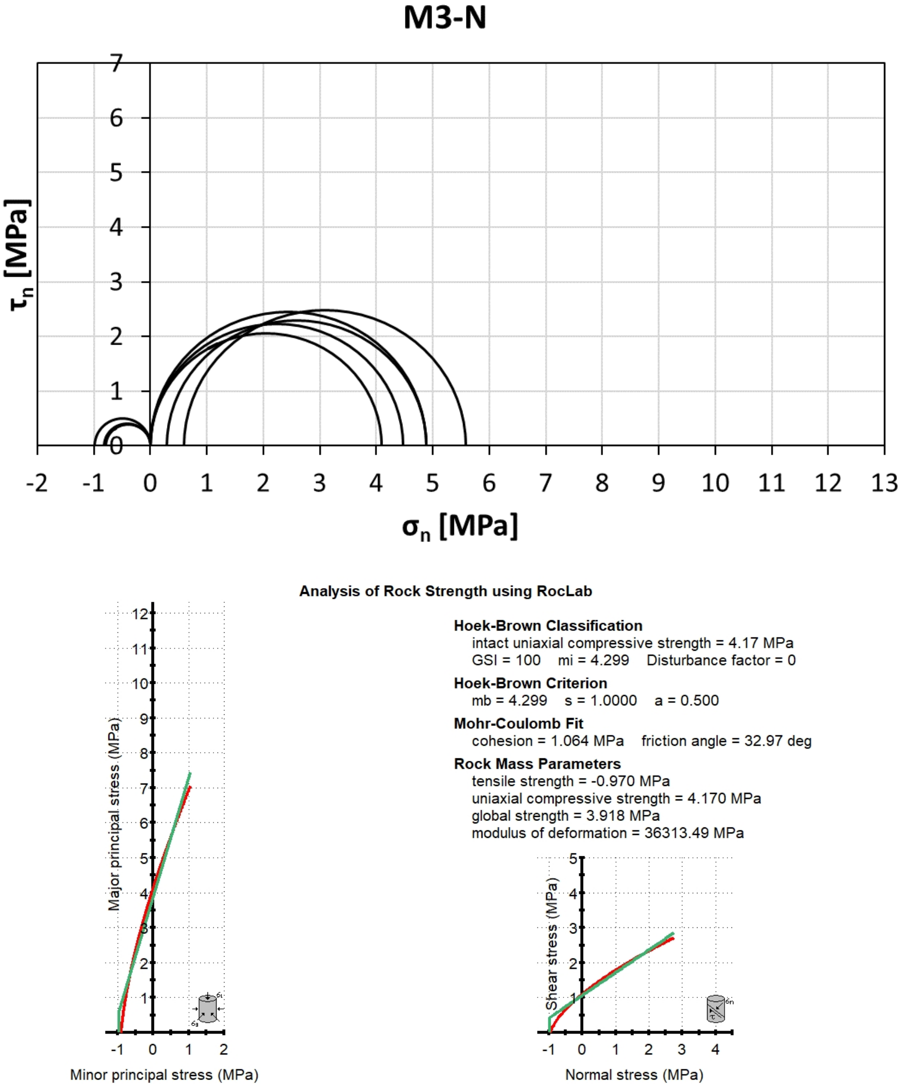

Analysis of Rock Strength using RocLab

Hoek-Brown Classification
intact uniaxial compressive strength = 4.17 MPa
GSI = 100 mi = 4.299 Disturbance factor = 0

Hoek-Brown Criterion
mb = 4.299 s = 1.0000 a = 0.500

Mohr-Coulomb Fit
cohesion = 1.064 MPa friction angle = 32.97 deg

Rock Mass Parameters
tensile strength = -0.970 MPa
uniaxial compressive strength = 4.170 MPa
global strength = 3.918 MPa
modulus of deformation = 36313.49 MPa

Figure 2.40: Mohr circles and Mohr-Coulomb failure criteria developed by RocLab1.0 of M3-N frozen soil sample.

Table 2.42: Results of unconfined compression test performed on concrete samples (CO) under different thermal conditions.

Soil specimen	Thermal condition	σ_c [MPa] mean	$E_{sec0.4}$ [GPa] mean
CO/u-e	T= 20 °C	43.46	28.22
CO/u-s	T_{top}= -30°C; T_{bottom}= -80°C	62.44	28.81
CO/u-f	T= -20°C	47.36	35.19
CO/u-c	T= 20°C (after freezing cycle at -10 °C)	38.10	23.90

The tests, carried out under different temperature conditions on concrete specimens taken directly from a tunnel lining subjected to AGF, made it possible to investigate the effects of a freezing intervention on the mechanical properties of a concrete structure. In general, it can be concluded that the tests at T<0°C returned overall higher values of σ_c. It is interesting to note that σ_c at -20° has a strength of +8% as expected from the model developed by Wang et al. (2020) according to which this finding was due to the gradual decrease in the pore radius of the water–ice phase transformation of concrete, and the amount of ice increased. This condition forms a complete and compact ice body and concrete bond, which gradually reduces concrete porosity. The values obtained by *CO/u-s* tests are not yet part of previous studies, so a comparison is therefore difficult.

The mechanical tests performed on soil specimens treated with a cement mixture were input into *RocLab1.0* to compute the friction angle and cohesion values, which were found to be 33.9° and 2.94 MPa (see Figure 2.41). The triaxial tests did not provide satisfactory results as the value of σ_n never exceeded the values of σ_c of the uniaxial tests. As can be seen from Table 2.41, treated-and-frozen sand has greater cohesion than only frozen soil. The introduction of a cement bonding agent, as studied by Shooshpasha and Shirvani (2015), results in a significant increase in mechanical parameters, including the friction angle, which can increase by almost 50%. Other authors, such as Dano et al. (2004), studied the strength of specimens injected with cement mixtures, obtaining friction angle values of 40° and cohesions of around 0.5 MPa. The difference with the c value found in this study is therefore ascribed to the temperature at which the test was performed, as well as to the coarser grain size; while the lower friction angle can be attributed to the presence of bentonite within the mixture injected into the soil, which confers plasticity to the mixture.

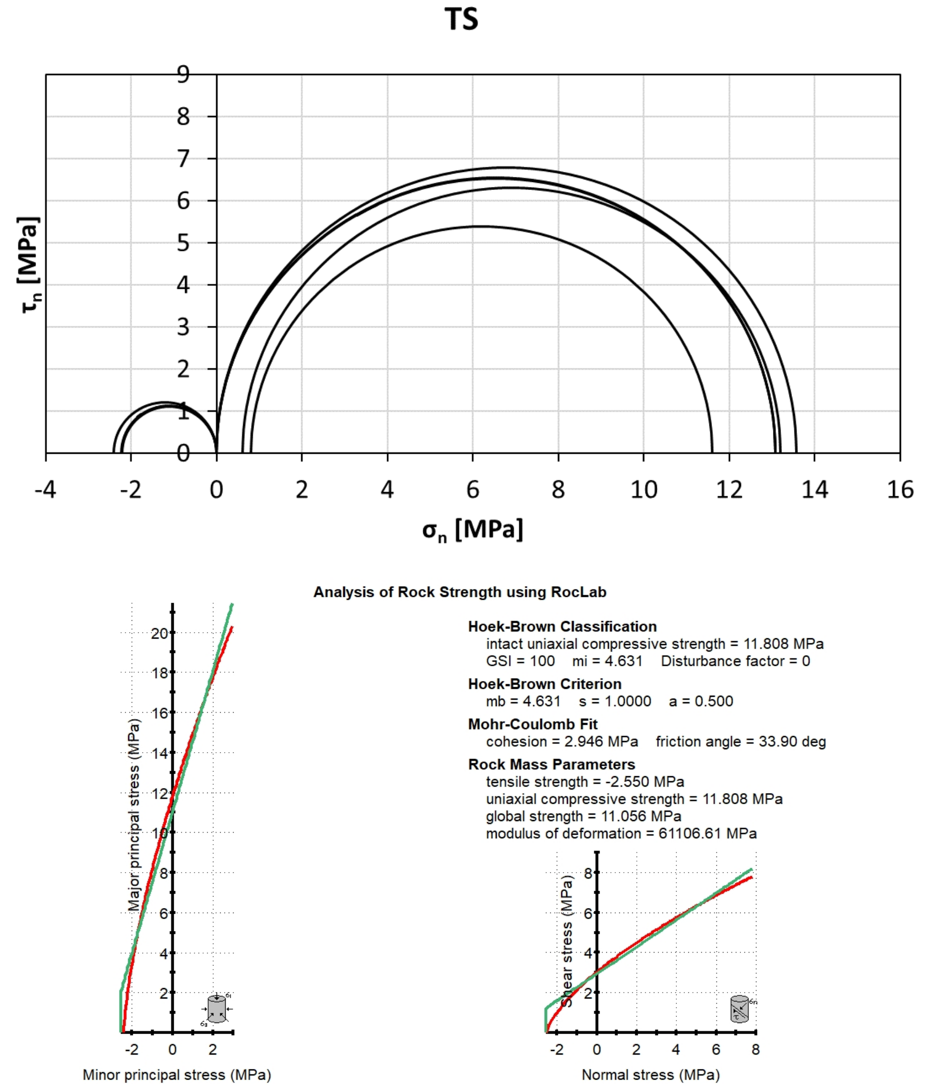

```
Hoek-Brown Classification
    intact uniaxial compressive strength = 11.808 MPa
    GSI = 100    mi = 4.631    Disturbance factor = 0
Hoek-Brown Criterion
    mb = 4.631    s = 1.0000    a = 0.500
Mohr-Coulomb Fit
    cohesion = 2.946 MPa    friction angle = 33.90 deg
Rock Mass Parameters
    tensile strength = -2.550 MPa
    uniaxial compressive strength = 11.808 MPa
    global strength = 11.056 MPa
    modulus of deformation = 61106.61 MPa
```

Figure 2.41: Mohr circles and Mohr-Coulomb failure criteria developed by RocLab1.0 of T-S frozen sample.

All the mechanical tests were performed on soil specimens prepared and frozen in the laboratory. For this reason, the mechanical parameters identified represent a useful estimate to guide the design choices of those who need to carry out an AGF operation at a preliminary stage. Based on the values found, in fact, the frozen soil walls are sized with reference to their temperature and consequently the time and cooling power required to reach this target.

2.4.2 Thermal properties

Thermal conductivity

Comparison between measured and estimated thermal conductivity value shows that the Johansen (1975) and Donazzi (1977) equations provided values very similar to those measured by the needle test. In Figure 2.42, it can be observed that Côté and Konrad (2005) provided higher values than measured for each sample investigated, both in the unfrozen and frozen state.

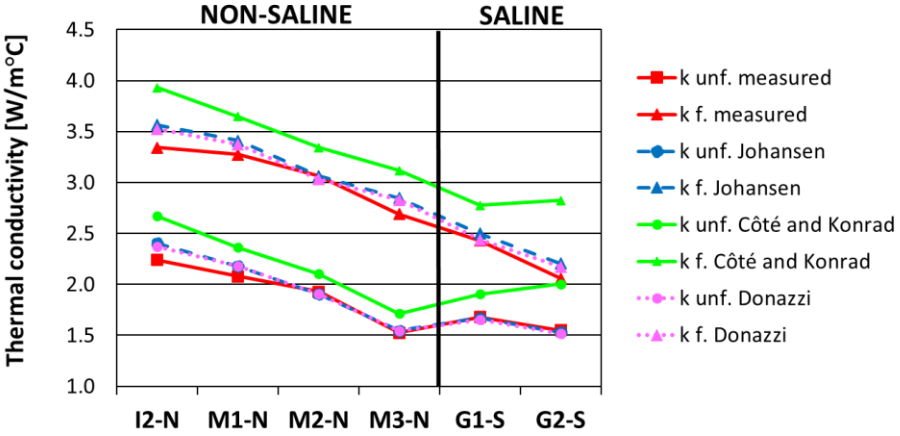

Figure 2.42: Comparison between measured and estimated thermal conductivity value at unfrozen and frozen state. In saline soils porewater salinity is considered equal to 35‰.

While the calculation of thermal parameters for soils containing fresh water is straightforward, in soils containing salty pore water the definition of thermal parameters in the frozen and unfrozen state is far more complex. As described by Andersland and Ladanyi (2004), Pounder (1965) and Fukusako (1990) during the freezing of a salt solution, a portion of water freezes and turns into pure ice and the remaining brine increases its concentration of dissolved salts. This process proceeds until a temperature is reached, which for a NaCl solution is -22.9 °C, below which only pure ice and salt grains are embedded within it. Before reaching this point within the pores of the medium, portions of pure ice, water, salt dissolved in water and precipitated salt coexist. All these components are involved in the soil thermal properties definition. The thermal conductivity and specific heat of sea ice are a function of temperature as described by Sakazume and Seki (1980) and Ono (1967). Anyway, the decision to measure the parameter k or the choice of a given empirical solution to calculate it may depend on the resources available: measurement with a conductivity meter is very quick and direct but requires some experience in performing the tests; estimation by empirical equations requires the definition of the physical and chemical characteristics of the soil (n, Sr, XRD) to identify all the phases that compose it. This implies performing complex tests that require specialists.

Freezing point

Freezing tests on I1-N and I2-N soil samples taken from Isarco showed that in a gravelly sand saturated with distilled water the freezing point is equal to 0°C, as verified by Vu et al. (2022). Saturation with distilled water was chosen due to the lack of in situ porewater salinity data.

Similarly, the freezing point of distilled water, used as a reference point, was found to be 0°C.

The brackish water sample taken from the borehole used to recover the saline soil samples showed a freezing point of -1.24 °C, very close to the freezing point of seawater, which is -1.92 °C (see Doherty and Kester, (1974)). Kester (1974) gives us an equation that provides the freezing temperature of water starting from salinity:

$$T_{fp} = -0.0137 - 0.05199 S_w‰ - 0.00007225 (S_w‰)^2 \qquad (2.26)$$

When the salinity of the brackish water is substituted into the equation, it turns out that the freezing point should be -0.67°C, and that a freezing point of -1.24 is associated with a salinity of 23‰.

The salinity of the porewater therefore remains uncertain as the sampling was done immediately after drilling and the freezing point revealed a value that did not correspond to the salinity value measured with a conductivity meter.

For this reason, two scenarios are considered when discussing the results of G1-S and G2-S: porewater salinity= 12.39‰; porewater salinity= 35‰. On the basis of these assumptions, it is therefore possible to calculate the salinity S of the soil, expressed as g salt/g soil, which in the first case is equal to 0.37% and 0.30% in G1-S and G2-S respectively, and in the second case equal to 1.04% and 0.85% in G1-S and G2-S respectively.

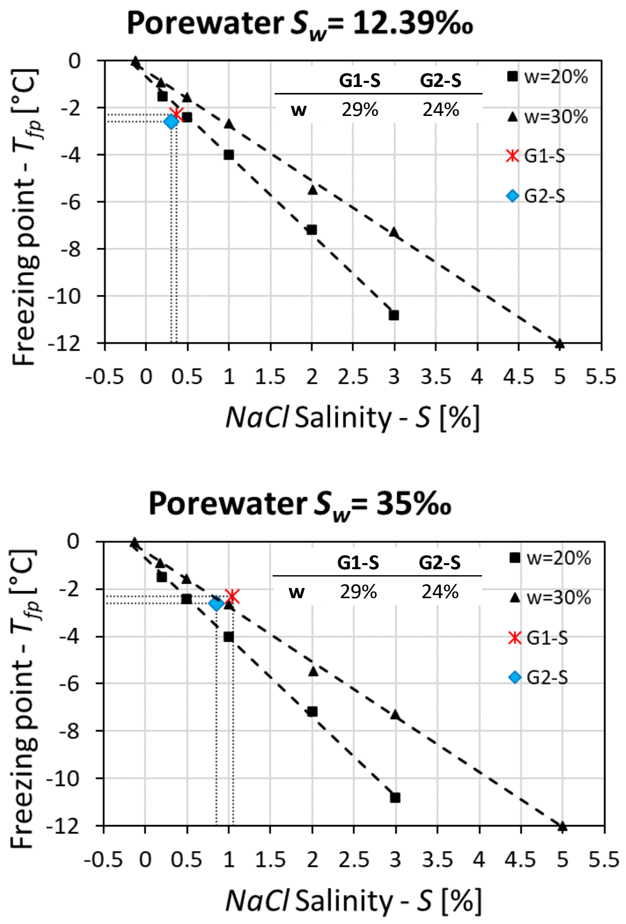

Figure 2.43: Comparison between freezing point values measured and identified by Bing and Ma (2011) considering different porewater salinity S_w *(12.39 and 35 ‰).*

Plotting the values of S and T_{fp} determined for the two samples on the graph of Bing and Ma (2011), which provides curves linking the freezing point of a loess to salinity and water content w, it can be stated that considering porewater salinity=35‰ gives the best fitting, as w= 29% and 24% in G1-S and G2-S respectively. This result also agrees with the findings of Xiao et al. (2018). However, a perturbation is evident in the freezing curve of the brackish water at a T=-0.8 °C, which can be ascribed to a change in the density of the liquid or an initial formation of pure ice crystals.

The conductivity parameters of the Isarco and Milano soils were measured on soil specimens reconstructed in the laboratory and therefore represent indicative values to be considered during the thermal modelling phases. The parameters determined on undisturbed samples, on the other hand, are considered reliable and truthful.

Once these parameters are known, it is possible to implement them in a numerical code and be able to perform thermal analyses useful for defining the time and cooling power required to reach the target frozen wall thickness to support and/or to waterproof the excavation.

Chapter 3

3 FEM & IRT: laboratory validation and calibration

Heat transfer modeling is a widespread practice in an ever-growing number of fields of study, ranging from drilling to slope stability analysis in permafrost conditions (Arenson, 2002 and Yamamoto and Springman, 2019), rock glacier stability (Haeberli et al., 2006), and to settlements due to permafrost thawing (Hong et al., 2014). Since Artificial Ground Freezing (AGF) was developed, the need to have analytical or numerical tools to provide support to the design of the freezing scheme has been crucial. Due to its power and versatility, especially in 3D problems, over the years numerical modeling has become the most used tool to predict the propagation of cold in the ground during an AGF intervention.

The most important issue of a code is its predictive capacity since an incorrect forecast could lead to errors in the evaluation of temperature front propagation and consequently an increased consumption of time, resources, and costs.

The numerical code validation needs the definition and knowledge of the physical and thermal properties of material which govern the propagation of heat (De Vries, 1963). Several authors, as already shown in *Chapter 2*, developed solutions to calculate the thermal conductivity and volumetric heat capacity of unfrozen and frozen soils from several physical and chemical characteristics such as porosity, degree of saturation, particle size distribution and mineralogical composition.

To verify its predictivity power, a thermal FEM model must be validated by experimental tests, which should preferably be easy to handle, replicable and inexpensive, as described by Johnsson (1995), and which require a known portion of the soil to be subjected to controlled thermal perturbations.

The simplest experimental test, involving a phase transition, implies unidirectional freezing of a partially or fully saturated soil sample. The full saturation of the specimen and the assumption of no convective water flow within it allow a simplification in the calculation of thermal parameters and heat flow.

Unidirectional freezing tests were performed to evaluate the freezing method that induced the least amount of heave (see Hu et al., 2022), and in some cases combined with numerical models that considered thermal and mechanical aspects and reproduced the experimental results of heave tests, as carried out on saturated coarse-grained soil and saturated rock by Li et al., (2017) and Lv et al., (2019), respectively. After an empirical model of unidirectional bottom-up freezing tests on silty-clay samples with different salt contents was developed, Liu et al., (2023) investigated the use of electrical conductivity as a method to estimate the frozen wall evolution in real AGF cases. Modelling the freezing process requires many parameters that can be measured, estimated by empirical equations, or taken from literature. Through experimental tests, Luo et al., (2023) measured the freezing temperature of saline soil, saturated volumetric water content, dry density and soil particle density and used them for modelling unidirectional freezing experimental tests. Once a numerical code has been validated, based on experimental tests, it is possible to perform a sensitivity analysis of the input thermal parameters such as porosity and conductivity of the solid matrix (see Go et al., 2019) or to calculate some soil thermal parameters, such as the thermal diffusivity, from back analysis, as Kodikara et al. (2011) did on kaolin soil samples at positive temperatures by measuring temperature through infrared thermal imaging camera. An experimentally validated numerical code is definitely applied to real three-dimensional AGF intervention to predict the temperature distribution and the frozen soil propagation during an AGF intervention considering a thermal or thermal-hydraulic coupled model as performed by Hu et al., (2018) and Song et al., (2016), respectively.

To support the validation of the numerical model, one-way bottom-up experimental freezing tests were developed and performed on cylindrical samples of saturated soil using different cooling systems that reproduce the thermal perturbations generated by freezing pipes. The results of these investigations provided data for the validation of the TEMP/W 3D numerical code.

An additional test was carried out to verify the effectiveness and reliability of using Infrared Thermography (IRT) for temperature monitoring on frozen soil samples. IRT is a scientific application for the acquisition and analysis of thermal information, based on the detection of the thermal radiation emitted by an object (Mineo and Pappalardo, 2021). This technology, which is being greatly expanded in the world of geotechnics, makes it possible to remotely investigate the thermal behavior of a body and to be able to associate this behavior, for example, with lithological characteristics (see Mineo and Pappalardo, 2021) or the fracturing state of a rock mass (Franzosi et al., 2023). This technique allows investigating portions of the rock mass that cannot be investigated by other methods, as demonstrated by Guerin et al. (2019), who applied IRT to the detection of rock bridges on the El Capitan cliff in Yosemite Valley. Authors who have applied this technique to unfrozen soil include Kodikara et al. (2021), and Zhao et al. (2018), that used infrared thermal imaging camera to detect cracks on frozen soil during unconfined compressive tests.

3.1 Materials and Methods

3.1.1 Heat flow modeling

The principal mechanism for heat flow in soils in most engineering applications involving freezing and thawing is conduction (Harlan and Nixon, 1978). Heat flux due to conduction is governed by Fourier’s law:

$$q = -k\frac{\partial T}{\partial x} \tag{3.1}$$

where k is the thermal conductivity [W/m°C] and $\frac{\partial T}{\partial x}$ is the temperature gradient [°C/m]. The governing differential equation used in the formulation of the FEM code is:

$$\frac{\partial}{\partial x}\left(k_x\frac{\partial T}{\partial x}\right) + \frac{\partial}{\partial y}\left(k_y\frac{\partial T}{\partial y}\right) + \frac{\partial}{\partial z}\left(k_z\frac{\partial T}{\partial z}\right) + Q = C_a\frac{\partial T}{\partial t} \tag{3.2}$$

where Q is the applied boundary flux and C_a is the apparent volumetric heat capacity (i.e., capacity for heat storage). Under steady-state conditions, the flux entering and leaving an elemental volume is the same at each time, which means the right side of the equation reduces to 0. The equation for the capacity to store heat in freezing/thawing soil is constituted of two parts:

$$\frac{\partial}{\partial x}\left(k_x\frac{\partial T}{\partial x}\right)+\frac{\partial}{\partial y}\left(k_y\frac{\partial T}{\partial y}\right)+\frac{\partial}{\partial z}\left(k_z\frac{\partial T}{\partial z}\right)+Q \\ =\left(C+\rho_w L_f\frac{\partial\theta_{uwc}}{\partial T}\right)\frac{\partial T}{\partial t} \tag{3.3}$$

where C is the volumetric heat capacity of soil [kJ/m^{3}°C]; L_f is the latent heat of fusion of water [kJ/kg]; θ_{uwc} is the unfrozen volumetric water content of soil.

The phase change of water to ice in soil results in a change in its thermal parameters (conductivity and volumetric capacity) because water and ice have different thermal properties. The phase change doesn't occur at a specific temperature value (Freezing point - T_{fp}) but over a temperature range since the early stages of freezing a portion of water remains unfrozen. The unfrozen volumetric water content is a function of temperature and is defined by the equation:

$$\theta_{uwc}=\theta_w\theta'_{uwc} \tag{3.4}$$

where θ_w is the volumetric water content and θ'_{uwc} is the normalized unfrozen volumetric water content function ($0<\theta'_{uwc}<1$).

The magnitude of the temperature range over which the water phase change takes place depends on the particle size of the soil and can range from 0.1°C (from T_{fp} to $T_{fp}-0.1°C$) to 5°C (from T_{fp} to $T_{fp}-5°C$) for gravels and clays, respectively. In this temperature range, the thermal parameters of a soil (conductivity and volumetric capacity) vary as a function of θ_{uwc}.

In the TEMP/W code two porous medium models are available: *simplified* or *full thermal*. In the first case, it is assumed that all latent heat is absorbed or released at a single-phase change temperature; in the second it is assumed that the water within a porous medium changes phase over a temperature range.

The full thermal model more closely reflects the behaviour of a soil, especially in presence of fine material, during the freezing process with no volumetric water content variation. Table 3.1 lists the input parameters required by the full thermal material model.

Table 3.2. Input parameters for the Full thermal material model in TEMP/W, after Geoslope (2020).

Parameters	**Symbol**	**U.M.**
Thermal conductivity function	$k(T)$	[W/m°C]
Volumetric heat capacity: Unfrozen	C_u	[kJ/m^3°C]
Volumetric heat capacity: Frozen	C_f	[kJ/m^3°C]
Normalized unfrozen volumetric water content function	θ'_{uwc}	[-]
In situ Volumetric water content	$\theta_w = n$	[-]
Freezing point	T_{fp}	[°C]

TEMP/W provides several sample functions for the normalized unfrozen volumetric water content based on soil particle size distributions.

Figure 3.1 shows the change over temperature of thermal parameters considered in the full thermal material model. Once a freezing point temperature T_{fp} is set, thermal conductivity varies within a range of temperature as a function of θ'_{uwc}. Volumetric heat capacity values, on the other hand, do not consider θ'_{uwc}, so for temperatures higher or lower than T_{fp}, constant values are assumed.

In order to properly define the material model, it is therefore necessary to follow direct or undirect approaches in order to measure or estimate: porosity, n; particle-size distribution to select the θ'_{uwc} function; saturation degree, S_r; freezing point of the soil, T_{fp}; unfrozen and frozen thermal conductivity, k_u, k_f(white diamonds in Figure 3.1), linked by the θ'_{uwc} function; unfrozen and frozen volumetric heat capacity C_u, C_f (green diamonds in Figure 3.1).

To solve the differential equation the geometry of the problem must be simplified, and create a tetrahedral or hexahedral (or mixed) mesh of a size that satisfies the requirements of the problem. Once the mesh has been created, the initial conditions of the problem must be defined, usually represented by prescribed temperature values distribution in the problem domain at instant t_0.

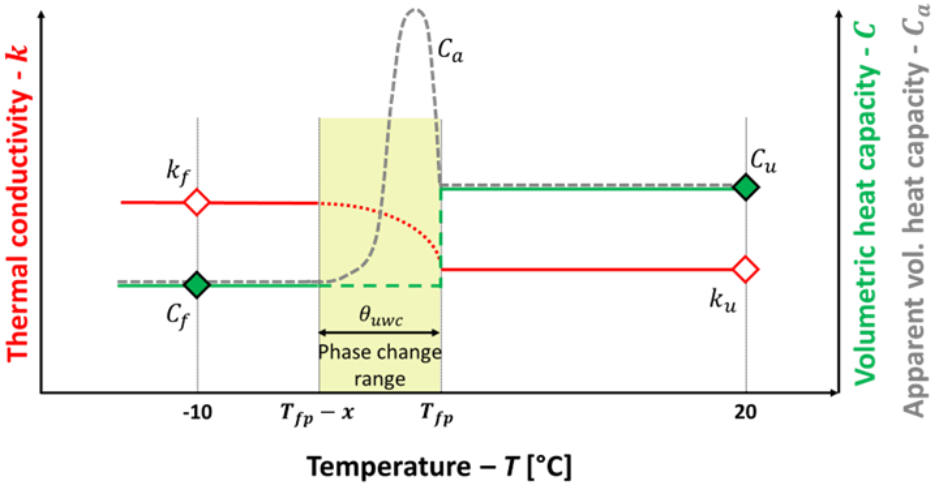

Figure 3.2: Thermal properties as a function of temperature in the Full thermal material model in TEMP/W: Thermal conductivity, red line; Volumetric heat capacity, green line; Apparent volumetric heat capacity, dashed grey line.

Among the various boundary conditions (BCs) implemented in the FEM code, two were considered: temperature and convective heat transfer surface. Temperature BC can be applied to nodes, lines, surfaces, or volume elements as a fixed value ($T = const$) or as a time-varying function ($T = f(t)$).

Convective heat transfer surface BC can be described as a heat transport that occurs between a moving fluid (e.g., air) and a bounding surface (e.g., the ground) when the two are at different temperatures (Incropera et al., 2007). In this case heat transport follows the Newton's Law:

$$q = h(T_{sur} - T_{\infty}) \tag{3.5}$$

where q is the surface heat flux due to convection [W/m^2], h is the convection heat transfer coefficient [W/m^2°C], T_{sur} is the temperature of the bounding surface, and T_{∞} the temperature of the fluid outside the thermal boundary layer [°C].

3.1.2 Unidirectional freezing tests

Soil specimens (ϕ=38 mm, H=90 and 76mm) were prepared for both non-saline (M1-N, M2-N and M3-N) and saline (G1-S and G2-S) soils. The non-saline soil specimens were prepared by tamping and saturated with distilled water (see Table 2.1). The saline soil samples were resampled from the Shelby samples to remove the outermost weathered part of the cores.

The cylindrical specimens were placed vertically above a cylindrical stainless-steel base (ϕ=38mm and H=50mm) to ensure proper thermal contact between the two. Externally, a latex membrane held the specimen to the metal base to prevent water leakage from the soil. The membrane has small holes at different heights (0, 40, 80mm for non-saline soil; 0, 10, 20, 30 and 40 for saline soil) into which T-type thermocouples were inserted horizontally up to reach the vertical axis of the specimen. In this way, temperature sensors were placed along the vertical at different heights (acquisition levels) and were connected to a Datascan 7220 datalogger. A 24 mm-thick neoprene foam insulation tube was placed around the specimen to prevent outward radial cold leakage. Once the test layout was prepared, it was left 24 hours for all components to reach thermal equilibrium with the laboratory and the initial constant temperature inside the soil specimen.

In tests performed on non-saline soil samples (Figure 3.2a-b), the entire device was placed inside a metal/plexiglass tray (ϕ=150 mm and H=30mm), with a stainless-steel base equipped with a threaded hole attached to the base tray leaving a gap of 10mm. Freezing from the bottom to the top was attained by pouring Liquid Nitrogen (LN_2) inside the tray.

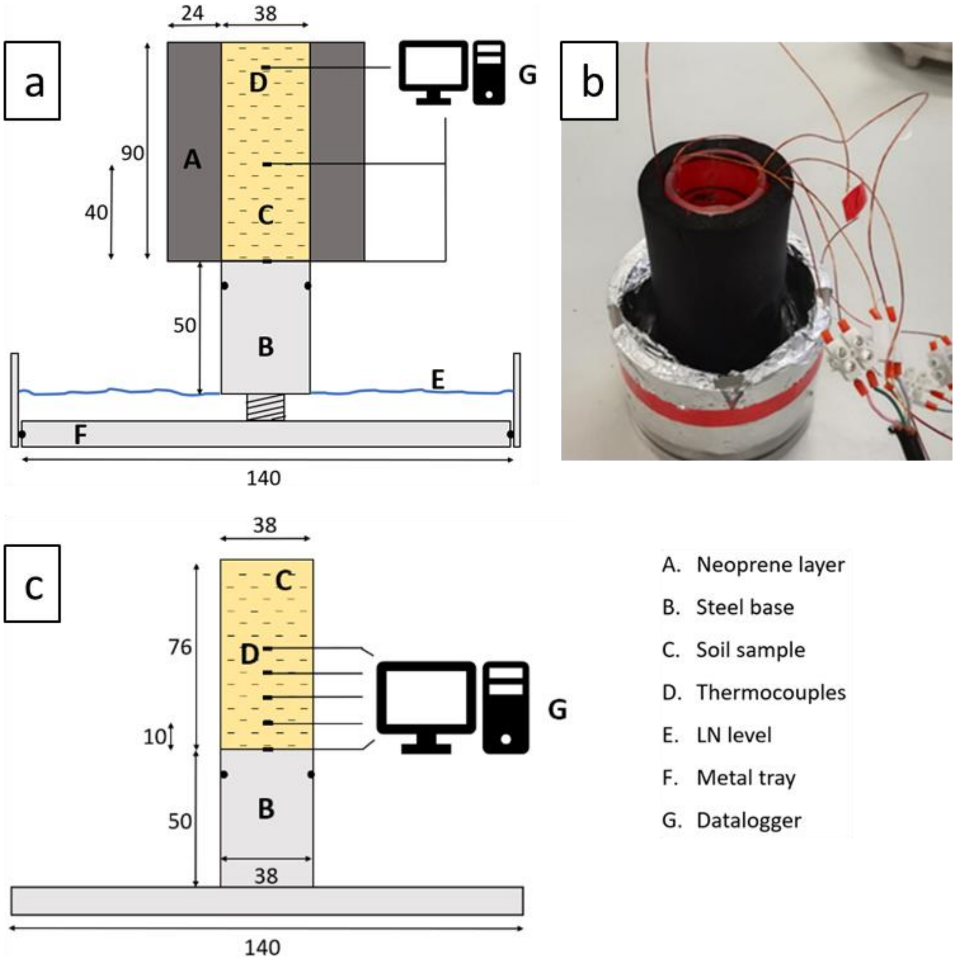

Figure 3.2: Bottom-up freezing test layout for: a) non-saline soil samples; b) detail on neoprene layer and thermocouple wires; c) saline soil samples. Dimensions are expressed in mm.

The space between the bottom of the tray and the metal base allowed LN_2 to wet the bottom of the metal base inducing a cold front to move from the bottom to the top. The LN_2 flow rate was manually adjusted to ensure a constant LN_2 level inside the tray. Temperatures were recorded every 2 seconds with the thermocouple positioned at the 0 mm level recording the temperature at the metal/soil interface. The test was ended when it was found, with the help of a metal needle, that the top of the specimen had become stiff and thus frozen (see Bavaresco et al., 2023a).

In the tests performed on Genoa saline soil samples (Figure 3.2c), the entire system was placed inside a cold room set at -30°C above a steel plate. In this way, the contact between the steel plate and cylindrical steel base and the cold air around the specimen allowed the cold front to move mainly upward axially and latterly inward radially.

In both types of freezing tests, the recorded temperature series were labelled "E" (i.e. experimental) followed by the acquisition level it refers to (e.g."*E-10mm* is the temperature series recorded at height 10 mm).

3.1.3 Infrared Thermography technology - IRT

According to the Plank radiation law, a blackbody (i.e., a body absorbing all incident radiation) emits electromagnetic radiations at different wavelengths depending on its temperature. For earth surface conditions, the peak of radiation falls in the infrared band of the electromagnetic spectrum. Thus, it is possible to measure the surface temperature of object based on their emitted radiation in specific IR wavelength, using a technique called Infrared Thermography (IRT) (Shannon et al., 2005).

The thermal radiant exitance, i.e., the energy emitted from a body in the infrared band, is a function of the surface temperature according to the Stefan-Boltzmann law as follows:

$$J = \varepsilon\sigma T^4 \tag{3.6}$$

Where J is the thermal radiant exitance [W/m^2], ε is the emissivity of the surface [-], σ is the Stefan-Boltzmann constant [W/m^{2}K^4] and T refers to the temperature of the body [K].

Thermal emissivity ranges between 0 and 1 and represents the object’s ability to emit radiation. A perfect emitter (i.e., black body) has an emissivity coefficient of 1 (Hillel, 1998), while grey bodies, that has $\varepsilon<1$, emit less energy by radiation than a block body at the same temperature.

Infrared thermal cameras measure the infrared radiation emitted by bodies in the spectral band 7.5-14µm. Nevertheless, the signal received by the sensor includes contributions from the surrounding environment (i.e., “reflected radiation”) modulated by the thermal transmittance of the atmosphere between the emitting object and the sensor of the camera. These components must be considered during the measurement. When multiple images are collected in time, time histories of temperature can be extracted from multi-temporal stacks of thermograms.

For laboratory experiment in controlled conditions, temperature of soil sample was monitored over time using a FLIR T1020 high-resolution thermal camera (1024 x 768 pixels), characterized by a measurement sensitivity within 0.02 °C and a field of view (FOV) of 28° x 21°.

In order to be able to measure the temperature of a soil specimen, it must have sufficient cohesion to preserve its initial cylindrical shape in a near-saturated condition without any external support. For this reason, the material chosen for this test was kaolin (K-N) (Figure 3.3), also used by Kodikara et al. (2011) for their laboratory tests.

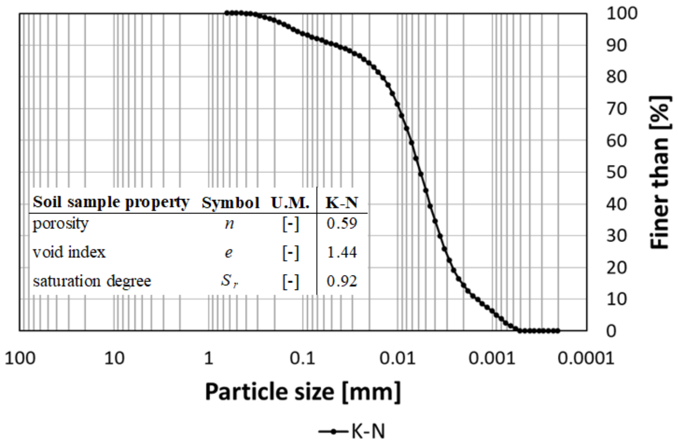

Soil sample property	Symbol	U.M.	K-N
porosity	n	[-]	0.59
void index	e	[-]	1.44
saturation degree	S_r	[-]	0.92

Figure 3.3: Particles size distribution of kaolinite sample and physical properties of the kaolinite specimen.

A cylindrical specimen of soil (D= 38mm and H= 62.5mm) and distilled water was prepared. The same layout as used in the Milan soils was used to perform the test (see Figure 3.2a). One thermocouple was placed at the interface between the metal base and the specimen, and additional 6 thermocouples were placed at 6 different heights (10, 20, 30, 40, 50 and 60mm) and inserted into the specimen at a depth of ~1mm. These sensors made it possible to measure and record the temperature over time during the bottom-up freezing test.

For the experiment the camera was mounted on a tripod located 1 m from the specimen. Specimen temperature during freezing test was monitored by capturing thermograms every 2 minutes in time-lapse mode.

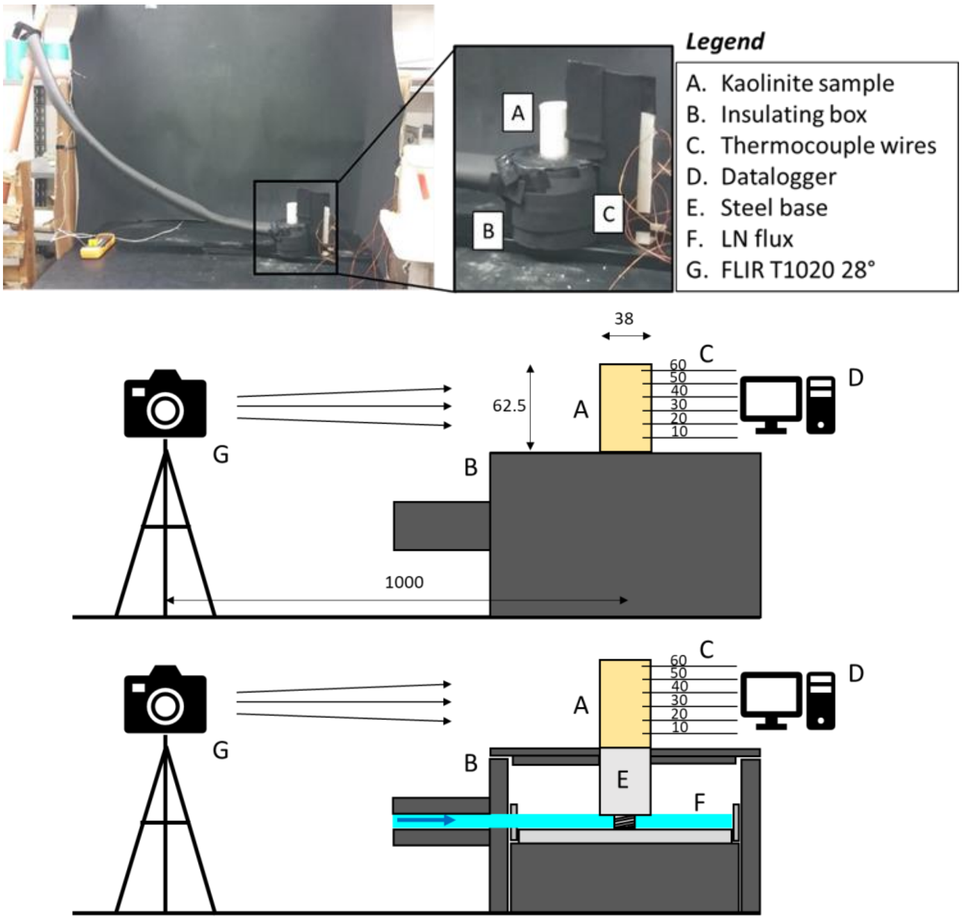

Figure 3.4: IRT experiment set-up: a) general overview of specimen location and background b) layout of IRT camera disposition; c) cross section layout of LN cooling system. Dimensions are expressed in mm.

Acquisition via IRT required several technical expedients:

- The unidirectional LN_2 freezing test set up was covered with a thick insulating neoprene layer (Figura 3.4a) to reduce thermal disturbance from the cooling agent (i.e., LN_2) and metal components. Only the soil specimen was visible.
- LN_2 fedding system was moved away (~1m) so that it did not fit into the camera frame. The tube in which the LN_2 flowed to the

steel/plexiglass tray at the base of the specimen was covered by an insulating tube.

- High-emissivity neoprene background (ε~1) to avoid disturbances around the sample due to reflected thermal radiation components was assembled.
- Laboratory temperature and humidity were kept constant (20 °C and 33%, respectively) by a thermal-hygrometer. A rough aluminium panel was placed in the scene to allow the measurement of the reflected thermal radiation component.

The test ended after 80 min of freezing due to the thick layer of ice around the soil portion at T<0°C that began to form 40 min after the test started.

3.1.4 Numerical model - FEM

In this study, Geostudio 3D TEMP/W was used to simulate laboratory tests. For non-saline soil samples neoprene layer on the lateral side of the specimen was considered in the domain; for saline soils just the soil cylinder was considered. Numerical analyses involve the discretization of space and time (Sidebodham, 2015). A hexahedral 3D mesh of 0.002 m mean size was created for all the components. Observation points were inserted into the model where the thermocouples were located in the freezing tests (Bavaresco et al., 2023a).

The following boundary conditions were imposed on the domain (Figure 3.5-3.6):

- $T_0 = const$ on every node as an initial thermal condition.
- $T = f(t) \rightarrow T = "E - 0mm"$ series on the bottom face of the soil sample.
- $q = h(T_{sur} - T_\infty)$ on the lateral and upper faces of the domain: freezing tests were performed in the laboratory under stable temperature conditions with no forced air convection (v_{air}= 0 m/sec) so the h coefficient was assumed to be equal to 7 W/m^2 (Maranzana et al., 2002); temperature of air in the laboratory was 22 °C and -30 °C for non-saline and saline soils, respectively.

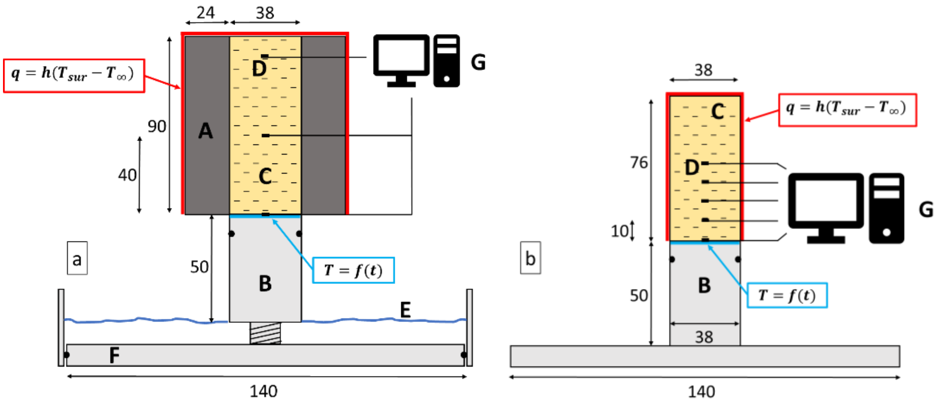

Figure 3.5: Bottom-up freezing test BCs imposed in modelling phase for: a) non-saline soil samples; b) saline soil samples. Dimensions are expressed in mm.

Once the numerical model was created, three calculation scenarios were assumed: *Scenario #1*: soil thermal conductivity values at frozen (-10 °C) and unfrozen (20 °C) state measured by needle probe method; *Scenario #2*: soil thermal conductivity values at frozen (-10 °C) and unfrozen (20 °C) state calculated through Johansen (1975) empirical solution (Eq. 2.11, 2.12, and 2.17); *Scenario #3*: soil thermal conductivity values at frozen (-10 °C) and unfrozen (20 °C) state calculated through Côté and Konrad (2005) empirical solution (Eq. 2.13, 2.14, 2.18); *Scenario #4*: removal of the lateral BCs of 2nd type in order to obtain a 1D problem. The remaining physical and thermal soil properties and temperature boundary conditions were maintained unchanged in each scenario.

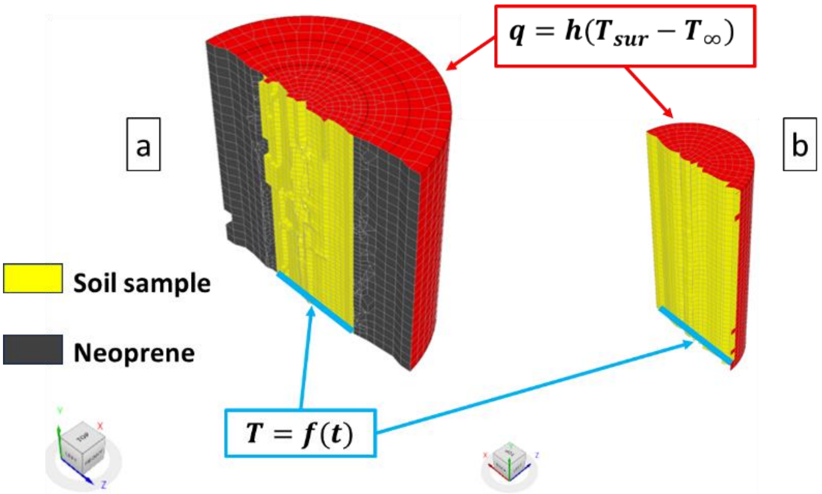

Figure 3.6: Numerical models of freezing tests on non-saline (a) and saline (b) soil samples. Specific BCs were applied on lateral faces of domain. Mesh size of soil sample=0.002 m

3.2 Results

3.2.1 Unidirectional freezing test

Thermocouples inserted inside the specimens recorded a decrease in temperatures during the freezing tests. In the non-saline soil specimens (Figure 3.7a, b, c), the temperatures reached very low values because LN_2 (T= -196 °C) was used as a coolant. In all three M specimens, the thermocouple time series with lower temperatures was the one at the steel base/soil interface. While the M1-N and M2-N specimens exhibit similar behaviours, the M3-N specimen needed more time to cool down. This is attributed to the higher porosity and low quartz content of M1-N and M2-N resulting in a lower unfrozen and frozen thermal conductivity. The freezing point is not noticeable in any of the non-saline specimens because of the large freezing rate given by LN_2 use.

Thermocouples inserted inside the specimens recorded a decrease in temperatures during the freezing tests. In the non-saline soil specimens (Figure 3.7a, b, c), the temperatures reached very low values because LN_2 (T= -196 °C) was used as a coolant. In all three M specimens, the thermocouple time series with lower temperatures was the one at the steel base/soil interface. While the M1-N and M2-N specimens exhibit similar behaviors, the M3-N specimen needed more time to cool down. This is attributed to the higher porosity and low quartz content of M1-N and M2-N resulting in a lower unfrozen and frozen thermal conductivity. The freezing point is not noticeable in any of the non-saline specimens because of the large freezing rate given by LN_2 use.

The results of freezing tests performed on saline soils show very similar behaviour among them (Figure 3.7d,e). The freezing point, at which pore water starts to freeze, is increasingly evident going from E-10mm to E-40mm temperature time series. In G2-S, E-30mm series is interrupted at freezing temperature value due to loss of thermocouple signal. Again, the “0 mm” time series has lower values as it reports the temperature of the metal base/sample interface. The G2-S specimen took longer to cool down. Temperatures drop across the sample domain to -30°C after about 3 hours in both.

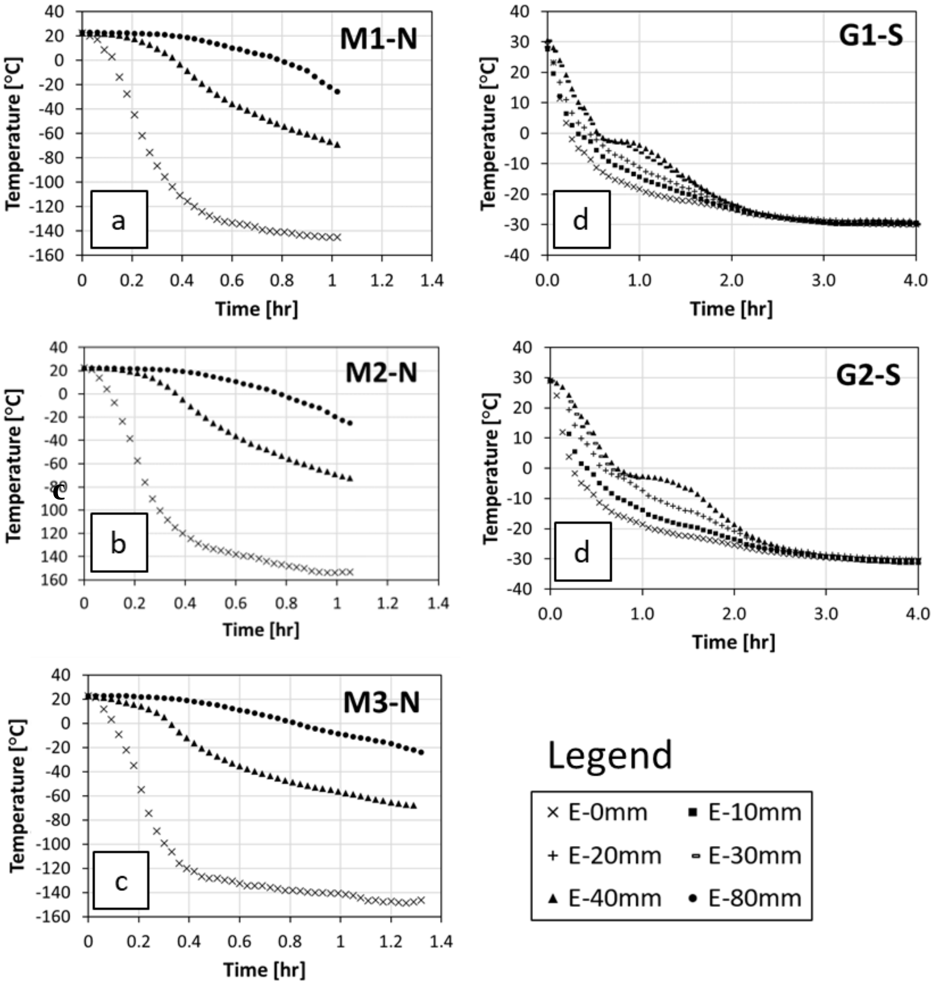

Figure3.7: Freezing test temperature trends recorded by thermocouples over time in non-saline (M1-N, M2-N and M3-N) and saline (G1-S and G2-S) soil samples at different acquisition levels.

3.2.2 IRT test

Thermocouples placed on the external face of the kaolin test specimen enabled the temperature to be recorded for the duration of the test. At the end of the test (80 min), the specimen was examined. At the base, a thick layer of ice crystals, which began to form after 40 min, prevented direct observation of the test specimen. With the help of a thin metal needle, the specimen was punched to check the height of the frozen portion, which was found to be 44mm (Figure 3.8).

Acquired thermal images of the freezing test (Figure 3.10) were imported into the software FLIR ResearchIR Max^{TM} and all the relevant corrections constant for the entire duration of the experiment (i.e. sample-camera distance, air temperature and humidity, reflected temperature, sample emissivity) were set. By means of this software, a line of pixels along the height of the specimen was interrogated and isochronous temperature curves were extracted. The thermal imaging camera measured the gradual lowering of the specimen from below throughout the duration of the test. From 40 minutes onwards, the portion of frozen soil at the base caused the water to gradually condense and subsequently freeze, thus forming an increasingly thick layer of ice crystals. As can be seen from Figure 3.10, in fact, the shape of the specimen in the thermographic images is no longer cylindrical but has a widening towards the base. By setting a threshold to display only the portion of the ground at T<0°C, it was possible to measure the height of the frozen front, which was 44mm (Figure 3.11).

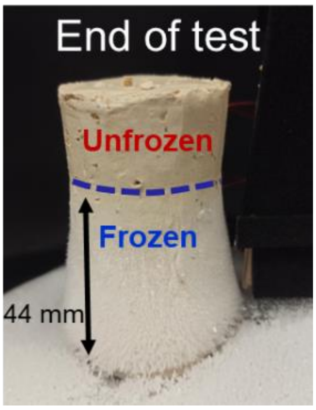

Figure 3.8: Kaolinite sample after 80 minutes of unidirectional freezing test. Frozen fringe reached 44mm of height.

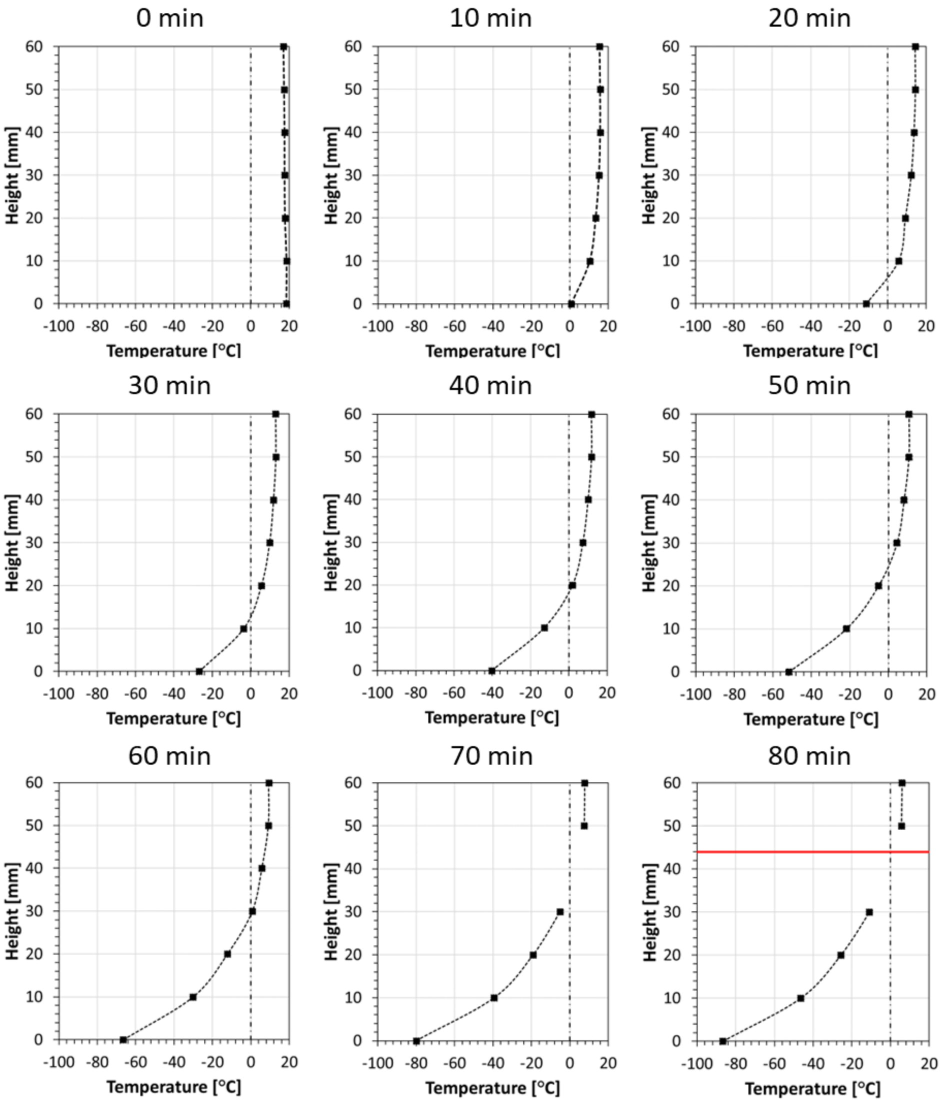

Figure 3.9: Temperature profile of kaolinite sample at specific time steps. Temperatures were recorded by T-type thermocouples. Red line represents frozen front at 80 min.

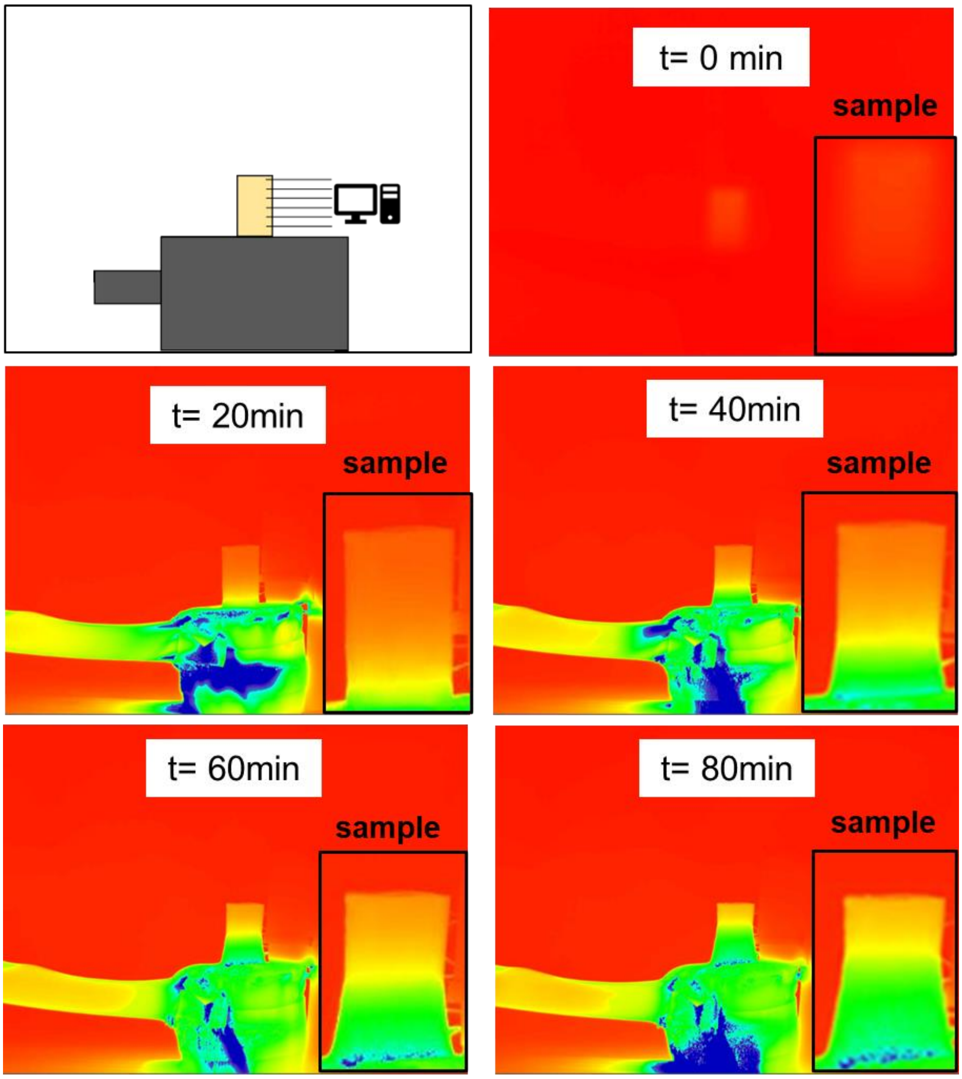

Figure 3.10: Thermal images of the kaolinite specimen at specific time steps taken by FLIR T1020.

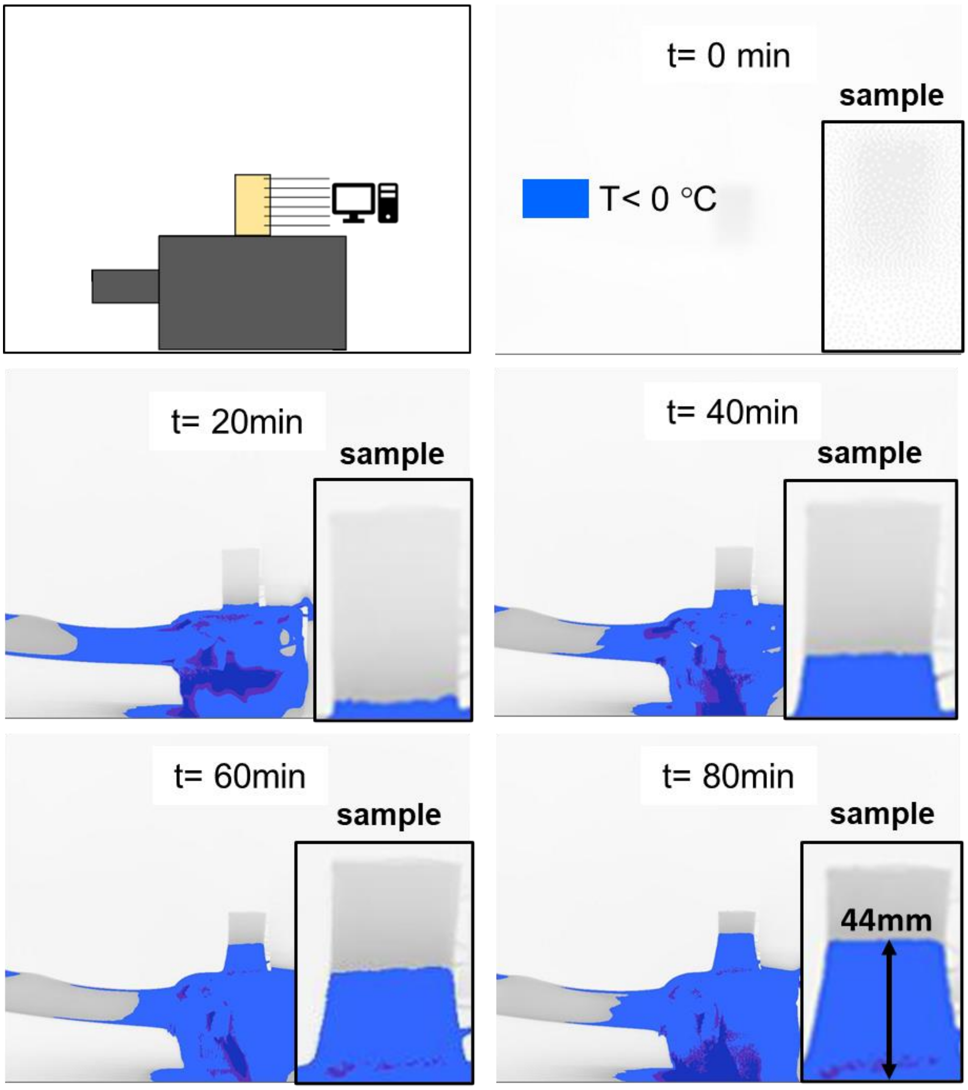

Figure 3.11: Portions of domain with T<0°C of the kaolinite specimen at specific time steps taken by FLIR T1020.

3.2.3 Numerical data

Simulation time was considered equal to that of experimental temperature time series. Four scenarios were evaluated: scenarios #1, 2, 3 to assess the impact of method adopted for measuring or estimating the thermal conductivity parameters of a soil; scenario #4 was performed to test the importance of considering the actual lateral BCs and justify the use of a 3D code despite the freezing occurs mainly in one direction (from bottom to top). All parameters and BCs considered in the four scenarios are given in Table B1.

The E-0mm time series of the thermocouple was set as the base BC in each analysis and was labelled as N-BC (see Figure 3.12-3.13). The numerical time series at the corresponding points of the thermocouples were acquired and the temperature time series was extracted from them.

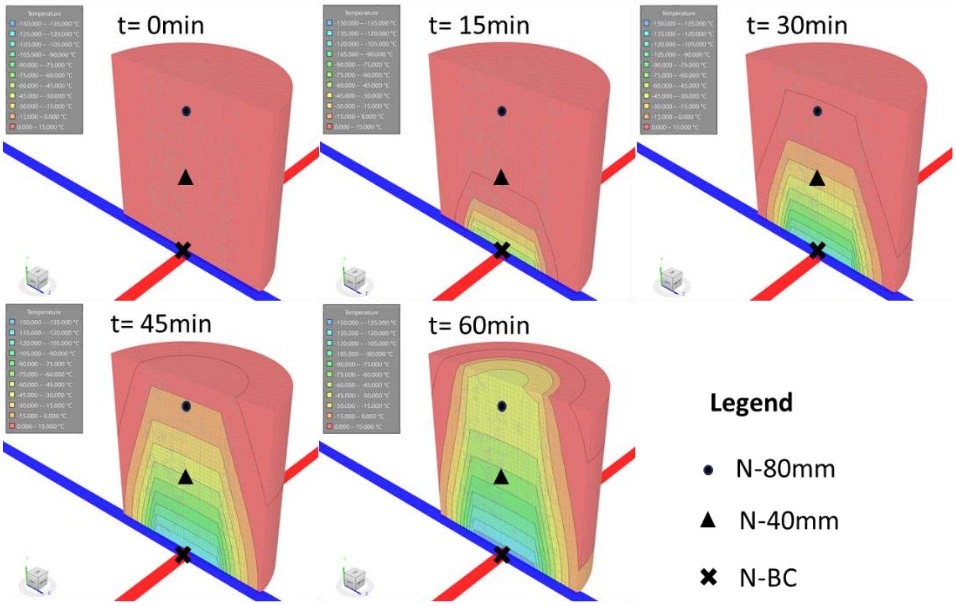

Figure 3.12: Temperature distribution results of numerical modeling on M1-N soil specimens. The circle, the triangle and the "x" are the position of the observation points at 80, 40 and 0 mm, respectively.

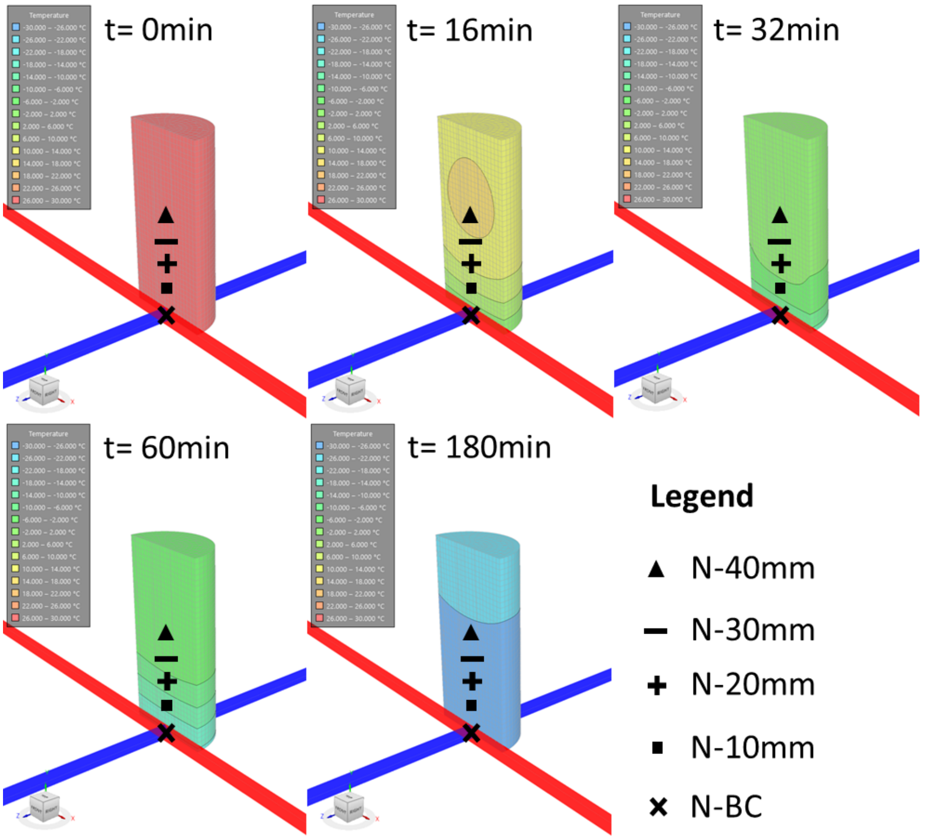

Figure 3.13: Temperature distribution results of numerical modeling on G1-S soil specimens. The triangle, the line, the cross, the square and the "x" are the position of the observation points at 40, 30, 20, 10 and 0 mm, respectively.

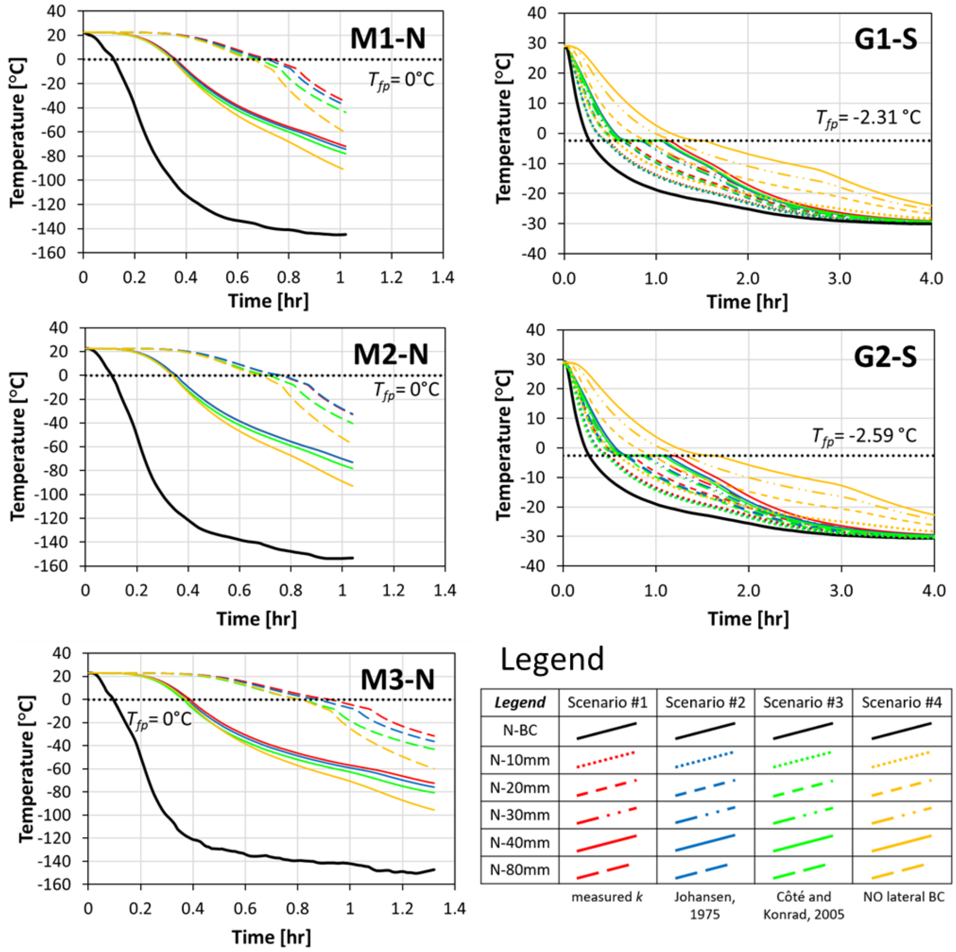

Figure 3.14: Numerical results of freezing test simulations carried out on non-saline (M1-N, M2-N and M3-N) and saline (G1-S and G2-S) soil samples. 4 different scenarios are shown for each numerical simulation.

In each test, freezing started from the bottom. As expected, the differences between results obtained in scenarios #1 and #2 were very small since the unfrozen and frozen thermal conductivity values considered for both scenarios were very similar (especially in M2-N analysis where results of scenarios #1 and #2 were not distinguished from each other) (Figure 3.14). In contrast, scenario #3 showed more pronounced differences for both the N-40mm and N-80mm series, since Côté and Konrad (2005) solution gives significantly higher *k* values than in scenarios #1 and #2. For non-saline soils, there was no noticeable phase transition of water, attributable to the high freezing rate; on the other hand, in saline soils, the slow cooling allows a clear phase transition to be detected at the prescribed freezing point temperature. Scenario #4 returns the most different results.

In addition, the effect due to the mesh size adopted in the 3D models was investigated. As seen from the graph in Figure 3.15, increasing the mesh size the temperature values decrease.

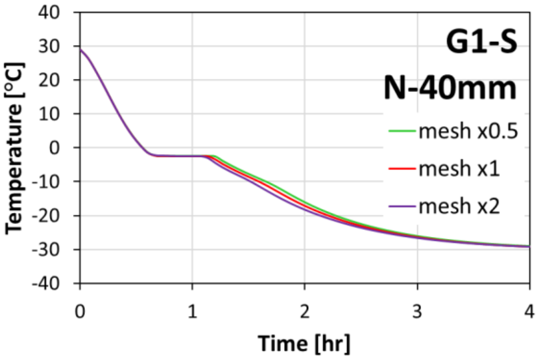

Figure 3.15: Results of mesh dependency analysis on “N-40mm” temperature series of G1-S. Mesh reference size was 0.002m (line mesh x1).

3.3 Discussion

In order to create a reliable transient thermal numerical model, knowledge of all the processes that take part during ground freezing is essential. It is also crucial to know the pros and cons of the methods used to estimate the thermal parameters required, and how they vary as a function of temperature and their impact on the final results.

The thermal imaging camera was used to measure the external temperature of a cohesive soil specimen during rapid freezing with nitrogen, in order to assess its ability to measure frozen soils under transient thermal conditions.

3.3.1 Experimental vs. numerical

Bottom-up freezing is a small-scale test that requires few resources. The temperature logging system made it possible to monitor temperature trends within the samples and provided data useful for code validation. Comparison between experimental data and numerical modelling results allows to identify which scenario best reproduces the freezing test. Plotting the experimental and numerical data on the same graph (see Figure 3.16 - 3.17), in non-saline and saline soil samples, Scenario #1 and Scenario #2 provide the curves most similar to those obtained experimentally, respectively.

To evaluate and quantify the similarity between numerical and experimental curves, three statistical methods were applied. Pearson's Correlation Coefficient (PCC), the area between the curves and Dynamic Time Warping (DTW).

The Pearson correlation coefficient measures linear correlation between two datasets. This coefficient is calculated as the ratio of the covariance of two variables to the product of their standard deviations. PCCs are the most commonly used method for assessing the similarity between curves. PCC ranges from -1 to 1 and measures the high correlation between two variables (1: variables are perfectly positively correlated; -1: two variables are perfectly negatively correlated; 0: data are uncorrelated). The two curves that are compared need to have the same number of time acquisitions. Table 3.2 shows the PCCs between the numerical and experimental data computed for the four scenarios of M1-N. Values of PCC higher than 0.8 mean a very strong linear correlation. The results of the analysis are graphically visualised using a linear relationship to fit the scatter plot of the numerical and experimental data (Figure 3.18). If the experimental and numerical series match (e.g., E-0mm and N-BC), all points are positioned along a straight line, otherwise, the points diverge from the straight line.

The R-Square values give the Coefficient of determination, which represents the proportion of variance that the two variables have in common. Table 3.3 reports R-Square values computed for each scenario considering the M1-N soil. The PCCs obtained for samples M2-N, M3-N, G1-S and G2-S are reported in the supplementary material.

As a second method, given a baseline curve (numerical data) and a candidate curve (experimental data), the area bounded by the two curves is a measure of similarity. (area=0, two curves are equal). Considering the M1-N sample, the areas were computed for each scenario (Table 3.4).

Finally, DTW is based on the calculation of the distance between points of one curve to the other curve, finding the optimal DTW distance, which minimizes the cumulative distance between points. (e.g., DTW=0, two curves are equal). For each scenario the DTW distance was computed (see Table 3.5).

Results of statistical analyses of M1-N are reported in Table 3.2, 3.3, 3.4 and 3.5. For M2-N, M3-N, G1-S and G2-S results are reported in supplementary materials: from Table B2 to Table B5 (M2-N), from Table B6 to Table B9 (M3-N), from Table B10 to Table B13 (G1-S), from Table B14 to Table B17 (G2-S) and from Figure B1 to Figure B4.

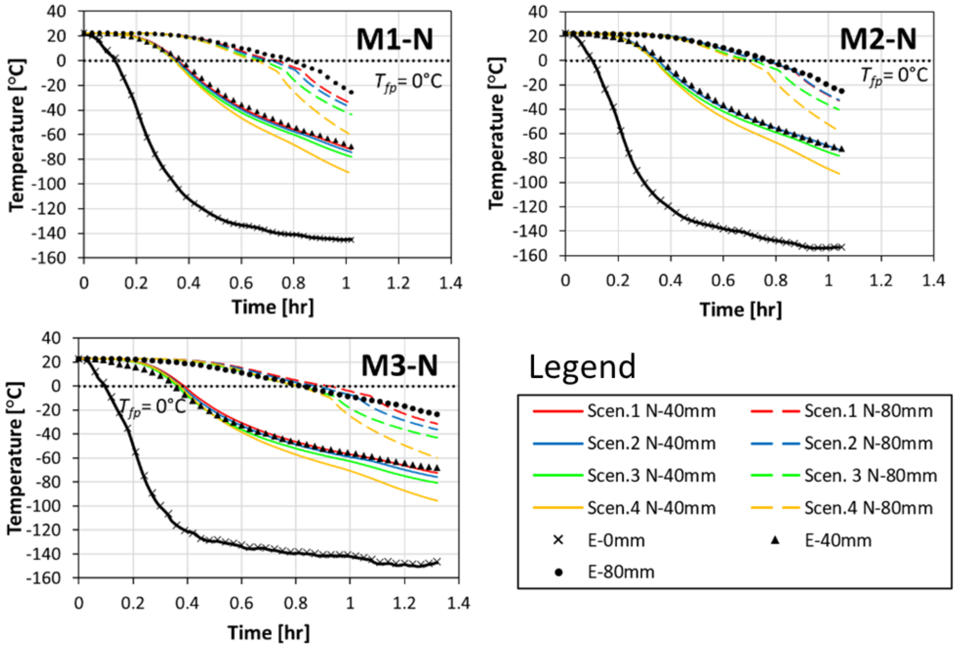

Figure 3.16: Numerical vs. experimental results of freezing test carried out on non-saline (M1-N, M2-N and M3-N) soil samples. Four different scenarios are shown for each numerical simulation.

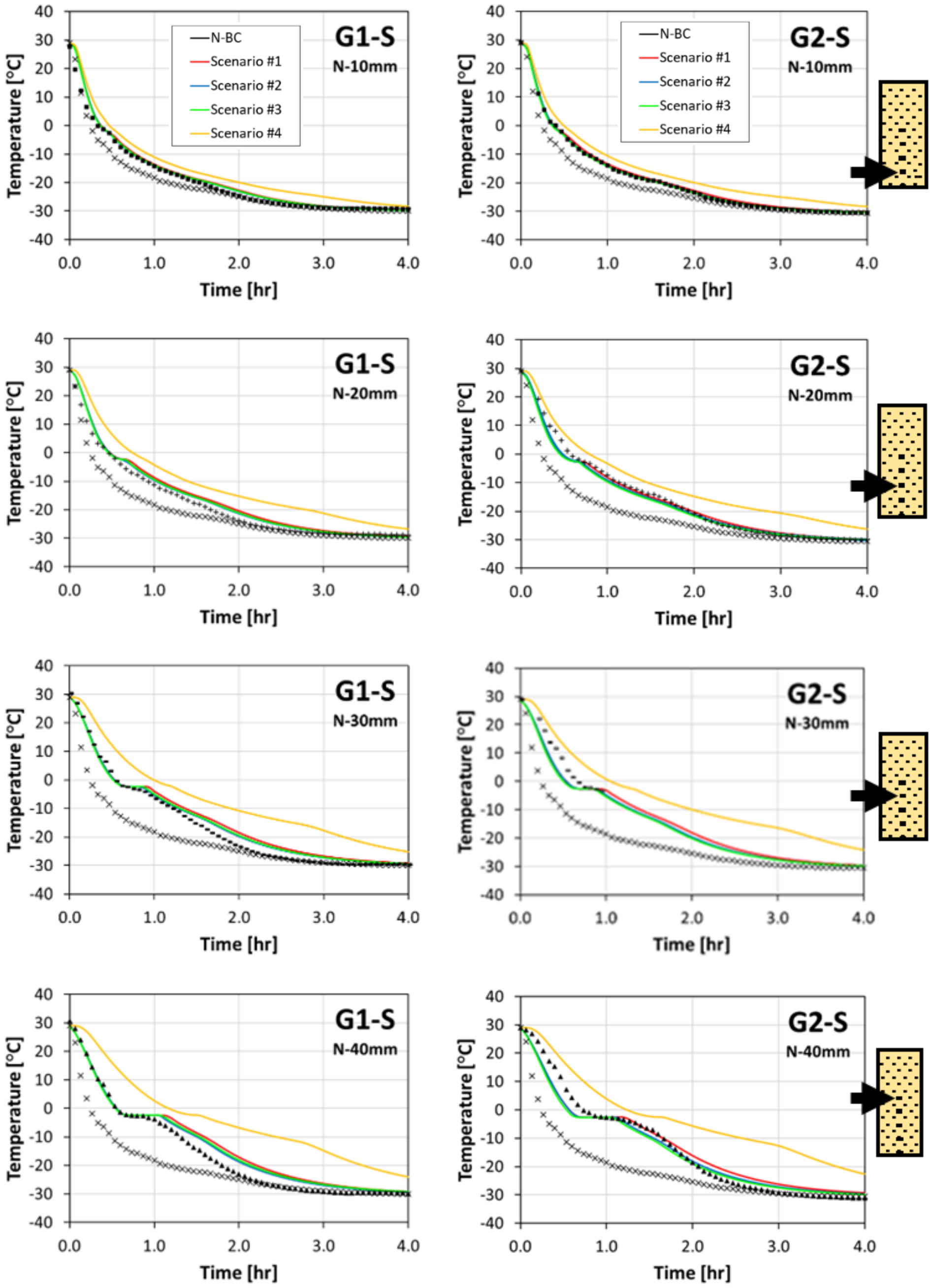

Figure 3.17: Numerical vs. experimental results of freezing test carried out on saline (G1-S and G2-S) soil samples. Four different scenarios are shown for each numerical simulation.

Table 3.2: The Pearson correlation coefficients (PCC) computed for each scenario considering the freezing test on M1-N soil sample.

Scenario	**1**	**2**	**3**	**4**
	Pearson Correlation			
E-0mm - N-BC	1	1	1	1
E-40mm - N-40mm	0.99945	0.9993	0.99894	0.9993
E-80mm - N-80mm	0.9974	0.99707	0.99605	0.99327

Table 3.3. R-Square of the linear regression computed for each scenario considering the freezing test on M1-N soil sample.

	R-Square			
Scenario	**1**	**2**	**3**	**4**
40 mm	0.99889	0.9986	0.99788	0.99861
80 mm	0.99481	0.99415	0.99211	0.98658

Table 3.4: Values of the area between the two considered curves computed for each scenario considering the freezing test on M1-N soil sample.

Scenario	**1**	**2**	**3**	**4**
	Area between curves			
E-0mm - N-BC	0	0	0	0
E-40mm - N-40mm	1.32	2.48	4.55	8.65
E-80mm - N-80mm	1.07	2.37	4.75	8.29

Table 3.5: DTW computed for each scenario considering the freezing test on M1-N soil sample.

Scenario	**1**	**2**	**3**	**4**
	DTW			
E-0mm – N-BC	0	0	0	0
E-40mm - N-40mm	24.4	40.75	77.01	272.57
E-80mm - N-80mm	36.66	62.99	130.2	369.44

The four statistics considered to assess the similarity between the experimental and numerical results curves indicate that for the M1-N sample test, scenario #1 provides the best fit. Considering the statistics as a whole, it can be said that for tests performed on M2-N, M3-N and G1-S specimens, the best results are provided by scenario #2 (i.e., considering the thermal conductivity parameters calculated by Johansen's method). As far as the G2-S test is concerned, the scenario that provides the curves most similar to the experimental ones is scenario #3.

Observation of the scatterplots (Figure 3.18, B1 and B2) in each case clearly indicates that for all non-saline soil samples, the best scenarios are #1 and #2 since the N-40mm and N-80 series deviate little. This is the consequence of small difference between the thermal conductivity values considered in scenarios #1 and #2.

In saline-soil samples, scatterplots (Figures B3 and B4) show that scenarios #2 and #3 report curves that deviate the least. Scenario #4 reports the worst data in that all curves (10mm, 20mm, 30mm and 40mm) deviate markedly from the experimental temperature series.

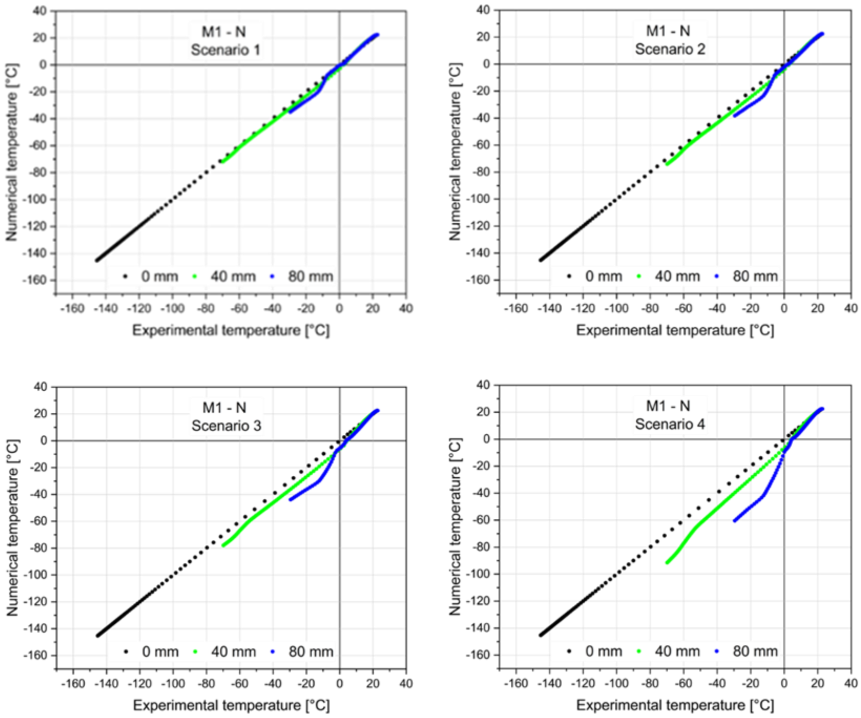

Figure 3.18: Scatterplot of comparison between experimental and numerical results of four scenario of freezing test performed on M1-N soil sample: a) Scenario #1; b) Scenario #2; c) Scenario #3; d) Scenario #4.

In all the samples, scenarios #1, #2 and #3, where just the thermal conductivity in the unfrozen and frozen state varies, the curves are clustered whereas scenario #4 provides markedly distinct curves.

The results for Scenario #4 underscore the importance of the boundary conditions built into the numerical model and justify the use of a 3D code despite a 1D. In this scenario, where lateral heat convective surface BC was removed and no-flux surface was imposed, temperature curves doesn’t fit experimental ones as showed in Table 3.4 and 3.5 and Tables B4, B5, B8, B9, B12, B13, B16 and B17 where the area between numerical and experimental curves and DTW are the largest. This means that freezing from the bottom up cannot be reduced to a 1D problem since lateral BCs affect the final result.

3.3.2 IRT vs. Thermocouples

The formation of ice crystals from 40 minutes onwards caused disturbances in the acquisition of thermal images, so only the temperature profiles extracted from the thermographic images up to 50 minutes were analysed, where only in the lower portion (0-10 mm) temperature fluctuations are noted. The extracted temperature profiles were then compared with the experimental results measured with thermocouples. Figure 3.19 shows the results obtained with the two methods, direct and indirect, at time steps 0, 10, 20, 30, 40 and 50 min. The fitting between the curves is good, particularly for positive temperatures and for the definition of the frozen front (0°C isotherm); while small uncertainties are visible for negative temperatures, up to the formation of ice crystals. It is then possible to conclude that the thermal imaging camera, once the input parameters have been set and certain technical and logistical details have been considered, is a valid tool for measuring the temperature of frozen ground that allows for a greater number of measurement points (i.e., the number of pixels) distributed homogeneously over the domain of interest compared to classical temperature sensors. This represents a great potential for this technology, which can thus also be used in artificial freezing operations during excavation phases to verify the thermal conditions of the excavation face.

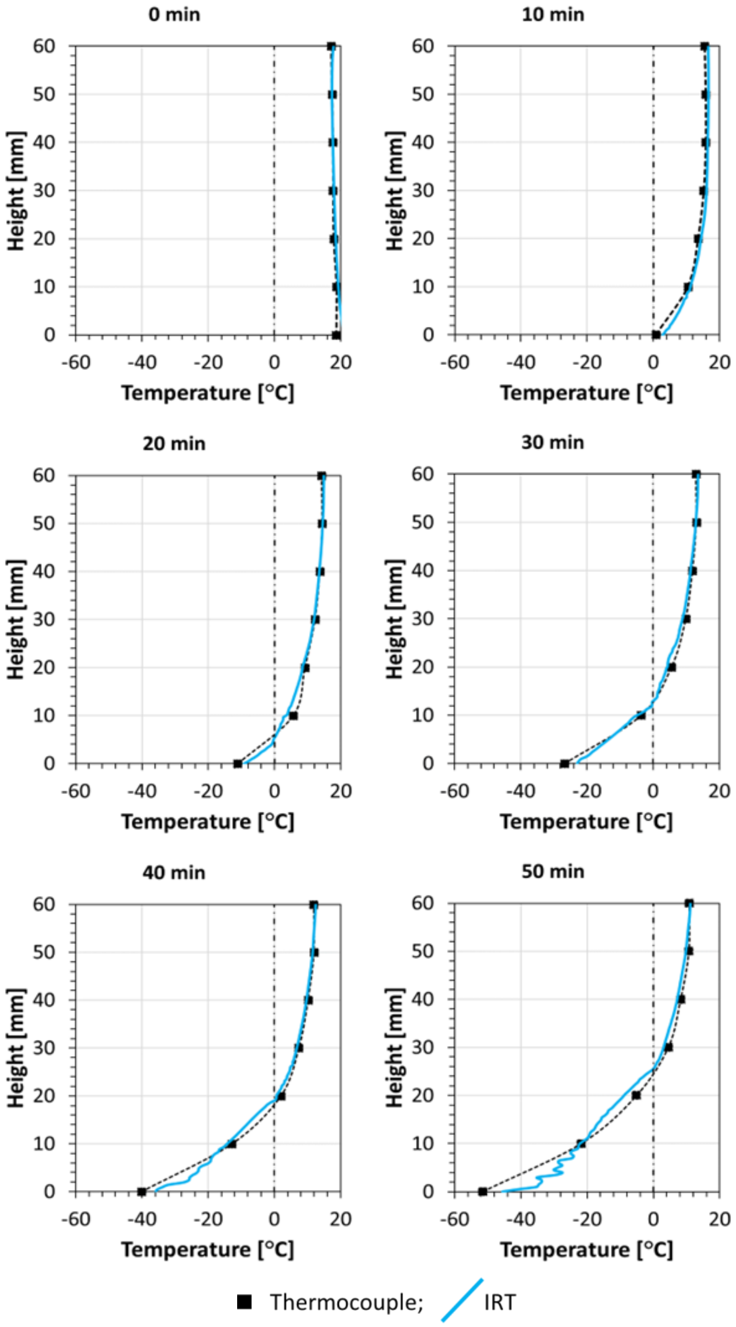

Figure 3.19: Comparison between temperature profiles measured with thermocouples and extracted from IRT images through FLIR ResearchIR Max^{TM}

Chapter 4

4 On-site innovative aspects

As seen in *Chapter 1*, artificial ground freezing is mainly composed of a design phase and an execution phase. In the former, it is necessary to investigate the mechanical resistance values and thermal parameters of soil to carry out feasibility studies of the intervention and excavation stability investigations (see *Chapter 2*) and to perform thermal analyses using numerical codes, possibly after validation of the code used (see *Chapter 3*).

In the execution phase, on the other hand, a series of activities can be carried out to:

- verify the predictions made on the physical, mechanical and thermal properties of the frozen mass through a chain of operations tested in this study (sampling, storage, coring, testing);
- monitor temperature distribution at the excavation face with innovative and validated methods (IRT technology)

The data obtained from these activities represent an important benchmark for the predictions made, increase the level of safety during operations and provide the basis for designing future interventions under similar conditions.

During several visits to the Isarco underpass - BBT construction site since 2020, site investigations (i.e., point load tests, IRT images, frozen block recovering) were carried out at the excavation face of one of the four tunnels below the Isarco River, followed by laboratory tests (i.e., UCS, PLT, TRX and thermal conductivity measurement, see Bavaresco et al., 2023b).

The collection, storage and transport of the frozen soil samples were carried out based on the recommendations of Baker (1976), but these were not followed for the specimen shaping stage, as they were not applicable to the heterogeneous and pebbly soil which constituted the frozen soil blocks collected. The internal structure of the blocks was investigated using X-ray Computed Tomography (CT) to choose the best sampling methodology. This technology, used on frozen (see Torrance, 2008 and Chen et al., 2014) or thawing (see Liu et al., 2012 and Kang et al., 2016) soil samples, allows the internal structure of a soil specimen to be non-destructively investigated. CT scanning can also be used to characterise frozen soil damage (Chen et al., 2022).

As they were already frozen, sampling as performed by Kiaalhosseini et al. (2016) and Wride et al. (2000) was not possible, so coring, although it is very challenging as Le et al. (2016) explained, can be identified as sampling method considering the use of different cutting tools and instruments (see Zubrzycki, 2012 and Hani et al., 2023) depending on the environmental conditions and equipment availability. The blocks were drilled and subjected to mechanical and thermal tests described in detail in *Chapter 2*.

4.1 Materials and Methods

The soil under study in the on-site and laboratory operations, picked up directly in situ in the frozen state during the brine maintenance phase, was labelled according to the criterion used and illustrated in *Chapter 2*. Iu-N means that the soil from the Isarco site is undisturbed (u) and non-saline (-N).

4.1.1 On-site activities

The site surveys at the Isarco Underpass were carried out during the excavation of the fourth tunnel in which the support and waterproofing of the excavation were ensured by maintaining a shell of frozen soil employing the brine method. The excavation was carried out with an hydraulic hammer that detached blocks of frozen soil of varying sizes (up to 1m). After each metre of progress in the excavation, the material was placed on a truck and transported to an accumulation area. Once the excavation face was bared, shotcrete enriched with metal fibres was projected on surface. Then the iron ribs and various iron reinforcements were placed, with additional shotcrete, to form a temporary lining of the tunnel. These excavation processes were conducted from the two shafts so that each tunnel was excavated from two opposite sides. Once the excavation was completed and temporarily covered, the final covering consisting of reinforced concrete cast within appropriate formwork was placed. The final phase involved the excavation and lining of the invert. The activities described below were carried out inside the tunnel, and at moments when the excavation face was bare and visible.

4.1.1.1 Infrared thermography

Infrared thermography (IRT) technology is widely used for monitoring with geotechnical applications, as demonstrated by the works of Guerin et al. (2019), Mineo and Pappalardo (2021) and Franzosi et al. (2023). After a laboratory test to verify the reliability of the FLIR T1020 28° thermal imaging camera on the frozen ground (see *Chapter 3*), it was used on-site to monitor the temperatures of the excavation face. The infrared imaging camera was positioned at a distance to capture the entire surface area. Environmental temperature and air humidity values were measured. A rough aluminium panel of approximately 1x0.8m was placed within the frame to measure the reflected temperature of all bodies surrounding the framed object and the camera. Finally, the distance between the camera and the object was measured. These parameters were directly input into the control panel of the thermal imaging camera and infrared images were taken of various bodies during different phases of the excavation, including the shotcrete before demolition (Figure 4.1a), the demolition phase (Figure 4.1b), the bare excavation face (Figure 4.1c) and the outer wall of a freezing pipe (Figure 4.1d). During the excavation of a section, a freezing pipe emerged in the lower portion of the right side. Infrared imaging revealed that the outer wall of the pipe was -33.4°C, which agrees with the temperature of the brine used for maintenance, which measured -34°C at the refrigeration system.

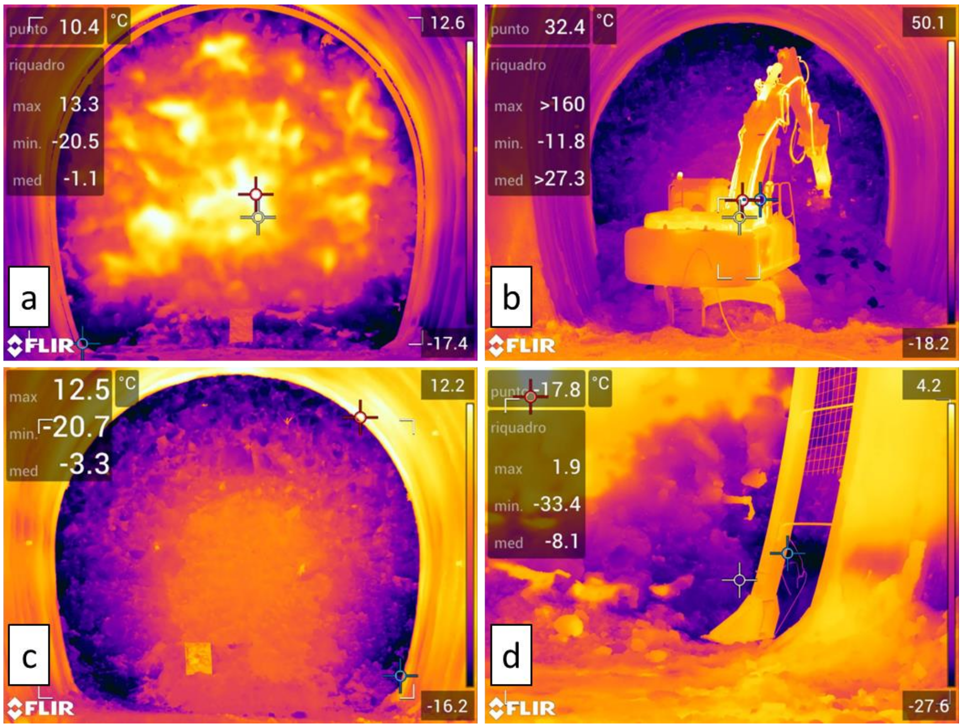

Figure 4.1: IRT images from Isarco Underpass site during excavation phase: a) excavation face covered by shotcrete; b) hydraulic hammer detaching frozen soil blocks; c) free excavation face of frozen soil; d) freezing pipe fed with brine as coolant.

4.1.1.2 Point load tests

The point load test (PLT), as already described in detail in *Chapter 2*, is a quick test for determining a rock strength index. This test was used to evaluate its suitability for frozen soil samples to provide a simple tool on site to estimate the mechanical parameters of the soil to verify excavation stability. The type of specimens considered, and the thermal conditions adopted are listed in Table 4.1.

With the use of the thermal imaging camera, centimetric blocks of frozen soil composed of matrix were identified from among those that had just been detached from the front by the hydraulic hammer (see Figure 4.2). Due to the impossibility of stabilising the samples at the desired temperatures and the difficulty of finding a sufficient number of them at a given temperature, those with a temperature of -15<T<-5°C were considered, which falls within the thermal test condition /p-s shown in Table 4.1.

Once identified, the samples were measured and subjected to PLT, which returned the sample resistance value $I_{s(50)}$(see Figure 4.3). During all these steps, the samples were handled with cryogenic gloves to prevent melting. Only those tests in which the sample fracture satisfied the standards of acceptability expressed in ASTM D5731-02 were considered, as that one in Figure 4.3e. The results of these tests and the characteristics of the samples are shown in Table C1.

Table 4.1: List of thermal conditions applied to considered samples during PLT tests on undisturbed Iu-N samples.

PLT Specimen	Sample	Thermal condition
Iu-N/p-s	Isarco undistrubed - non saline	-15 < T < -5°C
Iu-N/p	Isarco undistrubed - non saline	T= -10°C
Iu-N/p-h	Isarco undistrubed - non saline	T= -6°C

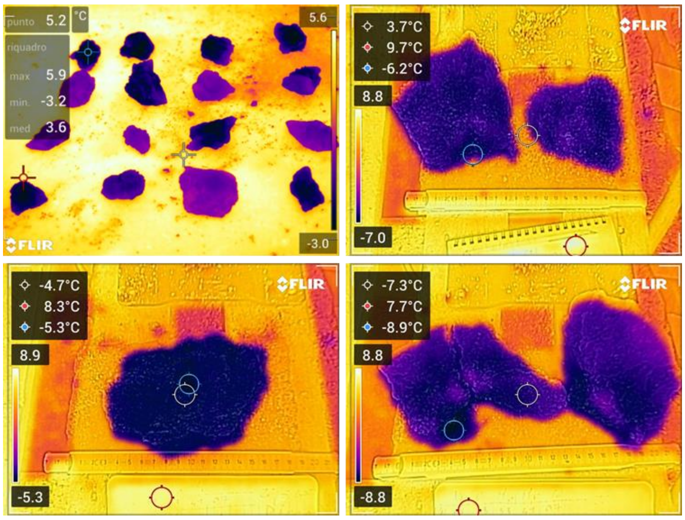

Figure 4.2: Some centimetric frozen soil blocks identified on-site through FLIR camera to point load tests.

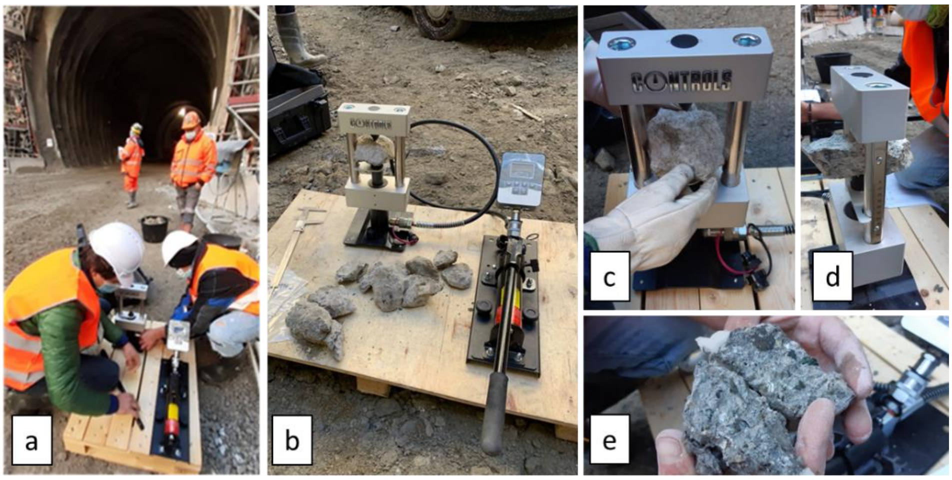

Figure 4.3: On-site point load tests execution on frozen blocks: a) in the shaft in front of the tunnel; b) PLT equipment; c) gloves for cryogenic use; d) frozen block located between cones; e) cracks faces of frozen block post-failure.

4.1.1.3 From site to laboratory

From the material detached from the front, a few decimetric-sized blocks of frozen soil composed of gravelly or sandy material were taken (Figure 4.4a). These, weighing enough to be lifted and handled by two persons (max. 25-30 kg), were wrapped with transparent film, sealed with adhesive tape, labelled and placed inside insulating boxes. Dry ice was added to prevent the melting of frozen blocks (**Figure 4.4b).**

Figure 4.4: Frozen blocks recovering: a) directly from excavation face during excavation with a hydraulic hammer; b) dry ice added to avoid melting of pore-ice; c) isothermal van used to bring blocks to San Gerardo Hospital.

These boxes were loaded inside an isothermal van (Figure 4.4c) and transported to the San Gerardo Hospital in Monza, where 7 of them were analysed by X-ray CT (see Figure 4.5). Given the size and weight of the samples to be CT scanned, it was decided to use a machine employed for humans (Table 4.2). This technique consists of exposing an object to a beam of X-rays that are attenuated in intensity by an exponentially decreasing mass attenuation coefficient. This coefficient depends on the density of the material passed through and the energy of the X-ray beam.

Table 4.2: Physical parameters of recovered frozen blocks.

Frozen Block	**Volume** [mm^3]	**Weight** [kg]	**Specific Weight** γ_n [kN/m3]	**n** [-]	**e** [-]	**Sr** [-]
A1	8,868,030.0	20.42	23.03	0.18	0.22	0.82
A2	10,277,300.0	24.61	23.94	0.14	0.16	0.86
B1	6,878,990.0	14.38	20.90	0.30	0.43	0.85
B2	8,616,140.0	18.25	21.18	0.27	0.36	0.71
B3	10,516,000.0	0.00	21.41	0.33	0.49	0.89
C1	4,243,580.0	6.34	14.93	0.50	1.01	0.37
C2	2,299,330.0	4.53	19.68	0.32	0.46	0.54

Figure 4.5: CT analysis on the frozen block at San Gerardo Hospital, Monza (Italy).

CT returns 2D images with a resolution of 0.625mm x 0.625mm in greyscale where each shade represents a relative density, in which the densest pixel is white, and the least dense pixel (air) is black. In this way it is possible to 'see' the inside of a sample, distinguishing pebbles and gravel (lighter) from the ice-particles matrix (darker). This analysis made it possible to investigate the internal structure of the blocks and to identify the portions suitable to be cored or drilled, avoiding the predominantly pebbly portions, which would make coring difficult and would provide a specimen not representative of the behaviour of the ground. Furthermore, by plotting all the 2D slices obtained from CT on the Avizo software in a Cartesian axis system (the distance between each slice along the three dimensions is 0.625mm), it was possible to reproduce the 3D model and measure the volume of each block, as shown in Figures 4.6, C1, C2, C3 and C4).

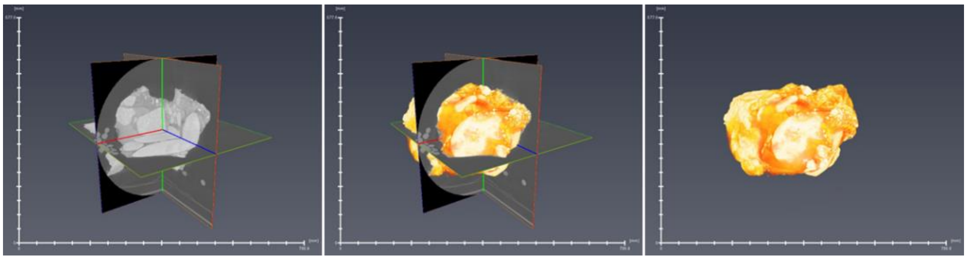

Figure 4.6: Orthogonal slices from CT analysis and 3D views of A1 frozen block elaborated by Avizo.

After the CT scan, the samples were taken to EuroCold Lab in Milan, where they were weighed and stored in a cold chamber at -20°C, and specimen preparation activities were started (Figure 4.7).

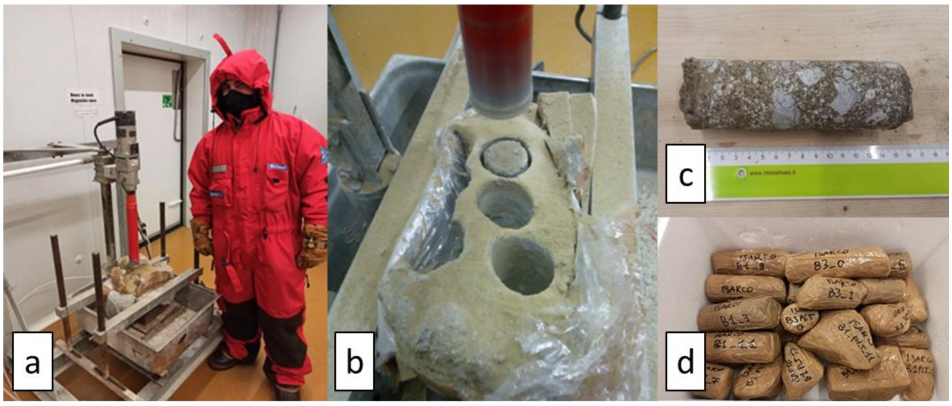

Figure 4.7: Undisturbed frozen soil specimen preparation in EuroCold Lab: a) at -20 °C; b) dry coring of B1 block; c) undisturbed frozen soil cored; d) storage of cylindrical and irregular specimen in Eurocold Lab.

Inside the cold chamber, a Cardi core drilling machine was brought in, equipped with a Larica core barrel (internal D = 50mm) with embedded diamonds and a block fixing system. Once all the components had reached thermal equilibrium with the environment, dry core drilling was carried out using air as the purging fluid. The air, pressurised by a compressor outside the cold chamber, was connected to the core barrell via a 10m-long rilsan tube placed entirely in the cold chamber, which allowed the air to cool before exiting the core barrel. After the blocks were positioned to avoid the pebbly portions identified by CT, they were cored by slowly lowering the core barrel along a rack in such a way that the friction between the cutter tool and the block did not cause temperatures to rise. These operations, performed at a temperature of -20 °C, resulted in frozen soil cores up to 17 cm long.

The cores were inserted into 60-mm PVC tubes and the gap was filled by wrapping the specimen in a layer of cauchu so that the core and PVC were joined together. The PVC and cauchu had been pre-cooled. Once the temperature of -20°C had been reached, the cores in the PVC were cut across using a circular saw with a disc coated with diamond paste. The cut caused a small melt on the face of the specimens, but the holding system ensured that the cores maintained a cylindrical shape during the cut. Once cut, the specimens were packed and stored in the cold chamber.

4.1.2 Laboratory tests

The height, diameter and weight of the specimens obtained were measured and the physical parameters (n, e, S_r) were determined. The EuroCold Lab cold chamber was set at -10°C and UCS and TRX tests, and PLT were performed on the specimens following the test procedures described in *Chapter 2*. Subsequently, the cold chamber temperature was set to -6°C and UCS and PLT tests were performed. The physical characteristics of all tested specimens are shown in Table C2-C6.

Due to the small size of the cylindrical specimens, thermal conductivity measurements were performed directly on some blocks at T= -10°C by drilling holes in the specimen with a drill. The position of the holes was established from the images provided by the CT. Once the hole was drilled, with D=4mm and L=50-55mm, the Thermtest Portable TLS-100 conductivity meter was used following ASTM D5334-08 (see Figure C5). Then the soil portions were allowed to melt with the needle probe inserted so that conductivity in the unfrozen state could be easily measured.

The list of tests performed is summarised in Table 4.3 and the thermal conditions to which the specimens were subjected for the UCS and TRX tests, and PLT in the laboratory are shown in Tables 4.4, 4.5 and 4.1 respectively.

Table 4.3: Mechanical and thermal tests performed on the considered soil sample.

		mechanical tests				thermal tests	
Sample code	**Sample**	***UCS***	***TRX***	***BRZ***	***PLT***	k_u ; k_f	T_{fp}
Iu-N	Isarco undistrubed - non saline	X	X	-	X	X	-

Table 4.4: Thermal conditions applied to considered samples during UCS tests.

UCS Specimen	Sample	Thermal condition
Iu-N/u	Isarco undistrubed - non saline	T= -10°C
Iu-N/u-h	Isarco undistrubed - non saline	T= -6°C

Table 4.5: *Thermal conditions applied to considered samples during TRX tests.*

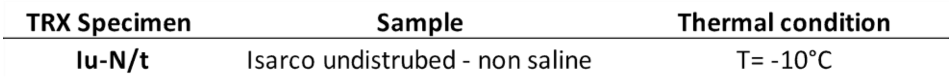

TRX Specimen	Sample	Thermal condition
Iu-N/t	Isarco undistrubed - non saline	T= -10°C

4.2 Results

The results obtained from on-site and laboratory tests are shown below.

4.2.1 On-site

The infrared imaging camera allows the distributed temperature of the framed bodies to be displayed instantaneously during its use. Thermographic images of the same excavation face were acquired at two times: during the excavation phase (Figure 4.13), in which only the upper half of the excavation profile is visible and the detached blocks are visible on the lower part; at the end of the excavation (Figure 4.14), after three hours, in which the whole face can be seen and the excavation profile is well defined, apart from the inverted. In Figure 4.13a, the portion of frozen ground at the crown and the mass of frozen blocks at the bottom are distinctly visible, with a portion of darker (colder) blocks detached more recently.

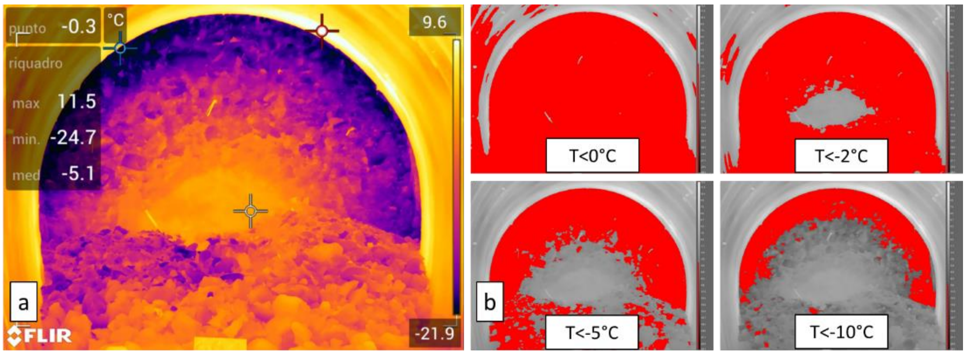

Figure 4.13: IRT applied to temperature monitoring of AGF intervention: a) during excavation phase; b) IRT images processed by FLIR ResearchIR.

In Figure 4.14a, on the other hand, the entire frozen ground profile can be clearly seen, as all the material was collected and removed.

Better results can be obtained by processing thermography images with FLIR ResearchIR software, which allows the user to interrogate regions of interest (ROIs) such as surfaces or lines.

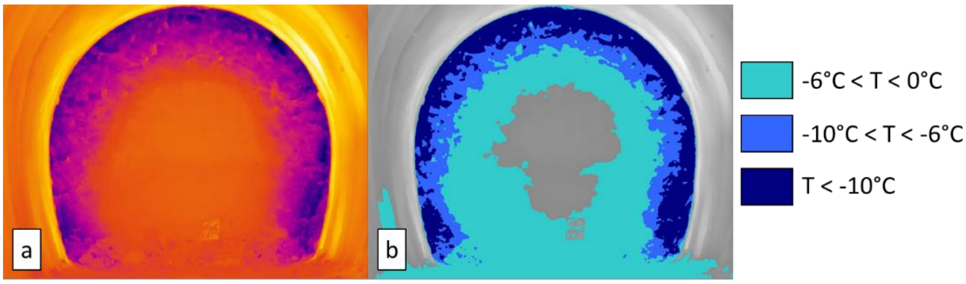

Figure 4.14: IRT applied to temperature monitoring of AGF intervention: a) at the end of excavation phase; b) IRT images processed by FLIR ResearchIR.

As shown in Figures 4.13b and 4.14b, portions of the ground with defined temperature ranges can be identified from a thermal image. Five temperature profiles were extracted at 0°, 45°, 90°, 135°, and 180° C from the horizontal, respectively, as shown in Figure 4.15. From the obtained results, it is possible to observe that during excavation, the entire visible mass is at T<0°C, which, however, due to contact with the air, ($0<T_{air}<10°C$) gradually warms up until the creation of a central area with a positive surface temperature.

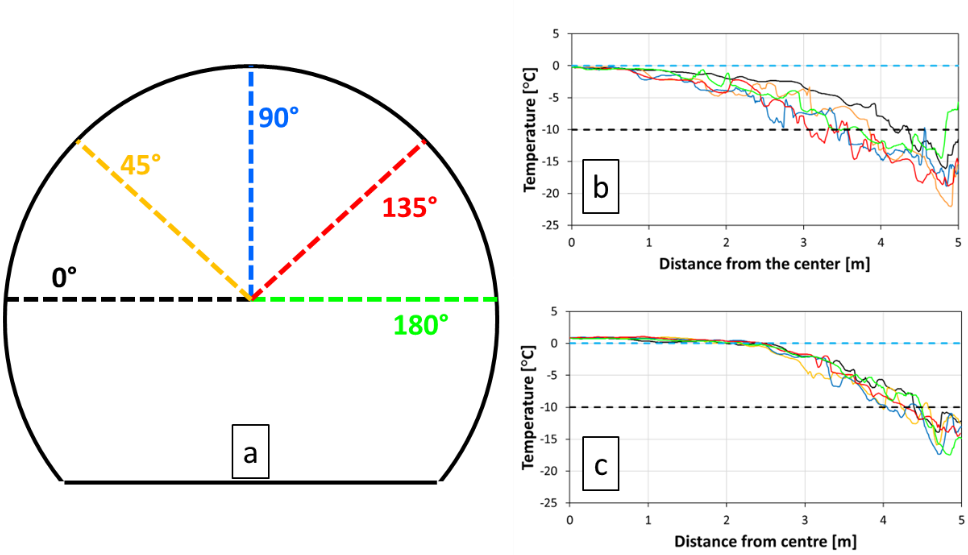

Figure 4.15: Temperature profiles (a) extracted from IRT images of: b) Figure 4.13a; b) Figure 4.14a.

The specimen data subjected to PLT and the results obtained are shown in Table C1. These data, grouped into classes are represented as a frequency histogram and as a normalised frequency curve (Figure 4.16) showing an average value of di $I_{s(50)}$=1.14 MPa and a St. Dev. of 0.42 MPa.

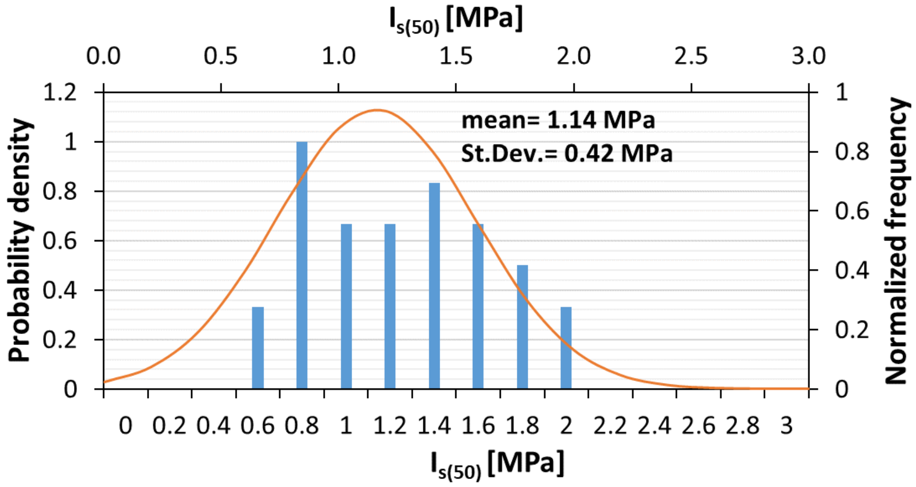

Figure 4.16: $I_{s(50)}$ index values from on-site point load tests on the frozen block.

4.2.2 Laboratory tests

Table 4.6: Unconfined compression tests results of Iu-N soil sample at -10 °C.

Soil specimen	**Frozen Block**	**Axial strain rate [%/min]**	**σ_3 [MPa]**	**σ_c [Mpa]**	**E_{t50} [Gpa]**
Iu-N/u1	B1	1	-	7.61	0.39
Iu-N/u2		1	-	8.25	0.36
Iu-N/u3	B3	1	-	9.29	0.57

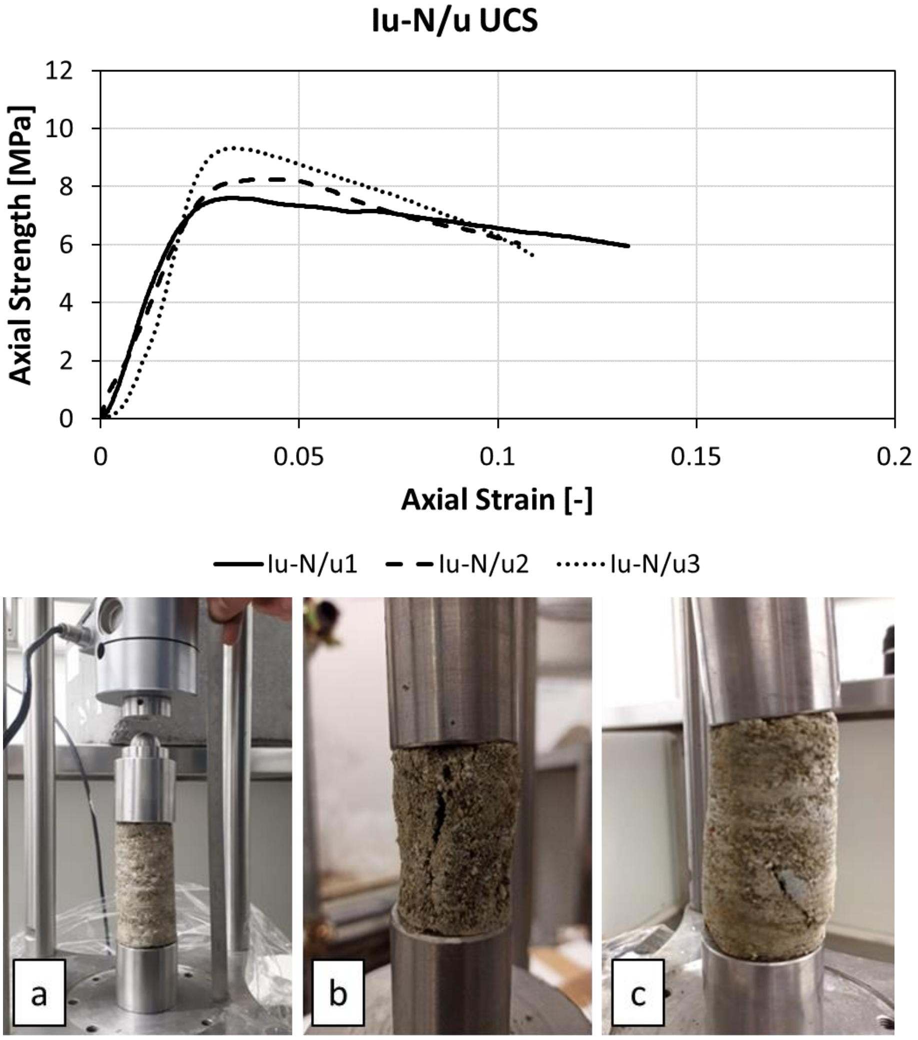

Figure 4.17: Uniaxial compression test results of undisturbed Iu-N soil sample at -10 °C. a) pre- and b-c) post-failure.

Table 4.7: Unconfined compression test results of Iu-N soil sample at -6 °C.

Soil specimen	Frozen Block	Axial strain rate [%/min]	σ_3 [MPa]	σ_c [Mpa]	E_{t50} [Gpa]
Iu-N/u1-h	B1	1	-	6.55	0.68
Iu-N/u2-h		1	-	5.54	0.29
Iu-N/u3-h		0.5	-	6.39	0.29
Iu-N/u4-h		0.5	-	7.13	0.69
Iu-N/u5-h	B3	1	-	7.35	0.33
Iu-N/u6-h		1	-	7.30	0.74

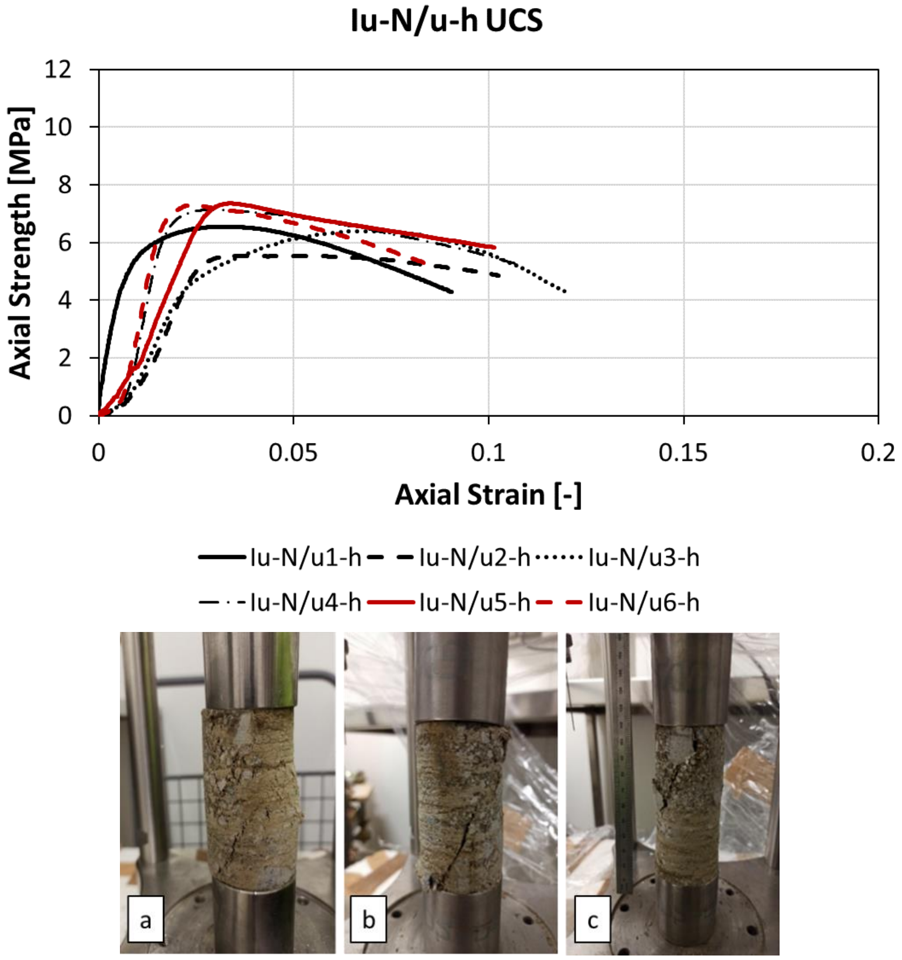

Figure 4.18: Uniaxial compression test results of undisturbed Iu-N soil sample at -6 °C. a-b-c) post failure.

Table 4.8: Triaxial compressive test results of Iu-N soil sample at -10 °C.

Soil specimen	Frozen Block	Axial strain rate [%/min]	σ_3 [MPa]	σ_c [Mpa]	E_{t50} [Gpa]
Iu-N/t1	B3	0.43	0.4	8.25	0.36
Iu-N/t2		0.43	0.8	10.01	0.74

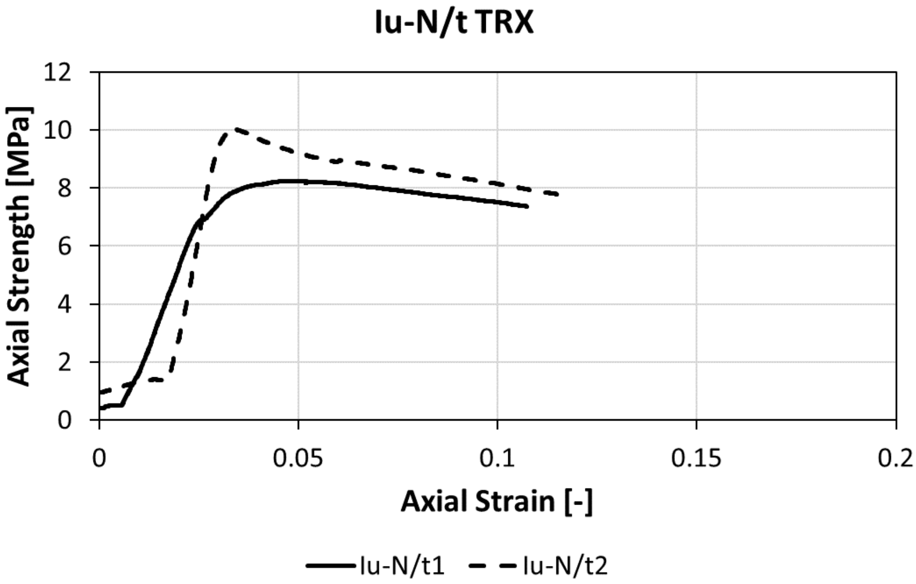

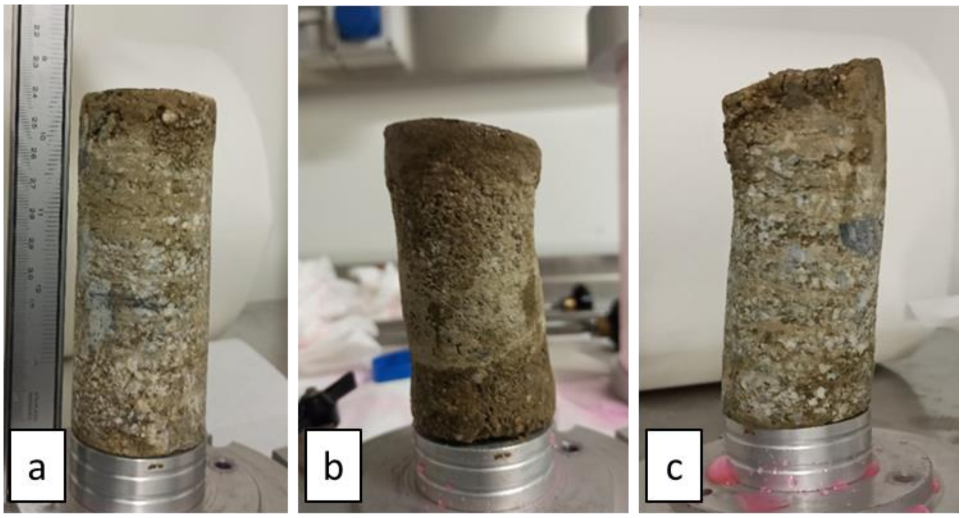

Figure 4.19: Triaxial compressive test results of undisturbed Iu-N soil sample at -10 °C. a) pre- and; b-c) post-failure.

The results of thermal conductivity measurements performed with the needle probe method directly on undisturbed blocks are shown in Table 4.9.

Table 4.9: Thermal conductivity value of frozen blocks A1, B1, B2 and B3 at unfrozen and frozen state.

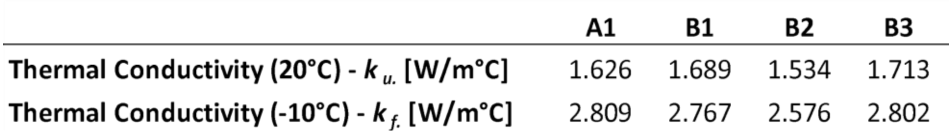

	A1	**B1**	**B2**	**B3**
Thermal Conductivity (20°C) - $k_{u.}$ [W/m°C]	1.626	1.689	1.534	1.713
Thermal Conductivity (-10°C) - $k_{f.}$ [W/m°C]	2.809	2.767	2.576	2.802

4.3 Discussion

The chain of operations carried out starting at the construction site and concluding at Eurolcold Lab made it possible to create a workflow that led to interesting results and considerations.

The PLT proved to be quick tests to be carried out on-site, using which it was possible, with the help of the infrared imaging camera, to determine an average value of the $I_{s(50)}$ relating exclusively to the frozen soil mass, excluding the rocky portion.

The infrared imaging camera was also used to assess the condition of the frozen soil shell around the excavation of the tunnel. The processing with FLIR ResearchIR made it possible to extrapolate information within the areas of interest.

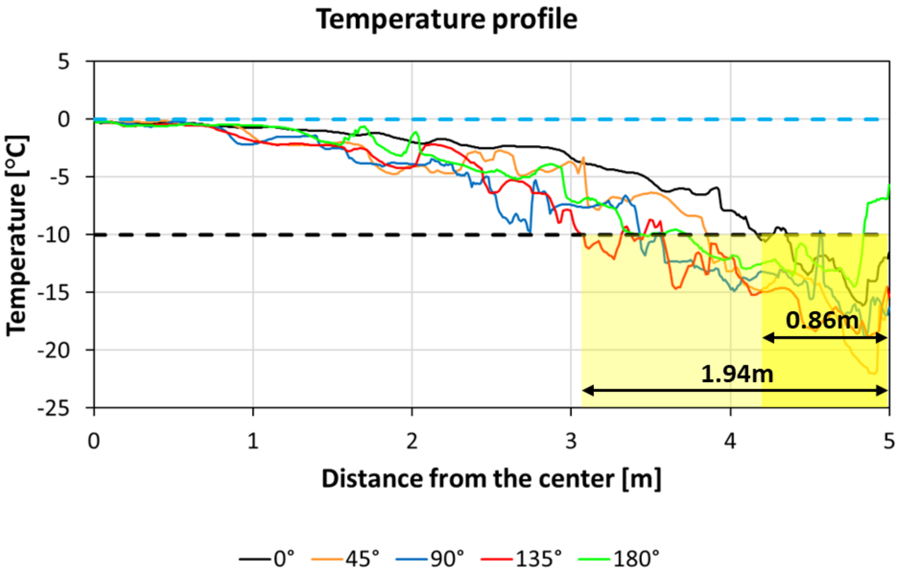

Figure 4.27: Temperature profiles extracted from IRT image of excavation surface during the excavation phase. Max and min thickness of the frozen wall inside the excavation profile are estimated.

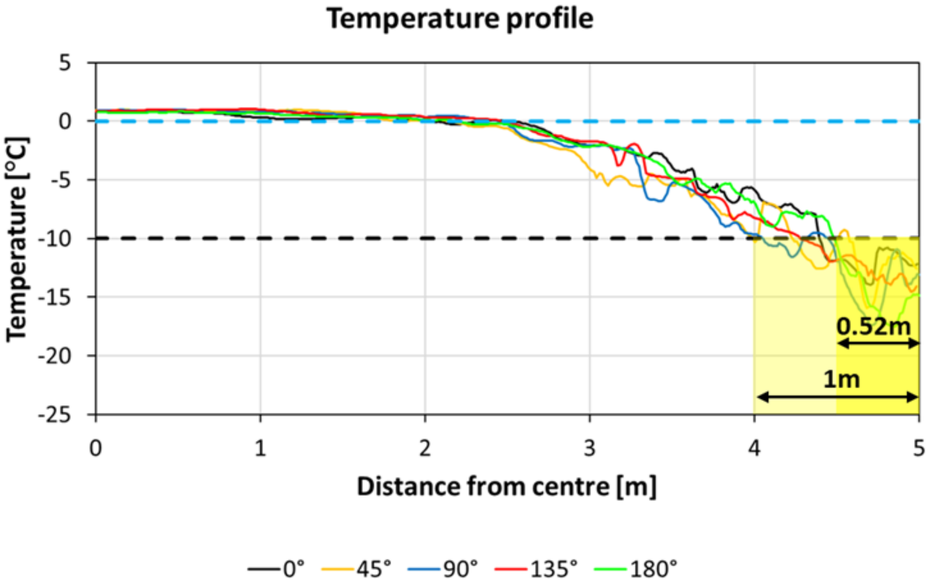

Figure 4.28: Temperature profiles extracted from IRT image of the excavation surface at the end of the excavation phase. Max and min thickness of the frozen wall inside the excavation profile are estimated.

From the images considered, it was possible to extrapolate the temperature distribution along five radial profiles. A comparison between the graphs of the excavation face during excavation (see Figure 4.27) and the excavation face completely excavated and waiting for the shotcrete (see Figure 4.28) shows how it changes from a completely frozen mass to a mass that has a central core with a radius of approximately 2-2.5 m with T slightly above 0°C.

This indicates that the time between the beginning of the excavation and the end of the excavation causes a significant increase in the external temperature of the face, as the temperature trend at depth was not investigated. The wall thickness at T<-10 °C is also affected by the period it is exposed to air, in fact, it decreases from a thickness varying between 0.86 and 1.94m to a thickness varying between 0.52 and 1m.

These thicknesses actually correspond to the portion of frozen soil placed inside the excavation profile. To this thickness must be added the wall thickness given by the distance between the axis of the freezer pipes and the excavation profile (~0.5m) and the portion of frozen ground formed outside the line of the freezer probes. The propagation of the frozen wall beyond the pipes is measured by the thermometric probes set according to a predefined scheme, while internally thermometric probes are rarely placed, as they would make excavation tricky. The acquisition of the temperatures inside the excavation, therefore, not only represents a system for monitoring temperatures during excavation and provides support for aspects related to safety, but also provides a lot of useful data for the validation of the numerical model of the intervention, if one has been developed.

The CT scan proved to be an essential analysis, otherwise the definition of the specific weights of the blocks, which are so heterogeneous, would have been difficult, and the coring would have returned a large number of specimens consisting of rock only and therefore not representative of the frozen soil mass. In fact, the resolution of the machinery used, chosen for the size of the sample analysed, did not allow the internal structure of the soil to be studied in detail as was done by Torrance et al. (2008) and Kang et al. (2016), who therefore limited it to a more general observation.

It revealed that the specific weight of the blocks is highly variable, showing a porosity ranging from 0.14 to 0.50 and a degree of saturation from 0.37 to 0.89. This can be explained by the presence of centimetric and decimetric pebbles within the mass that vary the specific weight of the block, which are not large enough to mitigate this scaling effect. The undisturbed specimens, on the other hand, cored in the blocks that contained fewer pebbles showed porosity and saturation values (see Table C4 and C6) congruent with those of the blocks from which they were extracted, and were, therefore, more representative.

The uniqueness of the collected samples, given the short-term nature of the AGF intervention in the Isarco River underpass and the impossibility of direct access to the construction site to take further samples, did not allow a complete set of tests with different temperature and strain rate conditions to be carried out. However, the values obtained from unconfined compression tests on undisturbed specimens showed, as illustrated by Haynes and Karalius (1977) and Bragg and Andersland (1981), that increasing temperatures lead to a reduction in the mechanical strength of frozen soil. The results in fact, if only the average values of the tests performed at a strain rate of 1%/min are compared, show that it goes from 8.38 to 6.69 MPa, at -10 and -6°C respectively.

From the results of the unconfined compression and triaxial compressive tests at -10°C on undisturbed material, it was possible, using RocLab1.0, to calculate the friction angle and cohesion values relative to the Mohr-Coulomb failure criterion, which for moderate confinements (see Lai et al, 2010 and Yang et al. 2010) can be applied to describe the failure of frozen ground. It turns out that the friction angle is 19.87° and the cohesion is 2.89 MPa.

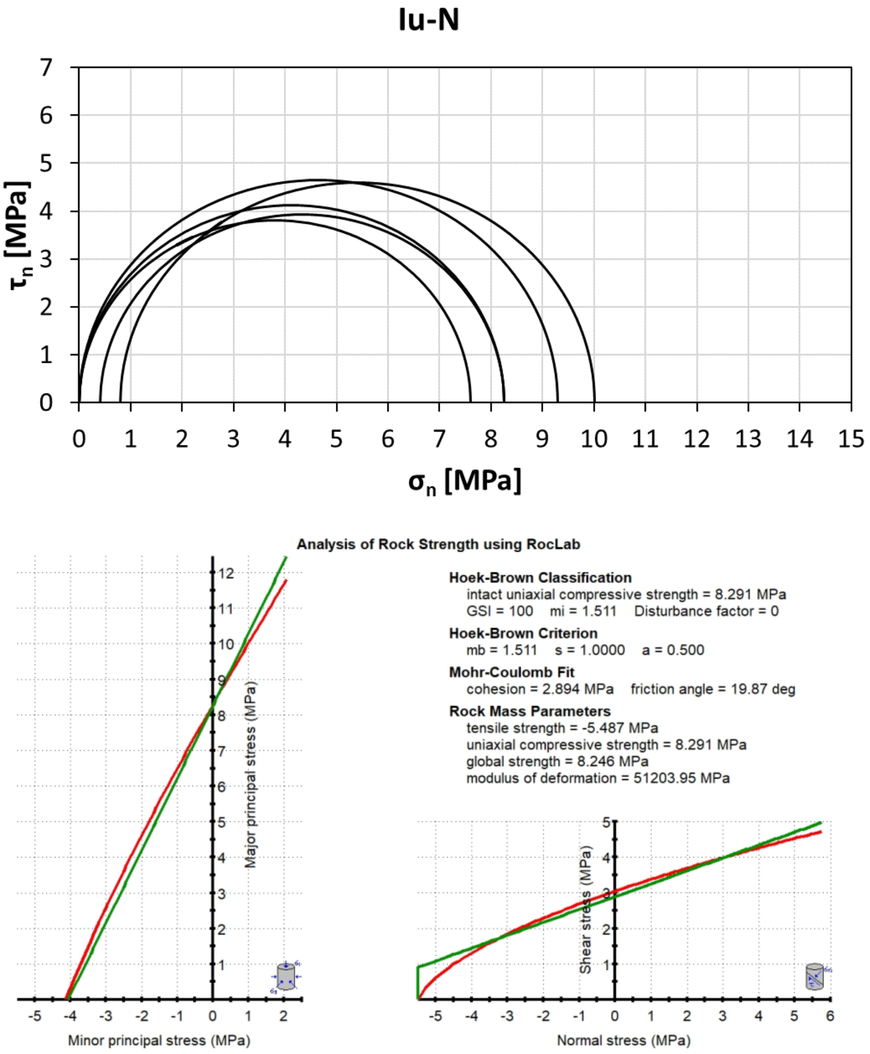

```
Analysis of Rock Strength using RocLab

Hoek-Brown Classification
    intact uniaxial compressive strength = 8.291 MPa
    GSI = 100    mi = 1.511    Disturbance factor = 0
Hoek-Brown Criterion
    mb = 1.511    s = 1.0000    a = 0.500
Mohr-Coulomb Fit
    cohesion = 2.894 MPa    friction angle = 19.87 deg
Rock Mass Parameters
    tensile strength = -5.487 MPa
    uniaxial compressive strength = 8.291 MPa
    global strength = 8.246 MPa
    modulus of deformation = 51203.95 MPa
```

Figure 4.29: Mohr circles and Mohr-Coulomb failure criteria developed by RocLab1.0 of Iu-N frozen soil sample at -10 °C.

From the mechanical tests on undisturbed soils, comparisons were performed with the results obtained in *Chapter 2* on reconstructed laboratory specimens from the same site.
To perform a comparison on UCS tests, only tests performed at a strain rate of 1%/min on soils of Iu-N and I2-N, having more similar porosity, were considered (see Table 4.10). From this comparison, it can be observed that the increase in temperature causes a reduction in strength in both cases and that overall, the undisturbed soil values are higher.

Table 4.10: UCS values of I2-N and Iu-N samples at different temperatures (-10 and -6 °C) shown in Chapter 2 and Chapter 4, respectively.

	Chapter 2	*Chapter 4*
Temperature [°C]	**I2-N**/Disturbed	**Iu-N**/Undisturbed
-10	6.26 MPa	8.38 MPa
-6	5.35 MPa	6.69 MPa

The specimens of undisturbed material subjected to unconfined compression tests at -6°C were melted and dried in an oven and a particle size analysis (ASTM D422-63) was carried out on the constituent material and the results are shown in Figure C6. The particle size curves, when compared with those in Figures 2.1a-b, show a more homogeneous soil with a D_{max}= 25mm and a D fraction of D<0.150mm still less than 5%. A coarser soil may therefore have resulted in a higher mechanical strength.

From the UCS and PLT performed on the undisturbed material taken from the excavated and cored face, it is possible to calculate the correlation factor C that relates σ_c to $I_{s(50)}$ (see *Paragraph 2.4.1)* obtaining 7.42 and 9.19 at -10 and -6°C respectively (Table 4.11).

Table 4.11: "C" factor calculated for undisturbed samples at -10 and -6°C.

Soil specimen	**Temperature** [°C]	**mean $I_{s(50)}$** [MPa]	**mean σ_c** [MPa]	**C** factor
Iu-N/p	-10	1.13	8.38	7.42
Iu-N/p-h	-6	0.73	6.71	9.19

Combining the results obtained on soil specimens reconstituted in the laboratory with those obtained on cored soil specimens shows that regardless of the temperature and the nature of the sample (particle size, porosity) if an average value of factor C is calculated for the two temperatures considered, the results are 7.98 and 7.97, while if an average value is obtained based on the degree of disturbance of the sample, the values are 7.75 and 8.30 (see Table 4.12). It can therefore be stated that the value of factor C that links σ_c and $I_{s(50)}$ is 8.

Table 4.12: "C" mean values calculated from previous tests at -10 and -6°C for both reconstituted and undisturbed frozen specimens.

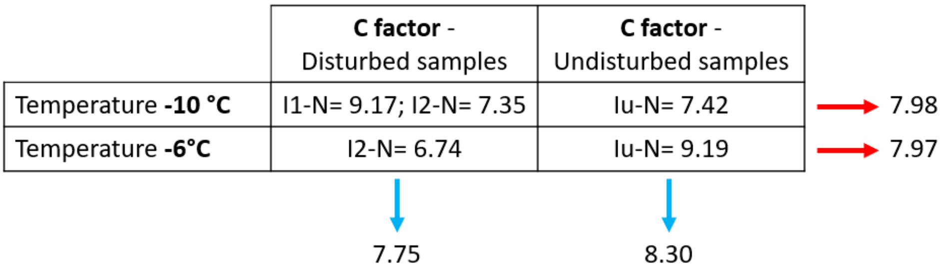

	C factor - Disturbed samples	**C factor** - Undisturbed samples	
Temperature **-10 °C**	I1-N= 9.17; I2-N= 7.35	Iu-N= 7.42	→ 7.98
Temperature **-6°C**	I2-N= 6.74	Iu-N= 9.19	→ 7.97
	↓ 7.75	↓ 8.30	

According to these estimations, it is possible to calculate the strength values of the frozen soil mass existing around the excavation site of the Isarco underpass from the PLT data collected on-site. This calculation shows that the average σ_c value of the soil could be 9.26 MPa with a standard deviation of 3.39 MPa. This wide range of possible values is caused by uncontrolled and measured temperature variability of the blocks subjected to PLT on site. This leads to such a wide spectrum of mechanical strength values. However, these values are all greater than 5 MPa, which was the UCS threshold value set by the designers at the project design stage.

Thermal conductivity measurements at -10°C and 20°C were performed using the needle probe method directly on undisturbed blocks. Comparing the measured values with those estimated using Johansen's method (1975), described in *Section 2.2.3.1*, and based on the physical (Table 4.2) and mineralogical (Table 2.2) characteristics of the Isarco soil, it emerges that in contrast to the tests illustrated in *Section 2.4.2.1*, the results do not agree. The values obtained using needle probes are always lower, both in the frozen and unfrozen states than those estimated (see Figure 4.30). This could be explained by two main factors: the first is the disturbance caused by drilling around the borehole, which may not guarantee perfect thermal contact between soil and needle probe (e.g., not perfectly cylindrical borehole, detachment of soil on the borehole walls); the secondo is that the estimation of thermal conductivity values is based on physical parameters of the entire block (including pebbles) but concretely a portion consisting mainly of finer material is investigated through needle probe method.

This suggests that for material containing pebbles, the Thermtest Portable TLS-100 is not a suitable tool for performing representative thermal conductivity measurements of the inner frozen mass. Anyway, the values obtained by this method, which are lower than those estimated can be considered for performing thermal analysis in favor of safety.

Figure 4.30: Comparison between measured and estimated thermal conductivity value at the unfrozen and frozen state of investigated frozen soil blocks.

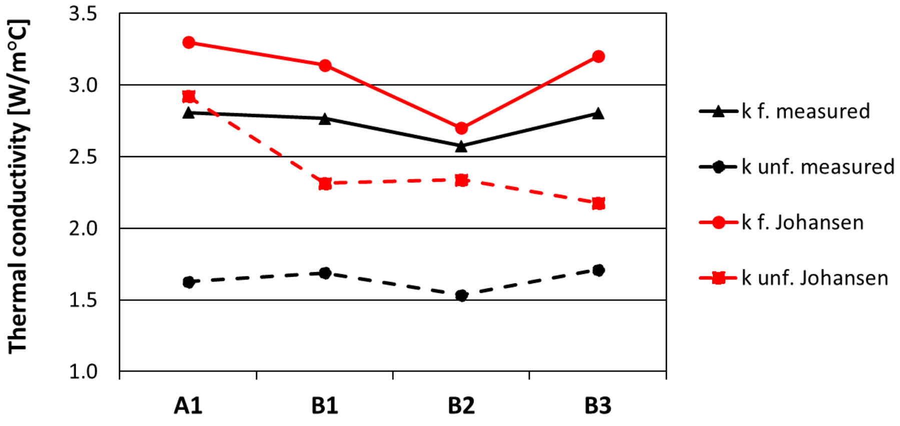

Chapter 5

5 Liquid Nitrogen Freezing Pipe

The time spent at the construction sites also helped to personally see the operation of a liquid nitrogen-fed and brine-fed freezing system and understand its operating mechanisms. This, coupled with the need for increasingly high-performance numerical models capable of representing physical phenomena that could numerically simulate the freezing induced by a liquid nitrogen-fed freezing pipe as described in Section 1.2.2, inspired the creation in the laboratory of a freezing pipe capable of reproducing a variety of operating conditions and returning useful data for the development of a numerical or analytical model and to identify any new criteria for supplying coolant to the system. Conducting a laboratory experiment of this kind of process has already been carried out for different purposes and with more or less complex methods. Mainly the aim of the work done by many authors was to induce freezing around one or more brine- or nitrogen-fed freezing pipes of a known volume of soil and to collect data, exclusively of temperature, within the domain, useful for the validation of numerical or analytical models. Gioda et al (1992) and Gioda et al. (1994) for example made a steel LN_2-fed freezing pipe inside a cylinder with D= 1m and H= 1m, and induced freezing and recorded the temperature trend at different distances from the pipe, which were used for model validation; Pimentel et al. (2012), on the other hand, investigated the effect of multiple brine-fed probes within a volume of soil in which seepage flow was present and made comparisons with a closed-form analytucal solution. Seepagflow conditions were also considered by Marwan et al. (2016) who based on a coupled thermomechanical model and algorithm (ANO - Ant Colony Optimization) identified a method to find the optimal position of the freezing pipes considering the seepage flow. The possibility of conducting these experiments at the laboratory scale allows many tests to be performed by varying certain parameters such as material making up the pipes (see Cai et al. 2020), the outer diameters of the pipes, different type of coolant (see Evirgen and Tuncan, 2019), and the arrangement of pipes in series, which are thus differentiated into individual and sequential (see Evirgen 2021). Some authors have also tried to improve the freezing pipes by changing the pattern of nitrogen flow inside them, as done by Cai et al., (2020) or Hu et al., (2018), or by trying to exploit only a part of it, insulating the portions of the pipe not needed for freezing (see Zueter et al., 2020), and developing the associated mathematical modeling. Kim et al. (2018), to evaluate the use of freezing as a method of sampling undisturbed soils to perform liquefaction tests, moved from laboratory to field trials by scaling the problem and using 2D electrical resistivity thomography at this point to evaluate the creation of a frozen soil body.

In the studies just mentioned much attention has been paid to the measurement of the temperature inside the volume of soil; the same is not true for the external and internal temperature of the pipe, which has never been studied in depth. In addition, the laboratory experiments carried out so far are exclusively done on vertical pipes; in reality, however, the AGF is mainly used to support tunnel excavation for which the pipes are placed sub-horizontal. This discrepancy can be explained by considering two aspects: first from a practical point of view, moving and rotating a volume (and mass) of soil between 0.5 and 1m^3 (volume usually considered) is very difficult within a laboratory with standard equipment, considering also that the assembling and filling of soil would be done in any case in the vertical position; secondly, in the vertical position the distribution of coolant in the probe, especially LN, would follow an axisymmetric behavior with respect to the axis of symmetry of the probe, and consequently also in the surrounding soil domain and this would provide more easily interpretable conditions.

5.1 Material and Methods

Starting from the freezing pipe developed by many authors, and in particular by Cai et al., (2020), and from what was observed on Isarco and Milano building sites, a new liquid nitrogen-fed freezing pipe was designed for experimental use and built by GTS Riva Srl (see Figure 5.1).

This Liquid nitrogen freezing pipe (LNFP) consisted of two coaxial stainless steel tubes, which formed the outer and inner parts of the pipe. The outer one was formed by an L= 1800mm long pipe closed at one end with external diameter D of 50mm and thickness S of 2mm. At the other side, the pipe was welded to a larger portion of the pipe (D= 76mm, S= 2mm) in the shape of a "T" so that the portion on axis with the pipe was 200mm long and the portion placed transversely measured 200mm. A DN50 perforated flange was placed at the end of the on-axis section. Another plugged DN50 flange was placed on this flange, with a special Swagelock through-hole with double teflon ogive. This special component allowed the inner pipe, steel made with D= 16mm, S=2mm, L= 2000mm, to be inserted inside the outer pipe so that there was a 100mm gap between the end of the inner one and the bottom of the outer pipe. The inner tube has been equipped with centering devices so that it remains on axis with outer tube. The teflon double ogive passer allows the grip on the inner tube to be tightened and loosened, allowing, without having gas leaks, the inner probe to be positioned at the desired depth. The top apex of the inner tube was connected to an annealed copper tube, which in turn was connected to a 250 lt LN_2 pressurized tank. This tank was hung from a load cell so as to measure LN consumption, by continuously recording the weight change of the tank. The pipe was fed as commonly done during on-site activities, i.e., nitrogen was flowed inside the inner tube and ascended, in gaseous form, into the gap between the inner and outer tubes. Once it became a gas, the nitrogen expands 650 times and rises back up inside the "T" and here it was taken through an insulated aluminum pipe inside a ventilation chimney to be vented away. To prevent excessive cooling inside the chimney a second tube, connected to a heat gun, was brought inside and placed below the first so that the hot air, as it rose, would mix with the gas leaving the probe, heating it.

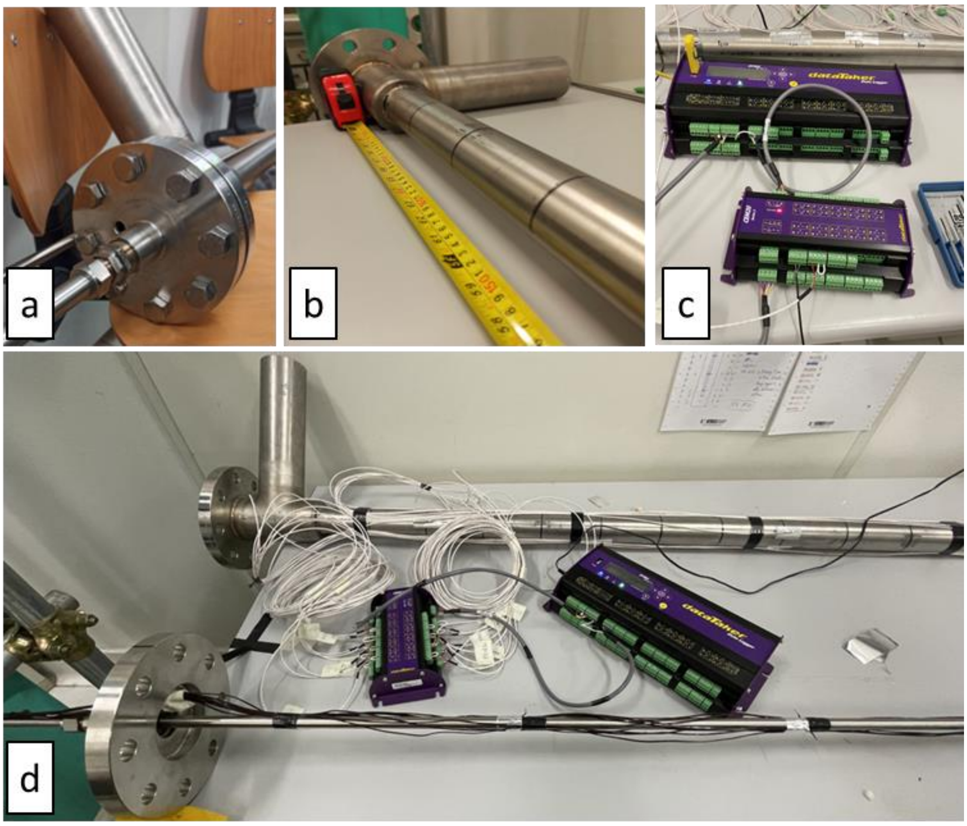

Figure 5.1: LN_2 freezing pipe general view: a) flanges system on the upper part of pipe; b) outer tube with marked acquisition levels; c) datalogger DataTaker-DT85; d) inner (bottom) and outer (top) tube equipped with T-type thermocouples and thermistor, respectively.

27 temperature sensors were placed on the probe: 17 cryogenic PT100 resistance temperature detector (RTD) were placed on the outer wall of the probe at different acquisition levels and along 3 planes positioned at 90° to each other (see Figure 5.2a); 9 thermocouples were placed along the inner pipe so that the hot junction would measure the temperature inside the gap between the outer and inner tube (see Figure 5.2b). The wires were routed through a hole drilled on the top closed flange. In this case for each acquisition level The sensors were placed in two directions 180° from each other and connected to the DataTaker DT85 plus CEM20 modulus

datalogger. An additional thermocouple was placed on the exhaust gas outlet.

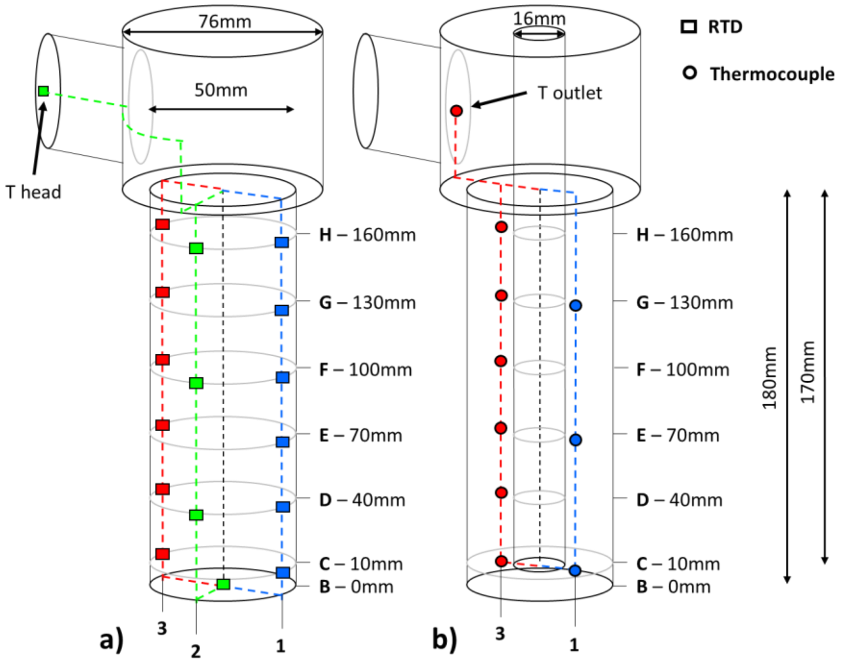

Figure 5.2: Layout of thermal sensors disposition on FP along three investigated planes: a) on the external surface of the outer tube; b) into the gal between the outer and inner tubes.On the side of the gas outlet pipe (red plane and sensors); on the opposite plane (blue plane and sensors); in the middle beween the previous ones (green plane and sensors).

The pipe was placed by means of platic centering devices inside a polyvinyl chloride (PVC) green tube with internal D of 270mm and H of 2000mm closed at the bottom so that just the part of LNFP with D= 50mm was embedded in the soil. From the PVC wall, a layer of soft insulating neoprene such as to accommodate radial deformations induced by freezing of water, and a layer of Tenax drainage filter were placed internally to allow saturation of the soil. This filter, placed along the entire height of the volume, ensured an even distribution of the water head, imposed by means of 3 faucets connected to a distilled water tank placed at 2m height. Inside the green pipe, 3 thermometric probes consisting of a PVC pipe with outer *D* of 16mm and *L* 2000mm, equipped internally and externally with T-type thermocouples positioned at the same acquisition levels as the sensors placed on the freezing pipe, were attached at 10 mm from the filter. These probes were fixed vertically along planes at 90° to each other at planes 1, 2 and 3 along which the sensors of the freezing pipe were positioned, as illustred in Figure 5.3.

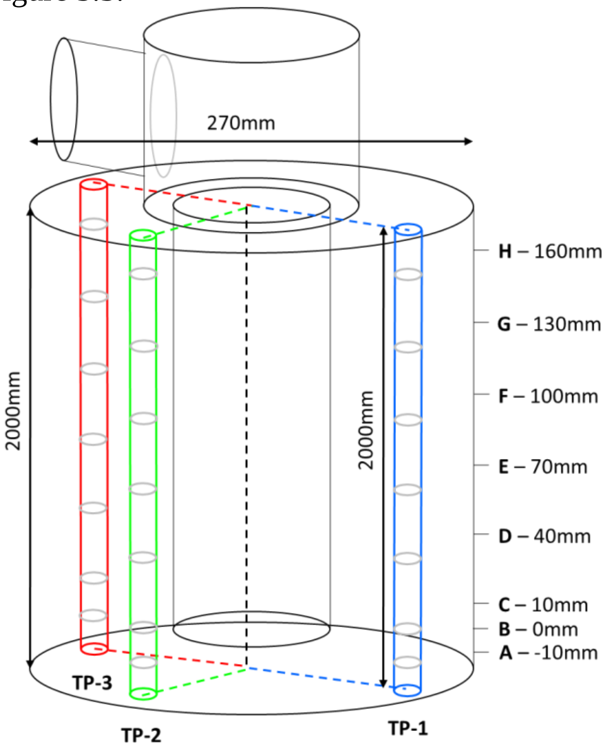

Figure 5.3: Layout of thermometric probes (TP) disposition into the considered volume along three investigated planes: on the side of the gas outlet pipe (red plane and sensors); on the opposite plane (blue plane and sensors); in the middle beween the previous ones (green plane and sensors). Thermocouples was located at all acquisition level for both internal and external to TP.

The volume, at this point with a reduced diameter, was backfilled with Hostun quartz sand (see Figure 5.4). The backfilling was done by imparting continuous blows with a rubber hammer to the outer wall of the volume so that the vibrations would cause the soil compaction as much as possible, not having to reach predetermined relative density values in this case. After the filling was completed, liquid silicone was poured over the soil so as to form a plug that could accommodate the presence of the many thermocouple and RTD cables inside the volume and that was not rigid.

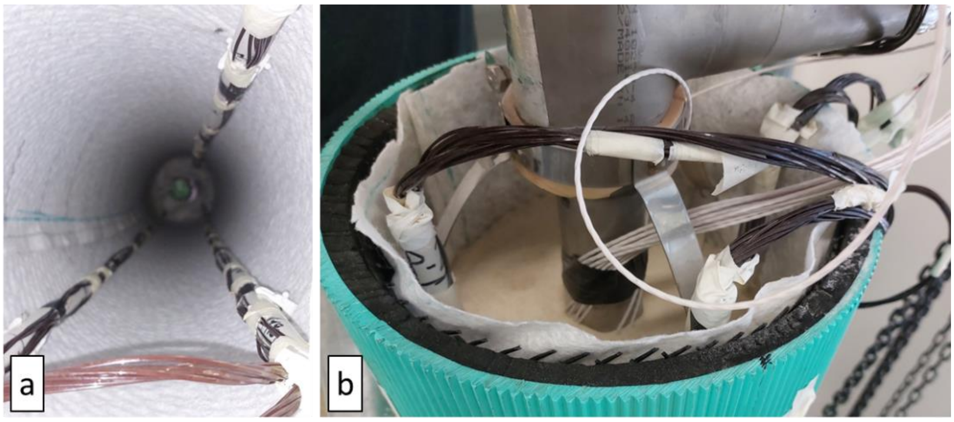

Figure 5.4: External volume filling operations with Hostun dry sand: a) view of the empty volume, thermometric probes, and water drain (white fabric) are visible; b) filling almost completed, all the components are embedded in the sand.

The entire device was assembled and filled inside a steel structure consisting of two main parts: a cage that wraps around the volume of soil and supports it, an "L-shaped" part resting on the ground via 6 legs, which allows the cage to rotate from a vertical to a horizontal position around a pivot. This rotation was done by means of a manual winch along planes 1-3. The probe was positioned inside the structure so that in the horizontal position, part of the sensors were on the bottom of the probe, and part of the sensors were on the top, and the nitrogen gas collection system was positioned at the top, to prevent any liquid nitrogen from flowing through the gas collecting system (Figures 5.5). The supply line and green PVC pipe were covered with an insulating material.

Once the entire System was assembled, a trial testing was done. Then two sets of tests were performed in which different conditions were changed:

- LN$_2$ distribution criteria. Three different liquid nitrogen supply criteria were considered in order to provide an overview of possible scenarios that can be used in real cases: Test 1) constant gas outlet temperatures (used in real AGF interventions); Test 2) complete replenishment and emptying of liquid nitrogen from the freezer probe;

Test 3) maintaining a constant LN_2 level inside the freezer probe. All these tests were done on dry ground with the probe in vertical position.

- External conditions. Once the nitrogen supply criterion was established (i.e., such that there was a constant outlet gas temperature), two tests were made on dry soil, one in the vertical position (Test 4), and one in the horizontal position (Test 5), and a final one with wet soil in the vertical position (Test 6).

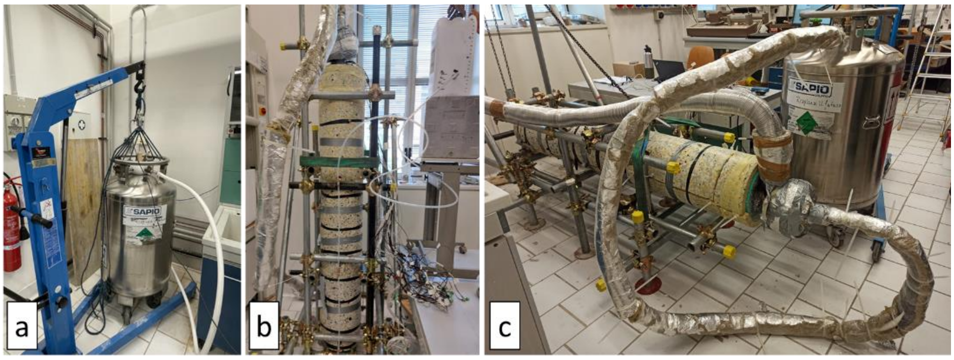

Figure 5.5: Overview of LN_2 freezing pipe test: a) LN_2 tank hanging from load cell; b) vertical test; c) horizontal test.

During all stages of assembly and testing all necessary PPE was worn, especially an oxygen meter that measured the oxygen level in the laboratory during all tests performed.

5.2 Results

The tests performed with the LNFP were successful and provided much data to compare the effect of LN supply or external conditions considered. Overall, the RTDs placed on the external surface of the freezing pipe efficiently recorded temperature down to -196°C responding instantaneously to the cryogenic inputs given by the liquid nitrogen. Similarly, the thermocouples inside the probe made it possible to monitor the level of liquid nitrogen inside the pipe. The transition to the gaseous state was signaled by a marked change in temperature that increased from the -196°C measured by the internal sensors. The silicone stopper made to plug the hole in the flange through which the thermocouple wires passed ensured a seal. This is probably also due to the very low rise pressure of the nitrogen gas. Figure 5.6 shows the valid legend for the graphs obtained for tests 1, 2, 3, 4, 5 and 6 shown in Figures 5.7, 5.8, 5.9, 5.10, 5.11 and 5.12, respectively.

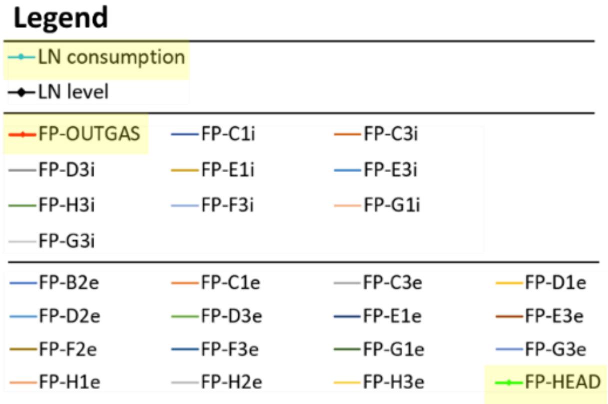

Figure 5.6: Legend of time series of the reported graphs on Figure from 5.7 to 5.12

Test 1: freezing pipe in vertical position with dry sand and costant outlet gasseous nitrogen temperature. Stop at 23lt of LN$_2$ consumption.

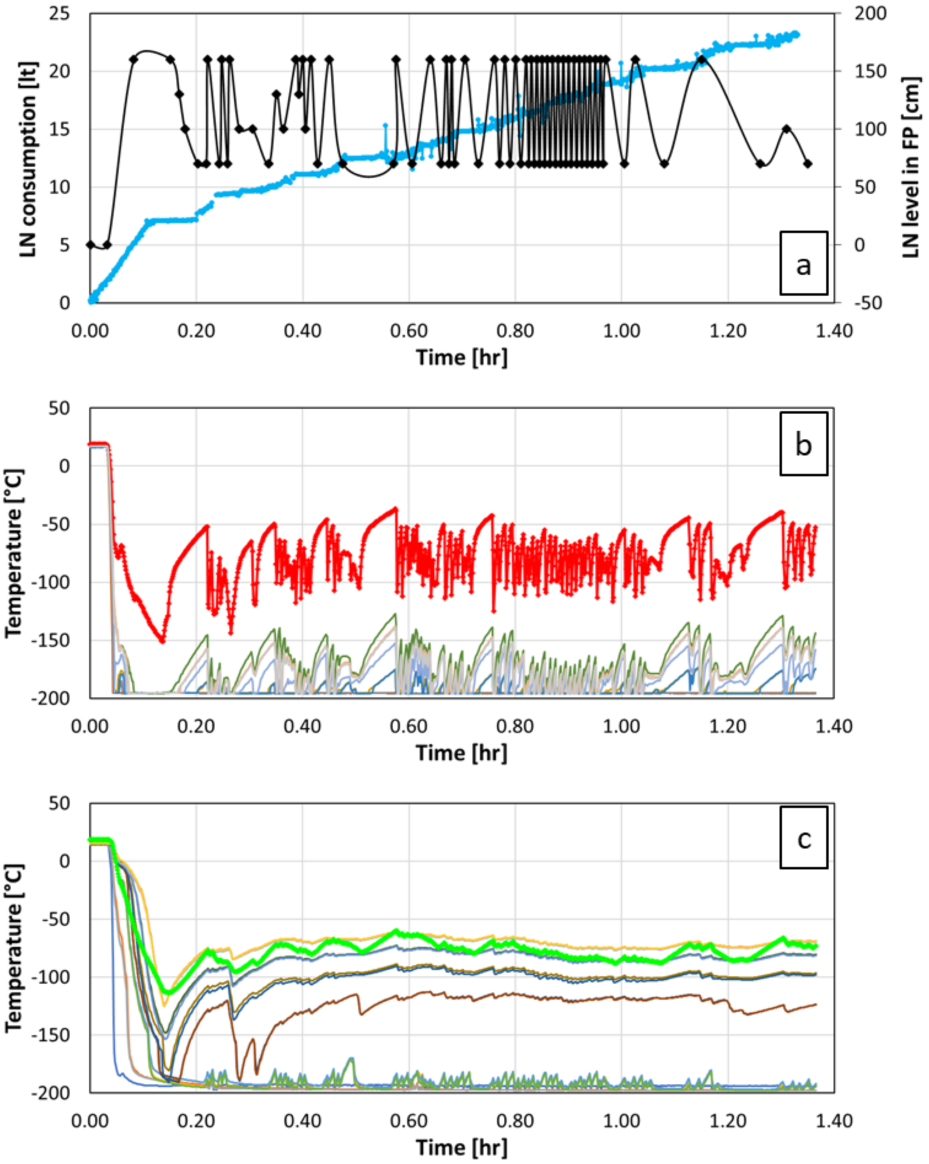

Figure 5.7: Data obtained from Test 1: a) Liquid nitrogen consumption and level inside the freezing pipe; b) measured temperatures in the gap between the inner and outer tube at different acquisition levels; c) measured temperature on the external face of the freezing pipe at different acquisition levels.

Test 2: freezing pipe in vertical position with dry sand and total refill of LN_2 for 3 cycles. Stop at 23lt of LN_2 consumption.

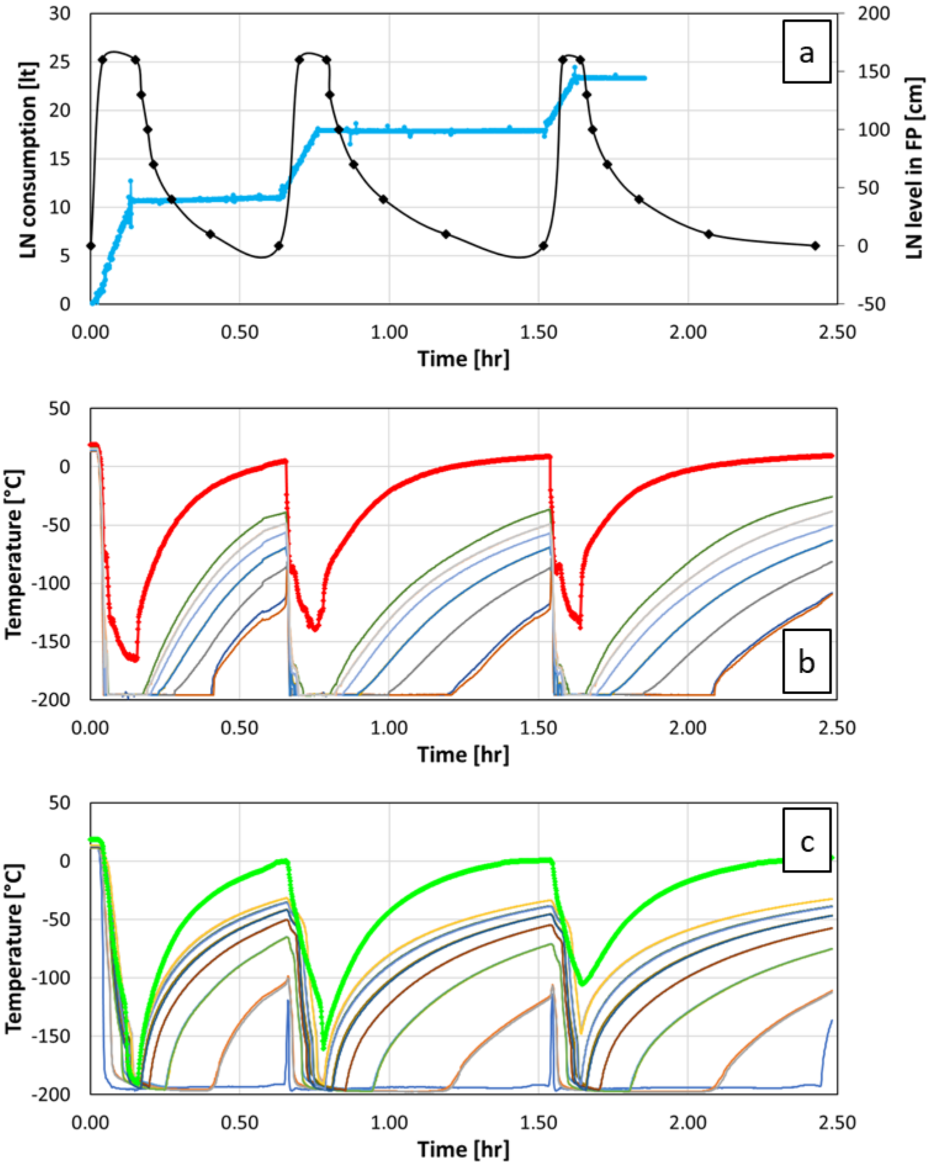

Figure 5.8: Data obtained from Test 2: a) Liquid nitrogen consumption and level inside the freezing pipe; b) measured temperatures in the gap between the inner and outer tube at different acquisition levels; c) measured temperature on the external face of the freezing pipe at different acquisition levels.

Test 3: freezing pipe in vertical position with dry sand and a costant LN_2 level into the FP (level D=40cm). Stop at 19lt of LN_2 consumption.

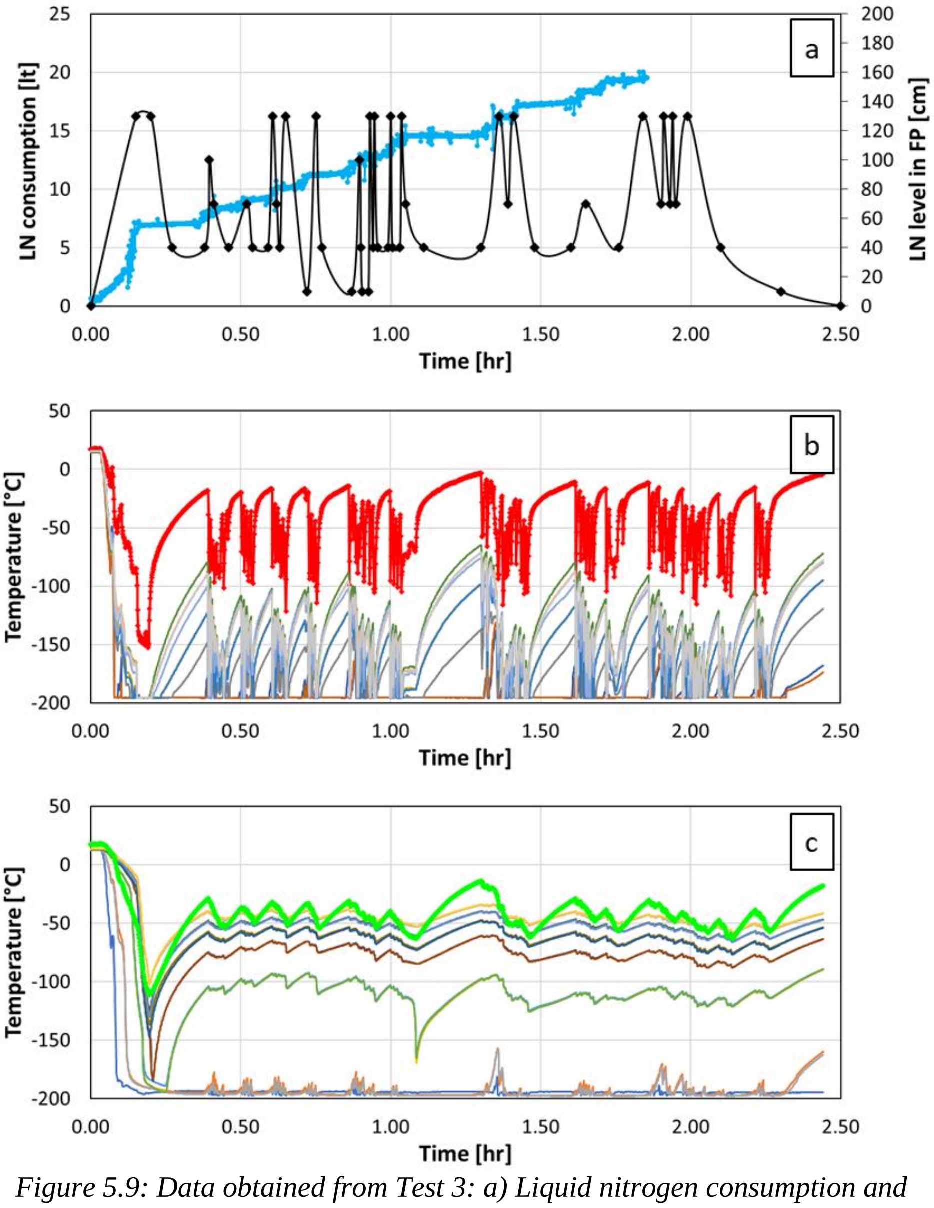

Figure 5.9: Data obtained from Test 3: a) Liquid nitrogen consumption and level inside the freezing pipe; b) measured temperatures in the gap between the inner and outer tube at different acquisition levels; c) measured temperature on the external face of the freezing pipe at different acquisition levels.

Test 4: freezing pipe in vertical position with dry sand and a costant outlet gasseous nitrogen temperature. Stop at 16lt of LN_2 consumption.

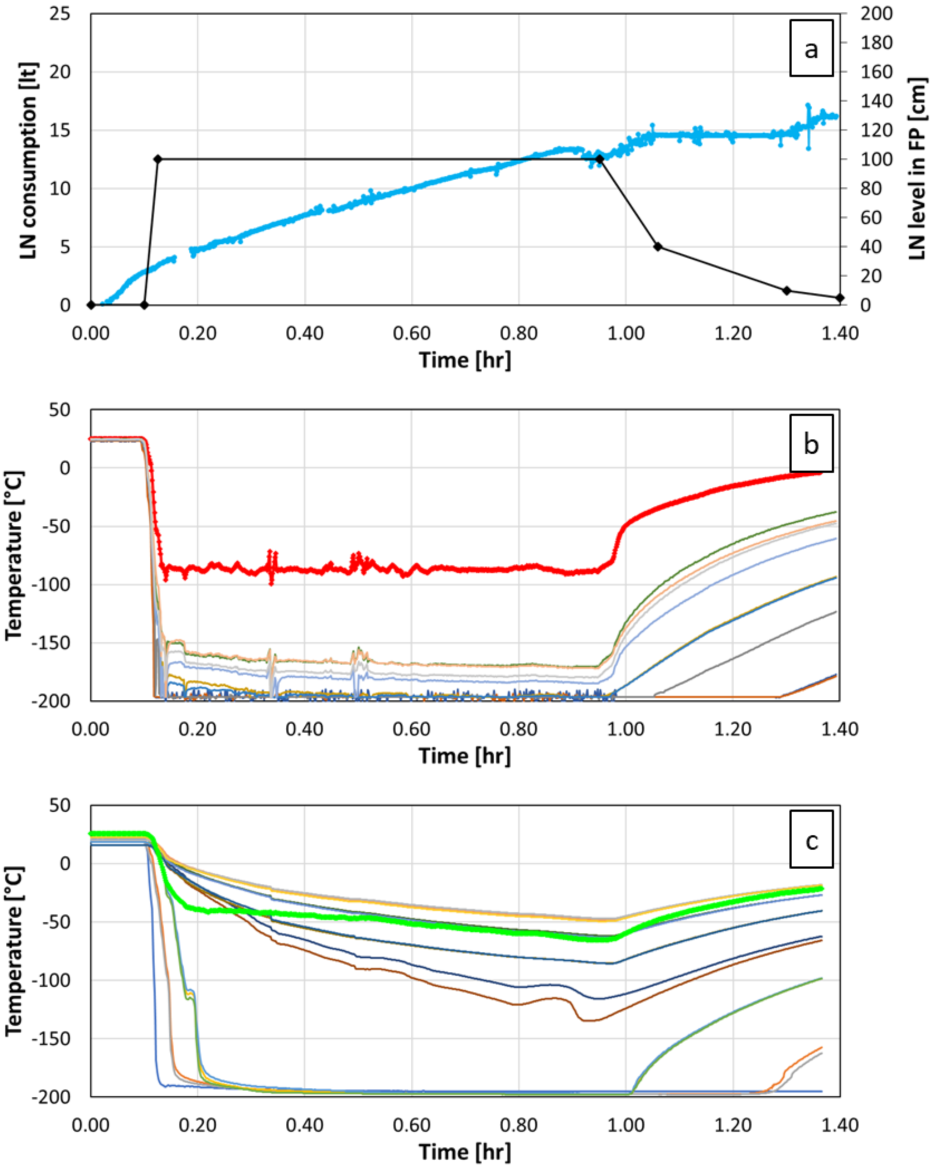

Figure 5.10: Data obtained from Test 4: a) Liquid nitrogen consumption and level inside the freezing pipe; b) measured temperatures in the gap between the inner and outer tube at different acquisition levels; c) measured temperature on the external face of the freezing pipe at different acquisition levels.

Test 5: freezing pipe in horizontal position with dry sand and a costant outlet gasseous nitrogen temperature. Stop at 13lt of LN_2 consumption.

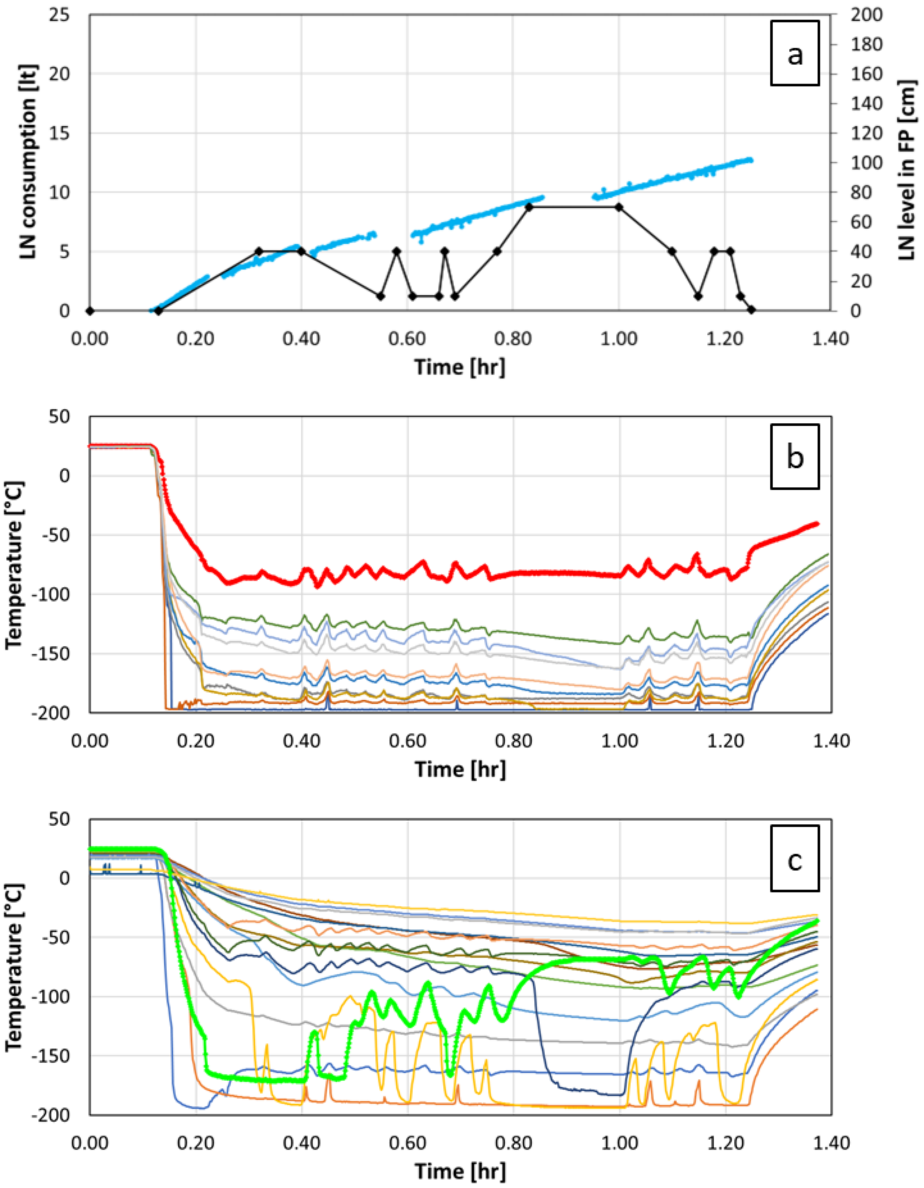

Figure 5.11: Data obtained from Test 5: a) Liquid nitrogen consumption and level inside the freezing pipe; b) measured temperatures in the gap between the inner and outer tube at different acquisition levels; c) measured temperature on the external face of the freezing pipe at different acquisition levels.

Test 6: freezing pipe in vertical position with wet sand and a costant outlet gasseous nitrogen temperature. Stop at 13lt of LN_2 consumption.

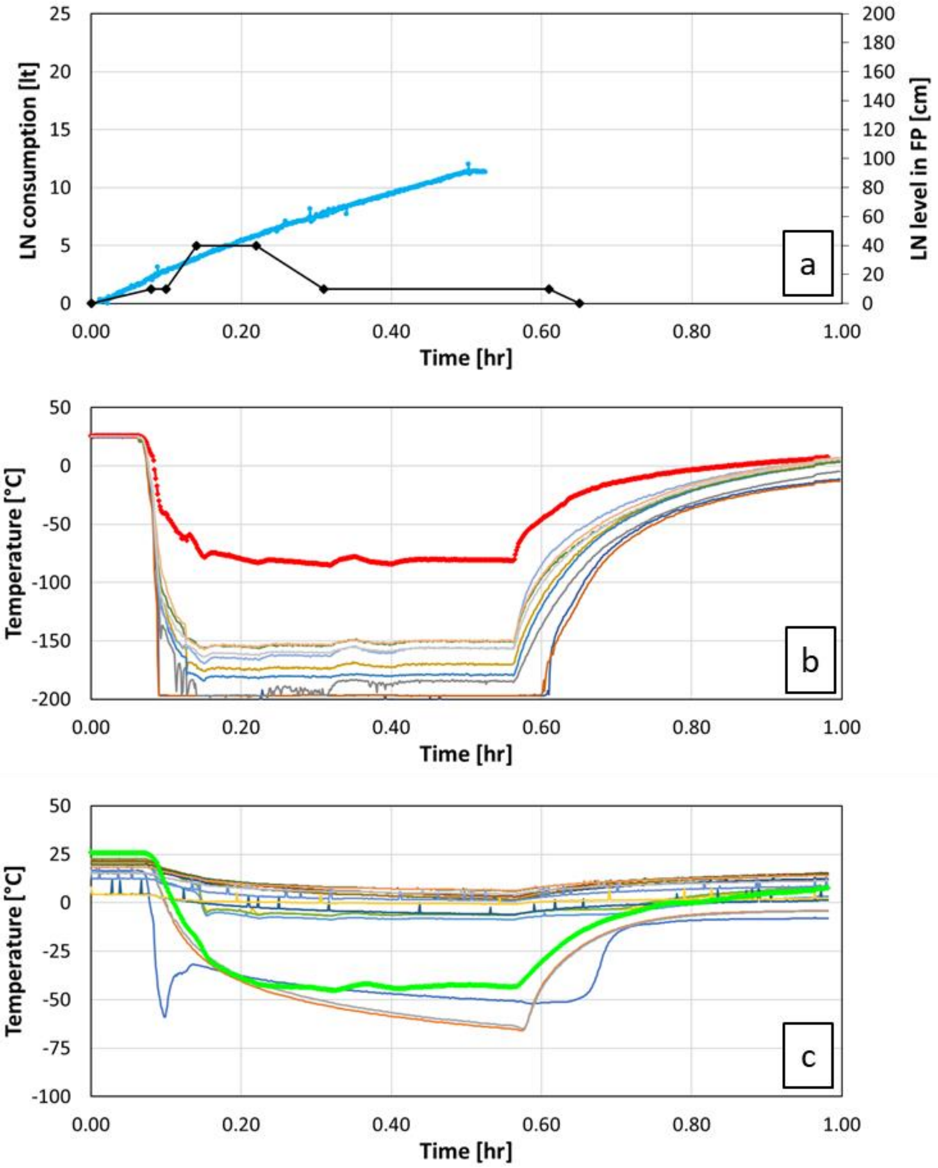

Figure 5.12: Figure 4.26: Data obtained from Test 5: a) Liquid nitrogen consumption and level inside the freezing pipe; b) measured temperatures in the gap between the inner and outer tube at different acquisition levels; c) measured temperature on the external face of the freezing pipe at different acquisition levels.

5.3 Discussion

The manufactured device proved to work well under different conditions providing for each type of test performed many useful data to understand the processes that occur during the circulation of a LN_2 flow inside a freezing piepe. The implementation of several preventive procedures made it possible to work under safe conditions. Both the supply and exhaust gas collection systems proved to be efficient and never leaked. The structural skeleton built around the volume of soil together with the tilting system allowed the position of the probe to be changed several times (from vertical to horizontal, and vice versa) with simple operations. The monitoring system, consisting of the temperature sensors, load cell and datalogger, was able to precisely monitor the ongoing processes of nitrogen consumption and cooling within the domain.

In Tests 1, 2, and 3 in which the total LN_2 consumption of each test was 23lt, very different temperature curves were obtained. While in test 2, the temperature sensors, internal and external show nonscattered curves, given by net opening and closing phases of LN_2 supply, in tests 1 and 3, in which the outlet temperature was kept stable at -75°C and the level of liquid nitrogen in the LNFP, respectively, the sensors, especially the internal ones report very scattered curve. This makes the data difficult to interpretation (see LN level in Figures 5.7 and 5.9). After several investigations, this behavior was attributed to imperfect insulation of the supply system. Indeed, it was observed that the insulating coating of the copper tubing used to connect the tank with the freezing pipe was not thick enough, and that at some points in the line the metal components were not insulated. This with any certainty caused evaporation of the nitrogen at some points in the line, thus creating bubbles that expanding caused a kind of boiling of the liquid nitrogen at the bottom of the LNFP, causing a mixed turbulent flow of liquid and gas that resulted in continuous abrupt temperature changes inside and also secondarily outside the pipe. In each case, the temperatures measured in the internal and external sensors have almost identical behaviors for same level of acquisition, clearly indicating that the problem could be reduced to an axisymmetric 2D.

Next, for the execution of tests 4 and 5, insulation with 6cm-thick rock wool was installed to cover the entire line; in addition, the flanges and the entire part of the LNFP exposed to air were also insulated with thick layers of insulation. In this way, as is evident from Figures 5.12b-c the temperatures measured inside and outside the probe were less scattered than in the previous tests. This allowed the desired test conditions to be obtained, i.e., a constant gas outlet T equal to -75 °C in both vertical and horizontal conditions. Comparison of the data obtained from these tests is crucial to understanding the substantial difference in thermal behavior in a freezing pipe at different positions and the quality of data that can be extracted with this device for numerical model development.

Referring to the arrangement of temperature sensors in the LNFP illustrated in Figure 5.2, it can be seen that in test 4 gravity pushes liquid nitrogen to the bottom of the pipe so that the coldest points are at the C level, both internally and externally, while temperatures become gradually higher going upward and away from the liquid nitrogen level. Internally, colder temperatures are always measured than externally, and in both situations the values along planes 1 2 and 3 are almost equal (i.e., E1-i and E3-i are almost overlapping, likewise are G1-e and G2-e as shown in Figures 5.13a-b). Considering also the few measurement points along plane 2 it appears that it also gives values equal to those in planes 1 and 3, considering the same level of acquisition (see Figures 5.13c). A very different situation, as might be expected, is observed when the LNFP is used in a horizontal position. Again, gravity pushes the liquid nitrogen downward and this results in an arrangement of the coolant along the lower side of the horizontal pipe and the formation of nitrogen gas on the upper portion. This was verified by test 5, in which the internal thermal sensor C3-i (in the horizontal position, radial plane 3 is upward) measures liquid coolant for only a very short time at the beginning of the test (see Figure 5.14a). Throughout the test the internal sensors along this plane always measured temperatures relative to the gaseous state, while the sensors along plane 1 (radial plane downward) measured at different times arrival of LN2 (C1-i always , E1-i between 0.85 and 1 hr). Then looking at the external sensors placed in the same acquisition levels this behavior is even more evident (see Figure 5.14b). Figure 5.14c shows the temperatures in C E G along planes 1, 2 and 3 and one can see the occurrence of very large gradients (up to 50 °C) between the top and bottom of a horizontal pipe. It should be mentioned that such a gradient is present on stainless stell pipe with outer D= 50mm.

The only test performed on saturated ground (test 6) showed a completely different behavior, compared to the corresponding test performed under dry conditions (test 4). Maintaining in both cases an outlet gas temperature between -70 and -80°C and consuming the same amount of nitrogen over time, the measured temperatures are very different. Figure 5.15 shows the temperature curves for the thermocouples inside and outside the FP. Being in a vertical position, again the sensors placed at the same acquisition level show similar trends. However, it is evident that the presence of water inside the soil directly affects the external face pipe temperatures, which reach minimum temperatures of -64°C at the C level and values around -10 or 0°C at the other acquisition levels (see Figure 5.15b). The internal sensors make it possible to verify the actual presence of LN_2 at the bottom of the probe up to the C level, and as shown in Figures 5.15a all sensors reach values below -150°C. This general behavior is the system's response to the presence of water in the soil. The temperature on the external surface of LNFP remains high for two main reasons: the heat exchange between freezing pipe and soil is no longer composed exclusively of the contact points between pipe and soil grains, and in the soil between soil particles contacts, but of contact points surrounded by water, for this reason the thermal conductivity increases (up to a factor of 5) so that heat moves more easily at the same thermal gradient; the specific heat and latent heat of the water provide for a large heat capacity volume to the soil, which requires the extraction of a lot of heat for cooling.

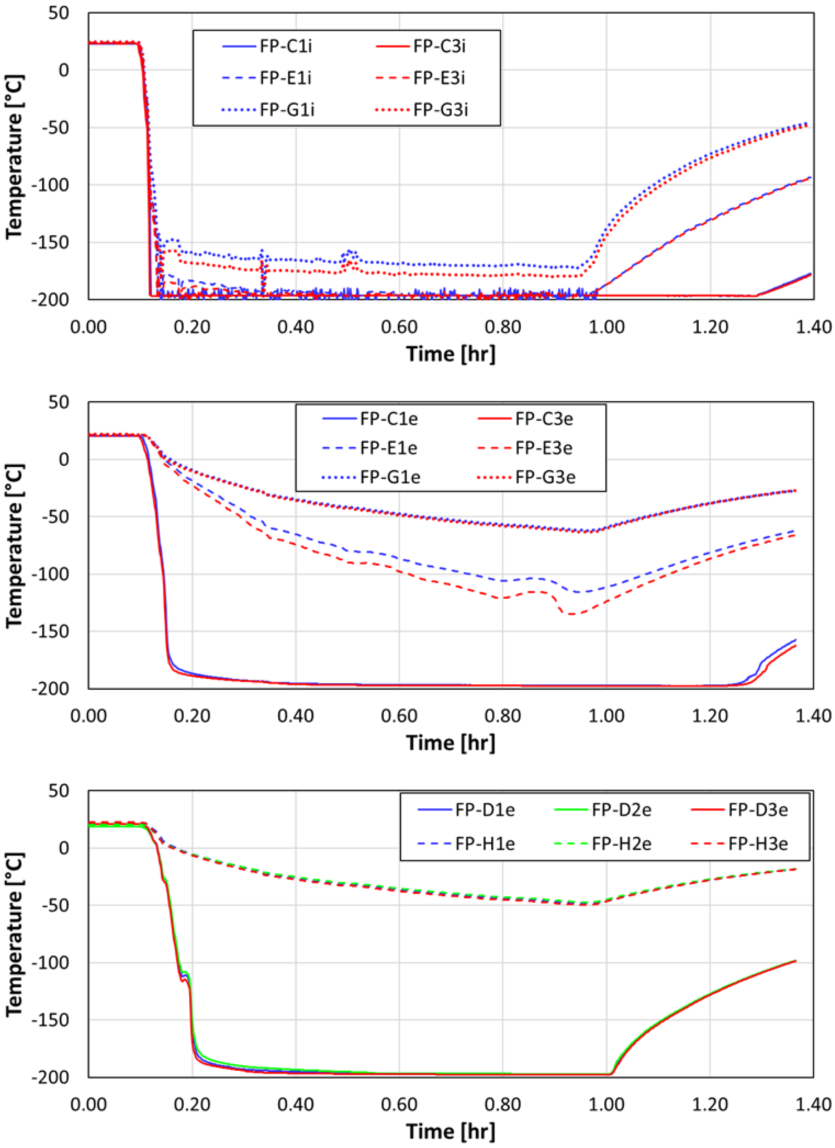

Figure 5.13: Comparison of temperature curves about Test 4 betweene thermal sensor along different planes: a) internal sensors on plane 1 and 3; b) external sensors on plane 1 and 3; c) external sensors on plane 1,2 and 3.

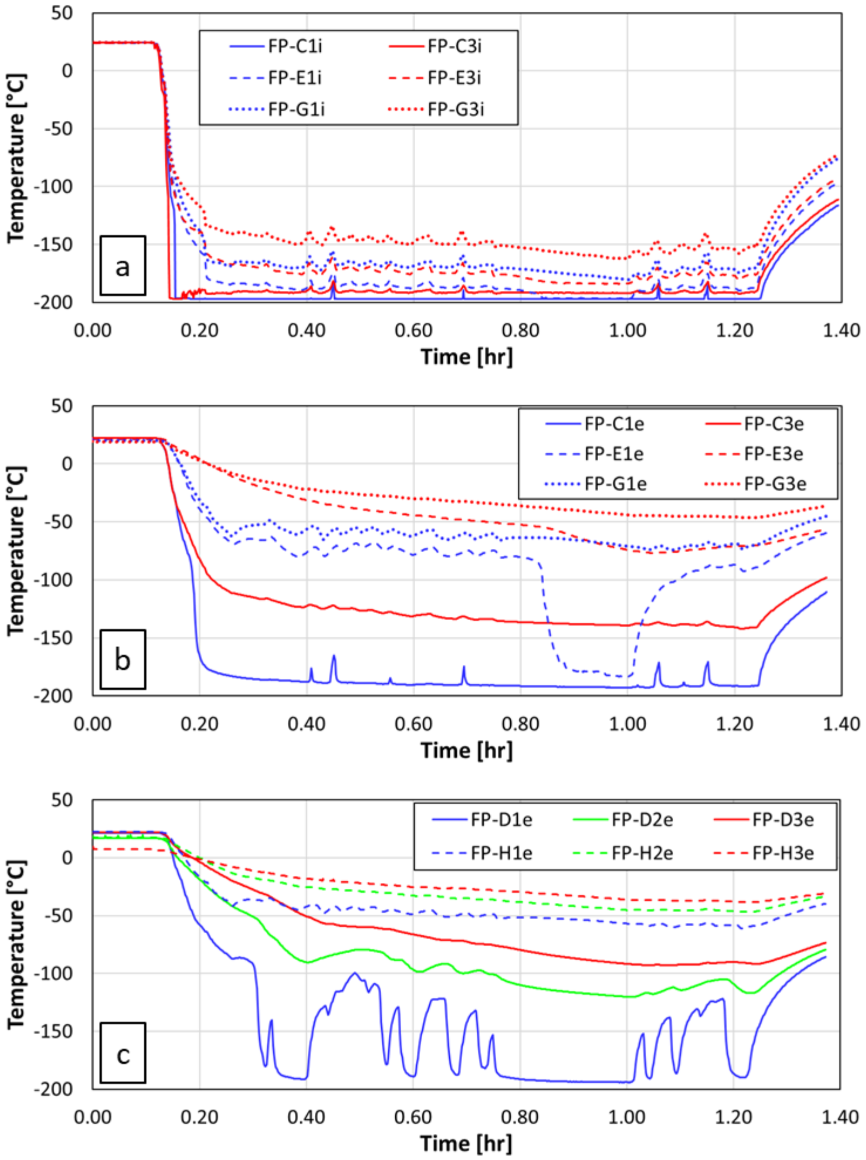

Figure 5.14: Comparison of temperature curves about Test 5 betweene thermal sensor along different planes: a) internal sensors on plane 1 and 3; b) external sensors on plane 1 and 3; c) external sensors on plane 1,2 and 3.

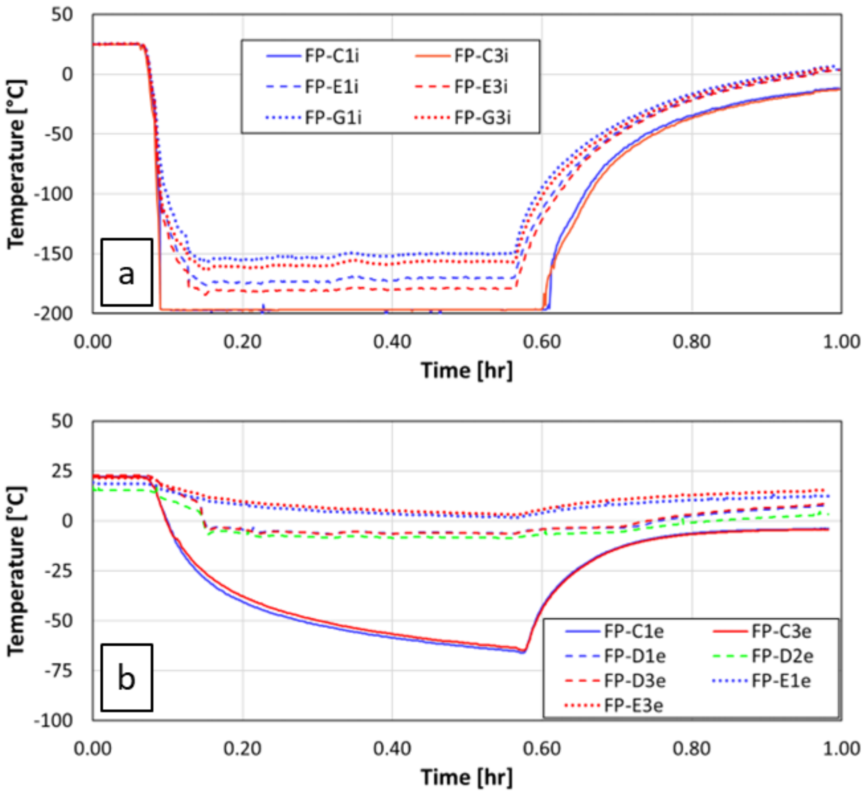

Figure 5.15: Comparison of temperature curves about Test 6 betweene thermal sensor along different planes: a) internal sensors on plane 1 and 3; b) external sensors on plane 1,2 and 3.

LNFP as well as being reliable and showing consistent results has been used under different working conditions. The laboratory activity showed critical issues that were addressed and solved by improving the insulation system. This device allows obtaining useful data for process study and modeling as it provides temperature trends at different points of the **freezing pipe** and by knowing the level of liquid nitrogen allows identifying the portion of the **device** that extracts a lot of heat from the ground due to the LN_2 phase transition. The measurement of general nitrogen consumption also allows an energetic balance between all the processes that occur.

Chapter 6

6 Conclusions

Chapters 2, 3, 4, and 5 described some of the innovative activities developed and proposed within the large chain of activities required to implement an artificial ground freezing intervention. These activities are mainly part of the design phase, in which the knowledge of the mechanical and thermal behavior of the geomaterials involved is crucial and the code used to do thermal analysis has to be validated, and a later part, when the intervention is in progress, where some control activities are proposed and illustrated.

At the end of this project, seven aspects of innovation applied to artificial ground freezing can be identified:

- A detailed and multidisciplinary global study was applied to the AGF so as to have a broad view on some of the shadowy areas existing to date, ranging from laboratory testing to thermal modeling to some aspects related to site control and safety. The cooperation between different players of the industry such as general contractors, construction management, workers, and the opportunity to visit very important construction sites allowed to focus on the aspects to be explored. (Chapter, 2, 3, 4 and 5).

- A comprehensive investigation of mechanical and thermal parameters of geomaterials that may be affected by thermal perturbation during an AGF intervention. A soil-only analysis, which is essential at the design stage, must be supported by a test campaign involving all geomaterials that may be affected by freezing such as concrete and treated soil. The preliminary study provided useful estimates for designers to investigate the response of the system to freezing, which as seen has direct effects on some materials. In addition, methods of performing mechanical and thermal tests on frozen geomaterials are illustrated, starting with the loose and/or unfrozen material. These tests showed that from a mechanical point of view, even soil with a temperature of -6°C can provide acceptable strengths, so the target value of -10°C that is usually considered can be rediscussed (Chapter 2).

- Given the importance of the reliability of a numeric model, a very simple and fast innovative laboratory test, requiring few resources and time, was developed to validate a commercial numeric code (TEMP/W). This test, which consists of a unidirectional freezing test of a cylindrical soil specimen can be done in a way that simulates the use of the two most common coolants (LN_2 and brine), and also allows to verify the sensitivity of the model to the type of boundary conditions considered and the thermal parameters taken into account. This promoted to the validated model a large predictive power (Chapter 3).

- Infrared Thermography technology was successfully applied to monitoring the temperature of excavation surfaces during the construction phases of the 4th tunnel under Isarco River. After a laboratory calibration by unidirectional freezing test that ensured its reliability down to -40°C, this technology was introduced to the construction site and its potential evaluated. Given its ease of use and its affordable cost, the introduction of this method for temperature monitoring can increase safety at the construction site and can provide a very important database to be used as a benchmark for numerical models of the intervention. In addition, a thorough and systematic study of the data obtained through this technique could help to estimate the overengineering of some interventions, as frozen soil is often excavated. This means excessive energy expenditure to freeze portions of soil that will have neither the role of mechanical nor hydraulic support as they will be mined. For these reasons, an implementation of this technology to common temperature data collection methods is recommended (Chapter 4).

- The opportunity to visit the Isarco site during the excavation phases allowed the development of a new workflow linking the site to the laboratory, through a chain of activities that began with the collection of undisturbed blocks and ended with the execution of mechanical and thermal tests on undisturbed frozen soil specimens. Between these two phases, initial and final, were positioned some innovative procedures including x-ray CT analysis that helped to study the internal structure of the frozen blocks and returned impressive results. This non-destructive technique saved time in dry coring and the selection of representative portions of the frozen blocks for mechanical and thermal testing. This technology, preceded and followed by the activities described in this study, is recommended for those interested in testing a material with particle size distribution and mineralogical composition equal or similar to that of Isarco (Chapter 4).

- The use of the point load test on undisturbed frozen soil samples detached from the excavation face was tested. This test is commonly used on rocks and provides very quickly an estimate of mechanical strength, based on appropriate correlation coefficients. The ability to perform parallel on-site and laboratory tests under controlled conditions has given the possibility of identifying this correlation coefficient that links point load tests with unconfined compressive strength of frozen soil. This campaign of investigation, although needing further tests on other types of soils and different temperatures have given positive results that advance the proposal for the inclusion of this test among the practices to be performed on site to estimate the real values of frozen soil shell strength, verify the stability of the excavation, increase safety and compare the results with those obtained experimentally at the preliminary stage in order to be able to assess the impact of the preparation of the specimens on their mechanical strength (Chapter 4).

- An innovative freezing pipe (LNFP) was developed and tested. This device, designed and built to work easily at different inclinations (from vertical to horizontal) in dry and wet soils, and equipped with several internal and external temperature sensors proved to be very rigorous and versatile. The whole system provided a full understanding of the workings of a refrigeration plant and gave the opportunity to test unconventional LN_2 supply methods. The decomposability of the LNFP and the small size of the whole apparatus (in terms of mass and volume) allow setting up sensitivity analyses of different components, which can be represented by the soil, the material and diameter of inner and outer tubes, and coolant considered. The LNFP also allows qualitative and quantitative data to be collected that can provide an excellent starting point for numerical code developers who wish to develop a mode of simulation of a nitrogen-fed freezing pipe in a subhorizontal position, taking into account energy balance (Chapter 5).

The importance of visiting some of the construction sites in which the AGF was used should be emphasized as they were indispensable, enlightening and unforgettable experiences and the only way to be aware of the responsibility and seriousness with which these challenges must be faced.

Regulations and References

API RP 13B-1/ISO 10414-1, (2003). Recommended Practice for Field Testing Water-based Drilling Fluids.

ASTM D4320-02. Standard Test Method for Laboratory Preparation of Chemically Grouted Soil Specimens for Obtaining Design Strength Parameters.

ASTM D5334-08. Standard Test Method for Determination of Thermal Conductivity of Soil and Soft Rock by Thermal Needle Probe Procedure.

ASTM D5731-02. Standard Test Method for Determination of the Point Load Strength Index of Rock.

ASTM D5918-13: Standard Test Methods for Frost Heave and Thaw Weakening Susceptibility of Soils.

ASTM STP 1568. Triaxial Testing of Frozen Soils - State of the Art.

UNI EN 12504-1. Prove sul calcestruzzo nelle strutture - Parte 1: Carote - Prelievo, esame e prova di compressione

Abbas, S. and Nehdi, M.L. (2021). Mechanical behavior of ultrahigh-performance concrete tunnel lining segments. *Materials*, 14, 2738.

Abu-Hamdeh, N. H. (2003). Thermal properties of soils as affected by density and water content. *Biosystems Engineering*, *86*(1), 97–102.

Abu-Hamdeh, N.H. and Reeder, R.C. (2000). Soil thermal conductivity: effect of density, moisture, salt concentration, and organic matter. *Soil Science Society of America Journal,* 64(4): 1285-1290.

Adivarahan, P., Kunii, D. and Smith, J.M. (1962) Heat transfer in porous rock through which single-phase fluid are flowing. *Society of Petroleum Engineers Journal*, 2(3): 290-296.

Akagawa, S. and Nishisato, K. (2009). Tensile strength of frozen soil in the temperature range of the frozen fringe. *Cold regions Science and Technology*, 57: 13-22.

Aksenov, V.I., Kal'bergenov, R.G. and Leonov, A.R. (2003). Strength characteristic of frozen saline soils. *Soil Mechanics and Foundation Engineering*, Vol.40, No 2: 55-59.

Anagnostopoulos, C.A., Chrysanidis, T. and Anagnostopoulou, M. (2020). Experimental data of cement grouting in coarse soils with different superplasticisers. *Data in Brief*, 30, 105612.

Andersland, O.B. and Ladanyi, B. (2004). Frozen ground engineering. John Wiley & Sons, Inc.

Andersland, O.B., Sayles, F.H. and Ladanyi, B. (1978). Mechanical properties of frozen ground. Chap. 5 in *Geotechnical Engineering for Cold Regions*, ed. O. B. Andersland and D. M. Anderson. New York: McGraw-Hill, pp. 216–75.

Andersland, O.B., Wiggert, D.C. and Davies, S.H. (1996). Hydraulic conductivity of frozen granular soils. *Journal of Environmental Engineering*, 122(3): 212-216.

Anderson, D.M. and Tice, A.R. (1972). Predicting unfrozen water contents in frozen soils from surface area measurements. *Highway Research Record*, 393(2): 12-18.

Anderson, D.M., Tice, A.R. and McKim, H.L. (1973). The unfrozen water and the apparent specific heat capacity of frozen soils. *Second International Conference on Permafrost*, Yakutsk, USSR.

Arenson, L.U. (2002). Unstable alpine permafrost: a potentially important natural hazard - variations of geotechnical behaviour with time and temperature. *Ph. D. Dissertation, Swiss Federal Institute of Technology Zurich*, 14801.

Arenson, L.U., Springman, S.M. and Sego, D.C. (2006). The rheology of frozen soils. *Applied Rheology*, 17(1):12147-1-12147-14.

Aubrey-Wake, C., Lamontagne-Hallé, P., Baraër, M., McKenzie, J.M. and Pomeroy, J.W. (2023). using ground-based thermal imagery to estimate debris thickness over glacial ice: fieldwork considerations to improve the effectiveness. *Journal of Glaciology*, 69(274): 353-369.

Baker, T.H.W. (1976). Transportation, preparation and storage of frozen soil samples for laboratory testing. *Soil Specimen Preparation for Laboratory testing, ASTM STP599*: 88-112.

Baker, T.H.W. 1979. Strain rate effect on the compressive strength of frozen sand. In *Proc. First International. Symposium on Ground Freezing,* Bochum, Germany, ed. H. L. Jessberger. Amsterdam: Elsevier, pp. 223–31; *Engineering Geology,* 13: 223–31.

Balossi Restelli, A., Rovetto, E. and Pettinaroli, A. (2016). Combined ground freezing application for the excavation of connection tunnels for Centrum Nauki Kopernik Station - Warsaw Underground Line II. *WTC* San Francisco, USA.

Bavaresco, N., Castellanza, R., Galli, A., Pettinaroli, A. and Lebeau, M. (2023a). Artificial ground freezing with liquid nitrogen: experimental investigation and numerical modelling. *11th International Symposium on Ground Freezing, Proceedings,* 24: 215-223.

Bavaresco, N., Castellanza, R., Pettinaroli, A. and Caffaro, P. (2023b). Artificial frozen soil at Isarco river underpass site: laboratory and site tests measurements to evaluate thermos-mechanical frozen soil behavior. *11th International Symposium on Ground Freezing, Proceedings,* 35, 313-320.

Bing, H., and Ma, W. (2011). Laboratory investigation of the freezing point of saline soil. *Cold Regions Science and Technology*, *67*(1–2), 79–88.

Bourbonnais, J. (1984). Étude du comportement des sols gelés jusqu’aux températures cryogéniques. Ph.D. diss., École Polytechnique, Montréal.

Bragg, R. A. and O. B. Andersland (1981). Strain rate, temperature, and sample size effects on compression and tensile properties of frozen sand. *Engineering Geology*, 18(1-4): 35-46.

Braun, B., Shuster, J. and Burnham, E. (1979). Ground freezing for support of open excavations. *Engineering Geology*, 13: 429-453.

Bristow, K.L. (1998). Measurement of thermal properties and water content of unsaturated sandy soil using dual-probe heat-pulse probes. *Agricultural and Forest Meteorology*, 89: 75-84.

Burt, T.P. and Williams, P.J. (1976). Hydraulic conductivity in frozen soils. *Earth Surface Processes*, 1(4): 349-360.

Cai, H., Li, P. and Wu, Z. (2020). Model test of liquid nitrogen freezing-temperature field of improved plastic freezing pipe. *Journal of Cold Regions Engineering*, 31(1): 04020001.

Cai, H., Xu, L., Yang, Y. and Li, L. (2018). Analytical solution and numerical simulation of the liquid nitrogen freezing-temperature field of a single pipe. *AIP Advances*, 8: 055119.

Calderón, D.S., Palacio, S.O., Ibáñez García, S.J. and Bock, S. (2023). An adjusted analytical solution for thermal design in artificial ground freezing. *International Journal of Rock Mechanics and Mining Sciences*, 164: 105310.

Carlaw, H.S. and Jaeger, J.C. (1959). Conduction of heat in solids, 2nd Ed. Oxford University Press, Oxford.

Celot, A., Restaini, A., Pettinaroli, A. and Caffaro, P. (2023). The construction of the new Brenner Basis railway line passage under the Isarco river protected by artificial ground freezing treatment. *11th International Symposium on Ground Freezing, Proceedings* 39: 343-352.

Chamberlain, E.J. (1981). Frost susceptibility of soil. U.S. Army Cold regions Research and Engineering Laboratory monograph 81-2, Hanover, New Hampshire.

Chamberlain, E.J. and Gow, A.J. (1979). Effect of freezing and thawing on the permeability and structure of soils. *Developments in Geotechnical Engineering*, 26: 73-92.

Chen, S.X. (2008). Thermal conductivity of sands. *Heat mass Transfer*, 44: 1241-1245.

Chen, J., Li D, Bing, H and Deng, Y. (2013). The experimental study on the uniaxial compressive strength of frozen silt with different salt content. *Engineering Mechanics*, 30(12): 18-23.

Chen. S., Ma, W. and Li, G. (2022). A novel approach for characterizing frozen soil damage based on mesostructured. *International Journal of Damage Mechanics*, 31(3): 444-463.

Chen, S., Zhao, S.P., Ma, W., Zhu, Q.T. and Xing, L.L: (2014). Status and prospects of frozen soil studies using CT technology. *Science in Cold and Arid Regions*, 6(2): 107-115.

Colombo, G. (2010). Il congelamento artificiale del terreno negli scavi della metropolitana di Napoli: valutazioni teoriche e risultati sperimentali. *Rivista italiana di geotecnica*, 4.

Côté, J., and Konrad, J. M. (2005). A generalized thermal conductivity model for soils and construction materials. *Canadian Geotechnical Journal*, *42*(2): 443–458.

Dano, C., Hicher, P.Y. and Tailliez, S. (2004). Engineering properties of grouted sands. *Journal of Geotechnical and Geoenvironmental Engineering*, 130(3): 328-338.

De Vries, D.A. (1963). Thermal Properties of Soils. *In the Physics of Plant Environment*. Edited by W.R. van Wijk. Amsterdam, p. 382.

Doherty, B.T. and Kester, D.R. (1974). Freezing point of seawater. *Journal of Marine Research*, 32(2): 285-300.

Domaschuk, L. (1982). Frost heave forces on embedded structural units. *Proceedings of 4th Canadian Permafrost Conference:* 487-496.

Donazzi F., (1977) Soil thermal and hydrological characteristics in designing underground cables. Proc IEE 123: 506–516.

Elhakim, A. F. (2015). The use of point load test for Dubai weak calcareous sandstones. *Journal of Rock Mechanics and Geotechnical Engineering*, *7*(4), 452–457.

Evirgen, B. (2021). Comparison of individual and sequential copper piping system in an experimental artificial ground freezing model. *Arabian Journal of Geosciences*, 14: 926.

Evirgen, B. and Tuncan, M. (2019). A physical soil freezing model for laboratory applications. *Cold Regions Science and Technology*, 159: 29-39.

Farouki, O. T. (1981). Thermal Properties of Soils. CRREL Monograph 81-1. U.S. Army Cold Regions Research and Engineering Laboratory. Hanover, New Hampshire.

Franzosi, F., Casiraghi, S., Colombo, R., Crippa, C. and Agliardi, F. (2023). Quantitative evaluation of the fracturing state of crystalline rocks using infrared thermography. *Rock Mechanics and Rock Engineering*, 56: 6337-6355.

Frivik, P.E. and Thorbergsen, E. (1981). Thermal design of artificial soil freezing systems. *Engineering Geology*, 18: 189-201.

Fukusako, S. (1990). Thermophysical properties of ice, snow, and sea ice. *International Journal of Thermophysics*, *11*(2): 353–372.

Gallavresi, F. (1981). Ground freezing – The application of the mixed method (brine - liquid nitrogen). *Engineering Geology*, 18: 361-375.

Geoslope International Ltd. (2020). Heat and mass transfer modelling with GeoStudio 2020 (First Edition). Calgary, Alberta, Canada.

Gioda, G., Locatelli, L. and Gallavresi, F. (1992). Sul congelamento artificiale dei terreni. *Rivista Italiana di Geotecnica*, 3: 173-184.

Gioda, G., Locatelli, L. and Gallavresi, F. (1994). A numerical and experimental study of the artificial freezing of sand. *Canadian Geotechnical Journal,* 31: 1-11.

Glatzmaier, G.C. and Ramirez, W.F. (1985). Simultaneous measurement of thermal conductivity and thermal diffusivity of unconsolidated materials by the transient hot wire method. *Review of Scientific Instruments* 56(7), 1394.

Go, G. H., Lee, J., Shin, H. S., Ryu, B. H., Jin, H. W., and Kim, D. W. (2019). Evaluation of one-dimensional freezing behavior for ice-rich sandy soil. *International Journal of Heat and Mass Transfer*, *130*, 960–967.

Gruber, S., Hoelzle, M. and Haeberli, W. (2004). Permafrost thaw and destabilization of Alpine rock walls in the hot summer of 2003. *Geophysical Research Letters, 31: 13504.*

Guerin, A., Jaboyedoff, M., Collins, B.D., Derron, M-H, Stock, G.M., Matasci, B., Boesiger, M., Lefeuvre, C. and Podladchikov, Y.Y. (2019). Determination of rock bridges by infrared thermal imaging and modelling. *Nature Research,* Scientific Reports, 9, 13138.

Haeberli, W., Hallet, B., Arenson, L., Elconin, R., Humlum, O., Kääb, A., Kaufmann, V., Ladanyi, B., Matsuoka, N., Springman, S., and Vonder Mühll, D. (2006). Permafrost creep and rock glacier dynamics. *Permafrost and Periglacial processes*. 17: 189-214.

Haigh, S.K. (2012). Thermal conductivity of sands. *Géotechnique,* 62(7): 617-625.

Hani M. and Evirgen, B. (2023). A frozen soil sampling technique for granular soils and thermal modelling. *Bulletin of Engineering Geology and the Environment*, 82: 354.

Harlan, R.L. and Nixon, J.F. (1978). Ground thermal regime. In *Geotechnical Engineering for Cold Regions*, McGraw-Hill, 103-163.

Harris, J. (1995). Ground freezing in practice. Thomas Telford, London.

Harris, S.A., French, H.M., Heginbottom, J.A., Johnston, G.H., Ladanyi, B., Sego, D.C. and Van Everdingen, R.O. (1988). Glossary of permafrost and related ground-ice terms. *National Research Council of Canada*, Technical Memorandum No.142.

Harris, C., Vonder Mühll, D., Isaksen, K., Haeberlu, W., Sollid, J.L., King, L., Holmlund, P., Dramis, F., Guglielmini, M. and Palacios, D. (2003). Warming permafrost in European mountains. *Global and Planetary Change*, 39: 215-225.

Haynes, F. D., & Karalius, J. A. (1977). Effect of temperature on the strength of frozen silt. *U. S. Army Cold Regions Research and Engineering Laboratory*, (No 77-3).

Heinrich, D., Müller, G. and Voort, H. (1978). Ground freezing monitoring techniques. *Engineering Geology*, 13: 455-471.

Hendry, M.T., Onwude, L.U. and Sego, D.C. (2016). A laboratory investigation of the frost heave susceptibility of fine-grained soil generated from the abrasion of a diorite aggregate. *Cold Regions Science and Technology*, 123: 91-98.

Hillel, D. (1998). Environmental soil physics: fundamentals, applications, and environmental considerations. Academic press.

Hivon, E.G. and Sego, D.C. (1995). Strength of frozen saline soils. *Canadian Geotechnical Journal*, 32(2): 336-354.

Hong, E., Perkins, R., and Trainor, S. (2014). Thaw Settlement Hazard of Permafrost Related to Climate Warming in Alaska. *Arctic Institute of North America Stab*. *67*(1), 93–103.

Hopke, S.W. (1980). A model for frost heave including overburden. *Cold Regions Science and Technology*, 3: 111-127.

Horai, K.I. (1971). Thermal conductivity of rock-forming minerals. *Journal of Geophysical Research*, 76(5): 1278–1308.

Hu, X., Fang, T., Chen, J., Ren, H. and Guo, W. (2018). A large-scale physical model test on frozen status in freeze-sealing pipe roof method for tunnel construction. *Tunneling and Unnderground Space Technology*, 27: 55-63.

Hu, R., Liu, Q., and Xing, Y. (2018). Case study of heat transfer during artificial freezing with groundwater flow. *Water*, 10, 1322.

Hu, K., Wu, Y., Gao, Z., Wang, S., and Yang, Z. (2022). Experimental study on freezing mode to reduce frost heave. *Buildings*, 12, 1367.

Hu, X., Yu, J., Ren, H., Wang, Y. and Wang, J. (2017). Analytical solution to steady-state temperature field for straight row-piped freezing based on superposition of thermal potential. *Applied Thermal Engineering*, 111: 223-231.

Incropera, F. P., DeWitt, D. P., Bergman, T. L. and Adrienne, S. L. (2007). *Fundamentals of Heat and Mass Transfer*, 6th Edition. John Wiley & Sons Inc. New Jersey, USA.

Jessberger. H.L. (1981). A state-of-the-art report. Ground freezing: mechanical properties, processes and design. *Engineering Geology*, 18: 5-30.

Jessberger, H.L. (1980). Theory and application of ground freezing in civil engineering. *Cold Regions Science and Technology*, 3:3-27.

Johansen, O. (1975). Thermal Conductivity of Soils, Draft Translation Report 637. *Ph.D. Dissertation, Norwegian University of Science and Technology*, 291.

Johnsson, H., Thunholm, B., and Lundin, L. C. (1995). Experimental system for one-dimensional freezing of undisturbed soil profiles. *Soil Technology*, *7*(4), 319–325.

Jones, S.J. (1978). Triaxial testing of polycrystalline ice. Proceedings of the third International Conference on Permafrost, 1: 670-674.

Jones, J.S., Jr. (1981). State-of-the-art report – Engineering practice in artificial ground freezing. *Engineering Geology*, 18: 313-326.

Jones, J.S. and Brown, R.E. (1979). Design of tunnel support system using ground freezing. *Engineering Geology*, 13: 375-395.

Kang, X.F., Zhang, H. and Martins, V. (2016). Experimental study on thawing process of frozen soil based on CT scanning. *Journal of Mechanical Engineering Research and Developments*, 39(2): 340-346.

Kersten, M.S. (1949). Thermal Properties of Soils. Bullettin No. 28. *Engineering experiment station*, Vol. LII, No. 21.

Kester, D.R. (1974). Comparison of recent seawater freezing point data. Journal of Geophysical Research, 79(30): 4555-4556.

Khakimov, K. R. (1957). The theory and practice of artificial soil freezing. Akademiia Nauk SSSR.

Kiaalhosseini, S., Johnson, R.L., Rogers, R.C., Irianni Renno, M., Lyverse, M. and Sale, T.C. (2016). Cryogenic core collection (C_3) from unconsolidated subsurface media. *Groundwater Monitoring & Remediation*, 36(4): 41-49.

Kim, Y., Hwang, B. and Cho, W. (2018). Development of ground freezing system for undisturbed sampling of granular soils. *Advances in Civil Engineering*, 1541747.

Kinosita, S. (1966). Heaving force of frozen soils. *International Conference on Low Temperature – Physics of Snow and Ice*, 2: 1345-1360.

Kodikara, J., Rajeev, P., and Rhoden, N. J. (2011). Determination of thermal diffusivity of soil using infrared thermal imaging. *Canadian Geotechnical Journal*, 48 (8), 1295–1302.

Konrad, J.M. (1999). Frost susceptibility related to soil index properties. Canadian Geotechnical Journal, 36(3): 403-417.

Kotov, P.I. and Stanilovskaya, J.Y.V. (2022). Predicting changes in the mechanical properties of frozen saline soils. European Journal of Environmental and Civil Engineering. 26(12): 5716-5728.

Kozlowski, T. (2007). A semi-empirical model for phase composition of water in clay-water systems. *Cold Regions Science and Technology*, 49: 226-236.

Kurz, D., Alfaro, M. and Graham, J. (2017). Thermal conductivities of frozen and unfrozn soils at three project sites in northern Manitoba. *Cold Regions Science and Technology*, 140:3.-38.

Ladanyi, B. (1989). Effect of salinity and temperature on the behaviour of frozen soils. *Workshop on Impact of Saline Permafrost*, Winnipeg, Manitoba.

Le. T.M.H., Wold, M. and Bærverfjord, M.G. (2016). Challenges with sampling coarse-grained permafrost: an experience in Svalbard. *Geotechnical and Geophysical Site Characterisation 5* – Lehane, Acosta-Martinez & Kelly (Eds): 1167-1172.

Lee, J., Kim, Y.S., Chae, D. and Cho, W. (2016). Loading rate effects on strength and stiffness of frozen sands. *KSCE Journal of Civil Engineering*, 20: 208-215.

Li, Y., Jin, X., Lv, Z., Dong, J. and Guo. J. (2016). Deformation and mechanical characteristics of tunnel lining in tunnel intersection between subway station tunnel and construction tunnel. *Tunnel and Underground Space Technology*, 56: 22-33.

Li, A., Niu, F., Zheng, H., Akagawa, S., Lin, Z., and Luo, J. (2017). Experimental measurement and numerical simulation of frost heave in saturated coarse-grained soil. *Cold Regions Science and Technology*, *137*, 68–74.

Li, S., Wang, X., Xia, J. and Shen, D. (2018). Test methods for specific het capacity of frozen soil based on principles of mixing calorimetry. *Chinese Journal of Geotechnical Engineering*, 40(9): 1684-1689.

Linell, K.A. and Kaplar, C.W. (1966). Description and classification of frozen soils. *U.S. Army Cold Regions Research and Engineering Laboratory*. Technical Report n.150.

Liu, Y., Li, K.Q., Li, D.Q., Tang, X.S. and Gu, S.X. (2022). Coupled thermal-hydraulic modelling of artificial ground freezing with uncertainties in pipe inclination and thermal conductivity. *Acta Geotechnica*, 17: 257-274.

Liu, B., Li, D, Liu, L.I., Yao, W., Zhang, H., Liu, N. and Lou, X. (2012). CT scanning and images analysis during frozen soil thawing. *Journal of China Coal Society*, 37(12): 2014-2019.

Liu, J., Yang, P., Wang, J., Wang, S., and Jiang, H. (2023). Freezing front evolution in chloride soils under unidirectional freezing conditions and the characterization via electrical conductivity. *Cold Regions Science and Technology*, 213, 103913.

Lunardini, V. J. (1981). Heat Transfer in Cold Climates. New York: Van Nostrand Reinhold.

Luo, C. liang, Yu, Y. yan, Zhang, J., Tao, J. yan, Ou, Q. jie, and Cui, W. hao. (2023). Thermal-water-salt coupling process of unsaturated saline soil under unidirectional freezing. *Journal of Mountain Science*, *20*(2), 557–569.

Lv, Z., Xia, C., Li, Q., and Si, Z. (2019). Empirical frost heave model for saturated rock under uniform and unidirectional freezing conditions. *Rock Mechanics and Rock Engineering*, 52, 955-963.

Ma, W., Zhang, L. and Yang, C. (2015). Discussion of the applicability of the generalized Clausius-Clapeyron equation and the frozen fringe process. *Earth-Science Reviews*, 142: 47-59.

Malhotra, H.L. (1956). The effect of temperature on the compressive strength of concrete. *Magazine of Concrete Research*, 8(23): 85-94.

Maranzana, G., Didierjean, S., Rémy, B. and Maillet, D. (2002). Experimental estimation of the transient free convection heat transfer coefficient on a vertical flat plate in air. *International journal of heat and mass transfer*, *45*(16), 3413-3427.

Marwan, A., Zhou, M-M., Abdelrehim, M.Z. and Meschke, G. (2016). Optimization of artificial ground freezing in tunnelling in the presence of seepage flow. *Computers and Geotechnics*, 75: 112-125.

Mauro, A., Normino, G., Cavuoto, F., Marotta, P. and Massarotti, N. (2020). Modeling artificial ground freezing for construction of two tunnels of a metro station in Napoli (Italy). *Energies*, 13(5): 1272.

McKenzie, J.M., Voss, C.I. and Siegel, D.I. (2007). Groundwater flow with energy transport and water-ice phase change: numerical simulations, benchmarks, and applications to freezing in peat bogs. *Advances in Water Resources*, 30(4): 966-983.

Mellor, M. (1980). Mechanical Properties of Polycrystalline Ice. In: Tryde, P. (eds) *Physics and Mechanics of Ice*. International Union of Theoretical and Applied Mechanics. Springer, Berlin, Heidelberg: 217-245.

Michalowski, R.L. (1993). A constitutive model of saturated soils for frost heave simulations. *Cold Regions Science and Technoogy*.,22: 47–63.

Millero, F. J., Perron, G. and Desnoyers, J. E. (1973). Heat capacity of seawater solutions from 5 to 35 °C and 0.5 to 22‰ chlorinity. *Journal of geophysical research*, *78*(21): 4499-4507.

Mineo, S. and Pappalardo, G. (2021). Rock emissivity measurementfor infrared thermography engineering geological applications. *Applied Sciences*, 11, 3773.

Ming, F., Chen, L., Li, D. and Wei, X. (2020). Estimation of hydraulic conductivity of saturated frozen soil from the soil freezing characteristic curve. *Science of the Total Environment*, 698: 134132.

Mira-Cattò, F., Pettinaroli, A. and Rovetto, E. (2016). Ground freezing combined method for urban tunnel excavation. *DFI* Kolkata, India.

Morgenstern, N.R. and Nixon, J.F. (1971). One-dimensional consolidation of thawing soils. *Canadian Geotechnical Journal,* 8(4): 558-565.

Nishimura, S., Gens, A., Olivella, S. and Jardine, R.J. (2009). THM-coupled finite element analysis of frozen soil: formulation and application. Géotechnique, 59(3): 159-171.

Ono, N. (1967). Specific Heat and Heat of Fusion of Sea Ice. *Physics of Snow and Ice*, 1(1): 599-610.

Osterkamp, T.E. and Romanovky, V.E. (1999). Evidence for warming and thawing of discontinuous permafrost in Alaska. *Permafrost and Periglacial Processes*, 10: 17-37.

Othman, M.A. and Benson, C.H. (1993). Effect of freeze-thaw on the hydraulic conductivity and morphology of compacted clay. *Canadian Geotechnical Journal*, 30(2): 236-246.

Parameswaran, V.R. and Jones, S.J. (1981). Triaxial testing of frozen sand. *Journal of Glaciology*. 27(95).

Petrenko, V.F. and Whitworth, R.W. (1999). Physics of ice. Oxford University Press, Oxford, New York.

Pettinaroli, A., Caffaro, P., Celot, A., Restaini, A. and Gatti, M. (2023). A systematic use of artificial ground freezing technicque for tunnel excavation in urban context: the cross-passages for the Metro line 4 in Milan. *11th International Symposium on Ground Freezing, Proceedings*, 34: 303-311.

Pimentel, E., Sres, A. and Anagnostou, G. (2007). Modeling of ground freezing in tunnelling. *Underground Space – the 4th Dimension of Metropolises*. Barták, Hrdina, Romancov & Zlámal Ed.

Pimentel, E., Sres, A. and Anagnostou, G. (2012). Large-scale laboratory tests on artificial ground freezing under seepage-flow conditions. *Géotechnique*, 62(3): 227-241.

Pounder, E. R. (1965). The Physics of Ice. Pergamon Press, New York, p. 151.

Putkonen, K. (2003). Determination of frozen soil thermal properties by heated needle probe. *Permafrost and Periglacial Processes*, 14: 343-347.

Ramires, M. L. V., Nieto Castro, C. A., Nagasaka, Y., Nagashima, A., Assael, M. J. and Wakeham, W. A. (1995). Standard Reference Data for the Thermal Conductivity of Water. *Journal of Physical and Chemical Reference Data*, *24*(3): 1377–1381.

Rashid, T., Khawaja, H. and Edvardsen, K. (2016). Determination of thermal properties of fresh water and sea water ice using multiphysics analysis. *International Journal of Multiphysics*, *10*(3): 277–290.

Rocca, O. (2010). Congelamento artificiale del terreno. *Argomenti di ingegneria geotecnica*. Hevelius Edizioni.

Roman, L.T. (1994). Effect of chemical composition of soils on the strength and deformability of frozen saline soils. *Soil Mechanics and Foundation Engineering*, 31(6): 205-210.

Rubene, S. and Vilnitis, M. (2017). Impact of low temperatures on compressive strength of concrete. *International Journal of Theoretical and Applied Mechanics*, 2: 97-101.

Ruggieri, N., Castellano, M., Capello, M., Maggi, S. and Povero, P. (2011). Seasonal and spatial variability of water quality parameters in the Port of Genoa, Italy, from 2000 to 2007. *Marine Pollution Bulletin*, *62*(2): 340–349.

Sadovsky, A.V. and Dorman, Y.A., (1981). The artificial freezing and cooling of soils at construction sites. *Engineering Geology*, 18: 327-331.

Sakazume, S. and N. Seki (1980). Bulletin of J. S. M. E. 46 p. 1119-1126.

Samani, A.K. and Attard, M.M. (2012). A stress-strain model for uniaxial and confined concrete under compression. *Engineering Structures*, 41: 335-349.

Sanger, F.J. and Sayles, F.H. (1979). Thermal and rheological computations fo5r artificially frozen ground construction. *Engineering Geology*, 13: 311-337.

Sayles, F.H. (1968). Creep of frozen sand. *Cold Regions Research & Engineering Laboratory*, Tech. Rep. 190.

Sayles, F. H., and D. L. Carbee. (1980). Strength of frozen silt as a function of ice content and dry unit weight. In *Proc. 2nd International Symposium on Ground Freezing,* Trondheim, Norway, prepr. ed., 1: 109–119.

Shannon, H.R., Sigda, J.M., Van Dam, R.L., Hendrickx, J.M. and McLemore, V.T. (2005). Thermal camera imaging of rock piles at the Questa Molybdenum Mine, Questa, New Mexico. In *Proceeding of the 2005 national meeting of the America Society of Mining and Reclamation*, Lexington, 1015-1028.

Sharqawy, M. H. (2013). New correlations for seawater and pure water thermal conductivity at different temperatures and salinities. *Desalination,* 313: 97–104.

Shastri, A., Sánchez, M, Gai, X., Lee, M.Y. and Dewers, T. (2021). Mechanical behavior of frozen soils: experimental investigation and numerical modelling. Computers and Geotechnics, 138: 104361.

Shooshpasha, I. and Shirvani, R.A. (2015). Effect of cement stabilization on geotechnical properties of sandy soils. *Geomechanics and Engineering*, 8(1): 17-31.

Shuster, J.A. (1972). Controlled freezing for temporary ground support. Chap. 49 in Proc. First North American Rapid Excavation and Tunneling Conf., Chicago, e.d. K.S. Lande and L.A. Garfield. Baltimore: ASCE-AIME, vol. 2, pp. 863-895.

Sidebotham, G. (2015). Heat transfer modeling: an inductive approach. In *Choice Reviews Online*, 53(2).

Song, H., Cai, H., Yao, Z., Rong, C. and Wang, X. (2016). Finite element analysis on 3D freezing temperature field in metro cross-passage construction. *Procedia Engineering*, 165: 528–539.

Stoss, K. and Valk, K., (1979). Uses and limitations of ground freezing with liquid nitrogen. *Engineering Geology*, 13: 485-494.

Takashi, T., Yamamoto, H., Ohrai, T and Masuda, M. (1978). Effect of penetration rate of freezing and confining stress on the frost heave ratio of soil. *International Conference on Permafrost*, Edmonton, Alberta.

Tao, L., Zhi, H., Zhingang, Z., Shaoyou, H., Jia, L., Youzhi, L. and Hong, H. (2020). Artificial frozen soil bending test and bending property. *E3S Web of Conferences*, 165: 03028.

Tarnawski, V. R. and Leong, W. H. (2016). Advanced Geometric Mean Model for Predicting Thermal Conductivity of Unsaturated Soils. *International Journal of Thermophysics, 37*(2): 1–42.

Tarnawski, V. R., Momose, T. and Leong, W. H. (2011). Thermal conductivity of standard sands II. Saturated conditions. *International Journal of Thermophysics*, *32*(5): 984–1005.

Ting, J.M. (1981). The creep of frozen sands.: qualitative and quantitative models, part 2. *Massachussets Institute of Technology Report.*

Ting, J.M., Martin, R.T. and Ladd, C.C. (1983). Mechanisms of strength for frozen sand. *Journal of Geotechnical Engineering*, 109(10): 1286-1302.

Torrance, J.K., Elliot, T., Martin, R. and Heck, R.J. (2008). X-ray computed tomography of frozen soil. *Cold Regions Science and Technology*, 53: 75-82.

Turekian, K.K. (1968). Oceans, *Prentice-Hall*.

Veranneman, G. and Rebhan, D. (1979). Ground consolidation with liquid nitrogen (LN_2). *Engineering Geology*, 13: 473-484.

Viklander, P. (1998). Permeability and volume changes in till due to cyclic freeze/thaw. *Canadian Geotechnical Journal,* 35: 471-477.

Viklander, P. and Eigenbrod, D. (2000). Stone movements and permeability changes in till caused by freezing and thawing. *Cold Regions Science and Technology,* 31 (2): 151-162.

Vitel, M., Rouabhi, A., Tijani, M. and Guérin, F. (2015). Modeling heat transfer between a freeze pipe and the surrounding ground during artificial ground freezing activities. *Computers and Geotechnics*, 63: 99-111.

Vitel, M., Rouabbhi, A., Tijani, M. and Guérin, F. (2016). Modeling heat transfer during ground freezing subjected to high seepage velocities. *Computers and Geotechnics*, 73: 1-15.

Vu, Q.H., Pereira, J.M. and Tang, A.M. (2022). Effect of fines content on soil freezing characteristic curve of sandy soils. *Acte Geotechnica,* 17: 4921-4933.

Waite, W.F., Gilbert, L.Y., Winters, W.J. and Mason, D.H. (200&). Estimating thermal diffusivity and specific heat from needle probe thermal conductivity data. *Review of Scientific Instruments,* 77, 044904.

Wang, T., Li, P., Tang, C., Zhang, B., Yu, J. and Geng, T. (2022). Tensile characteristics and fracture mode of frozen fractured rock mass based on Brazilian splitting test. *Applied Sciences*, 12: 11788.

Wang, C., Li, S., Zhang, T. and You, Z. (2019). Experimental study on mechanical characteristics and fracture patterns of unfrozen/freezing saturated coal and sandstone. *Materials,* 12(6): 992.

Wang, X., Liu, C., Liu, S., Yan, C., Zhang, J. and Li, H. (2020). Compressive strength of pile foundation concrete in permafrost environment in China. *Construction and Building Materials,* 247: 118431.

Wang, J.C., Xu X.Z. and Wang Y.J. (1995). Thermal sieve effect and convectional migration of particles during unidirectional freezing. *Glaciology and Geocryology*, 18(3): 252-255.

Wang, P. and Zhou, G. (2018). Frost-heaving pressure in geotechnical engineering materials during freezing process. *International Journal of Mining Science and Technology*, 28(2): 287-296.

Waples, D. W. and Waples, J. S. (2004). A Review and evaluation of specific heat capacities of rock, minerals, and subsurface fluids. Part1: minerals and nonporous rocks. *Natural Resources research*, 13(2): 97-122.

Watanabe, K. and Osada, Y. (2016). Comparison of hydraulic conductivity in frozen saturated and unfrozen unsaturated soils. *Vadose Zone Journal*, 15(5): 0154.

Wierenga, P.J., Nielsen, D.R. and Hagan, R.M. (1969). Thermal properties of a soil based upon field and laboratory measurements. *Soil Science Society of America Journal*, 33: 354-360.

Winkler, B., Hofstetter, G, and Lehar, H. (2004). Application of a constitutive model for concrete to the analysis of a precast segmental tunneling lining. *International Journal for Numerical and Analytical Methods in Geomechanics*, 28(7-8): 797-819.

Wride, C.E., Hofmann, B.A., Sego, D.C., Plewes, H.D., Konrad, J.-M., Biggar, K.W., Robertson, P.K. and Monahan, P.A. (2000). Ground sampling program at the CANLEX test sites. *Canadian Geotechnical Journal*, 37: 530-542.

Xiao, Z., Lai, Y., You, Z. and Zhang, M. (2017). The phase change process and properties of saline soil during cooling. *Arabian Journal for Science and Engineering*, 42: 3923-3932.

Xiao, Z., Lai, Y., and Zhang, M. (2018). Study on the freezing temperature of saline soil. *Acta Geotechnica*, *13*(1), 195–205.

Yamamoto. Y. and Springman, S.M. (2014). Axial compression stress path tests on artificially frozen soil samples in a triaxial device at temperature just below 0 °C. *Canadian Geotechnical Journal*, 51:1178-1195.

Yamamoto, Y. and Springman, S.M. (2019). Triaxial stress path tests on artificially prepared analogue alpine permafrost soil. *Canadian Geotechnical Journal*, 56: 1448-1460.

Yang, Y., Lai, Y. and Li, J. (2010). Laboratory investigation on the strength characteristic of frozen sand considering effect of confining pressure. *Cold Regions Science and Technology*, 60(3): 245-250.

Yuanlin, Z. and Carbee, D.L. (1987). Creep and strength behavior of frozen silt in uniaxial compression. CRREL Report No 87-10

Zebovitz, S., Krizek, R.J. and Atmatzidis, D.K. (1989). Injection of fine sands with very fine cement grout. *Journal of Geotechnical Engineering*, 115(12).

Zhang, S., Lai, Y., Sun, Z. and Gao, Z. (2007). Volumetric strain and strength behavior of frozen soils under confinement. *Cold Regions Science and Technology*, 47: 263,270.

Zhang, L., Ma, W. and Yang, C. (2015). Pore water pressure changes of supercooling and ice nucleation stages during freezing point testing. *Geotechnique Letters*, *5*: 39–42.

Zhang, M., Pei,W., Li,S., Lu, J. and Jin, L. (2017). Experimental and numerical analyses of the thermo–mechanical stability of an embankment with shady and sunny slopes in a permafrost region. *Applied Thermal Engineering*, 127: 1478–1487.

Zhao, W., Gao, H., Chen, W., Liu, J., Peng, W. And Zhou, S. (2023). Experimental study on similar materials for tunnel lining concrete in geomechanical model tests. *Engineering Failure Analysis*, 152, 107456.

Zhao, Y., Li, R. and Seo, H. (2018). Crack detection in frozen soils using infrared camera. *Proceedings of 35th International Symposium on Automation and Robotics in Conctruction: 182-188*.

Zhou, M.M. and Meschke, G. (2013). A three-phase thermos-hydro-mechanical finite element model for freezing soils. *International*

Journal for Numerical and Analytical Methods in Geomechanics, 37: 3173-3193.

Zhu, Y. and Carbee, D.L: (1984). Uniaxial compressive strength of frozen silt under constant deformation rates. *Cold Regions Science and Technology*, 9:3-15.

Zubrzycki, S. (2012). Drilling frozen soils in Siberia. *Polarforschung*, 81(2), 150-152.

Zueter, A., Nie-Rouquette, A., Alzoubi, M.A. and Sasmito, A.P. (2020). Thermal and hydraulic analysis of selective artificial ground freezing usign air insulation: experiment and modeling. *Computers and Geotechnics*, 120: 103416.

Appendix A

Chapter 2

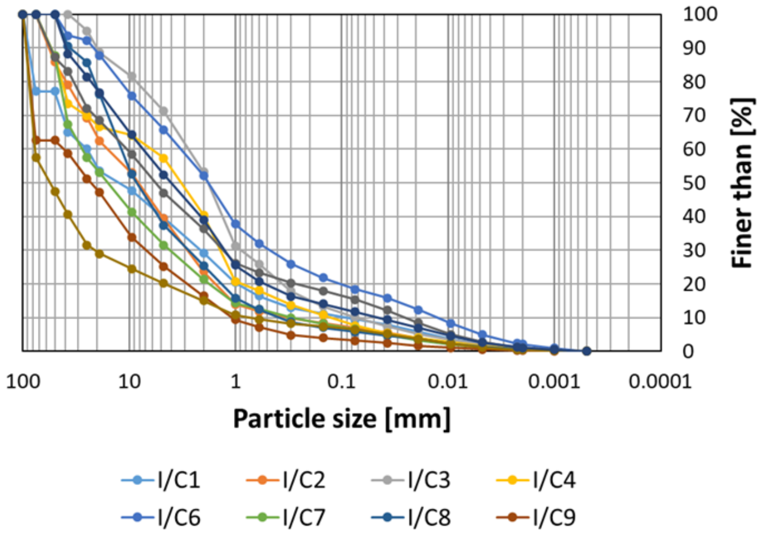

Figure A4: Preliminary particles size distribution on log collected from Isarco riverside.

Table A1:List of specimen subjected to UCS tests.

Specimen code	Sample	Section [mm-mm]	D [mm]	H [mm]	γ_n [kN/m^3]	n [-]
I1-N/u1	I1-N/C6	-	70.0	139.0	22.35	0.25
I1-N/u2	I1-N/C11	-	70.0	140.0	22.36	0.25
I1-N/u3	I1-N/C1	-	70.0	140.0	22.25	0.26
I2-N/u1	I2-N/C7	-	70.0	140.0	21.43	0.30
I2-N/u2	I2-N/C2	-	70.0	140.0	21.36	0.31
I2-N/u3	I2-N/C8	-	70.0	140.0	21.37	0.31
I2-N/u1-h	I2-N/C9	-	50.8	92.1	20.12	0.35
I2-N/u2-h	I2-N/C9	-	70.3	141.1	21.04	0.32
I2-N/u3-h	I2-N/C7	-	70.2	136.9	21.62	0.32
I2-N/u4-h	I2-N/C2	-	70.2	140.3	21.28	0.31
M1-N/u1	M1-N	-	70.0	140.5	21.06	0.33
M1-N/u2		-	70.0	141	20.98	0.33
M1-N/u3		-	70.0	141	20.98	0.33
M2-N/u1	M2-N	-	70.0	140	20.73	0.35
M2-N/u2		-	70.0	137	21.18	0.34
M2-N/u3		-	70.0	142	20.43	0.34
M3-N/u1	M3-N	-	70.0	141	19.08	0.45
M3-N/u2		-	70.0	139	19.35	0.45
M3-N/u3		-	70.0	140	19.21	0.45
CO/u1-e	Concrete core	-	45.0	99.1	24.9	-
CO/u2-e		-	45.0	96.5	24.0	-
CO/u3-e		-	45.0	96.5	24.0	-
CO/u1-s		-	45.0	98.0	23.8	-
CO/u2-s		-	45.0	99.3	24.1	-
CO/u3-s		-	45.0	91.2	23.8	-
CO/u1-f		-	45.0	96.9	26.1	-
CO/u2-f		-	45.0	95.5	24.1	-
CO/u3-f		-	45.0	94.3	24.5	-
CO/u1-c		-	45.0	100.5	24.8	-
CO/u2-c		-	45.0	96.6	24.4	-
CO/u3-c		-	45.0	102.2	24.8	-
TS/u1	Treated Soil	7.5-15.3	38.0	76.0	20.9	-
TS/u2		17.8-26.0	38.0	76.0	21.2	-
TS/u3		30.3-38.3	38.0	76.0	21.3	-

Tabella A2: List of specimen subjected to TRX tests.

Specimen code	Sample	Section [mm-mm]	D [mm]	H [mm]	γ_n [kN/m^3]	n [-]
I1-N/t1	I1-N/C6	-	70	140	22.36	0.25
I1-N/t2	I1-N/C10	-	70	140	22.36	0.25
I1-N/t3	I1-N/C4	-	70	149	22.01	0.27
I1-N/t4	I1-N/C4	-	70	143	22.08	0.26
I2-N/t1	I2-N/C3	-	70	140	21.54	0.30
I2-N/t2	I2-N/C9	-	70	140	21.54	0.30
I2-N/t3	I2-N/C3	-	70	140	21.51	0.30
I2-N/t4	I2-N/C3	-	70	141	21.38	0.30
M1-N/t1	M1-N	-	70	140	21.05	0.33
M1-N/t2		-	70	140	21.05	0.33
M2-N/t1	M2-N	-	70	142	20.43	0.36
M2-N/t2		-	70	140	20.73	0.34
M3-N/t1	M3-N	-	70	141.5	18.87	0.46
M3-N/t2		-	70	141.5	18.87	0.44
TS/t1	Treated Soil	47.0-55.0	38.0	80.0	21.4	-
TS/t2		38.3-46.5	38.0	80.0	21.1	-

Tabella A3: List of specimen subjected to BRZ tests.

Specimen code	Sample	Section [mm-mm]	D [mm]	H [mm]	γ_n [kN/m^3]	n [-]
M1-N/b1	M1-N	-	70	45	21.05	0.33
M1-N/b2		-	70	46	20.06	0.34
M1-N/b3		-	70	45	21.05	0.33
M2-N/b1	M2-N	-	70	46	20.49	0.36
M2-N/b2		-	70	46	20.49	0.34
M2-N/b3		-	70	45	20.95	0.35
M3-N/b1	M3-N	-	70	46	20.00	0.45
M3-N/b2		-	70	45.5	20.20	0.45
M3-N/b3		-	70	46	20.00	0.45
TS/b1	Treated Soil	5.2-7.5	38.3	23.0	20.9	-
TS/b2		15.3-17.8	38.1	21.0	20.8	-
TS/b3		26.2-28.1	39.0	19.0	21.3	-

Tabella A4: List of specimen subjected to PL tests.

Specimen code	Sample	Section [mm-mm]	D [mm]	H [mm]	γ_n [kN/m^3]	n [-]
I1-N/p1	I1-N	-	50	36	22.34	0.25
I1-N/p2		-	50	36	22.35	0.25
I2-N/p1	I2-N	-	50	32	21.41	0.30
I2-N/p2		-	50	39	21.39	0.30
I2-N/p1-h	I2-N	-	45	38	22.1	0.30
I2-N/p2-h		-	45	36.5	21.7	0.30
I2-N/p3-h		-	45	17.5	21.7	0.30
I2-N/p4-h		-	45	18	21.7	0.30
I2-N/p5-h		-	45	37	22.3	0.30
I2-N/p6-h		-	45	21	22.3	0.30
I2-N/p7-h		-	45	37	21.9	0.30
I2-N/p8-h		-	45	31	21.5	0.30
I2-N/p9-h		-	45	20	21	0.30
I2-N/p10-h		-	45	44	20.4	0.30

Appendix B

Chapter 3

Table B1: Physical and thermal parameters of soil sample and boundary conditions considered for each scenario of numerical simulations of freezing test performed on non-saline (M1-N, M2-N and M3-N) and saline (G1-S and G2-S) soils.

		NON -saline soils			**Sanline soils**	
Constant soil parameters	**U.M.**	**M1-N**	**M2-N**	**M3-N**	**G1-S**	**G2-S**
porosity - n	[-]	0.33	0.35	0.45	0.44	0.40
Saturation degree - S_r	[-]	1	1	1	0.99	0.99
Freezing point - T_{fp}	[°C]	0	0	0	-2.31	-2.59
Unfrozen volumetric heat capacity - C_{unf}	[kJ/m^3°C]	2,713.0	2,848.5	2,989.0	2,875.5	2,895.5
Frozen volumetric heat capacity - C_f	[kJ/m^3°C]	1,963.6	2,051.0	1,967.0	4,515.3	4,390.7
Initial temperature - T_0	[°C]	22.5	22.5	22.8	29.0	29.0
Temperature of air - T_{air}	[°C]	22.0	22.0	22.0	-30.0	-30.0
Constant neoprene parameters						
Volumetric heat capacity	[kJ/m^3°C]	400.0	400.0	400.0	-	-
Thermal conductivity	[W/m°C]	0.060	0.060	0.060	-	-
Scenario #1 - measured values						
Unfrozen thermal conductivity - k_{unf}	[W/m°C]	2.078	1.930	1.524	1.680	1.550
Frozen thermal conductivity - k_f	[W/m°C]	3.276	3.063	2.690	2.430	2.060
Heat convective coefficient - h	[kW/m^2°C]	0.007	0.007	0.007	0.007	0.007
Scenario #2 - Johansen, 1975						
Unfrozen thermal conductivity - k_{unf}	[W/m°C]	2.179	1.904	1.546	1.673	1.531
Frozen thermal conductivity - k_f	[W/m°C]	3.410	3.061	2.848	2.986	2.594
Heat convective coefficient - h	[kW/m^2°C]	0.007	0.007	0.007	0.007	0.007
Scenario #3 - Côté and Konrad, 2005						
Unfrozen thermal conductivity - k_{unf}	[W/m°C]	2.361	2.102	1.712	1.905	2.006
Frozen thermal conductivity - k_f	[W/m°C]	3.645	3.342	3.116	2.776	2.824
Heat convective coefficient - h	[kW/m^2°C]	0.007	0.007	0.007	0.007	0.007
Scenario #4 - no lateral BC						
Unfrozen thermal conductivity - k_{unf}	[W/m°C]	2.078	1.930	1.524	1.680	1.550
Frozen thermal conductivity - k_f	[W/m°C]	3.276	3.063	2.690	2.430	2.060
Heat convective coefficient - h	[kW/m^2°C]	0	0	0	0	0

Table B2: The Pearson correlation coefficients computed for each scenario considering the freezing test on M2-N soil sample.

Scenario	**1**	**2**	**3**	**4**
	Pearson Correlation			
E-0mm - N-BC	1	1	1	1
E-40mm - N-40mm	0.99925	0.99922	0.9987	0.99938
E-80mm - N-80mm	0.99715	0.997	0.99762	0.99568

Table B3: R-Square of the linear regression computed for each scenario considering the freezing test on M2-N soil sample.

	R-Square			
Scenario	**1**	**2**	**3**	**4**
N-40 mm	0.99851	0.99844	0.99741	0.99877
N-80 mm	0.99431	0.99401	0.99524	0.99138

Table B4: Values of the area between the two considered curves computed for each scenario considering the freezing test on M2-N soil sample.

Scenario	**1**	**2**	**3**	**4**
	Area between curves			
E-0mm - N-BC	0	0	0	0
E-40mm - N-40mm	1.06	1.01	3.73	8.5
E-80mm - N-80mm	1.16	1	4.02	8.06

Table B5: DTW computed for each scenario considering the freezing test on M2-N soil sample.

Scenario	**1**	**2**	**3**	**4**
	DTW			
E-0mm - N-BC	0	0	0	0
E-40mm - N-40mm	25.25	26.2	49.66	245.87
E-80mm - N-80mm	55.81	53.42	139.56	415.92

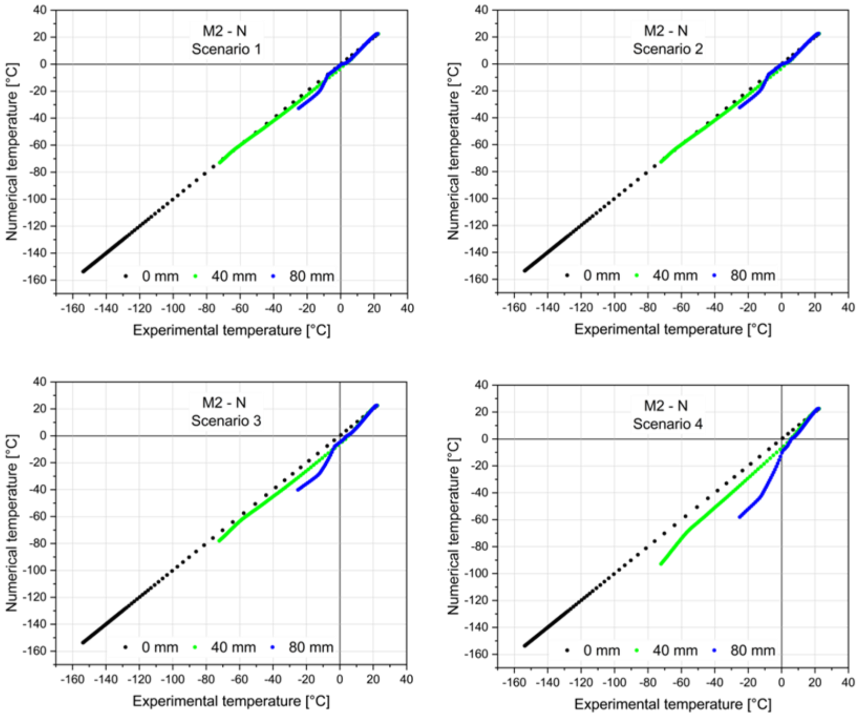

Figure B1: Scatterplot of comparison between experimental and numerical results of four scenarios of freezing test performed on M2-N soil sample: a) Scenario #1; b) Scenario #2; c) Scenario #3; d) Scenario #4

Table B6: The Pearson correlation coefficients computed for each scenario considering the freezing test on M3-N soil sample.

Scenario	**1**	**2**	**3**	**4**
	Pearson Correlation			
E-0mm - N-BC	1	1	1	1
E-40mm - N-40mm	0.99839	0.99877	0.9991	0.99556
E-80mm - N-80mm	0.98028	0.98125	0.98625	0.97412

Table B7: R-Square of the linear regression computed for each scenario considering the freezing test on M3-N soil sample.

	R-Square			
Scenario	**1**	**2**	**3**	**4**
N-40 mm	0.99678	0.99754	0.9982	0.99114
N-80 mm	0.96095	0.96286	0.97268	0.94892

Table B8: Values of the area between the two considered curves computed for each scenario considering the freezing test on M3-N soil sample.

Scenario	**1**	**2**	**3**	**4**
	Area between curves			
E-0mm - N-BC	0	0	0	0
E-40mm - N-40mm	1.53	0.88	4.90	10.46
E-80mm - N-80mm	1.81	0.75	5.37	9.51

Table B9: DTW computed for each scenario considering the freezing test on M3-N soil sample.

Scenario	**1**	**2**	**3**	**4**
	DTW			
E-0mm - N-BC	0	0	0	0
E-40mm - N-40mm	51.86	93.45	199.51	564.55
E-80mm - N-80mm	72.21	149.21	329.06	714.04

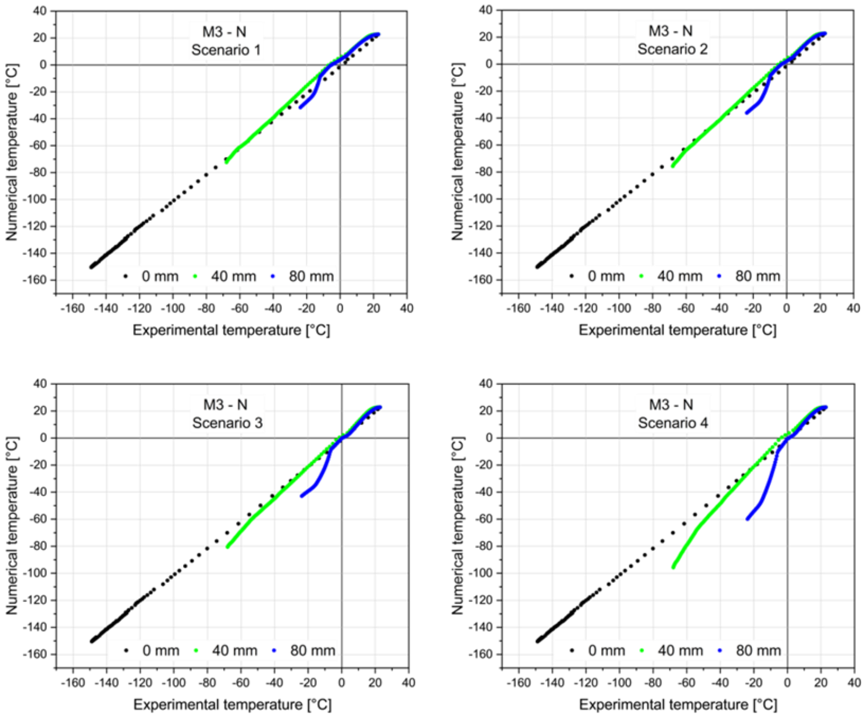

Figure B2: Scatterplot of comparison between experimental and numerical results of four scenarios of freezing test performed on M3-N soil sample: a) Scenario #1; b) Scenario #2; c) Scenario #3; d) Scenario #4.

Table B10: *The Pearson correlation coefficients computed for each scenario considering the freezing test on G1-S soil sample.*

Scenario	**1**	**2**	**3**	**4**
	Pearson Correlation			
E-0mm - N-BC	1	1	1	1
E-10mm - N-10mm	0.99684	0.99672	0.99703	0.99428
E-20mm - N-20mm	0.99598	0.99721	0.99684	0.98923
E-30mm - N-30mm	0.99488	0.99713	0.99628	0.98136
E-40mm - N-40mm	0.99106	0.9953	0.99375	0.96681

Table B11: R-Square of the linear regression computed for each scenario considering the freezing test on G1-S soil sample.

Scenario	**1**	**2**	**3**	**4**
	R-square			
N-10mm	0.99368	0.99346	0.99406	0.98859
N-20mm	0.99198	0.99442	0.99368	0.97858
N-30mm	0.98979	0.99427	0.99257	0.96307
N-40mm	0.98221	0.99062	0.98754	0.93472

Table B12: Values of the area between the two considered curves computed for each scenario considering the freezing test on G1-S soil sample.

Scenario	1	2	3	4
	Area between curves			
E-0mm - N-BC	0	0	0	0
E-10mm - N-10mm	4.99	3.72	4.01	15.35
E-20mm - N-20mm	7.65	5.54	6.01	27.81
E-30mm - N-30mm	8.98	6.30	6.89	37.65
E-40mm - N-40mm	10.73	7.71	8.38	46.32

Table B13: DTW computed for each scenario considering the freezing test on G1-S soil sample.

Scenario	1	2	3	4
	DTW			
E-0mm - N-BC	0	0	0	0
E-10mm - N-10mm	17.09	19.00	21.40	34.28
E-20mm - N-20mm	18.95	21.39	21.05	63.47
E-30mm - N-30mm	20.91	16.88	19.08	124.79
E-40mm - N-40mm	24.97	21.06	25.36	160.50

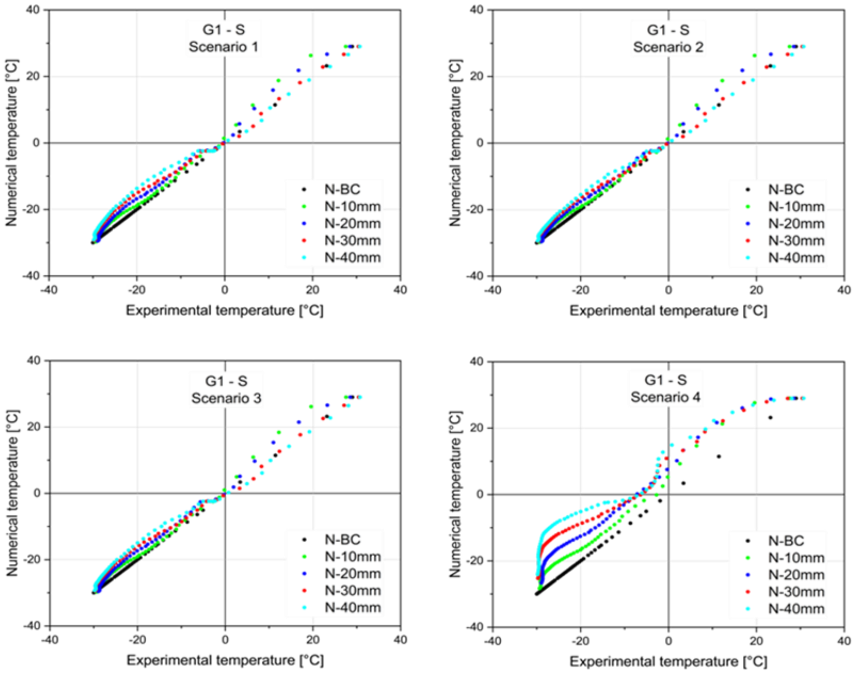

Figure B3: Scatterplot of comparison between experimental and numerical results of four scenarios of freezing test performed on G1-S soil sample: a) Scenario #1; b) Scenario #2; c) Scenario #3; d) Scenario #4.

Table B14: The Pearson correlation coefficients computed for each scenario considering the freezing test on G2-S soil sample.z

Scenario	**1**	**2**	**3**	**4**
	Pearson Correlation			
E-0mm - N-BC	1	1	1	1
E-10mm - N-10mm	0.99655	0.99659	0.99699	0.99452
E-20mm - N-20mm	0.9948	0.99643	0.99698	0.9895
E-30mm - N-30mm	0.99299	0.99611	0.99668	0.98203
E-40mm - N-40mm	0.98739	0.99316	0.99438	0.96736

Table B15: R-Square of the linear regression computed for each scenario considering the freezing test on G2-S soil sample.

Scenario	**1**	**2**	**3**	**4**
	R-square			
N-10mm	0.9931	0.99319	0.99399	0.98907
N-20mm	0.98963	0.99288	0.99396	0.97911
N-30mm	0.98604	0.99223	0.99337	0.96438
N-40mm	0.97494	0.98636	0.9888	0.93579

Table B16: Values of the area between the two considered curves computed for each scenario considering the freezing test on G2-S soil sample.

Scenario	1	2	3	4
	Area between curves			
E-0mm - N-BC	0	0	0	0
E-10mm - N-10mm	4.73	3.27	2.42	16.30
E-20mm - N-20mm	8.18	5.75	4.3	30.53
E-30mm - N-30mm	9.99	6.92	5.12	41.67
E-40mm - N-40mm	12.05	8.60	6.60	51.17

Table B17: DTW computed for each scenario considering the freezing test on G2-S soil sample.

Scenario	1	2	3	4
	DTW			
E-0mm - N-BC	0	0	0	0
E-10mm - N-10mm	18.05	21.93	24.8	35.6
E-20mm - N-20mm	19.88	21.66	27.81	77.27
E-30mm - N-30mm	17.8	20.17	16.23	154.21
E-40mm - N-40mm	21.42	17.85	21.52	203.07

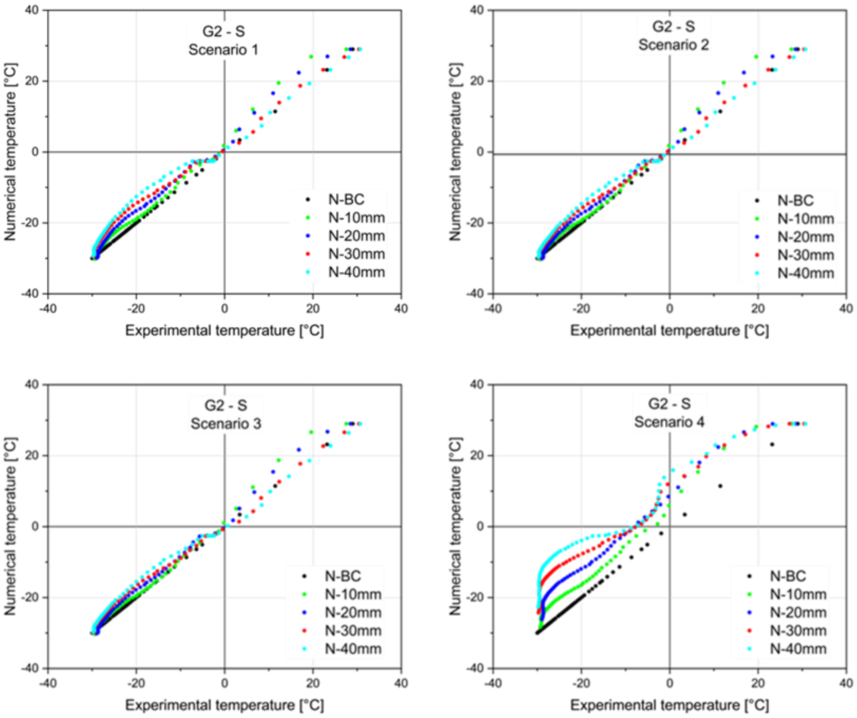

Figure B4: Scatterplot of comparison between experimental and numerical results of four scenario of freezing test performed on G1-S soil sample: a) Scenario 1; b) Scenario 2; c) Scenario 3; d) Scenario 4.

Appendix C

Chapter 4

Table C1: Results of on-site Point load tests on frozen blocks detached from excavation face at undefined temperature (T<0 °C).

Soil specimen	**Soil sample**	**W** [mm]	**D'** [mm]	**P** max load [kN]	I_s index PLS [Mpa]	$I_{s(50)}$ ASTM D5731 [MPa]
Iu-N/p1-s	Iu-N	112	25	5.02	1.41	1.53
Iu-N/p2-s	Iu-N	63	34	2.27	0.83	0.85
Iu-N/p3-s	Iu-N	102	32	4.43	1.07	1.20
Iu-N/p4-s	Iu-N	48	36	3.30	1.50	1.46
Iu-N/p5-s	Iu-N	88	18	0.86	0.42	0.40
Iu-N/p6-s	Iu-N	105	27	2.60	0.72	0.78
Iu-N/p7-s	Iu-N	81	48	2.61	0.53	0.61
Iu-N/p8-s	Iu-N	101	34	5.40	1.24	1.40
Iu-N/p9-s	Iu-N	62	54	3.11	0.73	0.82
Iu-N/p10-s	Iu-N	62	28	2.62	1.19	1.15
Iu-N/p11-s	Iu-N	61	24	1.08	0.58	0.54
Iu-N/p12-s	Iu-N	77	27	3.17	1.20	1.21
Iu-N/p13-s	Iu-N	63	40	3.75	1.17	1.24
Iu-N/p14-s	Iu-N	107	65	4.80	0.54	0.72
Iu-N/p15-s	Iu-N	100	72	4.80	0.52	0.70
Iu-N/p16-s	Iu-N	93	35	4.90	1.18	1.32
Iu-N/p17-s	Iu-N	96	36	3.50	0.80	0.90
Iu-N/p18-s	Iu-N	69	30	5.01	1.90	1.92
Iu-N/p19-s	Iu-N	72	25	3.20	1.40	1.37
Iu-N/p20-s	Iu-N	58	19	2.80	2.00	1.75
Iu-N/p21-s	Iu-N	112	18	2.30	0.90	0.90
Iu-N/p22-s	Iu-N	84	63	3.70	0.55	0.69
Iu-N/p23-s	Iu-N	112	40	8.30	1.46	1.75
Iu-N/p24-s	Iu-N	115	53	6.90	0.89	1.15
Iu-N/p25-s	Iu-N	84	51	7.20	1.32	1.57
Iu-N/p26-s	Iu-N	64	24	3.70	1.89	1.79
Iu-N/p27-s	Iu-N	69	21	2.30	1.25	1.16
Iu-N/p28-s	Iu-N	113	37	3.20	0.60	0.71
Iu-N/p29-s	Iu-N	80	23	4.30	1.84	1.81
Iu-N/p30-s	Iu-N	120	48	7.50	1.02	1.30

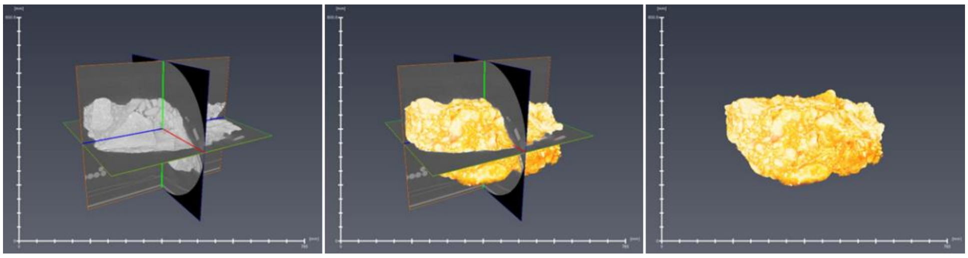

Figure C1: Orthogonal slices from CT analysis and 3D views of A2 frozen block elaborated by Avizo.

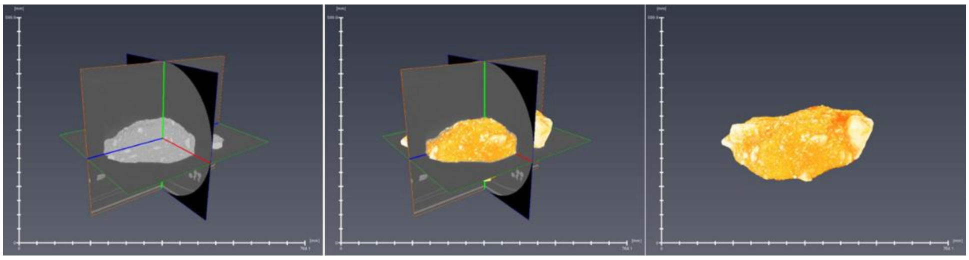

Figure C2: Orthogonal slices from CT analysis and 3D views of B1 frozen block elaborated by Avizo.

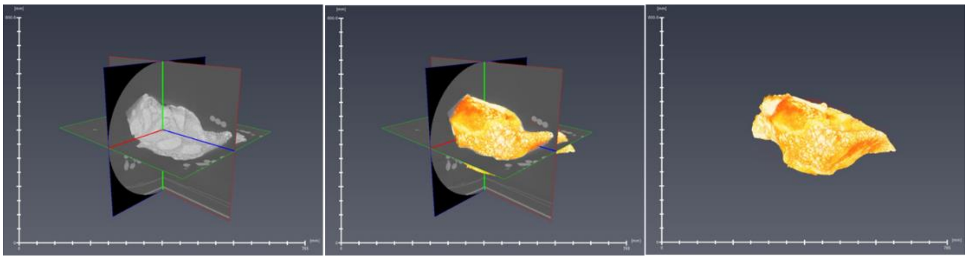

Figure C3: Orthogonal slices from CT analysis and 3D views of B2 frozen block elaborated by Avizo.

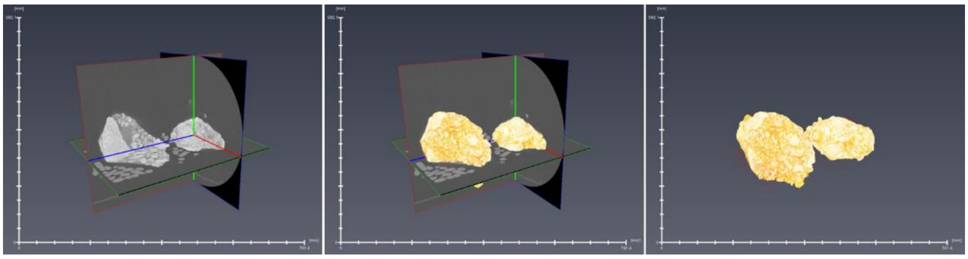

Figure C4: Orthogonal slices from CT analysis and 3D views of C1 and C2 frozen blocks elaborated by Avizo.

Table C2: Undisturbed soil specimen cored from blocks B1 and B3 subjected to UCS test at -10°C.

Specimen code	**Sample**	**Frozen block**	**D** [mm]	**H** [mm]	γ_n [kN/m^3]	**n** [-]	**Sr** [-]
Iu-N/u1	Iu-N	B1	39.0	60.0	18.84	0.4	0.81
Iu-N/u2	Iu-N	B1	32.9	47.2	18.48	0.39	0.67
Iu-N/u3	Iu-N	B3	46.5	94.9	19.85	0.37	0.93

Table C3: Results of Point Load test executed at -10 °C on undisturbed samples obtained from resulting material of blocks B1 and B3.

Soil specimen	**Soil sample**	**W** [mm]	**D'** [mm]	**P** max load [kN]	I_s index PLS [Mpa]	$I_{s(50)}$ ASTM D5731 [MPa]
Iu-N/p1	Frozen block B1	70.0	36.0	2.56	0.80	0.84
Iu-N/p2		54.0	27.0	1.30	0.70	0.65
Iu-N/p3		65.0	25.0	1.47	0.71	0.68
Iu-N/p4		42.0	35.0	1.89	1.01	0.95
Iu-N/p5		50.4	27.0	1.28	0.74	0.68
Iu-N/p6		62.3	22.0	1.76	1.01	0.93
Iu-N/p7		53.2	27.0	3.13	1.71	1.60
Iu-N/p8		94.4	40.0	4.59	0.96	1.11
Iu-N/p9		73.6	34.0	3.09	0.97	1.02
Iu-N/p10		48.2	40.0	1.36	0.55	0.55
Iu-N/p11	Frozen block B3	14.2	22.0	1.48	3.73	2.47
Iu-N/p12		29.6	19.0	1.43	2.00	1.51
Iu-N/p13		51.6	31.0	2.44	1.20	1.15
Iu-N/p14		47.6	28.0	2.23	1.32	1.21
Iu-N/p15		79.0	34.0	3.84	1.12	1.20
Iu-N/p16		55.0	24.0	2.18	1.29	1.18
Iu-N/p17		42.0	23.0	2.28	1.86	1.58
Iu-N/p18		68.0	45.0	5.57	1.43	1.58
Iu-N/p19		55.0	30.0	2.39	1.14	1.09
Iu-N/p20		67.7	19.0	1.28	0.78	0.71

Table C4: Undisturbed soil specimen cored from blocks B1 and B3 subjected to UCS test at -6°C.

Specimen code	**Sample**	**Frozen block**	**D** [mm]	**H** [mm]	γ_n [kN/m^3]	**n** [-]	**Sr** [-]
Iu-N/u1-h	Iu-N	B1	48.7	91.2	21.10	0.29	0.89
Iu-N/u2-h	Iu-N		48.5	87.1	19.30	0.37	0.76
Iu-N/u3-h	Iu-N		49.0	93.4	20.20	0.33	0.84
Iu-N/u4-h	Iu-N		49.0	80.9	20.00	0.35	0.85
Iu-N/u5-h	Iu-N	B3	48.8	61.0	20.40	0.33	0.89
Iu-N/u6-h	Iu-N		48.8	109.6	20.70	0.31	0.84

Table C5: Results of Point Load test executed at -6 °C on undisturbed samples obtained from resulting material of blocks B1.

Soil specimen	**Soil sample**	**W** [mm]	**D'** [mm]	**P** max load [kN]	I_s index PLS [Mpa]	$I_{s(50)}$ ASTM D5731 [MPa]
Iu-N/p1-h	Frozen block B1	52.0	19.5	1.26	0.98	0.84
Iu-N/p2-h		42.1	29.0	0.98	0.63	0.57
Iu-N/p3-h		72.8	30.0	2.91	1.05	1.07
Iu-N/p4-h		50.0	31.0	1.25	0.63	0.60
Iu-N/p5-h		67.2	22.0	1.63	0.87	0.81
Iu-N/p6-h		89.5	32.0	2.26	0.62	0.68
Iu-N/p7-h		71.0	24.0	1.54	0.71	0.69
Iu-N/p8-h		55.0	35.0	1.25	0.51	0.51
Iu-N/p9-h		51.6	36.0	1.68	0.71	0.70
Iu-N/p10-h		97.0	29.5	2.55	0.70	0.76
Iu-N/p11-h		67.0	18.0	1.69	1.10	0.98
Iu-N/p12-h		69.0	28.0	1.37	0.56	0.56
Iu-N/p13-h		71.4	42.0	3.30	0.86	0.95
Iu-N/p14-h		72.0	49.0	1.76	0.39	0.45
Iu-N/p15-h		99.9	26.0	2.40	0.73	0.77
Iu-N/p16-h		71.0	25.0	1.77	0.78	0.77
Iu-N/p17-h		68.0	19.0	1.20	0.73	0.66

Table C6: Undisturbed soil specimen cored from blocks B3 subjected to TRX test at -10°C

Specimen code	**Sample**	**Frozen block**	**D** [mm]	**H** [mm]	γ_n [kN/m^3]	**n** [-]	**Sr** [-]
Iu-N/t1	Iu-N	B3	46.0	105.6	19.96	0.36	0.91
Iu-N/t2	Iu-N		49.2	119.4	20.94	0.3	0.88

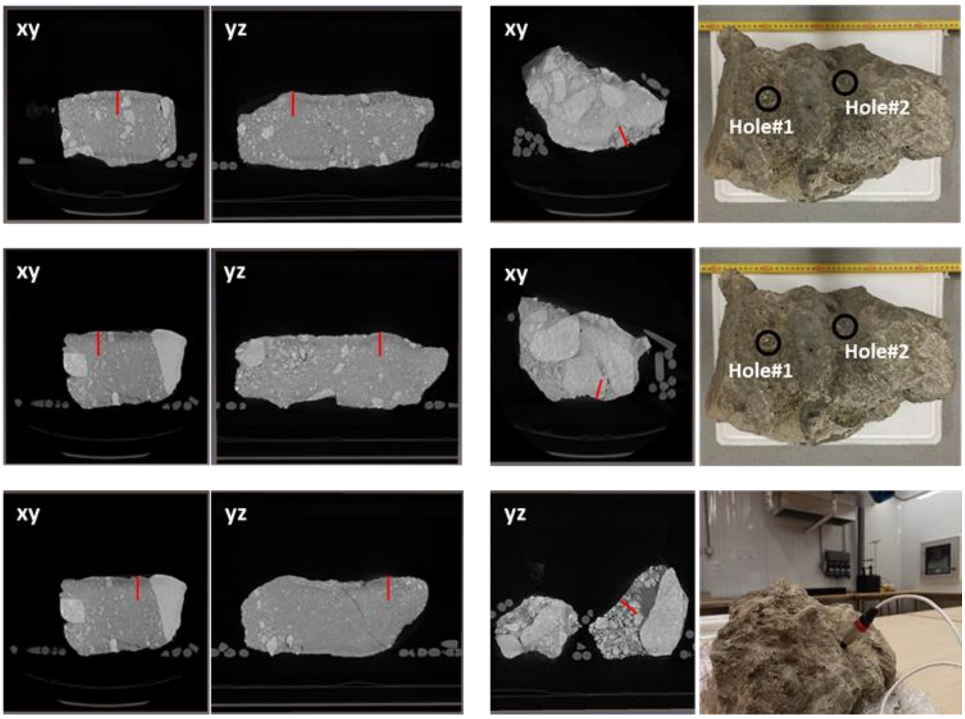

Figure C5: thermal conductivity - needle probe disposition (red line) into 2D slices from CT analysis of different frozen blocks: some pictures of block and drilled holes are provided.

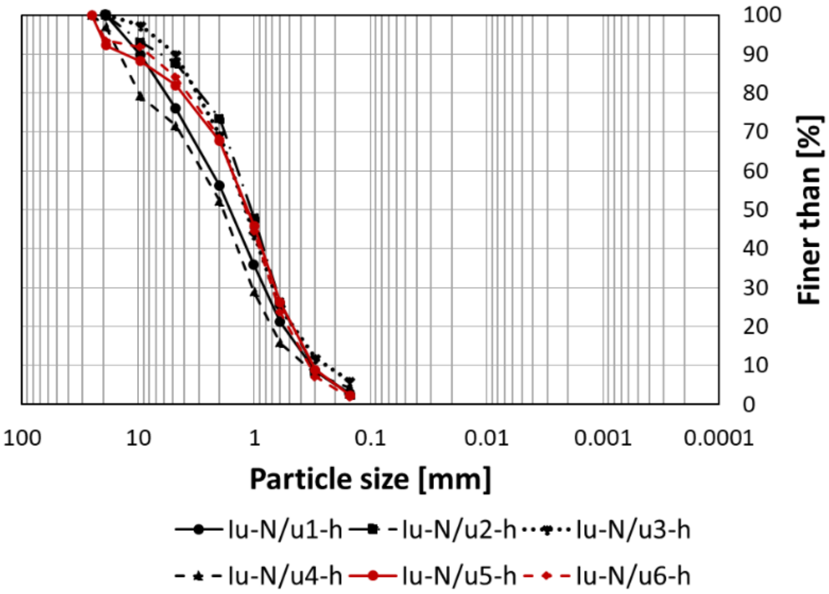

Figure C6: Particles size analysis of undistubed specimens subjected to unconfined compression tests at -6 °C.